Nanostructures magnetiques auto-assemblees sur des surfaces a faible energie par epitaxie par jets moleculaires

Fabiola Liscio

INSTITUT POLYTECHNIQUE DE GRENOBLE

N° attribué par la bibliothèque

|__|__|__|__|__|__|__|__|__|__|__|__|

THESE EN COTUTELLE INTERNATIONALE

pour obtenir le grade de

DOCTEUR DE l'Institut Polytechnique de Grenoble
et
de l'Université de "Rome Tre"

Spécialité: "Matériaux, Mécanique, Génie civil, Electrochimie"

préparée au Laboratoire de Science et Ingénierie des Matériaux et Procédés (SIMaP)
dans le cadre de **l'École Doctorale** "Ingénierie - Matériaux, Mécanique, Energétique, Environnement, Procédés, Production" (I-MEP2)

et au "Dipartimento di fisica E. Amaldi"
dans le cadre de **l'École Doctorale** de "Physique"

présentée et soutenue publiquement
par

Fabiola LISCIO

le 30 Janvier 2009

Self-assembled magnetic nanostructures prepared by molecular beam epitaxy on low energy surfaces

DIRECTEURS DE THESE

Dr. Mireille MARET
Prof. Settimio MOBILIO

JURY

M. Hubert RENEVIER,	Président
M. Maurizio DE CRESCENZI,	Rapporteur
M. Claude HENRY,	Rapporteur
Mme. Mireille MARET,	Directeur de thèse en France
M. Settimio MOBILIO,	Directeur de thèse en Italie
M. Manfred ALBRECHT,	Examinateur
M. Carlo MENEGHINI,	Invité

To my grandfather,
shyly proud of his granddaughter.
I did it once more.

Acknowledgements

A marvellous journey of almost four years has ended. It was rich in instructive experiences, sometimes difficult, but unforgettable nonetheless. I have met along the way a lot of travellers, some of them are still here to encourage me in this achievement, others were just passing companions but they have left their mark on my travel journal. It is a pleasant aspect to now have the opportunity to express my gratitude for all of them.

The first person I would like to thank is my direct supervisor Dr. Mireille Maret. During the three years of my PhD I have known Mireille as a sympathetic and principle-centred person. Her overly enthusiastic and integral view on research has made a deep impression on me. I owe her lots of gratitude for having shown to me her way of doing research and for pushing me to continue my work when faced with many difficulties.

I would like to thank Prof. Settimio Mobilio who kept an eye on the progress of my work and who gave me the opportunity to obtain another academic qualification. I would also like to thank the other members of my PhD committee who monitored my work and took effort in reading and providing me with valuable comments on earlier versions of this thesis: Prof. Claude Henry, Prof. Maurizio De Crescenzi and Prof. Hubert Renevier. I thank you all.

Although a PhD thesis is often seen as the author's own work, it is actually the result of many others helpful advice, useful suggestions and enthusiastic contributions.

I would like to express my deepest gratitude to Dr. Carlo Meneghini for his help in EXAFS analysis. Besides being my advisor, Carlo was as close as a relative and a good friend to me. He gave me the ticket of this journey four years ago and he is still following me. I am really glad that I have came to know Carlo in my life.

I would like to give my sincere gratitude to Prof. Manfred Albrecht for his collaboration in sample preparation and magnetic characterization in Konstanz University. In particular, I am grateful to Dr. Denys Makarov, who welcomed and helped me in Konstanz and provided me with measurements.

I would like to thank Jean Paul Simon with his useful ideas and help in performing the GISAXS measurements.

Béatrice Doisneau-Cottignies deserves a special thanks for her help and the quiet discussions during TEM measurements. Thank you for your kindness.

All my lab mates at the PM-SIMaP made it a convivial place to work. In particular, I would like to thank Ian, a colleague and a dear friend, for the many discussions between us and for providing me brotherly advice that helped me a lot in staying on the right

track. I thank Guillaume (and Steph) *the likeable* and Thorsten *the quiet* who gave me the feeling of being at home in the office. Thanks to Michel and Valérie who were very kind with me when I arrived at the ex-LTPCM without speaking French, and also Nico, Béchir, Oussama, Jean Louis, Benjamin, Eduardo, Gwanaël, Shin, etc... the PhD students of the PMD group. I would have had liked to know all of them better, but I have not spent enough time because my luggage was always ready for the next up-and-coming trip.

During this journey I participated in several international conferences and schools, where I could share new scientific knowledge and pleasant time with some nice people. Therefore, I would like to thank everybody I knew and in particular Louis, Christian and Nicolas.

Life is not only work, so, I would like to thank my dear friend Roberta, ti ho conosciuto all'inizio di questa avventura e sei stata per me il mio punto di riferimento, ed insieme ad Alex siete stati la mia famiglia grenobloise. È stato difficile vederti partire, ma bello scoprire che posso sempre contare su di te. Grazie Robiertina e grazie anche a te Alex. After them, I cannot forget to thank Fabri, Orietta, Margherita, Peppe, Mauro, Pedro, Alonso's family, Edmundiño's family, Giuliana, Angela, Bea, Lello, Lucia-Matilde, Julio, Miguel, Mario, Diletta&Ciccio, Elisa, Gianluca, Felisa, Valerio, Olga, Oke, Jorje, Christophe... and the newcomers Raffa, Sheeba and Davide.

Nella lista dei miei ringraziamenti non possono mancare tutti gli affetti che mi legano a Roma. A partire dalle vecchie amicizie che, anche se non ho più frequento quotidianamente, le ho sentite sempre vicine a me. Grazie a Saretta, la mia eterna compagnetta di (dis)avventure nel reame della fisica (e non solo). Grazie alla mia amica da sempre Lauretta che anche in questo momento di difficoltà non mi ha dimenticata. Grazie a Taty e Claudia che sempre sorridenti mi hanno accolto nella stanza 58. Grazie alla mia nuova cognatina Lia per avermi sempre trasmesso dolcezza e tenerezza. Grazie alla nuova famiglia Claudia, Claudio e Francy, per avermi trasmesso tanto affetto. Grazie a Fede, immancabile nelle uscitine romane.

La mia più profonda gratitudine va a mamma, papà e nonna per il loro instancabile amore e supporto, per avermi insegnato le cose più importanti della vita, il rispetto, la lealtà, il senso del dovere e la disponibilità verso gli altri. Un Tera grazie al mio fratellone Andrea, la mia fonte di ispirazione, che mi ha insegnato a ragionare e ad amare questo fantastico mondo della Scienza.

Un grazie Speciale a Otello, amico e compagno che questo viaggio mi ha portato a conoscere e ad amare. Grazie a te ho vissuto degli indimenticabili momenti, i più belli che abbia mai vissuto. Ti ringrazio per essermi stato sempre vicino anche quando questo viaggio ci ha separato. Grazie per avermi dato sostegno, conforto e coraggio perché senza di te non ce l'avrei fatta. E grazie per avermi aspettato così che ora potremo essere di nuovo insieme a condividere tutti i nostri interessi e a costruire una nostra famiglia.

The last acknowledgement goes to those who are going to read this manuscript. I hope it is useful.

Contents

Introduction

The last fifteen years have seen the explosive development of a new field, now commonly known as nanoscience [1]. This field extends through physics, chemistry and engineering and addresses a number of important issues, ranging from basic science to a variety of technological applications. The purpose of nanoscience and nanotechnology is to understand, to control and to manipulate objects of a few nanometers in size (1-100 nm). These nano-objects are thus intermediate between single atoms and bulk matter. Their properties varying strongly with the size can, therefore, be tuned by controlling precisely their formation.

For instance, the considerable increase in magnetization processes studies on nanometer length scale [2–4], has brought progress in ultra high density magnetic recording [5], based on media formed of the weakly coupled magnetic grains. In order to increase the areal storage density (number of stored bits/in^2) and substantially to reduce hard disk drives (HDD) size (figure 1), metal thin film media with smaller particles, very narrow size distributions and optimized compositions are required. The reduction of particle volume decreases the thermal stability of the stored information, leading to thermally activated fluctuations of the magnetization orientation of individual grain and to data loss [6]. In order to overcome this limit, materials with high perpendicular magnetic anisotropy (PMA) are necessary.

In this regard, the most promising candidates for future ultra-high density magnetic recording applications are the chemically $L1_0$ ordered FePt and CoPt alloys with magnetic

Figure 1: Hitachi microdrive (www.hitachigst.com)

anisotropy constants of about 10 MJ/m^3 and 3 MJ/m^3, respectively. However, the phase transformation from the disordered fcc to the chemically ordered fct phase occurs typically at high annealing temperatures above 800K which is not favourable for applications [7, 8]. Therefore, many studies are directed to lower the ordering temperature.

A reduction in ordering temperature was reported for the $CoPt_3$(111) nanostructures grown on the quasi-Van der Waals surface of WSe_2(0001) [9, 10] by molecular beam epitaxy. A surprising strong PMA was observed in nanoparticles grown at room temperature. Note that this out-of-plane easy axis magnetization is expected neither in the disordered fcc structure nor in the $L1_2$-ordered $CoPt_3$(111) phase. Such PMA was also observed in thin $CoPt_3$(111) films grown on different substrates, such as Pt(111) and Ru(0001), at higher deposition temperatures about 690K, before long-range $L1_2$-type chemical ordering [11, 12]. The magnetic anisotropy observed in continuous films was attributed to the appearance of a short range anisotropic chemical order, characterized by the preference of CoCo pairs in the film plane.

In this context, the first objective of this work is to probe such anisotropic local order effects in the fcc $CoPt_3$(111) nanostructures grown on WSe_2(0001) at room temperature, in order to understand the origin of the PMA obtained at low deposition temperature. For this purpose, the polarization sensitivity of the XAFS signal allows to sort out neighbor atoms that are located in the same (111) plane as the absorbing atom or out of this plane. Since structural and magnetic properties of epitaxial nanostructures are strongly correlated with the nature of substrate, the characterization of the local ordering is also presented for 001-oriented $CoPt_3$ nanostructures grown on the low energy surface NaCl(001). A comparison of these results will allow us to understand the role played by the WSe_2 substrate on the PMA and also on the lowering of the ordering temperature.

Since the formation of $L1_0$ ordered nanostructures is favorable to a PMA, an attempt to reduce the ordering temperature of the CoPt equiatomic alloy is performed by growing CoPt nanostructures on the WSe_2(0001) surface. Their structural and magnetic characterization is reported as a function of the deposition temperature. As the nature of the substrate, the growth temperature plays an important role in defining the size, the density and the size distribution of nanostructures. In general, the particle size increases and consequently the particle density decreases with increasing temperature. The size and the morphology of the self-assembled nanostructures are characterized by grazing incidence small angle x-ray scattering (GISAXS), coupled to other characterization techniques (TEM, STM and Field Emission-SEM). A comparison between the morphology resulting from the two growth directions, [111] and [001], is presented.

The formation of 001-oriented FePt nanoparticles with very narrow size distribution, which are the most promising candidates for ultra high density magnetic recording, are obtained by depositing on NaCl(001) substrate. The structural and magnetic properties of these nanoparticles are compared with those of nanoparticles formed simultaneously on MgO(001) substrates with a higher surface energy.

The thesis is organized as follows. The first chapter reports on the magnetic recording principles, the different growth modes of epitaxy, the description of the $M_{1-x}Pt_x$ (M=Co,Fe) binary alloys and previously results obtained on self-assembled nanostructures grown on WSe_2(0001) and NaCl(001). In chapter 2 the characterization techniques for the studies of structure at short as well as long range and morphology are reviewed. The chapter 3 deals with the determination of the structural origin of perpendicular magnetic anisotropy observed in nanostructured films of $CoPt_3$ grown on WSe_2(0001) and the study of their morphology as a function of the deposition temperature. The chapter 4 concerns the study of $CoPt_3$ nanostructures grown at different deposition temperatures on NaCl(001). Their morphology was characterised by HRTEM and GISAXS. The chapter 5 and 6 are related to the growth of the $L1_0$-ordered CoPt or FePt nanostructures. The fifth chapter reports on the growth, structure, morphology and magnetic properties of CoPt nanoparticles epitaxially grown on WSe_2(0001) at different temperatures. In the chapter 6 the growth and the structure of FePt nanostructures simultaneously prepared on NaCl(001) and MgO(001) substrates at different temperatures are compared and discussed. A summary of the most relevant results concludes the manuscript.

Chapter 1

Background

Owing to their magnetocrystalline anisotropy, the class of $M_{1-x}Pt_x$ binary alloy films, with M=Co, Cr and Fe, has been extensively studied as potential media for ultra high density magnetic recording. Their magnetic properties are correlated with the structural properties, chemical order and morphology which can be tuned acting on the fabrication parameters. For the last twenty years, numerous physics and engineering research studies have been thus carried out to improve the magnetic properties of Fe-Pt and Co-Pt alloys by reducing the grain size to increase the areal recording density. Therefore fundamental studies have been done to study the effects of reduced size on the physical and thermodynamic properties. In this chapter, I shall describe first the magnetic recording principles, secondly the different growth modes of epitaxy, thirdly the CoPt and FePt alloy phases including a state-of-art on the influence of size on chemical ordering. I will finish summing up the previous results obtained on self-assembled nanostructures grown on WSe_2 and NaCl.

1.1 Magnetic recording

For nearly 40 years, the disk drive industry has focused nearly exclusively on longitudinal magnetic recording, where the magnetization of the recorded bit lies in the plane of the disk [13]. These systems contain a recording head composed of separated read and write elements, which flies in the close proximity to a granular recording medium, as illustrated in figure 1.1. The inductive write element records the data in horizontal magnetization patterns. The information is then read back with the giant magnetoresistive (GMR) read element by measuring the stray magnetic field from the transitions between regions of opposite magnetization. Finally, a signal processing unit transforms the analog readback signal into a stream of data bits.

In longitudinal recording, the readback signal is roughly proportional to the magnetic thickness of the media $M_r t$, where M_r is the remanent magnetization and t is the physical thickness of the media. The magnetic width of the transitions is characterized by a transition parameter a, which depends both on the write head characteristics as well as

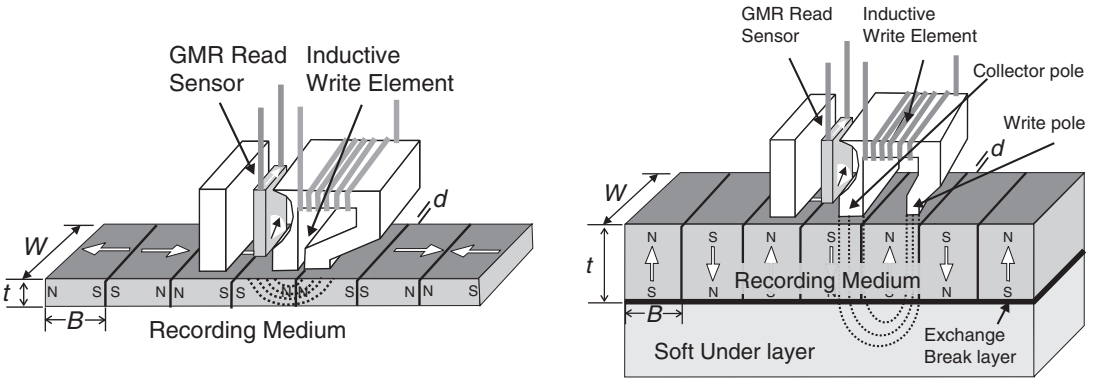

Figure 1.1: On the left, schematic drawing of a longitudinal recording system. B is the bit length, W is the track width and t is the medium thickness. d is the flying height of the head above the medium. On the right, schematic drawing of a one type of perpendicular recording system.

media parameters as the coercivity of the medium, H_c.

The required signal-to-noise ratio (SNR) needed for high-density recording is achieved by statistically averaging over many grains. In order to increase the areal density, i.e. reduce the bit length (B) and the track width W, traditional engineering requires that all design parameters of the head and the recording media be scaled to smaller dimensions. These scaling laws involve a reduction of the recording layer magnetic thickness $M_r t$ to reduce the transition parameter a and the grain diameter D in order to maintain a good SNR. This can be estimated from [14, 15]:

$$SNR \approx \frac{B^2 W_{read}}{\alpha^2 D^3 (1+\sigma^2)}, \tag{1.1}$$

where $\alpha = a/D$, σ is the normalized grain size distribution width and W_{read} is the read width of the head. In the eq. 1.1, valid only for uncorrelated noise, the grain size diameter D is to the 3rd power and therefore reducing D is very effective in improving SNR.

As the volume $V = \pi D^2 t/4$ of the grains is reduced in the scaling process, the magnetization of the grains may became unstable due to the thermal fluctuations, and data loss may occur [6]. This phenomenon, also referred to as the 'superparamagnetic effect', became increasingly important in recent years.

These thermal effects can be describe by the following simple model. The weak intergranular exchange coupling allows the longitudinal recording medium to be approximated as a collection of independent particles. The energy barrier for magnetization reversal in the presence of an external magnetic field H is given by

$$E_B(H,V) = K_u V \left(1 - \frac{H}{H_0}\right)^n \tag{1.2}$$

where K_u is the magnetic anisotropy density and H_0 is the intrinsic switching field. When considering finite temperatures, the energy barrier needs to be compared to the thermal

activation energy k_BT, where k_B is Boltzmann's constant and T is the absolute temperature. Thermally activated switching is characterized by a time constant τ following the Arrhenius Néel law [16]:

$$\tau \propto \exp\left(\frac{E_B}{k_BT}\right). \tag{1.3}$$

From eq. 1.2 and 1.3, it follows that a reduction of the grain volumes leads to smaller time constants that can, in turn, lead to signal decay and potential data loss as the medium is thermally demagnetized. The thermal stability is thus given by the factor K_uV/k_BT. One approach to overcome the superparamagnetic limit is to compensate the decrease of grain size by increasing the magnetic anisotropy. In this regard magnetic alloys like $L1_0$ ordered FePt [7] and CoPt films have attracted attention because of their high K_u value which is promoted by alternate pure Pt and pure Fe/Co layers along the tetragonal axis.

In 1975, Iwasaki and Takemura predicted and proposed the perpendicular magnetic recording, where the easy magnetization axis is pointing perpendicular to the film surface, to improve the thermal stability [17]. In this system (see figure 1.1) the tiny magnets are standing up and down. Adjacent alternating bits stand with north pole next to the pole; thus, they want to attract each other and are more stable and can be packed more closely than in longitudinal media. Weller et al. have calculated that FePt could be thermally stable, even for grain sizes as small as 3 nm. If it is possible to make such material, the areal density that can be achieved with FePt could easily surpass 1 Tbits/in^2. With this idea in mind, many researchers have been working on Fe/Pt and Co/Pt systems.

A way to improve the magnetic properties of these binary alloys is to act on the preparation method. Improving the epitaxial growth, for example, can enhance the thermal stability. In this regard, during the preparation several parameters can be tuned in order to improve their intrinsic properties: deposition temperature, deposition rate and chemical composition. The physical processes occurring during deposition are described in the next paragraph.

1.2 Growth mechanisms

1.2.1 Heteroepitaxy

Epitaxy refers to the deposition of a monocrystalline film on a monocrystalline substrate. The deposited film is denoted as epitaxial film or epitaxial layer.

Epitaxial films may be grown from gaseous or liquid precursors. Because the substrate acts as a seed crystal, the deposited film takes on a lattice structure and orientation identical to those of the substrate. This is different from other thin-film deposition methods which deposit polycrystalline or amorphous films, even on single-crystal substrates. If a film is deposited on a substrate of the same composition, the process is called homoepitaxy; otherwise, it is called heteroepitaxy.

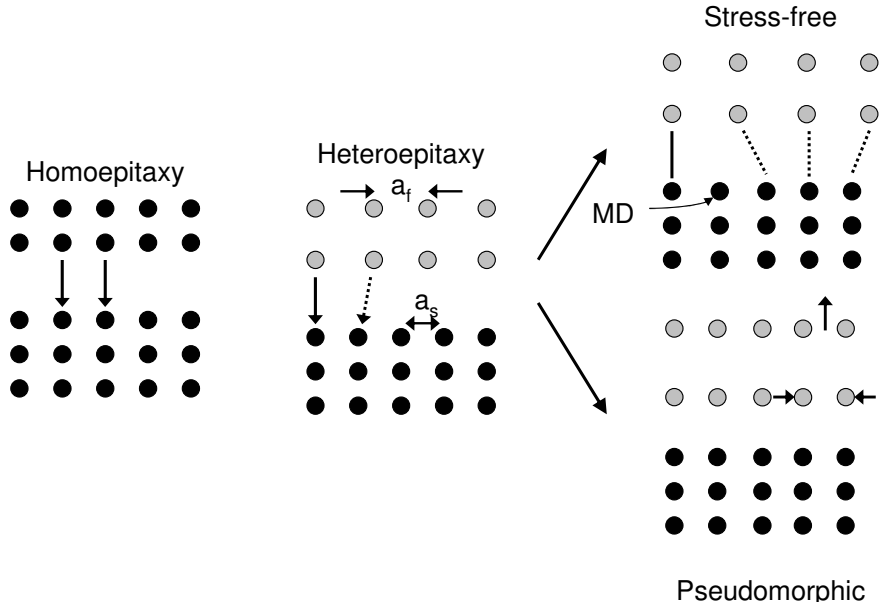

Figure 1.2: Schematic illustration of heteroepitaxial film growth with lattice mismatch.

In heteroepitaxial film growth, the substrate crystal structure provides a template for positioning the first impinging atoms, and each atomic layer has the same function for the next layer. When the mismatch in lattice parameter is not large, say below 0.5% or so, then growth tends to be planar. If the mismatch is large, the material tends to gather into islands on the surface but remain epitaxial.

In term of lattice parameters, this mismatch strain is

$$f = \frac{|a_s - a_f|}{a_s}, \tag{1.4}$$

where a_s and a_f denote the substrate and film in-plane lattice constants. When this value is different to zero, the heteroepitaxial layer structure is correlated both to the elastic and surface strains along the interface. The growth is pseudomorphic or coherently strained when the film is stretched or compressed such that the substrate and film in-plane lattice constants coincide. The growth is stress-free, or incoherent, when the substrate and film keep their parameters: to compensate for this deviation, misfit dislocations (MD) are formed.

The different types of heteroepitaxial growth are illustrated in figure 1.2.

When there is a lattice mismatch, the stress-free and pseudomorphic growths are in competition. In the pseudomorphic layer the elastic energy [18] is accumulated and the cell strain along the direction parallel to the surface is defined as

$$\epsilon_{\parallel} = \frac{|a_{f\parallel} - a_f|}{a_f}, \tag{1.5}$$

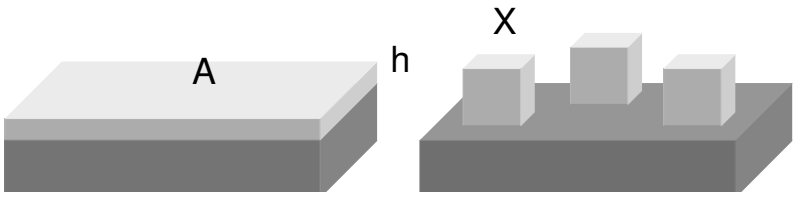

Figure 1.3: Planar and cubic island growth.

where $a_{f\parallel}$ is the lattice parameter of the deformed cell. The tetragonal distortion, called Poisson ratio, is

$$\nu = \frac{\epsilon_\perp}{\epsilon_\parallel}, \tag{1.6}$$

where $\epsilon_\perp$ is the deformation along the perpendicular direction. It follows that the elastic energy per unit volume of an isotropic film ($\epsilon = f$) is

$$E_{el} = 2\mu_f \left(\frac{1+\nu}{1-\nu}\right) f^2 h, \tag{1.7}$$

where μ_f is the shear force module and h the film thickness. Since this energy increases with h, the growth is coherent up to a critical thickness, over that the dislocation energy will be lower than elastic energy: the film plastically relaxes with the introduction of dislocations at a distance equal to $\lambda_{MD} = a_f/f$.

Another way to reduce the elastic energy is to form 3D islands. Such a growth mechanism increases the surface area and consequently the surface energy of the film.

To understand when the 3D growth is favored with respect to a planar film, their internal energies have to be compared. Let one consider on one hand a strained film with area A and atomic density N and on the other hand m stress-free cubic clusters with side X and atomic density n (figure 1.3). The total energy is given by the sum of surface and elastic energies.

Assuming that the surface energy density γ is the same for the film and substrate, the ratio of energies for the planar film (E_p) of thickness h and the clusters (E_c) will be:

$$\rho = \frac{E_p}{E_c} = \frac{A\gamma + E_{el}Ah}{A\gamma + 4X^2\gamma m} \tag{1.8}$$

where E_{el} is the elastic energy density defined in eq. 1.7 for the planar film and $4X^2\gamma m$ the additional surface energy for the 3D islands.

¿From mass conservation (i.e. $mnX^3 = NhA$) it follows:

$$\rho = \frac{A\gamma + E_{el}Ah}{A\gamma + \frac{4hAN\gamma}{nX}}. \tag{1.9}$$

The two configurations are in equilibrium when ρ=1. The critical island size is defined

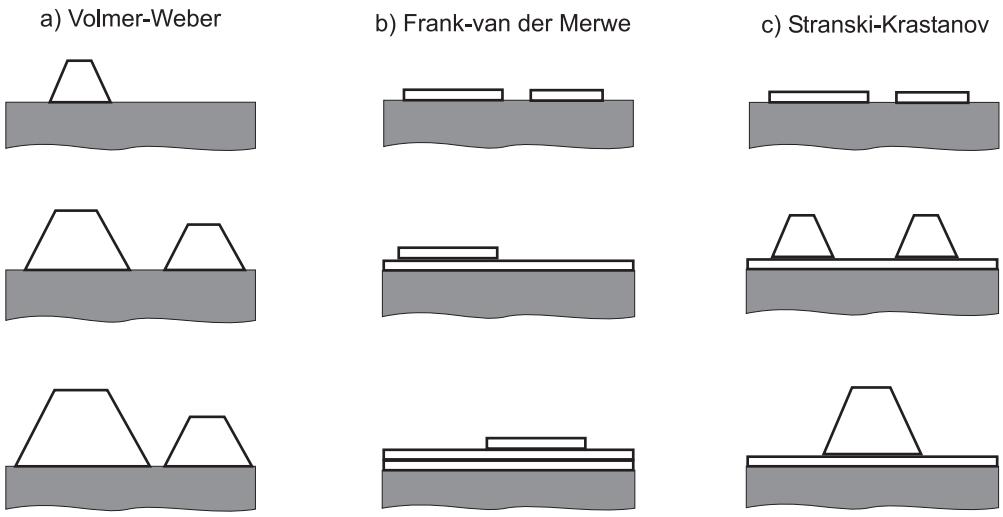

Figure 1.4: The three epitaxial growth modes according to the value of the adhesion energy: a) Volmer-Weber mode or 3D growth, b) Frank and Van der Merwe mode or layer by layer growth and c) Stranski and Krastanov mode, the intermediate mode.

such that ρ is 1, i.e.

$$X_c = \frac{4N\gamma}{nE_{el}}. \tag{1.10}$$

When islands are larger than X_c, the clustered configuration is favored. Since $E_{el} \propto f^2$ thus $X_c \propto f^{-2}$; it means that the larger the mismatch the smaller the critical island size.

1.2.2 The three modes of epitaxial growth

In the previous paragraph the surface energies of the substrate and heteroepitaxial film were considered the same; most often they are different. Let one consider γ_s and γ_f the surface energies of the substrate and film, respectively. When depositing the film on the substrate, this contact created an interface for which one defines a specific interfacial free energy γ_{int}. At the equilibrium, the work gained per surface unit is $-\beta$ and the balance of the transformation reveals the excess quantity:

$$\gamma_{int} = \gamma_f + \gamma_s - \beta \tag{1.11}$$

characterizing the interface [19]. The separation work β between the substrate and film is the adhesion energy. In the absence of misfit Bauer gives criteria [20, 21] for obtaining certain growth modes by considering the quantity $\Delta\gamma = \gamma_f - \gamma_s + \gamma_{int} = 2\gamma_f - \beta$. If $\Delta\gamma > 0$ the 3D islands will be stable; if $\Delta\gamma < 0$ the film will cover the substrate. Therefore, from this criterion the 2D and 3D growth modes illustrated in (figure 1.4) can be well separated:

The Volmer-Weber (VW) mode: the atoms of the vapor phase condensing on the substrate surface can nucleate and form 3D islands at supersaturation; it is typical for

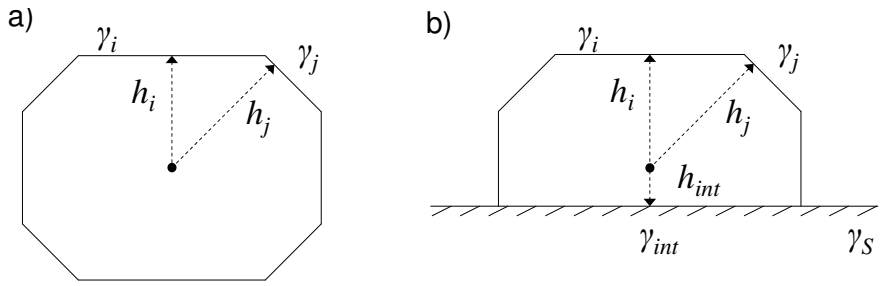

Figure 1.5: Definition of notation used on Wulff (a) and Wulff-Kaichev (b) theorem.

weak adhesion of the deposit on the substrate and large mismatch [22] (figure 1.4,a)

The Frank Van der Merwe (FVM) mode: the material can cover the whole substrate surface in a stack of layers at undersaturation; the layers remain planar and misfit dislocations are introduced [23] (figure 1.4,b)

The Stranski and Krastanov (SK) mode is more complex since the quantity $\Delta\gamma$ vary during the growth from negative to positive values. Thus the wetting of few atomic layers is followed by the formation of islands due to lattice mismatch and dislocations formation [24] (figure 1.4,c).

1.2.3 Macroscopic regime - Shape of self-assembled islands

At the macroscopic scale and down to some hundred of nanometers, the lattice symmetry and parameters of supported islands usually relaxed to their bulk values. In this case their shape is only determined by the minimization of surface and interface energies. It can be predicted using a geometrical construction named Wulff-Kaichev's theorem, based on the extension of the century-old Wulff's theorem for the isolated crystals [25]. It predicts the distance h_i between each i facet and the center of crystal:

$$\frac{\gamma_i}{h_i} = \frac{(\gamma_{int} - \gamma_S)}{h_{int}} \tag{1.12}$$

where γ_i is the surface energy of the i facet and h_{int} is the distance between the centre of the crystal and the interface (figure 1.12). If $\gamma_{int} - \gamma_s$ is negative, the height of the supported cluster becomes less than the height of the free cluster.

Wulff theorem does not consider the elastic energy accumulation due to the mismatch which gives a contribution to the interface energy and can influence the island shape. As it will be shown , deposition of metals on low energy surfaces leads to the formation of stress-free islands with equilibrium crystal facets

The parameters accessible to the experimentalist to tailor somewhat the morphology of self-assembled nanostructures are:

- *deposition rate* the higher the rate, the larger the island density.

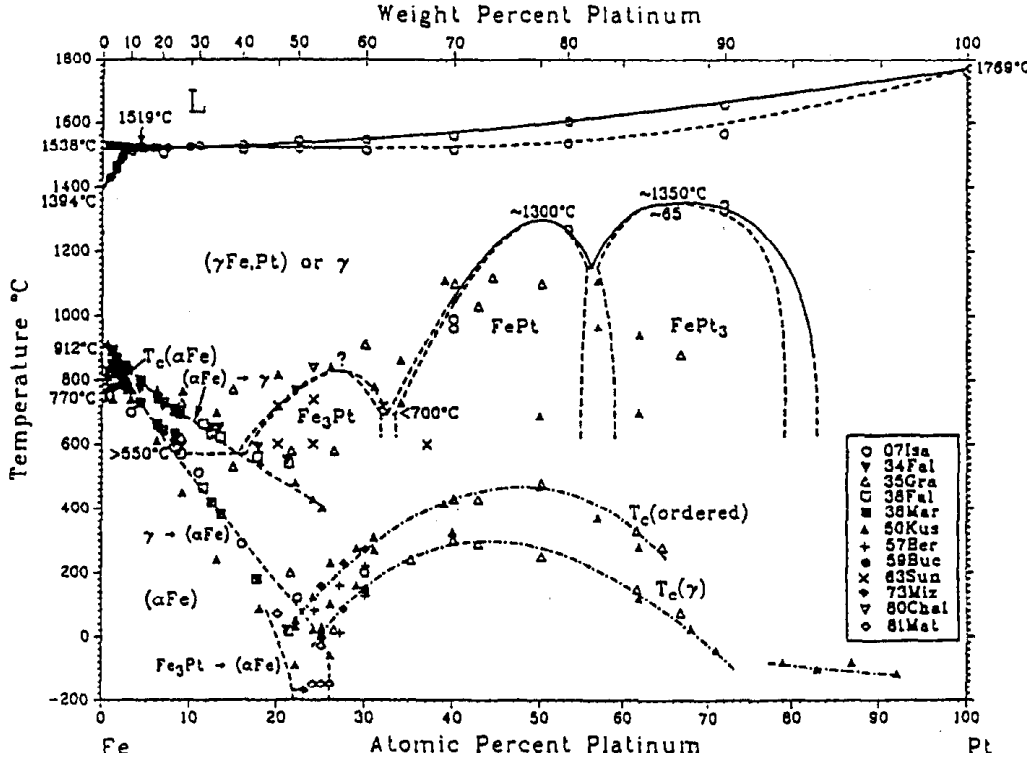

Figure 1.6: The Fe-Pt phase diagram from [26]

- *temperature*, that changes the mobility of adatoms and then the areal density of nanostructures on a defect-free surface; generally, the higher the deposition temperature, the larger the nanostructure.

- *deposit thickness*, the higher the thickness, the bigger the nanostructure; the increase in size often results from merging of smaller nanostructures.

- *crystalline structures of substrate and deposit* driving the growth direction and the nanostructure shape

1.3 Description of Fe-Pt and Co-Pt magnetic alloys

1.3.1 Fe-Pt alloys

According to the FePt phase diagram (figure 1.6), at high temperatures a fcc solid solution is observed. At temperatures below 1300°C, alloys close to the equiatomic concentration exhibit a disorder-order transformation from the disordered face-centred cubic A1-type structure (γ in figure 1.6) to the tetragonal $L1_0$-type superstructure with lattice parameters of $a = 3.836$Å and $c = 3.715$Å. Around the $FePt_3$ and Fe_3Pt stoechiometries, ordered alloys are formed below 1350 and 800°C respectively and adopt the $L1_2$-type phase.

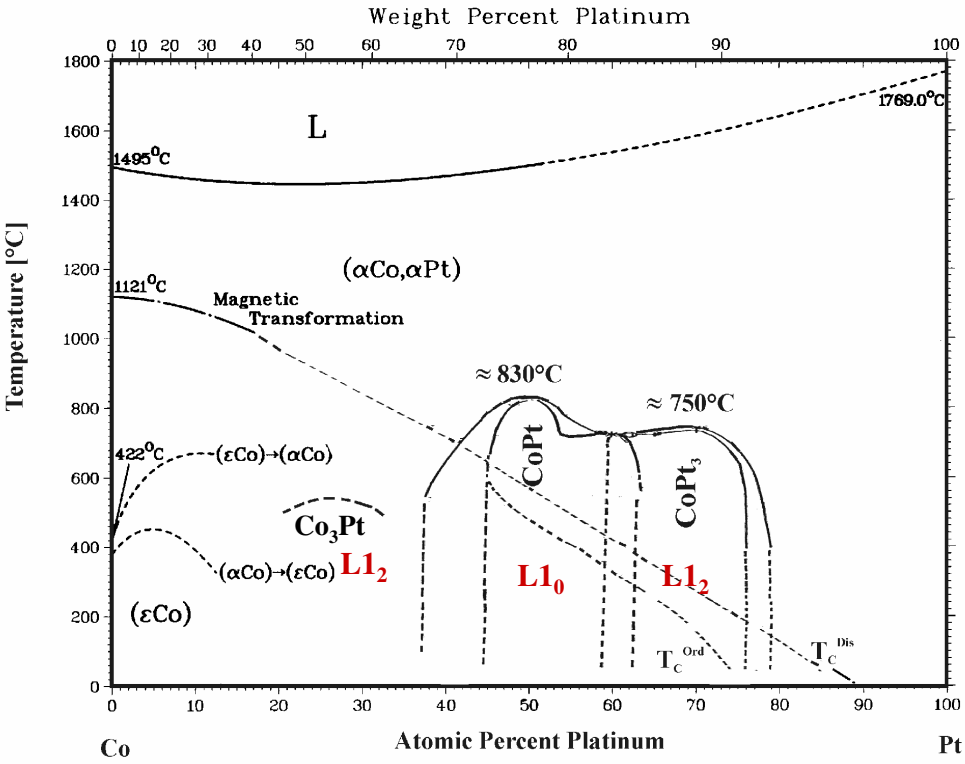

Figure 1.7: Equilibrium phase diagram of the Co-Pt system from [28]

The $L1_0$ FePt is ferromagnetic below 400°C and is one of the hardest magnetic materials. An uniaxial magnetic anisotropy energy K_u of 10 MJ/m^3 and a saturation magnetization M_s of 1150 kA/m were experimentally reported *Farrow et al.* [7], for K_u close to the theoretical prediction, 16 MJ/m^3 [27]. The high uniaxial anisotropy of FePt can be explained by the large spin-orbit coupling and strong hybridization of the polarized Pt d-band with the Fe d-band. The $L1_2$ ordered Fe_3Pt compound is ferromagnetic with a high value of room-temperature saturation magnetisation and a Curie temperature T_C of about 410K. It is characterized by a large in-plane anisotropy. The origin of this anisotropy is still under investigation. $L1_2$ $FePt_3$ is paramagnetic at room temperature and can exhibit two types of antiferromagnetic order below 160 K.

1.3.2 Co-Pt alloys

Figure 1.7 shows the phase diagram of the Co-Pt system [28]. At high temperatures the Co_xPt_{1-x} alloys crystallise in the fcc structure (Al). At lower temperatures ordered phases are formed. An ordered Co_3Pt phase ($L1_2$) has been reported [29] to occur with a congruent temperature of approximately 570°C. At the concentration x=0.5, a CoPt in $L1_0$ phase is observed with a maximum ordering temperature of 830 °C. It has a strong magnetic anisotropy with K_u = (2 - 4) MJ/m^3 (M_s ~1000kA/m) [30–32]. As the enthalpy

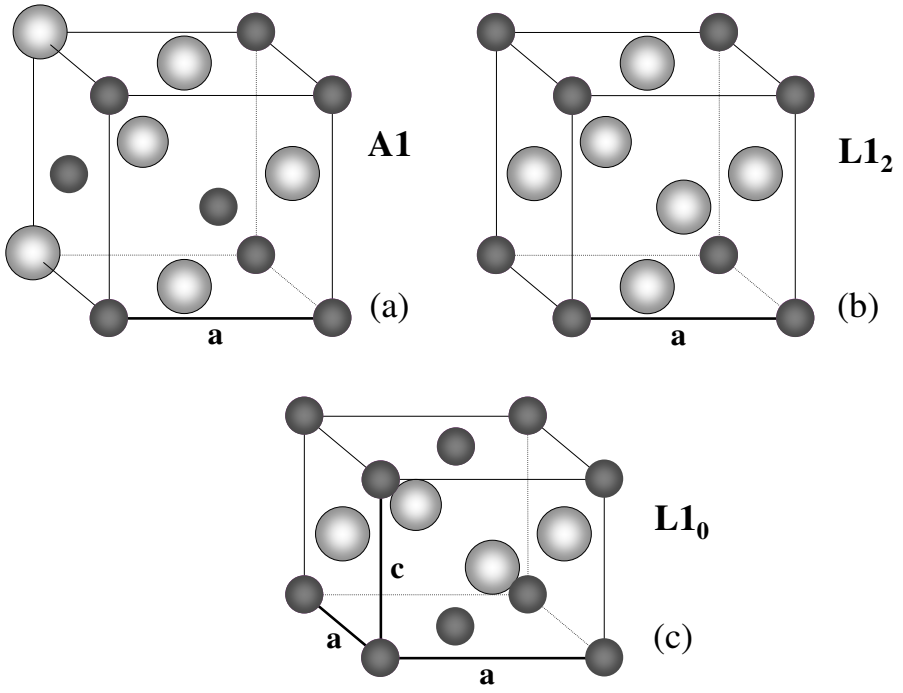

Figure 1.8: Schematic illustration of (a) the A1, (b) the $L1_2$ and (c) $L1_0$ structures.

change of the $L1_0$ CoPt phase formation ($\Delta H = -14$ kJ/mol) is less negative than that of $L1_0$ FePt ($\Delta H = -20$ kJ/mol [33, 34]), fully ordered CoPt films are expected more difficult to prepare than FePt [7, 35]). A $CoPt_3$ phase ($L1_2$) occurs with a transition temperature of 750 °C. When increasing the Pt content the Curie temperature decreases progressively and is lower than 20°C for the $L1_2$-$CoPt_3$ phase, while it is higher for the corresponding disordered alloy.

1.3.3 Crystalline structures of the $L1_2$ and $L1_0$ phases

Figure 1.8 shows the unit cells of the chemically ordered $L1_2$ and $L1_0$ structures, as well as that of the disordered A1 structure. The different chemical species appear as dark and light spheres.

The A1 phase (figure 1.8(a)) has a face-centered cubic (fcc) chemically disordered structure in which Co(Fe) and Pt atoms occupy the lattice sites randomly.

In the cubic $L1_2$ ordered structure (figure 1.8(b)) the minority atoms occupy the cube corners and the majority ones occupy the face-centre position.

The $L1_0$ structure (figure 1.8(c)) is tertragonal. The cubic symmetry is broken due to the stacking of alternate planes of M and Pt along the [001] direction. From the A1 phase three orientation variants can be formed with the tetragonal axis oriented along one of the three $< 100 >$ directions of the cubic A1 phase.

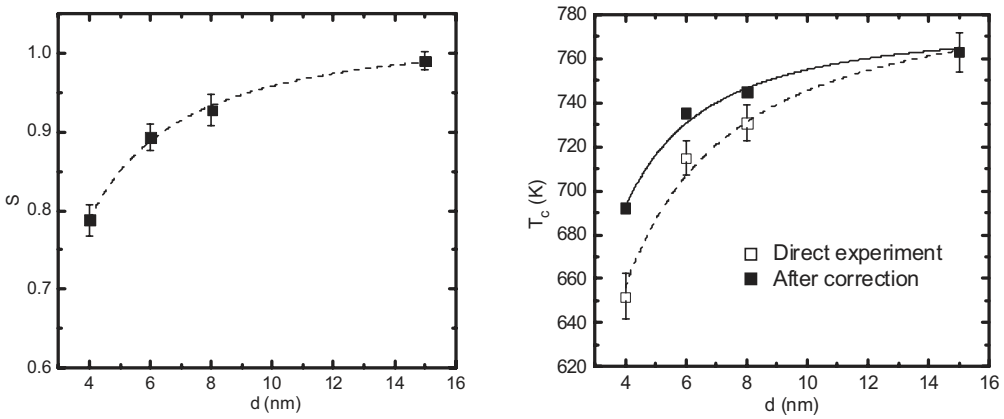

Figure 1.9: The dependence of the log-range ordering parameter (on the left) and the Curie temperature (on the right) on particle size [44]. The dashed line is a guide to the eye and the solid line is made by fitting the data.

1.3.4 Particle size effect on long-range chemical ordering

The properties of alloy particles depend strongly on their structure which is closely related to the fabrication method (molecular beam epitaxy, sputtering [36], cluster beam deposition [37], pulsed laser deposition [38, 39], chemical synthesis [4, 40]).

The influence of the reduced size on the long-range chemical ordering (LRO) was especially studied for the equiatomic CoPt and FePt alloys since for future ultra-high density magnetic recording, the magnetic anisotropy is closely related to the degree of $L1_0$ order. Among the most detailed studies found in the literature, let one cite the experimental work of Miyazaki et al [41] which shows that for FePt nanoparticles epitaxially grown at 973K on MgO(001) the long-range order sharply drops in particles of size below 3nm and disappears for particles smaller than 2nm. Theoretical calculations based on first, second and third nearest neighbor pair mixing [42], predict that the order-disorder transition in nanoparticles is not discontinuous as in bulk alloys but presents an inflexion point occurring at a temperature which decreases with decreasing size; the absence of LRO in 2nm-sized particles was attributed to a problem of kinetics rather than equilibrium. Very recent STEM nanodiffraction measurements in CoPt particles grown by pulsed laser deposition directly on a TEM grid covered by a carbon layer also indicate a reduction of the order-disorder transition down to 700K in particles smaller than 3nm [43].

The influence of the reduced size on the magnetic properties (Curie temperature T_C and magnetization M_s) was studied in FePt particles annealed at 973K in a salt matrix to prevent the coalescence of particles [44]. As shown in Fig 1.9, the Curie temperature also decreases when the size decreases. In addition of the particle size, the size distribution is also an important parameter for decreasing the signal-to-noise ratio in magnetic recording technology. A challenge is thus to identify an appropriate substrate that allows one to simultaneously achieve tunable uniformity in size, spatial distribution and crystallographic

orientation.

1.4 Self-assembly of epitaxial nanostructures

In order to produce nanostructures with regular size, self-assembly of three-dimensional islands under ultra-high vacuum conditions is a way to produce nanostructures in epitaxial orientation with the substrate surface. For example, metal deposition on layered dichalcogenide single-crystal, such as the Van der Waals $WSe_2(0001)$ surface ($\sim$260 erg/cm^2 [45]), which provides ideal chemically inert surface and therefore exhibits extremely high adsorbate mobility, or the NaCl(001) surface (230erg/cm^2) can lead to nanostructures with narrow size distribution [46].

1.4.1 On the Van der Waals $WSe_2(0001)$ surface

The crystalline structure of the WSe_2 layered chalcogenide, shown in figure 1.10, is characterized by two-dimensional sandwich units of Se-W-Se atomic layers along the crystallographic a-axis (the chalcogenides are close-packed). Figure 1.11 shows an STM image of $WSe_2(0001)$ surface; the hexagonal environment of Se atoms on the top layer is observed. Along the crystallographic c-direction the sandwich units are separated from each other by the so-called van der Waals-gap. The bonding interaction within the sandwich units is very strong and is based on covalent bonds. The metals are found in a trigonal prismatic coordination to optimize the covalent overlap. The bonding of the sandwich units to each other is weak along the crystallographic c-axis and often referred to as based on van der Waals-type interactions. The lattice constants of the compound are $a = 3.286$Å and $c =$ 2x6.488Å= 12.976Å [47]

The Concept of van der Waals-Epitaxy

The weak interaction across the van der Waals-gap is the conceptual basis for the growth of epitaxial layers of one type of layered compound on a layered chalcogenide substrate (2D/2D epitaxy, see figure 1.12). The interphase interaction between different layered chalcogenides may be rather similar to the intersandwich unit interaction within the bulk of one material. As a consequence epitaxial films may be grown combining such van der Waals-compounds even when the lattice mismatch, defined in eq.1.4, may be very large. This is schematically shown in figure 1.12 in contrast to the conventional epitaxy of lattice mismatched three-dimensional conventional (3D/3D) epitaxy.

The concept and term "van derWaals-epitaxy" (vdWe) have been introduced by Koma et al. which in their first paper studied the deposition of $NbSe_2$ on the $MoSe_2(0001)$ van der Waals-surface [48]. It was expected because of the specific structural properties of the vdWe-heterointerface that lattice matching conditions and differences in the thermal

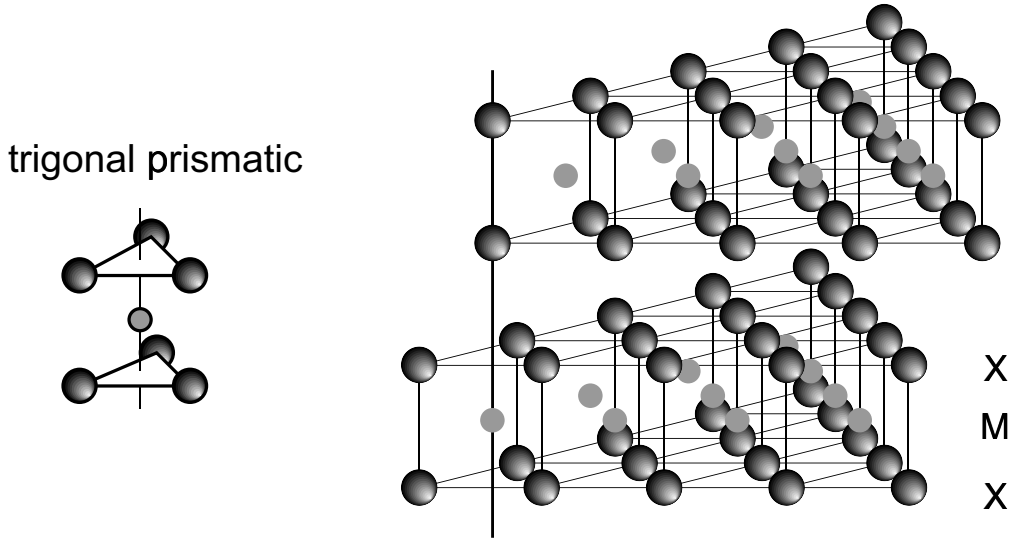

Figure 1.10: Crystallographic structure of layered chalcogenides, where M=W and X=S

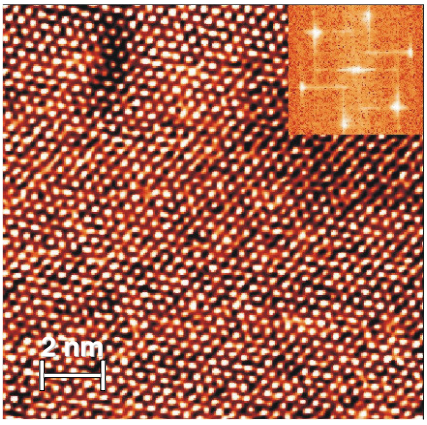

Figure 1.11: STM topographic images of WSe_2: atomically resolved Se top layer.

expansion coefficient are not important for obtaining high quality epitaxial layers with van der Waals-epitaxy.

After the introduction of van der Waals-epitaxy it has been shown that epitaxial layers with large lattice mismatch can also be grown when layered chalcogenides are combined with 3D materials. In figure 1.13 the typical 3D/2D material combinations of interest are schematically sketched. This type of heteroepitaxy was named quasi-van der Waals-epitaxy (qvdWe). As an example, the 2D/3D growth of GaSe on Si(111) surface has extensively been studied because of its technological interest [49]. The 3D/2D growth of fcc metals on layered compounds was also demonstrated. At low deposition temperature an 111-oriented film of Au was formed on $WSe_2(0001)$ while from 300K 111-oriented

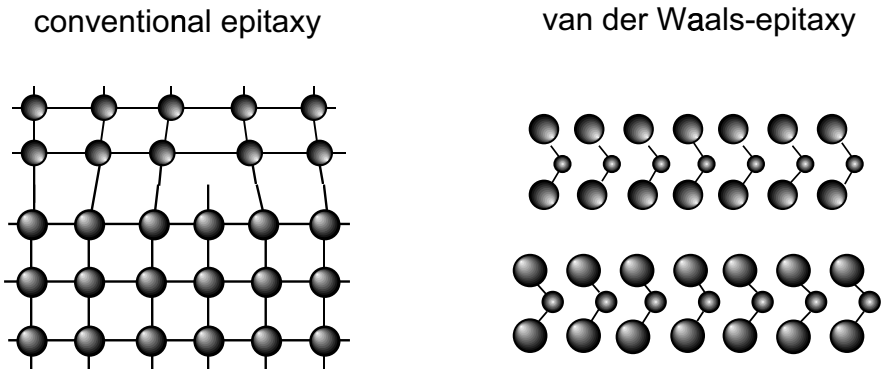

Figure 1.12: Interfaces of lattice mismatched materials as prepared by conventional (3D/3D) and van der Waals-epitaxy (2D/2D).

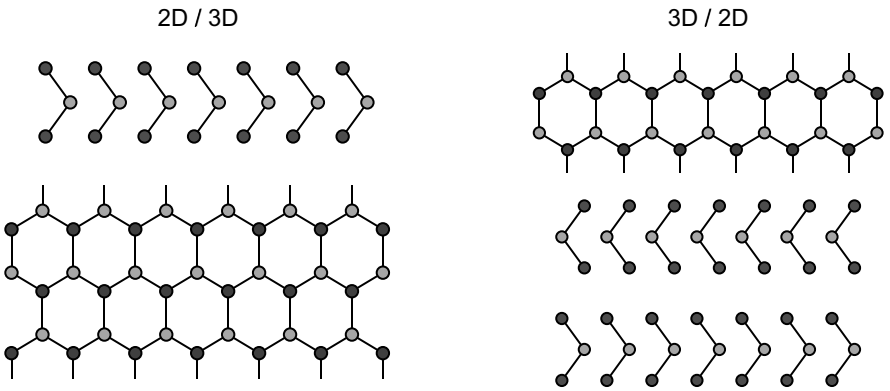

Figure 1.13: Combinations between two- and three-dimensional materials ("quasi-van der Waals-epitaxy").

nanostructures were usually observed such as Pd on $MoS_2(0001)$ [50].

The nucleation and growth of vdWe- and qvdWe-heterointerfaces should be completely different to classical 3D/3D epitaxy. In a naive approach it may be expected that the interactions on the van der Waals-surfaces, which define the adsorption energy as well as the surface diffusion constants of the precursor atoms (molecules), should be nearly identical for all van der Waals-substrates. Therefore nucleation and morphology of the epitaxial layers should mostly be governed by the thermodynamic properties and the kinetic processes of the growing film. However, it has been found experimentally that nucleation and film morphology can be different for different material combinations.

Pure metals grown on WSe_2

Several pure metals have been deposited on the $WSe_2(0001)$ surface at the University of Konstanz. Figure 1.14 shows STM images of 0.1 - 3 ML of pure metals deposited at

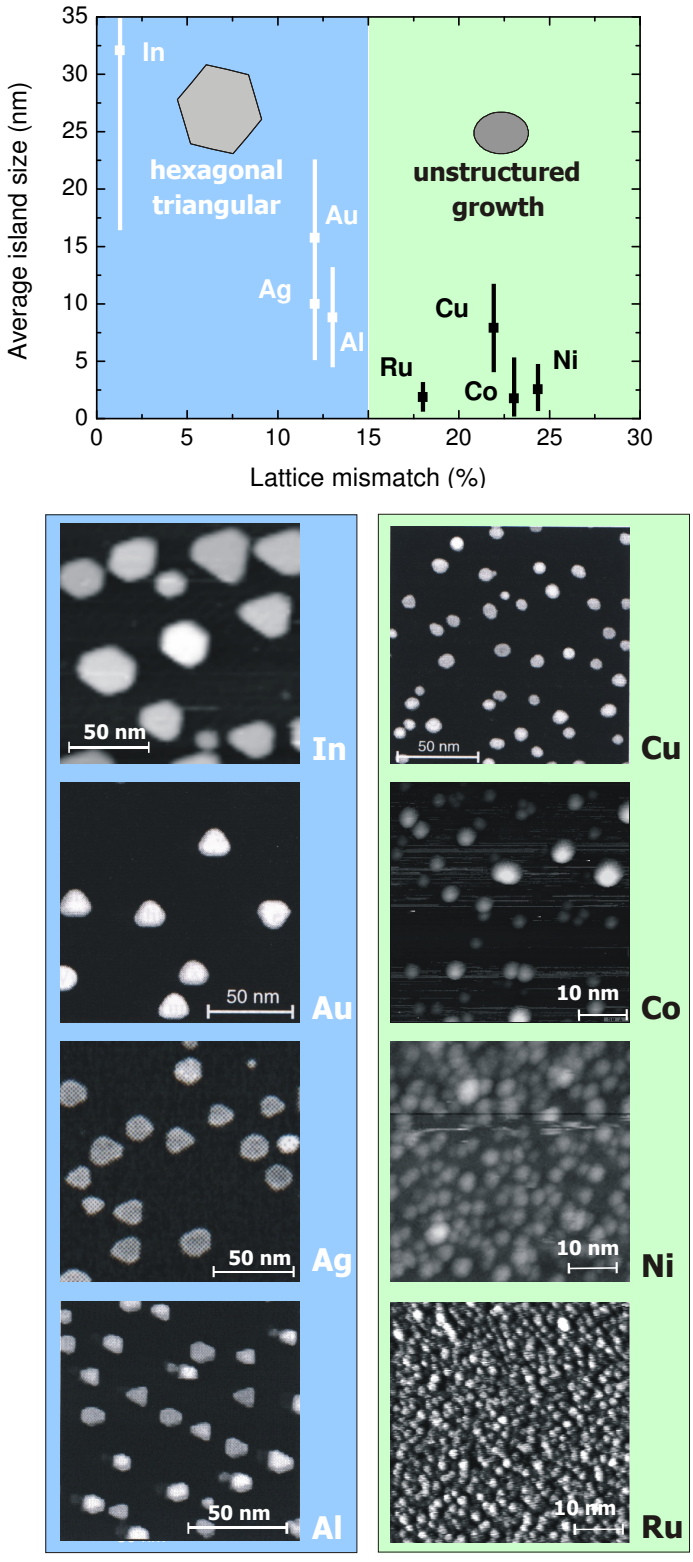

Figure 1.14: Pure metallic islands grown on $WSe_2(0001)$ surface at RT (coverage: 0.1 - 3 ML, deposition rete: 0.01 - 0.1 ML/s). The average island size with its width distribution is reported as a function of the lattice mismatch parameter (on the top). The insertions show the two characteristic shapes corresponding to the two different regions of lattice mismatch. The STM images of the different metals are reported on the bottom [46, 51, 52].

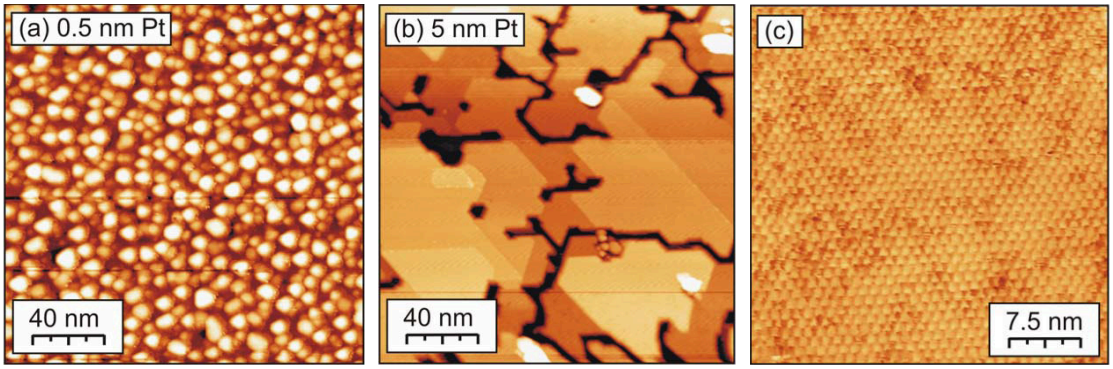

Figure 1.15: Series of STM topographic images taken after the deposition of Pt on WSe_2 at 720 K for different thicknesses of (a) 0.5 nm and (b, c) 5 nm. The STM images are taken at U=-1.5 V and I=0.1 nA [53].

RT with a deposition rate of 0.01 - 0.1 ML/s [46, 51, 52]. The epitaxial orientation and consequently the island shape are dependent on the lattice mismatch f determined by the difference between the Se-Se distance and the neareast metal-metal distance in the closely packed (111) plane. When f is lower than 15%, the metal islands are in epitaxial orientation with the substrate and adopt an hexagonal or triangular shape. While for $f > 15\%$, the islands take all orientations on the surface and have a rather rounded shape. As show after, this maximal value is somewhat larger for $M_{1-x}Pt_x$ binary alloys.

Se segregation

During metal deposition on WSe_2 vdWe-surface Se atoms tend to segregate at the growing surface even at low temperatures, as identified by Auger Electron Spectroscopy (AES) after FePt deposition [54] The consequences of such effect during the growth of Pt on $WSe_2(0001)$ [53] has been well observed by in-situ RHEED measurements. The initial growth at room temperature is characterized by the formation of 111-oriented Pt islands, while deposition at elevated temperatures shows the stabilization of metastable alloy islands, most likely a DO_{22}-type chemically ordered $Pt_3Se(112)$ alloy. Further deposition results in the disappearance of this phase and continuing segregation of the Se to the topmost layer would lead to the formation of a $PtSe_2$ alloy at the top surface. This assumption is based on the occurrence of a periodic surface structure revealing a hexagonal symmetry and a superlattice period of 1.1 nm. This superstructure is refereed to a Moiré pattern formed by the lattice mismatch between the Pt(111) planes and a $PtSe_2$ layer at the top surface. Figure 1.15 shows STM images obtained after 0.5 and 5nm deposits of Pt at 720K. The topgraphy of 0.5 nm Pt confirms the island growth. The average lateral size of the grains is about 7 nm with a height of 2 nm. Continuing Pt deposition leads to the coalescence between grains leading to atomically flat terraces separated by monoatomic steps as shown in figure 1.15(b). On the terraces (figure 1.15(c)) reveals an hexagonal

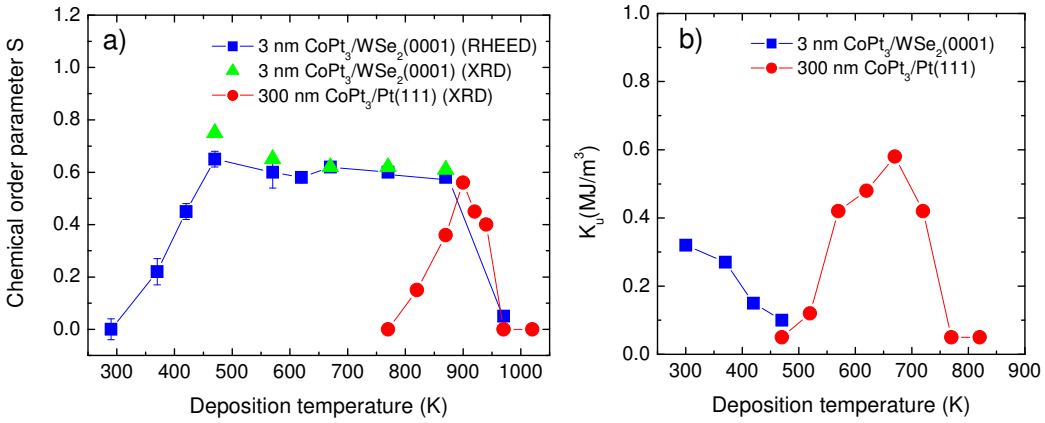

Figure 1.16: Change of the chemical order parameter S (a) and perpendicular magnetic anisotropy (b) for 3 nm $CoPt_3$ films grown on $WSe_2(0001)$, as a function of the growth temperature. S is extracted from both RHEED and X-ray diffraction. For comparison, the values measured in 300 nm continuous films grown on Pt(111) are included [10].

pattern consistent with the 1.1nm period of the Moiré pattern.

Deposition temperature effect on ordering and morphology for M-Pt alloys grown on $WSe_2(0001)$

The first attempt to grow an alloy by co-deposition on $WSe_2(0001)$ was applied to the $CoPt_3$ alloy which exhibits interesting magnetic properties. As a matter of fact, it was shown that the anisotropic short-range order reported in 40nm-thick continuous films of $CoPt_3$ grown on Ru(0001) [55] could explain the out-of-plane easy axis of magnetization observed in fcc disordered $CoPt_3(111)$ films [11, 12].

The deposition of a $CoPt_3$ submonolayer on $WSe_2(0001)$ leads to the formation of self-assembled single-crystalline islands which were in epitaxial orientation with the substrate surface in spite of the large misfit between WSe_2 ($a_{hcp} = 3.286$Å) and $CoPt_3$ ($a_{fcc}/\sqrt{2} = 2.72$Å) [9]. These 111-oriented islands have an hexagonal shape and a relatively narrow size distribution. $L1_2$-type ordering is already observed in nanostructures grown at 370 K, a temperature considerably lower than that required to order $CoPt_3$ continuous films. A study of the deposition temperature effect on chemical ordering was done on 3nm-thick deposits of $CoPt_3$ [10]. In figure 1.16(a) is reported the growth temperature dependence of the long-range chemical order parameter. Between 570 and 770 K chemical ordering remains relatively constant and disappears above 970 K, a temperature close to the order-disorder temperature in bulk alloys. In comparison with the continuous films which start to order above 770 K, the low onset temperature of ordering in films grown on $WSe_2(0001)$ was attributed to their nanostructured shape which enhances the atomic arrangements of both top and side-wall facets during the growth process.

The influence of the free surface on the ordering kinetics was previously observed near

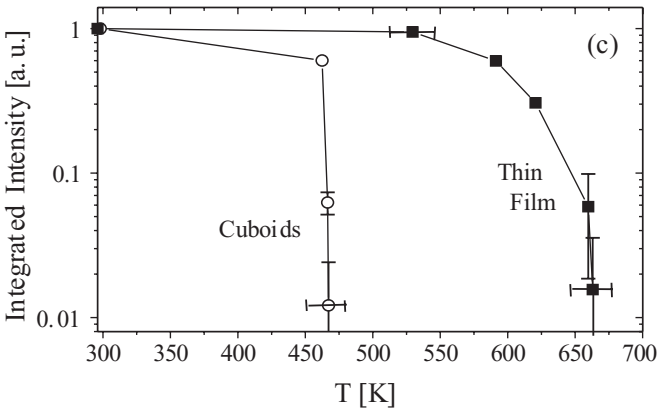

Figure 1.17: Integrated intensity of the $Cu_3Au(001)$ superstructure reflection of the cuboids (open circles) and the thin film (full squares) [57].

the surface of $Cu_3Au(001)$ (prototype of the $L1_2$ structure), leading to an ordering normal to the surface much faster than the lateral ordering [56]. This effect was correlated to the surface segregation profile of $Cu_3Au(001)$ observed above the order-disorder transition. Another study about the behaviour of the $L1_2$-A1 phase transition was carried out in an epitaxial Cu_3Au nano-cuboids array [57]. In-situ temperature dependence measurements of long-range order reveal a rather drastic reduction of the phase transition temperature in the nano-cuboids as compared to that observed in a neighbouring continuous thin film of the same thickness (figure 1.17).

The effect of the low temperatures of ordering in the 3nm-thick $CoPt_3/WSe_2(0001)$ deposits on the magnetic properties is illustrated in figure 1.16(b). Their growth temperature dependence of the uniaxial magnetic anisotropy (K_u) is compared with that of $CoPt_3$ continuous films [11]. In the temperature range between 570 and 770 K the continuous $CoPt_3$ films have larger K_u values. The decrease of K_u at higher temperatures is clearly attributed to the occurrence of the $L1_2$ ordering which is isotropic. Polarized X-ray absorption fine-structure (XAFS) experiments in the these films have revealed the existence of an anisotropic short-range order characterized by Co-Co bonds preferentially in the film plane balanced by Co-Pt bonds out of the plane [55].

In contrast, for $CoPt_3$ deposited on $WSe_2(0001)$ the largest K_u value is obtained for room temperature deposition. For higher temperatures K_u decreases rapidly with the onset of $L1_2$ ordering. By increasing the thickness above 5nm, a gradual approach to the behavior of continuous films is observed due to the coalescence of islands [58, 59]. The origin of PMA in these 3 nm thick films remains to elucidate, since a remaining in-plane tensile strain could not explain preferential perpendicular magnetization axis due to a positive magnetostrictive constant of $CoPt_3$ alloy [60]. Therefore, polarized EXAFS measurements have been performed to probe any anisotropic chemical order to understand

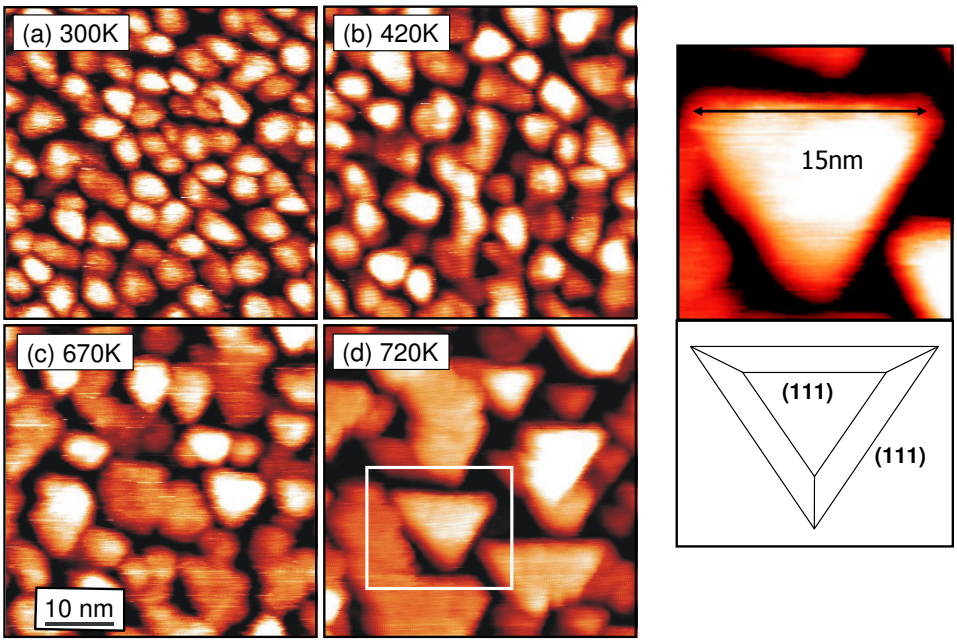

Figure 1.18: STM images of $CrPt_3(111)$ deposits grown at different deposition temperatures on $WSe_2(0001)$ revealing their surface morphologies. On the right is reported the magnification of the triangular island observed at T_d=720 K and its Wulff reconstruction [58].

the origin of such PMA. The analysis of these measurements will be presented in chapter 3. The morphology of the measured samples were studied in detail by STM and GISAXS.

The Se segregation at the growing surface has been detected by AES even in FePt deposited at room temperature [54]. Here, in contrast with that observed for the growth of FePd on ZnSe(001) [61], the Se surfactant effect does not prevent the $L1_0$ ordering which starts at a relatively low deposition temperature of about 470 K with the occurrence of the three possible variants. The magnetic measurements in 3 nm thick FePt(111) deposits show an easy axis of magnetization in the film plane, with a coercivity strongly enhanced with $L1_0$ order.

Another work that illustrates the importance of the substrate choice in reducing the ordering temperature of M-Pt alloys concerns the growth of 3nm thick $CrPt_3$ [62]. Assemblies of (111)-oriented fcc nanostructures were obtained with lateral sizes ranging from 5 to 15 nm for growth temperature increasing from 300 to 820 K. The nanoparticles develop a partial $L1_2$-type chemical long-range order starting at a deposition temperature as low as 300 K, much lower than reported for continuous films grown on other suitable substrate surfaces [63]. The ordering parameter was found slightly dependent on the deposition rate, since lowering the deposition rate by a factor of 5 results in an ordering parameter increase from 0.3 to about 0.4.

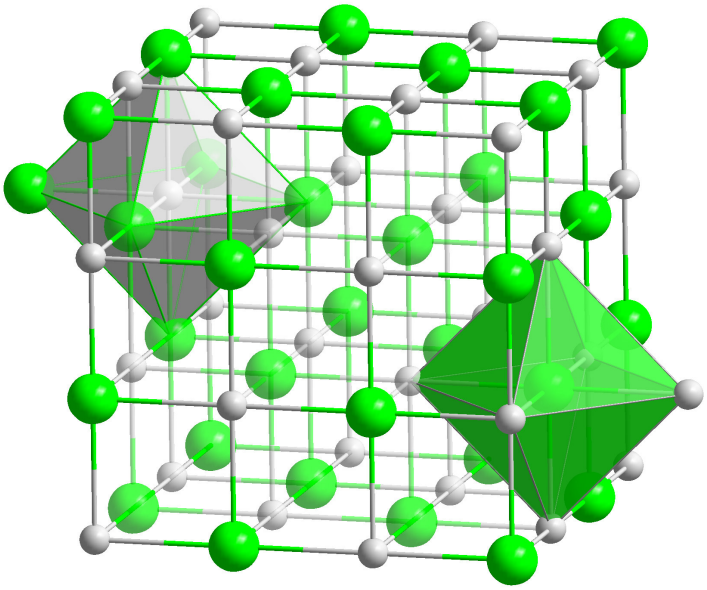

Figure 1.19: Schematic structure of NaCl.

1.4.2 On the low energy NaCl(001) surface

The crystal structure of NaCl is cubic with a lattice parameter equal to 5.64Å. As shown in figure 1.19, the larger chloride ions as green spheres, are arranged in a face-centered cubic (fcc) lattice, while the smaller sodium ions, as silver spheres, occupy the octahedral sites. Each ion is thus surrounded by six ions of the other kind.

Recently, NaCl was of great interest to order small FePt particles. The annealing treatments to convert the A1 into $L1_0$ phase cause the formation of larger nanoparticles, which renders the material useless for applications. This problem was overcome by adding a small amount of NaCl to nanoparticles before annealing [44, 64]. The salt keeps the FePt nanoparticles apart such that they can undergo the phase transformation to $L1_0$ structure without sticking together and sintering. The produced particles have diameters between 4 and 15 nm.

The NaCl(001) surface was found to be well suited to form 001-oriented alloy islands with very narrow size distribution [65]. For the preparation of alloys, the ratio of the atomic fluxes has to be corrected for an eventual difference between the condensation coefficients of two species. As shown for the CuPd alloy [66], the coefficient of Cu is very small compared to the one of Pd atoms, making difficult the formation of equiatomic CuPd particles.

$L1_0$ ordering in FePt, FePd and CoPt grown on NaCl(001) was investigated by Hirotsu et al [67] by TEM measurements. The increase in $L1_0$ ordering was followed by measuring the coercivity. It was shown that the ordering process scales with the ratio $\frac{T_c}{T_m}$ (T_c order-disorder transition temperature and T_m melting temperature). For FePt, FePd and CoPt,

the ratios are equal to 0.828, 0.606 and 0.550 respectively. $L1_0$ was observed in FePt particles of 2-3 nm diameter and not in FePd particles of diameter smaller than 5nm. The coercivities measured in CoPt particles remain very small even after annealing at 973K for 1h, indicating a slow rate of ordering. At our knowledge no x-ray diffraction measurements have been reported on alloy deposited on NaCl(001). In chapter 6 the determination of degree of $L1_0$ order in FePt deposits on NaCl(001) by x-ray diffraction will be presented and compared with that measured in FePt deposited simultaneously on MgO(001). The nature of the substrate on $L1_0$ ordering and the morphology of deposits determined by TEM will thus be discussed. In chapter 4, the growth of the $CoPt_3$ alloy on NaCl is reported and the influence of the growth direction on the short range order will be studied by polarized XAFS. Let one mention that a better comparison with $WSe_2(0001)$ would have been to grow 111-oriented islands on NaCl(111) surface, however this surface is charged and then unstable [68].

Chapter 2

Experimental techniques

The metallic alloy nanostructures were prepared by molecular beam epitaxy. The structural and magnetic properties of deposits were investigated using different techniques: 1) reflection high energy electron diffraction (RHEED) to follow the epitaxial growth during the deposition, 2) X-ray diffraction measurements (XRD) to characterize the structure and determinate the long range chemical order parameter, 3) X-ray absorption spectroscopy (XAS) to probe the local structure, 4) superconducting quantum interference devices (SQUID) to investigated the magnetic anisotropy, 5) grazing incidence small angle x-ray scattering (GISAXS) couple to other characterization techniques (TEM, STM and Field Emission-SEM) to studied the morphology. In this chapter, an overview of these methods used for the characterization is given with a careful description of the EXAFS and GISAXS techniques.

2.1 Preparation and in-situ characterization

2.1.1 Molecular Beam Epitaxy (MBE)

MBE is a method for depositing layers of materials on substrates with controlled atomic thicknesses. It relies on creating a 'molecular beam' of a material which impinges on a substrate. Deposition was done in a Varian VT-118 MBE chamber at the Konstanz University. A schematic view of the deposition apparatus is shown in figure 2.1.

The WSe_2(0001) and NaCl(001) substrates were freshly cleaved and fixed on STM plates using silver lacquer for the first ones and W-springs for the second ones (figure 2.2).

In order to reduce the amount of contaminants in the MBE chamber, a step-like sample introduction procedure is used. Firstly, the sample is placed in the load-lock chamber, which is evacuated by a turbo-molecular pump down to 10^{-7} mbar. The sample is then transferred to the preparation chamber, which is used (i) for storing the samples before or after deposition and (ii) as transfer compartment between the different chambers for sample characterization. The base pressure of $\sim$1x10^{-8} mbar in the preparation chamber is maintained by an ion-getter pump system. After outgassing in the preparation chamber, the sample can be transferred to the MBE chamber for alloy deposition.

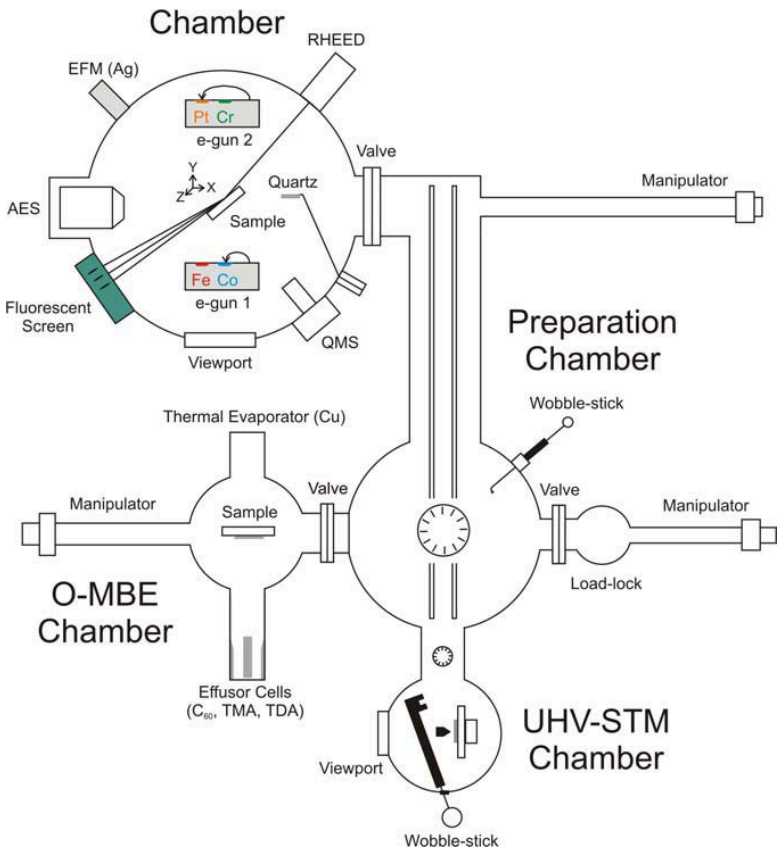

Figure 2.1: Schematic representation of the MBE, O-MBE, STM and preparation chambers.

The MBE apparatus is also equipped by an organic-MBE (O-MBE) chamber, where different organic molecules can be deposited (C60, TMA, TDA), and an ultra-high vacuum scanning tunneling microscopy (UHV-STM, OMICRON SPM SO V2.0) for sample surface characterization before or after deposition.

The deposition chamber has a base pressure of 2x10^{-10} mbar. The chamber has two independently controlled electron guns loaded with 4 materials (1^{st} gun: Fe and Co; 2^{nd} gun: Pt and Cr). This allows the deposition of individual metal layers as well as alloys (i.e. FePt, CoPt, CrPt, etc.) through co-deposition. The deposition rates and thicknesses are controlled with a quartz balance, calibrated from X-ray reflectivity measurements in pure metallic films.

Typical values for the deposition rates are 0.005-0.01 Å/s. During co-deposition, the composition of each species is controlled by a quadrupole mass spectrometer (QMS), calibrated for each metal with the quartz balance. In order to deposit the binary alloy with correct atomic composition $M_x\mathrm{Pt}_y$, the ratio between the two fluxes has to be adjusted. The definition of the flux Φ via thickness d of the deposited material is: $\Phi = d/t$, where t is the deposition time. Thickness can be expressed via mass m, density ρ and area S of

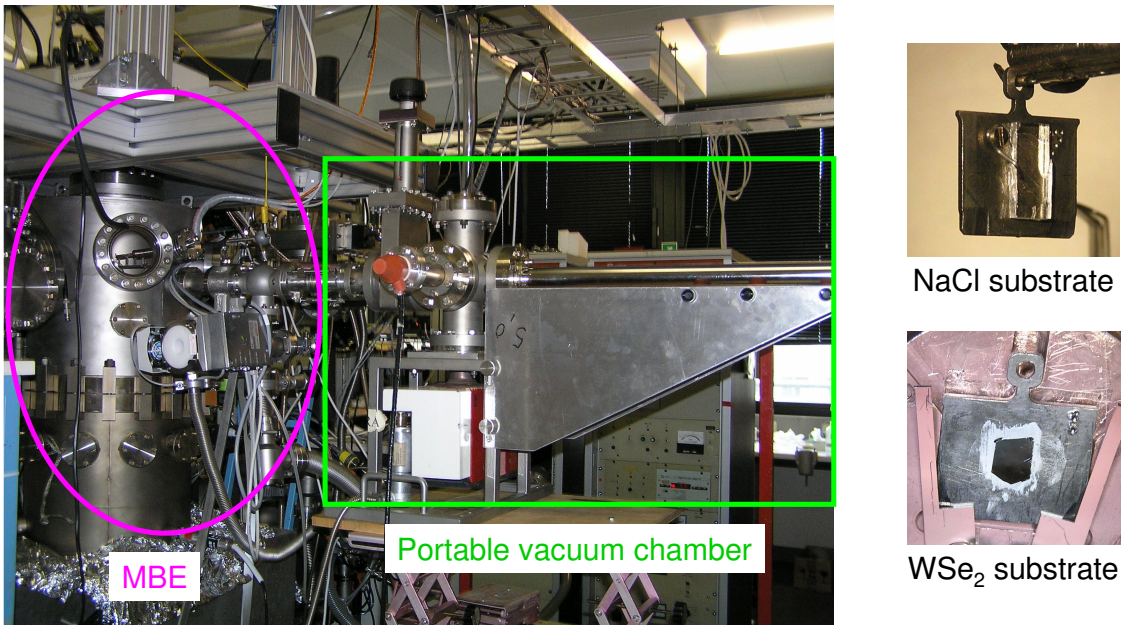

Figure 2.2: MBE laboratory at the Konstanz University: view of the portable vacuum chamber connected to the MBE chamber. On the right, the photos of $WSe_2(0001)$ and NaCl(001) substrates fixed on STM plates.

the deposited material: $d = m/\rho S$. The flux ratio is then:

$$\frac{\Phi(M)}{\Phi(Pt)} = \frac{m(M)}{m(Pt)} \cdot \frac{\rho(Pt)}{\rho(M)}. \tag{2.1}$$

The mass ratio is related to the ratio of the atomic weights A(M) and A(Pt):

$$\frac{m(M)}{m(Pt)} = \frac{x}{y} \cdot \frac{A(M)}{A(Pt)}, \tag{2.2}$$

which give the final expression for the flux ratio:

$$\frac{\Phi(M)}{\Phi(Pt)} = \frac{x}{y} \cdot \frac{A(M)}{A(Pt)} \cdot \frac{\rho(Pt)}{\rho(M)}. \tag{2.3}$$

For example, calculation according to equation 2.3 gives the flux ratio of 0.24 for $CoPt_3$, 0.72 for CoPt, and 2.1 for Co_3Pt.

Note that the expression 2.3 has to be corrected taking into account tooling factors T(N) and T(Pt), which include the information about the deposition geometry:

$$\left(\frac{\Phi(M)}{\Phi(Pt)}\right)_{corr} = \frac{x}{y} \cdot \frac{A(M)}{A(Pt)} \cdot \frac{\rho(Pt)}{\rho(M)} \cdot \frac{T(Pt)}{T(M)}. \tag{2.4}$$

The maximal deposition temperature in MBE chamber was restricted to 720K. The temperature is measured by a thermocouple placed near the back of the sample holder. Although this method is widely used in vacuum chamber, it is not always accurate. Read-

ings with this method can in fact differ greatly from the real temperature at the substrate surface.

After deposition, the samples can be moved into a portable vacuum chamber, equipped with an ion-getter pump, allowing their transfer towards other experimental apparatus without air exposure, such as the GISAXS chamber at BM02 ESRF beamline and STM apparatus at the Néel Institute in Grenoble. Figure 2.2 shows the portable vacuum chamber connected to the MBE load-lock chamber.

2.1.2 Reflection High-Energy Electron Diffraction (RHEED)

Due to the grazing incidence angle geometry, RHEED can be easily implemented in an MBE chamber for *in-situ* investigation. The technique was used to monitor the growth properties of alloy deposits on $WSe_2(0001)$ and NaCl(001) surfaces. Diffraction patterns were recorded under an angle $\sim 3^\circ$ and a beam energy of 10 keV.

RHEED on a flat substrate

Because of the grazing incidence geometry of the incoming beam, the sample surface has to be flat. Asperities shadow part of the surface. The diffracted beams are observed at similar small angels $(1^\circ - 3^\circ)$ in a fluorescent screen. In spite of the high energy of the primary beam, the grazing incidence and the detection angles mean that the electron penetration normal to the surface is only a few atomic layers. The sample can be considered as a two-dimensional layer, and leads to reciprocal lattice rods perpendicular to the sample surface. The Ewald sphere construction for RHEED is shown in Figure2.3 [69]. The intersection of the reciprocal rods with the Ewald sphere would correspond to spots. But due to angular and energy spread of the electron beam and defects of the surface, the diffraction patterns consist of streaks.

Transmission electron diffraction

In the case of nanometric islands on the surface, bulk scattering of the grazing electron beam can occur and the RHEED pattern will contain well pronounced spots due to transmission electron diffraction (inset in figure 2.3). In order to illustrate it, the RHEED pattern of differently thick $CoPt_3$ deposits on $WSe_2(0001)$ surface are shown in figure 2.4. In figure 2.4(a) for a low coverage 0.3 Å, both the streaks from the $WSe_2(0001)$ substrate and the weak spots from $CoPt_3$ epitaxial islands are observed. Further $CoPt_3$ deposition leads to the vanishing of substrate streaks, and well pronounced spots of $CoPt_3$ islands of which triangular shape is an indication of facetting (figure 2.4(d)). RHEED is a powerful technique to study the growth modes and detect eventual surface reconstruction.

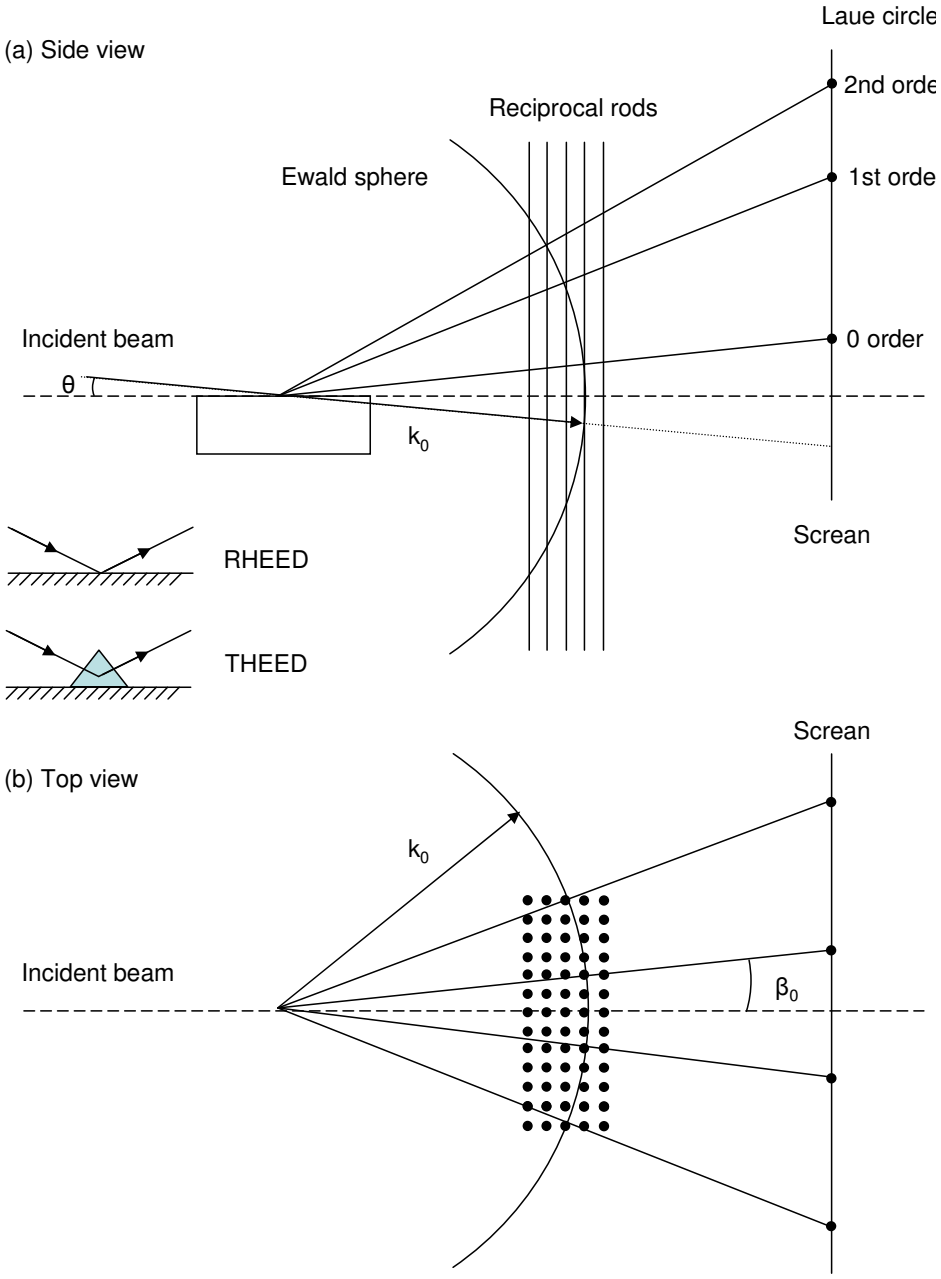

Figure 2.3: Ewald sphere construction and diffraction geometry of RHEED [69].

Chemical order

RHEED can also detects the chemical order by the appearance of additional intermediate spots. Using this technique the structural disorder-order transformation can be monitored in real time during the annealing treatment in the MBE chamber. Due to the dynamical

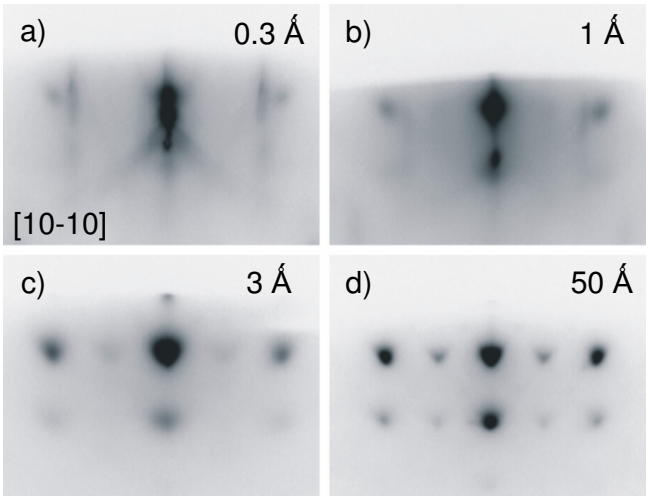

Figure 2.4: RHEED images taken after deposition of (a) 0.3Å, (b) 1Å, (c) 3Å and (d) 50Å of $CoPt_3$ on WSe_2(0001) at 570K, along the [10-10] azimuth of the WSe_2(0001) plane.

effects, the analysis of the spot intensities gives only a qualitative information about chemical ordering.

2.2 XRD: X-ray Diffraction

2.2.1 Structure factor

X-Ray Diffraction (XRD) is the ideal tool to investigate the periodic structure of materials, to measure the lattice parameters and to evaluate the long range chemical order in alloy compounds. This is an old technique which has seen its first patterns recorded at the beginning of century by Friedrich *et al.* [70] in the transmission (Von Laue) geometry and by Bragg [71] in the reflection geometry (Bragg). A description of the basic principles of XRD and of the equivalence of the Von Laue and Bragg's approach can be found in solid state textbooks (see for example Ashcroft and Mermin [72]). Here, the basic equations are recalled.

The diffraction condition by a family of parallel crystallographic planes occurs when the waves scattered by the planes interfere constructively each other. It leads to a relationship among the spacing of the lattice planes d_{hkl}, the wavelength λ and the incidence angle θ:

$$2d_{hkl}\sin\theta = \lambda \tag{2.5}$$

The subscript hkl are used because, for each family of planes, there are perpendicular vectors in the reciprocal space, the shortest of which has a length $\frac{2\pi}{d}$. The coordinates of this vector (h, k, l), referred to as "Miller indices", define the family of planes under study; in case of absence of high order harmonics (they are neglected in eq.2.5), this vector (let's

call it $\vec{q}$) is the exchanged wave vector of the scattering process.

For cubic crystals, the relationship between the lattice planes distances and their corresponding Miller indices is particularly simple and, if a is the lattice parameter of the crystal, the diffraction condition is:

$$2a \sin\theta = \lambda\sqrt{h^2 + k^2 + l^2} \tag{2.6}$$

This provides a very simple way to measure a, setting a well defined wavelength and performing an angular scan to determinate the angular position of the diffraction peak.

In the case of kinematical approximation the photon is described by a plane wave, the scattering is elastic and the photons are scattered only once. The intensity of a diffracted beam is given by:

$$I(q) \propto |F(q)|^2 = |\sum_j f_j e^{-\vec{q}\cdot\vec{r}_j}|^2 = |\sum_j f_j(hkl) e^{-2\pi i(hx_j + ky_j + lz_j)}|^2, \tag{2.7}$$

where r_j is the position of an atom j in the unit cell, $\vec{q}$ is a reciprocal lattice vector given by the difference between the scattered and incident wavevectors (k and k_0 in figure 2.5(a), respectively) and f_j is the atomic scattering factor of j-atom. The sum is over all atoms in the unit cell. $F(q)$ is the so called Structure factor. It describes the way in which an incident beam is scattered by the atoms of a crystal unit cell, taking into account the different scattering power of the elements through the term f_i. Since the atoms are spatially distributed in the unit cell, there will be a difference in phase when considering the scattered amplitude from two atoms. This phase shift is taken into account by the complex exponential term. The atomic form factor, or scattering power, of an element depends on the type of radiation considered.

2.2.2 Experimental diffraction methods

In this work three different methods were used.

Symmetric $\theta/2\theta$ scan

In the $\theta/2\theta$ or Bragg-Brentano geometry the sample and detector rotations are coupled: as the sample rotates of an angle θ about an horizontal axis perpendicular to the X-ray incident beam, the detector moves by an angle 2θ about the same axis in order to catch the reflection. Figure 2.5(b) illustrates the specular reflection geometry: the incident beam is specularly diffracted and the scattered wavevector is directed along the normal to the surface. Thus, this geometry is sensitive to the atomic planes parallel to the surface.

The width of the diffracted peaks ($\Delta(2\theta)$) is correlated with the coherent length $L_\perp$ along the growth direction according to the Scherrer law:

$$L_\perp = \frac{K\lambda}{\Delta(2\theta)\cos(\theta_B)}, \tag{2.8}$$

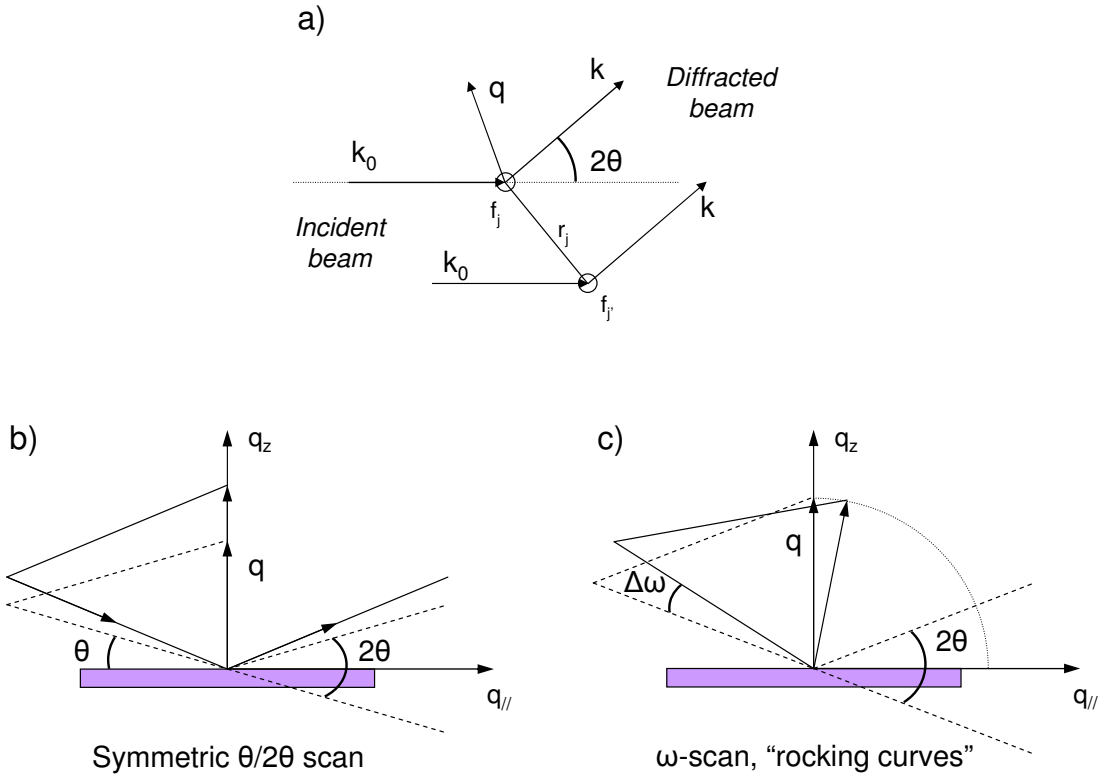

Figure 2.5: a) X ray diffraction from two scattered centres. b) symmetric $\theta/2\theta$ scan and c) rocking curve in reflection geometry.

where K is a constant generally equal to 0.9 and θ_B is the Bragg peak angle.

A pictorial view illustrating the θ and 2θ circles together with the others movements necessary for our measurements is reported in figure 2.6.

In order to measure reflections coming from plane not parallel to the surface, as the (113) reflection of 111-oriented $M_{1-x}\mathrm{Pt}{-}x$ alloys, the other rotation movements are adjusted on a 4-circle diffractometer, such as χ, around the direction of the incident beam, and ϕ, around the normal to the surface. Then, the $\theta/2\theta$ were performed.

Asymmetric $\theta/2\theta$ scan

On a two-circle diffractometer the (113) reflection can be measured only in asymmetric $\beta/2\theta$ geometry. β can be equal to $\theta+\alpha$ (grazing emergence) or $\theta-\alpha$ (grazing incidence), where α is the angle between the normal to the surface and the scattering vector.

Rocking curve scan

Information about the crystalline quality and mosaicity are obtained from rocking curve measurements. In these measurements the angle of incidence is varied, while the detector position is kept constant at 2θ.

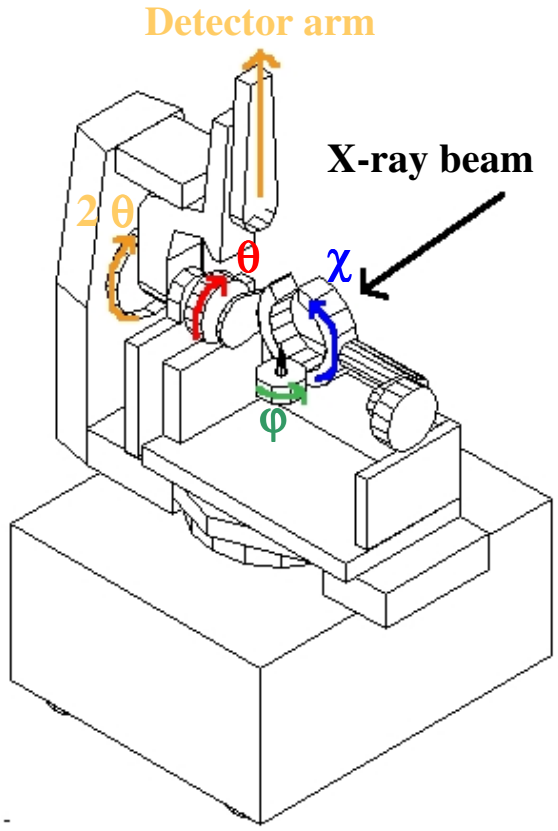

Figure 2.6: Pictorial view of a diffractometer for XRD in Bragg-Brentano geometry. The figure reports a modified scheme of the diffractometer of the D2AM CRG beamline of the ESRF; only the circles of interest are indicated. The sample is located on the tip, χ (blue) represents the rotation around the axis of the incident X-ray beam, ϕ (green) the rotation around the vertical axis.

The width of the rocking curve ($\Delta\omega$) depends on two contributions:

- the **mosaicity**, η, which is related to the diffracting domains disorientation respect to the normal to the surface;
- the lateral coherence length, $L_{\parallel}$. analogue to eq. 2.8.

$\Delta\omega$ can be written as:

$$\Delta\omega = \eta + \frac{K\lambda}{2L_{\parallel}\sin(\theta_B)}. \tag{2.9}$$

In principle, the two terms can be separated by measuring reflection of different orders. In fact, in q-space, η depends on q while the second term is independent.

2.2.3 Chemical long-range order parameter

The perfect AB (M=Co,Fe and B=Pt) $L1_0$ phase can be described as a stacking of pure A and pure B(001) planes defining two sublattices (α, β). The structural factors (eq. 2.7) are given by:

$$\begin{array}{rcl} F^F_{hkl} & = & 2(f_A + f_B) \text{ for fundamental peaks} \\ F^S_{hkl} & = & 2(f_A - f_B) \text{ for superlattice peaks} \end{array} \tag{2.10}$$

The chemical long-range order parameter (LRO) measures the degree of chemical order. It is given by:

$$S = \frac{r^A_\alpha - x_A}{1 - y_\alpha} = \frac{r^B_\beta - x_B}{1 - y_\beta}. \tag{2.11}$$

where x_A and x_B are the atomic fractions of the two components, A and B, y_α and y_β are the fraction of sites on sublattice α and β (for $L1_0$ $y_\alpha = y_\beta$=0.5) and r^A_α are the occupancy rate on α sublattice by A atoms and r^B_β the occupancy rate on β sublattice by B atoms.

When the system is partial ordered, the eq. 2.10 becomes:

$$\begin{array}{rcl} F^F_{hkl} & = & 2(f_A + f_B) \text{ for fundamental peaks} \\ F^S_{hkl} & = & 2S(f_A - f_B) \text{ for superlattice peaks.} \end{array} \tag{2.12}$$

Therefore, the LRO parameter can be determined experimentally from the ratio of the integrated intensities between the superlattice and fundamental reflections:

$$S = \frac{F^F_{hkl}}{F^S_{hkl}} \sqrt{\frac{I^S_{hkl} A^F_{hkl} L^F_{hkl} P^F_{hkl}}{I^F_{hkl} A^S_{hkl} L^S_{hkl} P^F_{hkl}}} \tag{2.13}$$

$I^{F(S)}_{hkl}$ is the integrated intensity of the fundamental (superlattice) peak including the width of rocking curve; it is corrected for sample absorption ($A^{F(S)}_{hkl}$), Lorentz ($L^{F(S)}_{hkl}$) and polarization factor ($P^{F(S)}_{hkl}$) which are given:

$$A_{hkl} = \frac{1}{2\mu}\left(1 - e^{-\frac{2\mu t}{\sin\theta_{hkl}}}\right) \quad \text{for symmetrycal reflection geometry} \tag{2.14}$$

where μ is the linear absorption factor of the alloy and t is the film thickness,

$$L_{hkl} = \frac{1}{\sin(2\theta_{hkl})} \tag{2.15}$$

$$P_{hkl} = \begin{cases} \frac{1+\cos^2(2\theta_{hkl})}{2} & \text{for unpolarized beam (SIMaP)} \\ 1 & \text{with synchrotrom radiation (BM02)} \end{cases} \tag{2.16}$$

2.2.4 Experimental apparatus

The X-ray diffraction experiments were performed on two different diffractometers: 1) at SIMaP using a 4-circle HUBER diffractometer equipped with a Cu-Kα (λ = 1.5418 A) rotating anode, 2) at the European Synchrotron Radiation Facility on the seven circle-diffractometer of the French D2AM CRG beamline using photon energy E=8.95 eV (λ =1.3851 Å). Samples were mounted on the diffractometer (illustrated in figure 2.6) where

the three Euler circles (θ, ϕ and χ) allow the orientation of the sample for measuring particular reflections; the vertical motion 2θ allows the displacement of the detector arm (same rotation axis of θ).

2.3 X-ray Absorption Fine Structure (XAFS)

X-ray Absorption Spectroscopy (XAS) is an experimental method in physics and chemistry for determining the bonding of solids by analyzing oscillations of the x-ray absorption coefficient versus photon energy.

The short range order character of the probe makes it complementary to XRD, which on the contrary gives information on the long range order.

Consider a monochromatic X-ray beam passing through a material of thickness t:

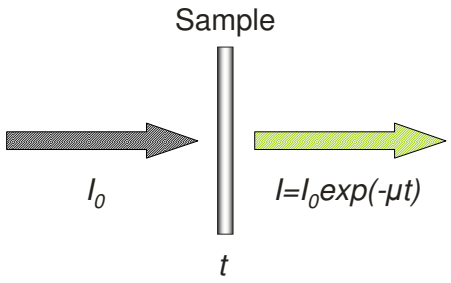

the transmitted intensity is reduced with respect to the incident one according to the equation:

$$I = I_0 e^{-\mu t}. \tag{2.17}$$

where μ, the linear absorption coefficient, depends on the photon energy, the atomic density and the atomic species of the alloy. The general trend of μ with energy is decreasing, interrupted by some discontinuities that represent specific absorption edges corresponding to the binding energies of deep electronic levels (figure 2.7(a)). Absorption edges corresponding to the extraction of an electron from the deepest level (1s) are those having the highest energy and are called K-edges. The following table establishes the connection between high energy edges and core electronic levels:

Edge	...	K	L_1	L_2	L_3	M
Level	...	$1s_{\frac{1}{2}}$	$2s_{\frac{1}{2}}$	$2p_{\frac{1}{2}}$	$2p_{\frac{3}{2}}$	$3s_{\frac{1}{2}}$

The edge energies depends on the binding energy of the corresponding core level. Since the binding energies grow monotonically with the atomic number Z (see figure 2.7(b)), an edge energy corresponds to a well defined atomic species.

After the absorption of a X-ray photon, an isolated atom can be either excited, if the photon energy corresponds to the energy difference between an electronic core level and

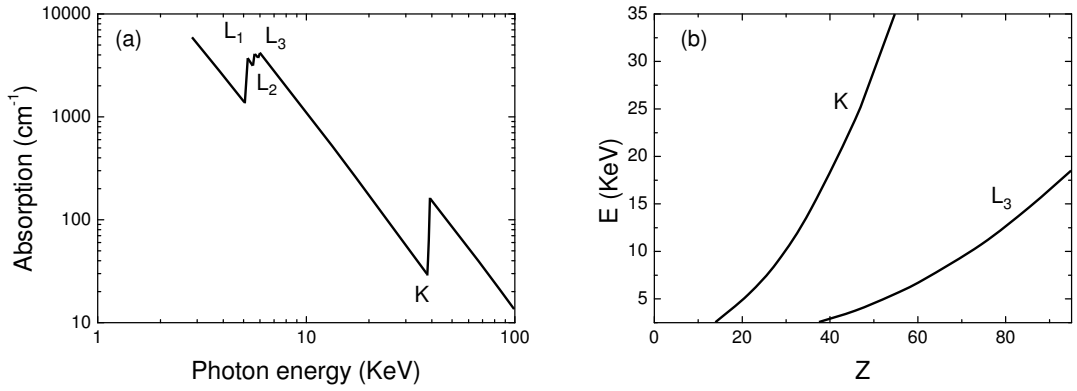

Figure 2.7: (a) Absorption coefficient evidencing the discontinuities associated to K-, $L_{1,2,3}$- edges. (b) Binding energy at the K- and L_3-edge as a function of the atomic number Z.

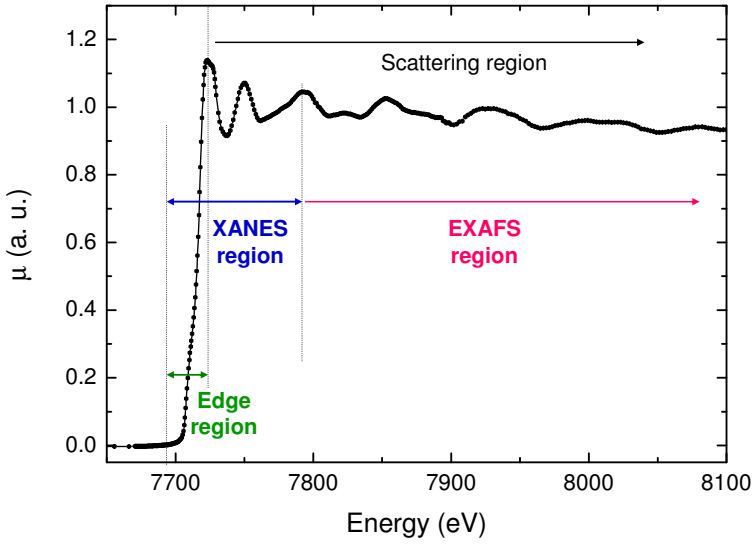

Figure 2.8: Absorption K-edge of the Co atom (E_0=7710 eV) eV).The edge, XANES and EXAFS regions are marked.

an unoccupied shallow level, or ionized, if the photon energy is larger than the binding energy, so that the electron (photoelectron) is ejected from the atom.

In correspondence of an edge, the absorption coefficient exhibits oscillations known as X-ray Absorption Fine Structure (XAFS). An absorption spectrum is usually divided into three main regions:

- the *edge region*, limited to a few eV around the edge energy (E_b), dominated by the effects of transitions to localized electronic states, multipole transitions; it is very sensitive to the details of the atomic potential;

- the energy region near the edge (*Near-edge Region*), extending up to a few tenths of

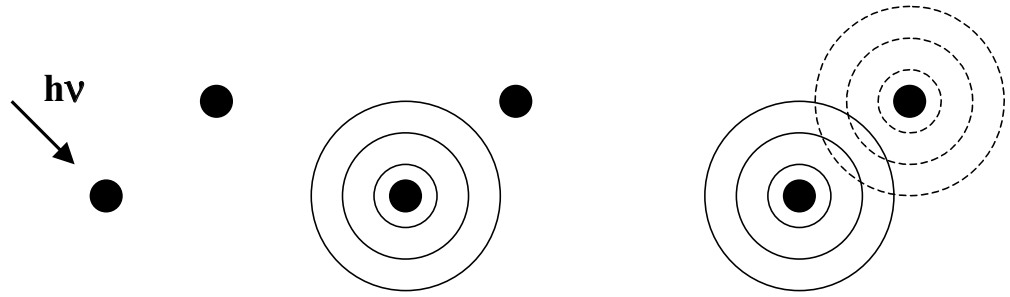

Figure 2.9: Schematic representation of the process generating EXAFS process. An atom absorbs a photon (on the left) then emitting a photoelectron described by an outgoing spherical wave. If the atom is isolated, the outgoing spherical wave can be backscattered by a nearby atom (in the central figure); the backscattered wave interferes with the outgoing wave (on the right, dotted line).

eV above the edge. Here, the fine structures (named XANES, X-ray Absorption Near Edge Structure) are dominated by multiple scattering processes of photoelectrons emitted with low kinetic energy. XANES contain information on the electronic structure of the investigated samples and on the geometric symmetry of the absorbing site;

- the energy region, starting from about 40-50 eV above the edge (*Extended Region*) is due mainly to single scattering events. These fine structures constitute the EXAFS signal (Extended X-ray Absorption Fine Structure) and contain information on the atomic local structure around the absorber atom.

For isolated atoms (noble gas or metallic vapors) fine structures are limited to a few eV around the edge, due to Rydberg levels and EXAFS structures are not present. On the contrary for condensed systems fine structures can extend up to a thousand of eV above the edge.

2.3.1 EXAFS: the phenomenological mechanism

When the X-photons have enough energy to ionize the absorbing atom, a photoelectron is emitted, with a kinetic energy given by the difference between the photon energy and the binding energy of the electron (E_b). From a quantistic point of view the photoelectron can be described by a spherical wave outgoing from the absorber atom. If the absorbing atom is not isolated the photoelectron waves interfere strongly with the potential generated by surrounding atoms, undergoing scattering processes from their potential. Every diffusion process generates a new outgoing wave from the scatterer atom. This implies that the final state of the photoelectron will be modified and given by the interference of the outgoing spherical wave with the waves back-scattered by the nearby atoms.

The interference of these photoelectron waves on the absorbing atom determines the oscillations of the absorption coefficient. Maxima and minima are function of the pho-

toelectron wavelength, the photoelectron path and the scattering processes. As a consequence they contain information on the atomic structure around the absorbing atom. In particular the frequency of EXAFS oscillations, properly normalized, gives information on the absorber-scatterer distance while their amplitude is connected to the number and type of scatterer atoms.

EXAFS is a powerful technique to probe the environment of a specific atom in a local range, because of the limited mean free path of photoelectron about a few tenths of Å.

Tthe EXAFS function $\chi(k)$ depends on the transition probability of the absorbing atom from an initial state to different possible final states. Disorder effects have also to be included: even in a statistically isotropic system the distance between the absorber atom and neighbouring atom of the selected coordination sphere has not a well defined value r_s; it varies according to a probability distribution $g(r)$ properly normalized ($\int_0^{\inf} g(r)dr = 1$).

Using the single electron and dipole approximations, as described in Appendix A, one can arrive to a formal expression for the EXAFS function associated to the s-th coordination sphere:

$$\chi_s(k) = \frac{S_0^2}{k} N_s Im \left[f_s(k,\pi) e^{2i\sigma_1} \int_0^{inf} g(r) \frac{e^{2r/\lambda}}{r^2} e^{2ikr} dr \right] \tag{2.18}$$

where k is the wave vector modulus, $k = \sqrt{(2m/\hbar^2)(\hbar\omega - E_b}$, S_0^2 a factor taking into account 'many-body' effects, N_s the coordination number of the s-th sphere, $f_s(k,\pi)$ the back-scattering amplitude, δ_1 a phase displacement and λ the mean free path of the photoelectron.

In the case of small disorder the radial distribution $g(r)$ can be parametrized by a gaussian function:

$$g(r) = \frac{1}{\sigma\sqrt{2\pi}} e^{\frac{(r-r_s)^2}{2\sigma}} \tag{2.19}$$

of mean value r_s and square deviation σ^2. In such a way the expression of $\chi(k)$ can be simplified and rewritten as *standard formula*:

$$\chi(k) = \frac{S_0^2}{k} \sum_s N_s |f_s(k,\pi)| \frac{e^{-2r/\lambda}}{r_s^2} e^{-2k^2\sigma_s^2} \sin(2kr_s + \Phi_s(k)) \tag{2.20}$$

where the factor $e^{-2k^2\sigma_s^2}$ is called *Debye-Waller factor.*

Characteristics of the standard formula

The standard formula is characterized by some empirical or semi-empirical parameters as well as by structural parameters:

$\mathbf{S_0^2}$: takes into account the contribution of the N-1 passive electrons representing the overlap integral of the initial and final states wave functions. It leads to an attenuation of

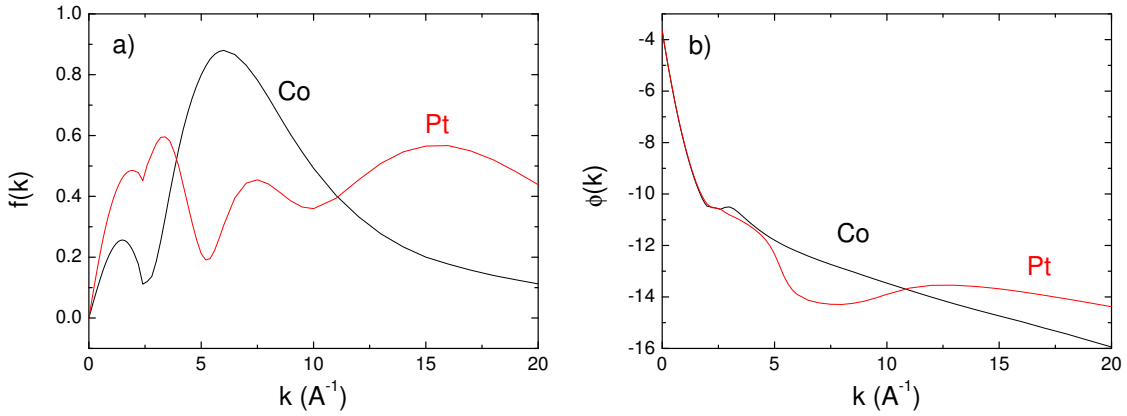

Figure 2.10: Trend of the amplitude (a) and phase (b) with wave vector k for a Co and Pt elements.

the signal amplitude.

λ: is the mean free path associated to the photoelectron. It takes into account inelastic contributions in the scattering process of the photoelectron together with core hole lifetime effects. The factor $e^{-2r/\lambda}$ contributes to reduce gradually the amplitude of EXAFS oscillations with increasing distances of scatterer atoms. This makes the signal sensitive to the local atomic arrangements around the absorber atom.

Each coordination shell is specified by three structural parameters:

coordination number: the signal amplitude is directly proportional to the number of atoms N in the shell;

interatomic distance: the frequency of the EXAFS signal depends on the main distance;

Debye-Waller factor: σ^2 represents the relative mean square deviation of the interatomic distance and includes a thermal (σ_T^2) and a static disorder (σ_S^2): $\sigma^2 = \sigma_T^2 + \sigma_S^2$.

The last two semi-empirical parameters are: the **scattering amplitude**, $f(k, \pi)$, and **phase shift** of the photoelectron, $\Phi(k)$, which depend on the chemical nature of the constituting elements. Figure 2.10 shows the changes of the amplitude and phase for a Co and Pt elements as a function of the scattering vector.

Using the standard formula the values of structural parameters can be extracted when the modulus of the backscattering amplitude, the phase shift and inelastic terms (S_0^2) are known. Two different procedures can be followed.

1. The backscattering amplitudes and phases can be extracted from the EXAFS signal of a reference sample of known structure, provided that the local structure of the reference and studied sample are similar.

2. The backscattering amplitudes and phases can be calculated using FEFF code [73, 74] starting from the potential in which the photoelectron moves. In a first step

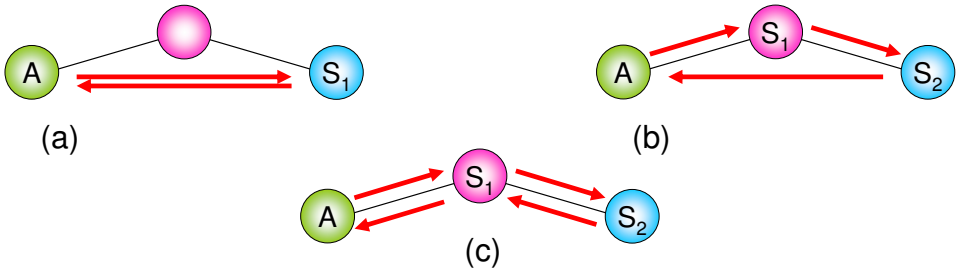

Figure 2.11: MS scattering up to the fourth order for an absorber A and two scatterer atoms S_1 and S_2: (a) single scattering path, (b) three-body scattering path (n=2), (c) four-body scattering path (n=3). The (b) and (c) contributions become quite important for the EXAFS signal when A, S_1 and S_2 are aligned.

the free atom potentials are used for each atomic species. Then the real potentials are determined by superimposing the charge densities of the free atoms, under the muffin-tin approximation. At the end the Hedin-Lunqvist self-energy is included for the excited states.

2.3.2 Multiple scattering

The introduction of multiple scattering effects represents an important development of the theory and interpretation of EXAFS signals. The EXAFS standard formula was derived under the single scattering approximation from nearby atoms: the outgoing photoelectron is scattered from a neighbor atom and then is backscattered towards the absorber. In the real system the photoelectron can be scattered by different atoms before returning back to the central atom (multiple scattering, MS). These MS effects can be introduced in order to obtain an exact calculus of the absorption coefficient for many compounds.

Though the amplitude of scattered waves becomes smaller and smaller as the number of available paths increases, some MS effects cannot be neglected [75]. Two example of MS are reported in figure 2.11 A strong increase in the signal amplitude is observed when the photoelectron is forward scattered. This effect is well known as *focusing effect* and can give a larger contribution to the EXAFS signal than SS paths of equal length.

Following the theory of multiple scattering, the standard formula of eq.2.20 is thus modified [76]:

$$\chi(k) = \sum_n \chi_n(k) \tag{2.21}$$

where:

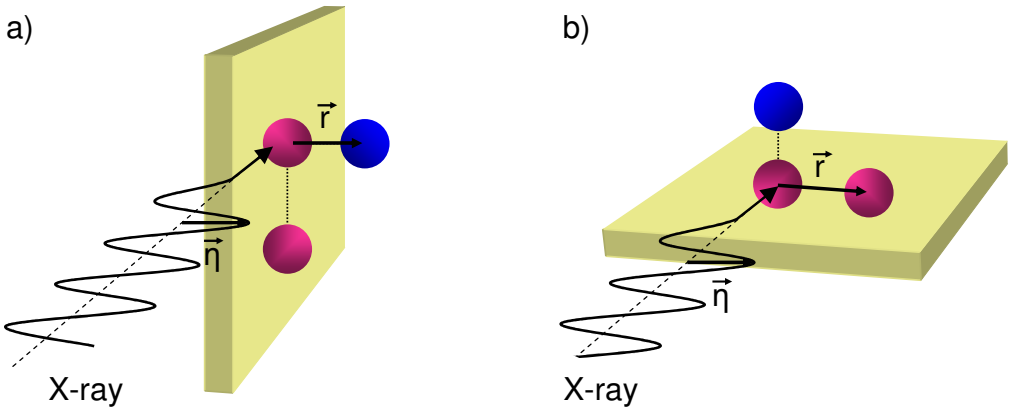

Figure 2.12: Schematic view of the directional dependence of the polarized EXAFS. (a) The beam linearly polarized out-of the film plane selects the out-of plane bonds, whereas (b) the beam linearly polarized in the film plane selects the in plane bonds.

$$\chi_n(k) = \sum_{p_n} \frac{N_{P_n} S_0^2}{k(R_{eff}^{p_n})^2} A_n(k, R_{eff}^{p_n}) e^{-2\sigma_{p_n}^2 k^2} e^{-2R_{eff}^{p_n}/\lambda} \sin(2kR_{eff}^{p_n} + \Phi_s(k, R_{eff}^{p_n})) \quad (2.22)$$

The sum of eq.2.22 is over all possible paths p_n of order n, while $R_{eff}^{p_n}$ is the total geometric length of path p. $A_n(k, R_{eff}^{p_n})$ and $\Phi_s(k, R_{eff}^{p_n})$ are the generalized scattering amplitudes and phases respectively.

$\chi_n(k)$ represents the partial contribution of order n to the EXAFS signal, deriving from all those processes in which the emitted photoelectron is scattered n times before turning back to the absorbing atom. In practice these processes bring information concerning the paths starting and finishing on the photoabsorbing site and that therefore touched n atoms. For $n = 1$ one obtains the EXAFS single scattering standard formula 2.20. In principle the sum of eq.2.22 extends up to an order n equal to infinity but the most relevant contributions to the EXAFS signal come from the first three terms.

2.3.3 Polarized EXAFS

The linear polarization of synchrotron radiation, coupled with the directional dependence of the photoabsorption process (polarized XAFS), allows probing the structural features along specific directions of the crystalline samples [76].

Following the calculation of the EXAFS signal, as reported in Appendix A, the χ signal can be written as:

$$\chi(k) \propto < \psi_i | \hat{\eta} \cdot \vec{r} | \delta\psi_f > \quad (2.23)$$

where $\hat{\eta}$ is the polarization vector of the incident beam, $\vec{r}$ is the vector position of the

neighbors measured from the absorber; $|\psi_i>$ and $|\delta\psi_f>$ are the wave function of the emitted photoelectron and the wave scattered from the potential of surrounding atoms, respectively.

For a non-isotropic structure, the coordination number N_s is replaced by an effective multiplicity number given by:

$$\widetilde{N}_s = 3\sum_{i=1}^{N_s} cos^2\alpha_{si} \tag{2.24}$$

where α_{si} is the angle between η and r_i, the vector between the absorbing atom and the ith scatter in the sth coordination shell.

For Co-Pt alloy, the analysis of XAFS data collected at Co K-edge as a function of the angle between the x-ray beam linear polarization and the film plane allows to sort the neighbors in one plane of the absorbing atom from the ones out of this plane.

2.3.4 Experimental apparatus

Polarized Co K-edge measurements were performed in fluorescence mode at the ESRF in the BM08 (GILDA) and CRG-BM30 (FAME) beamline.

The GILDA beam-line (General purpose Italian Line for Diffraction and Absorption) exploits the emission from a bending magnet and uses photons in the energy range 5-80 keV with high energy resolution, high flux on the sample and small beam spot. The monochromator is formed by two independent crystals, the first is flat and the second can be curved on a cylindric surface in order to focus the beam in the horizontal plane: in this way the incident beam is 2 mm wide. To cover the entire energy range (5-80 keV), there are three couples of crystals: Si(111), Si(311) for the low energy measurements and Si(511) for higher energy experiments. The energy resolution obtained is $\sim 5\cdot10^{-5}$ keV. In our experiment we used the Si(311) double-crystal. A couple of grazing incidence mirrors placed before the sample is used to clean the x-ray beam from higher-order harmonics (energy cut-off at about 10 keV). The mirrors collimate the beam before the monochromator in such a way to better the resolution, they reduce the incident power on the monochromator and vertically focus the beam [77, 78].

The measurements were performed at 14 K to enhance the EXAFS signals. The fluorescence intensity emitted by the sample was collected by a 7-element high-purity Ge detector (current limit sensitivity: 10^{14} at/cm^2).

For each sample, two spectra were collected using in-plane and out-of-plane polarizations as sketched in figure 2.13. As the synchrotron radiation is linearly polarized in the horizontal plane, for in-plane polarization geometry the sample holder was inclined of $\gamma =\sim 10^\circ$, where γ is the angle between the direction of the incident beam and the normal to the sample surface (figure 2.13(a)); for the out-of-plane polarization geometry the sample holder was inclined of $\gamma =\sim 80^\circ$ (figure 2.13(b)).

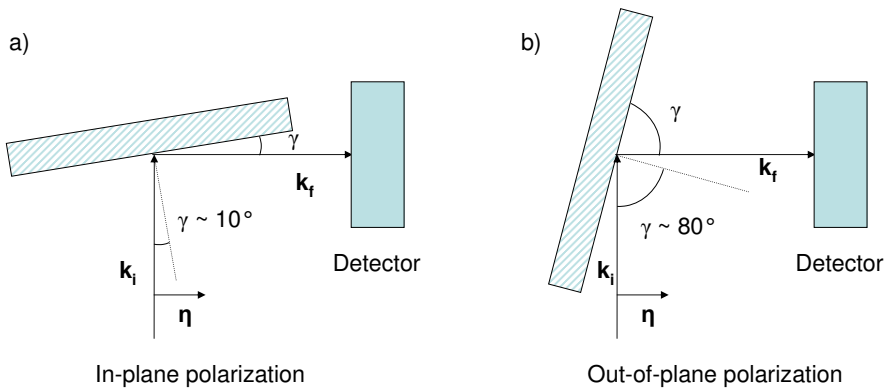

Figure 2.13: Top view of the in plane (a) and out-of-plane (b) polarization geometries.

The spectra can be contaminated by the intense Bragg peaks coming from the substrat. By collecting several spectra at slightly different γ ($\Delta\gamma = 5°$), Bragg peaks can disappear on a certain energy range. The acquisition of several spectra allows their suppression.

Note that for in-plane polarization geometry, the measured signal is less intense than that one for out-of-plane geometry, because some detector elements are hidden by the sample (see figure 2.13(a)).

Another series of polarized EXAFS measurement in fluorescence mode at Co-edge was carried out on the CRG-BM30 (FAME) at the ESRF [79]. The experimental apparatus is quite similar to GILDA beamline. However, the spectra present a worse statistic, due to a lower counting without having changed slightly γ from one spectrum to another to be able to remove totally the Bragg peak contributions.

2.4 Grazing Incidence Small Angle Scattering (GISAXS)

Grazing-Incidence Small-Angle X-ray Scattering (GISAXS) is a versatile tool for characterizing the shape of nanoscopic objects at surfaces, at buried interfaces, or in thin films [80–82]. It is a complementary technique to the near field microscopies. The small a ngle X-ray scattering under grazing incidence geometry presents several advantages: (*i*) it gives an average statistical information over the whole sample surface; (*ii*) it can be applied in various environments, ranging from ultrahigh vacuum to gas atmospheres, *in situ* and in quasi real time when kinetics phenomena are involved; (*iii*) using the variable probed depth as a function of the incidence angle, it offers the opportunity to characterize a range of phenomena from surface roughness to buried particles. By combining the advantages of synchrotron radiation and two-dimensional detectors with in situ sample preparation, the full potential of such a method can be realized [83].

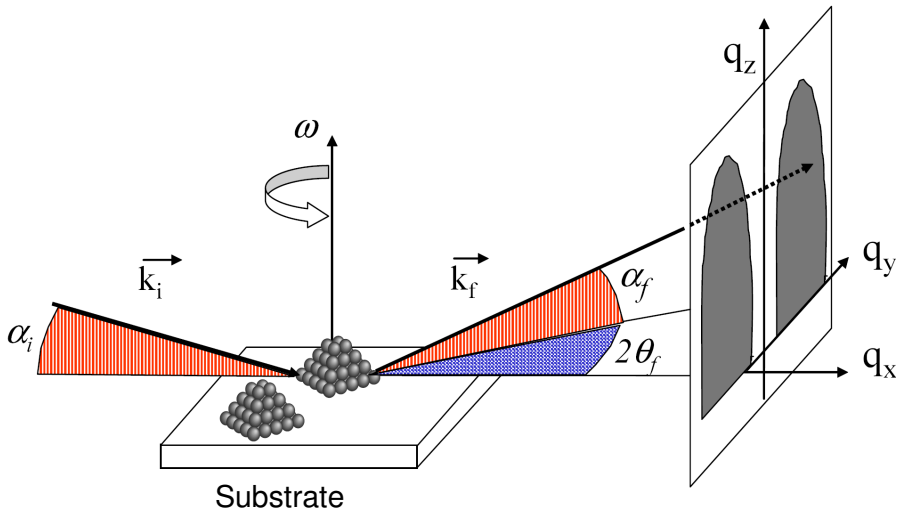

Figure 2.14: Principle of a GISAXS experiment applied to islands on a surface. The incident X-ray beam (wave vector $\vec{k}_i$) impinges on the surface at grazing angle α_i with respect to the surface. The transmitted and reflected beams are not represented here. The sample can be rotated around its surface normal by the angle ω. The scattered intensity is recorded on a plane as a function of the exit angle α_f with respect to the surface plane and of the in-plane angle θ_f. The momentum transfer is denoted $\vec{q}$=(q_x, q_y, q_z).

2.4.1 Theoretical background

The principle of GISAXS is sketched in figure 2.14. It consists in hitting a monochromatic beam of wavevector $\vec{k}_i$ in the X-rays range with a low divergence on the sample surface under grazing incidence, α_i. The light is scattered along $\vec{k}_f$ in the direction $(2\theta_f, \alpha_f)$ by any type of roughness on the surface. Because of energy conservation, the components of the scattering wavevector q are defined by

$$\vec{q} = \frac{2\pi}{\lambda} \begin{pmatrix} \cos(\alpha_f)\cos(2\theta_f) - \cos(\alpha_i) \\ \cos(\alpha_f)\sin(2\theta_f) \\ \sin(\alpha_f) + \sin(\alpha_i) \end{pmatrix}$$

This geometry ensures the surface sensitivity and the probed depth can be adjusted by varying the incidence angle. Any kind of roughness on the surface or any kind of electronic contrast variation in the subsurface region leads to beam scattering in an off-specular direction. In particular, this is the case for islands on a substrate or for buried particles or aggregates. The scattered beam is collected close to the specular beam in the small-angle range in order to probe typical length of the order of a few nanometers. Using a bidimensional detector, an image of the reciprocal space close to the origin is obtained. The spreading of t he scattered intensities over the q_y and q_z ranges informs directly on typical sizes of nanoobjects.

When the assembly of islands have a position and a shape statistically defined, the scattered intensity can be written as the sum of the coherent and incoherent term [84, 85]:

$$I(\vec{q}) = S(\vec{q}_{\parallel}) \times |\overline{F(\vec{q})}|^2 + \sum_m \Phi_m(\vec{q}) \times e^{-i\vec{q}\cdot\vec{r}_m}, \tag{2.25}$$

$S(\vec{q}_{\parallel})$ is the 2D interference function of the island assembly and corresponds to the FT of the island position autocorrelation function. $|\overline{F(\vec{q})}|$ is the spatial averaging of the island form factor that is the amplitude scattered by an island of volume V and electronic density ρ irradiated by the incident beam [86]. In the simple Born Approximation (BA), $F(\vec{q})$ is given by the FT of the island electronic density:

$$F(\vec{q}) = \int_V \rho(\vec{r}) e^{-i\vec{q}\cdot\vec{r}} \mathrm{d}V. \tag{2.26}$$

The $\Phi_m(\vec{q})$ coefficient in eq.2.25, describes the correlations between island; it is given by

$$\Phi_m(\vec{q}) = \overline{[F_n(\vec{q}) - \overline{F(\vec{q})}][F_{n+m}(\vec{q}) - \overline{F(\vec{q})}]^*}^n \tag{2.27}$$

where the n superscript denotes the average over all islands n and $F_n(\vec{q})$ is the form factor of the island n. The function $\Phi_m(\vec{q})$ is a measure of the correlation between the scattering amplitude of two islands separated by a vector r_m. The summation over $\Phi_m(\vec{q})$ in eq.2.25 yields the incoherent diffuse scattering arising from such correlations [87]. Three approximations are commonly used to evaluate this incoherent scattering.

I) Decoupling approximation (DA)

A current hypothesis known as the decoupling approximation [85, 86] is to suppose that the distance between islands is independent on their morphologies. The partial pair correlation functions depend only on the relative positions of the scatterers and not on the class types, i.e., $\Phi_m(\vec{q}) = 0$ for the $m \neq 0$. Thus only the $m = 0$ remains:

$$\Phi_0(\vec{q}) = \overline{|F(\vec{q})|^2} - |\overline{F(\vec{q})}|^2. \tag{2.28}$$

II) Local monodisperse approximation (LMA)

The Local monodisperse approximation is often used for polydispersed systems. Neighboring islands are assumed to have the same shape and size, over the coherent area of the x-ray beam [89, 90]. The intensity is thus the incoherent summation of that of monodisperse subsystems weighted by the size distribution. The intensity originating from one monodisperse domain i is

$$I_i(\vec{q}) = S_i(\vec{q}) \times |F(\vec{q})|^2 \tag{2.29}$$

The incoherent sum of the intensity over all the domains is then

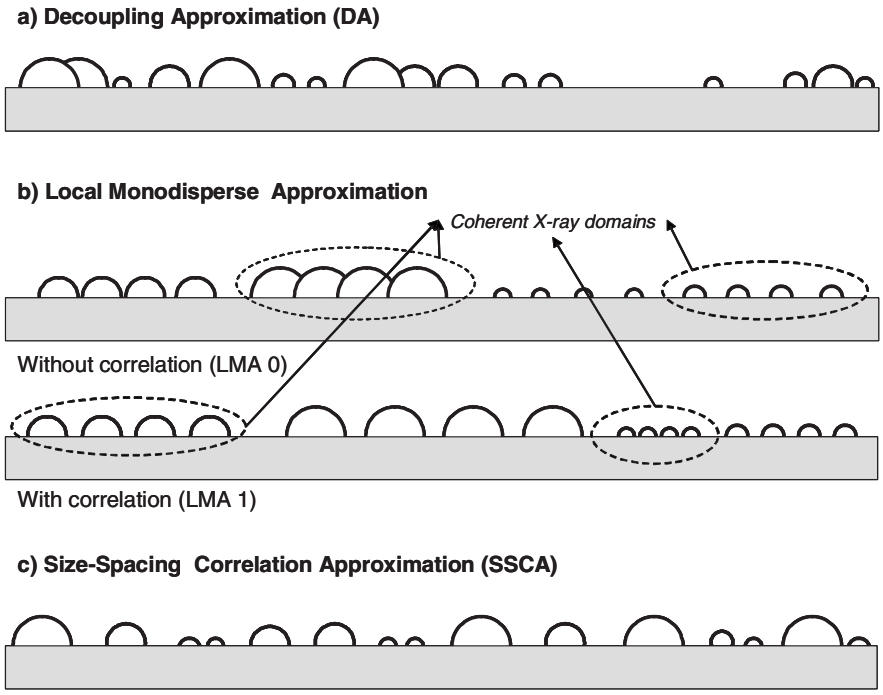

Figure 2.15: Schematics of the morphology corresponding to the various approximations used to calculate x-ray diffuse scattering. Particles are placed following (a) a full disorder without any correlations (DA), (b) sets of monodisperse domains over a length scale larger than the x-ray coherence length (LMA) without correlation between size and spacing (LMA 0) or with such a correlation (LMA 1), and (c) a correlation between particle separation and their respective sizes (SSCA) [88].

$$I(\vec{q}) = \sum_i I_i(\vec{q}) \approx S(\vec{q}) \times |\overline{F(\vec{q})}|^2 \tag{2.30}$$

assuming that the same interference function holds for all the domains.

For disordered systems, the DA and the LMA lead to the same results at high wave vector transfer where the scattering is sensitive only to the average particle form factor. However, measurements in such a high $q_{\|}$ limit are often hampered by the decrease of intensity and the residual background.

III) Size-spacing correlation approximation (SSCA)

The size-spacing correlation approximation introduces the coupling between the particle sizes and spacings [88]. To understand this approximation the one-dimensional (1D) paracrystal model has to be introduced.

• **One-dimensional paracrystal model (1DDL)** Information about the statistical distribution of the particles in the substrate is given by the interference function, $S(\vec{q}_{\|})$ in the eq. 2.25, defined as:

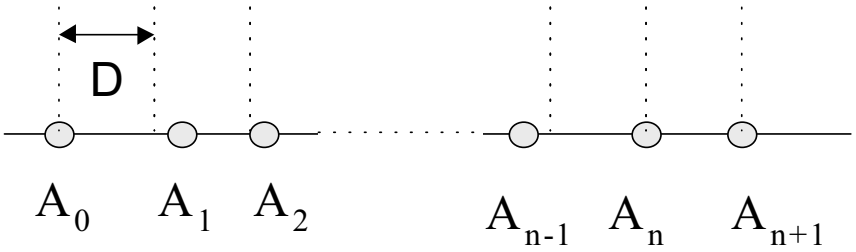

Figure 2.16: Schematic view of the 1D paracrystal model

$$S(\vec{q}) = 1 + \rho_s \int \mathrm{d}^2R \; g(\vec{R}_{\|}) \; e^{-i\vec{q}\cdot\vec{R}_{\|}} \tag{2.31}$$

where ρ_s is the number of particles per unit of surface and $g(\vec{R}_{\|})$ is the partial pair correlation functions. In the paracrystal model [86] the long-range order is destroyed gradually in a probabilistic way. Let one considere the 1D case [87].

To build the autocorrelation function $g(x)$ for the island positions, the distance between two successive points A_{n-1}, A_n (see figure 2.16) is chosen to be independent of the previous and next one, and to obey a statistical distribution $p(x)$ with

$$\int_{-\infty}^{\infty} p(x)\mathrm{d}x = 1, \qquad \int_{-\infty}^{\infty} xp(x)\mathrm{d}x = D. \tag{2.32}$$

Thus, after having placed the first island A_0 at the origin and a second island A_1 at a mean distance D from the first one (see figure 2.16), the probability of placing the third one A_2 at a distance x from the first one is given by the occurrence of a distance y between the first and the second and a distance $x - y$ between the second and the third. By integrating over all the y possibilities, one is led to

$$p_2(x) = \int_{-\infty}^{\infty} p(y)p(x-y)\mathrm{d}y, \tag{2.33}$$

which is the self-convolution product $p(x) \otimes p(x)$. By generalizing,

$$z(x) = \delta(x) + p(x) + p(x) \otimes p(x) + p(x) \otimes p(x) \otimes p(x) + ... \tag{2.34}$$

The interference function is then given by the Fourier transform of eq. 2.34:

$$S(q) = 1) + \mathcal{P}(q) + \mathcal{P}(q) \cdot \mathcal{P}(q) + \mathcal{P}(q) \cdot \mathcal{P}(q) \cdot \mathcal{P}(q) + ... \tag{2.35}$$

For a Gaussian probability distribution, which is the small disorder limit of any type of distribution,

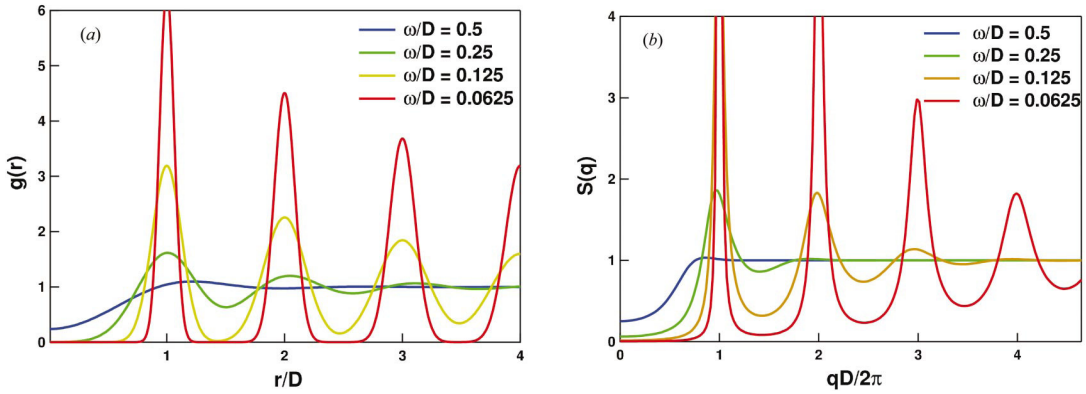

Figure 2.17: The pair correlation function (a) and the interference function (b) in the case of the one-dimensional paracrystal for various Gaussian disorder parameters ω/D [84].

$$\begin{aligned} p(x) &= \frac{1}{\sqrt{2\pi}\omega} e^{-\frac{(x-D)^2}{2\omega^2}}, \\ \mathcal{P}(q) &= e^{-\frac{q^2\omega^2}{2}} e^{iqD}. \end{aligned} \tag{2.36}$$

Taking into account also the particles along the negative x-axis, it follows:

$$S(q) = 1) + 2\sum_{n=1}^{\infty} e^{-n\frac{q^2\omega^2}{2}} \cos(nqD) = \frac{1 - e^{-q^2\omega^2}}{1 + e^{-q^2\omega^2} - 2e^{-\frac{q^2\omega^2}{2}} \cos(qD)}. \tag{2.37}$$

The results for this Gaussian disorder are depicted in figure 2.17 in direct and reciprocal space. The broadening of the peaks with increasing ratio ω/D reflects the transition from an ordered lattice to a disordered lattice.

• **SSCA** In the size-spacing correlation approximation the 1D paracrystal model is used and the probability to find the distance d_n separating two neighboring particles of size R_{n-1} and R_n follows the Gaussian law:

$$p(d_n/[R_{n-1}, R_n]) = \frac{1}{\sqrt{2\pi}\sigma_D} e^{-\frac{(d_n - < d_n/[R_{n-1}, R_n] >)^2}{2\sigma_D^2}}, \tag{2.38}$$

with a central value

$$< d_n/[R_{n-1}, R_n] >= D + \kappa[R_{n-1} + R_n - 2 < R >]. \tag{2.39}$$

D is the average distance between neighboring particles, $< R >$ is the mean particle radius, κ is the size-spacing coupling parameter and σ_D is the variance of the cumulative disorder within the paracrystal description of the lattice. The fluctuations of spacings given by $< (d_n - D)^2 >$ contain two contributions:

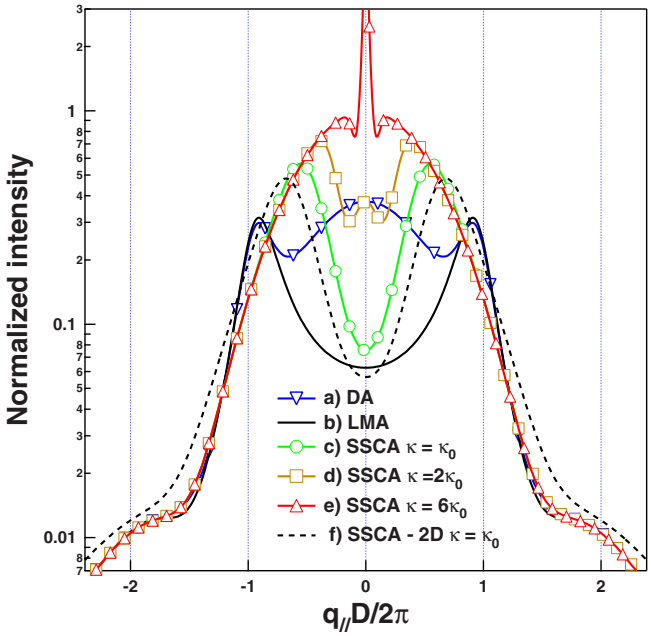

Figure 2.18: In-plane GISAXS intensities from 1D infinite chain of cylinders within various framework (DA, LMA, SSCA). For SSCA, $\kappa = \kappa_0(\vec{q}_\perp)$ is the special value of the coupling parameter for which the intensity is minimum at $q_\parallel$=0. Both the size and chain statistics are Gaussian with $\sigma_{R_\parallel} / < R_\parallel >= 0.25$, and $D = 3 < R_\parallel >$. The particle aspect ratio H/R=1 [88].

$$< (d_n - D)^2 >= \sigma_D^2 + 2\kappa^2\sigma_R^2. \tag{2.40}$$

The parameter σ_D^2 is intrinsic to the underlying paracrystal, while $2\kappa^2\sigma_R^2$ is linked to the fluctuations of the particle sizes $[\sigma_R^2 =< (R- < R >)^2 >]$. At the limit κ=0, the DA is recovered with a 1D paracrystal interference function as eq. 2.37.

An important point is that all approximations (DA, LMA, SSCA) are equivalent at large parallel wave vector transfer $\vec{q}_\parallel$; "large" means well beyond the correlation peak.

Figure 2.18 shows the scattered intensity along the parallel direction calculated using the three approximations. The intense scattering found at small $\vec{q}_\parallel$ values in DA vanishes in the LMA with a maximum of intensity slightly shifted from the first peak of paracrystal interference function (eq. 2.37), $q_\parallel D/2\pi$=1, because of the local slope of the form factor [84]. The introduction of correlation between particles size and separation distance yields strong modifications. In particular, the position of the maximum of intensity is no more simply related to the mean particle separation D as expected in DA or LMA approximations. Instead, in SSCA, the correlation peak position decreases when increasing κ.

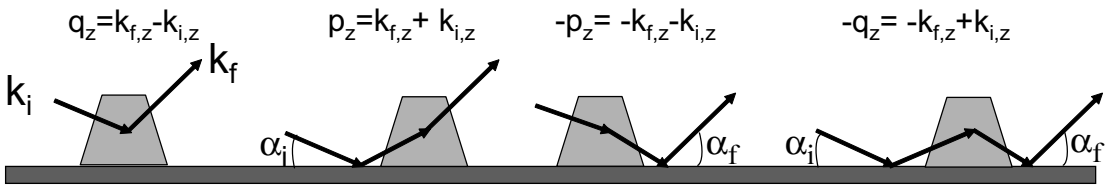

Figure 2.19: The four terms in the scattering for a supported island. The first term corresponds to the Born approximation.

Distorted-wave Born approximation (DWBA)

The BA takes into account only the scattering of the incident beam by the islands, but the substrate and the value of α_i close to the critical angle, α_c, introduces reflection-refraction effects. An appropriate theory has been developed called distorted-wave Born approximation. It corresponds to the first-order perturbation [91] induced by the island roughness to the correct unperturbed wave, i.e. the trio of incident-reflected-refracted waves at the substrate surface. Figure 2.19 represents the physical picture for the full calculation [92, 93] of the scattering cross section of a island in the DWBA.

The new $F(\vec{q})$ is replaced by the coherent sum of four terms, which represent different scattering events involving or not a reflection of either the incident or final beam on the substrate surface. Each term comprises the island form factor, evaluated at different values $\pm q_z = \pm(k_z^f - k_z^i)$ and $\pm p_z = \pm(k_z^f + k_z^i)$, and weighted by the Fresnel reflection coefficients $R(\alpha_i)$ and $R(\alpha_f)$ of the substrate:

$$F(\vec{q}_\parallel, k_z^i, k_z^f) = F(\vec{q}_\parallel, q_z) + R(\alpha_f)F(\vec{q}_\parallel, -p_z) + R(\alpha_i)F(\vec{q}_\parallel, p_z) + R(\alpha_i)R(\alpha_f)F(\vec{q}_\parallel, -q_z). \tag{2.41}$$

For substrates with an uncorrelated roughness, the Fresnel reflection coefficients are modified by a decreasing exponential term depending on the rms roughness σ, the z component of the wave vector in vacuum and that of the wave vector in the substrate [94]. In this GISAXS study, the reference system for DWBA is the bare substrate, although it might be useful to take into account the surface roughness induced by the islands in the form of a Debye-Waller factor for the Fresnel reflection coefficients [93].

The BA is valid only when $R(\alpha_i) = R(\alpha_f) = 0$, that is when α_i and α_f are much larger than α_c. In figure 2.20 the scattered intensities of a cylinder (H=5 nm) evaluated within the BA and the DWBA are compared along the perpendicular direction. Due to the multiple scattering effects, the intensity displays a sharp increase for $\alpha_f \approx \alpha_c$, corresponding to the so called Yoneda peak. Moreover, the BA intensity has deep minima as opposed to much slighter minima obtained within the DWBA. For $\alpha_i = \alpha_c$ or $\alpha_c/2$ ($2\alpha_c$), the minima obtained within the DWBA are shifted toward larger (smaller) exit angles with respect to those obtained within the BA. The contribution of each term of eq.

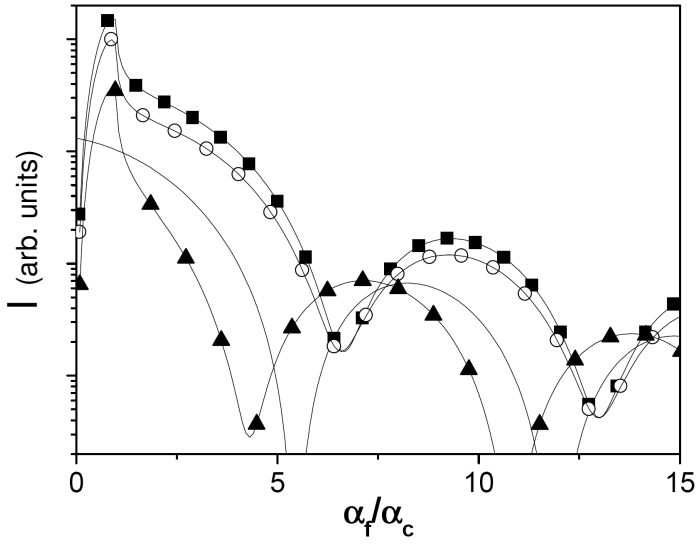

Figure 2.20: Out-of-plane GISAXS intensity for a cylinder (H=5 nm) as a function of a α_f/α_c and at $2\theta_f = 0$. Filled squares, DWBA for $\alpha_i = \alpha_c$; triangles, DWBA for $\alpha_i = 2\alpha_c$; open circles, DWBA for $\alpha_i = \alpha_c/2$; continuous line, BA. [95].

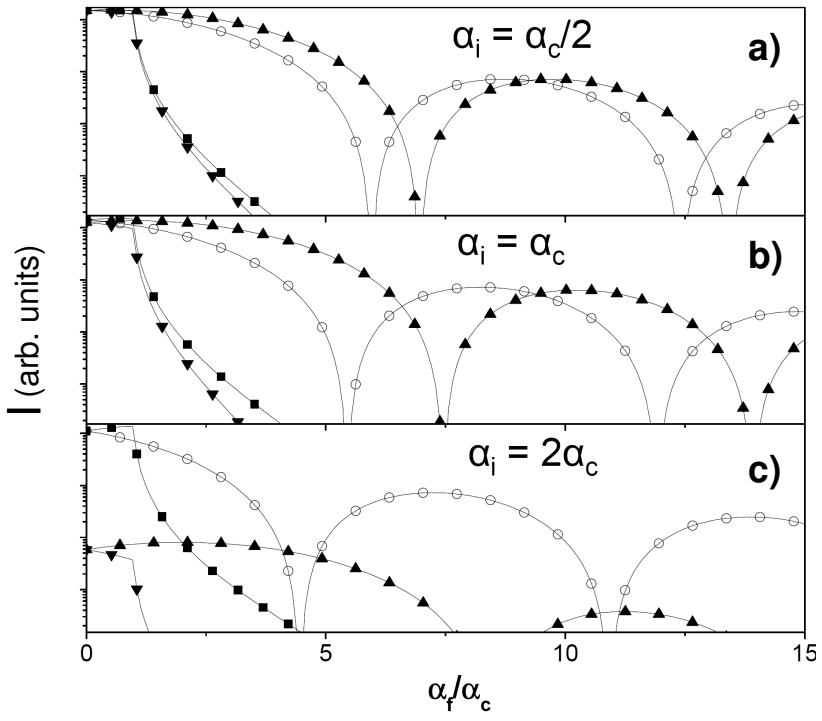

Figure 2.21: Square modulus of the four terms of eq. 2.41 for a cylinder (H=5 nm) as a function of a α_f/α_c and at $2\theta_f = 0$ for (a) $\alpha_i = \alpha_c/2$, (b) $\alpha_i = \alpha_c$, and (c) $\alpha_i = 2\alpha_c$. Open circles, $F(\vec{q}_\parallel, q_z)$; up triangles, $R(\alpha_i)F(\vec{q}_\parallel, p_z)$; filled squares, $R(\alpha_f)F(\vec{q}_\parallel, -p_z)$; down triangles, $R(\alpha_i)R(\alpha_f)F(\vec{q}_\parallel, -q_z)$ [95].

2.41 is reported in figure 2.21 as a function of $\alpha_i \approx \alpha_c$. When $\alpha_i = \alpha_c$ and $\alpha_c/2$ the first and third terms have a similar magnitude over the whole range of exit angles; whereas the second and fourth terms are negligible, except for $\alpha_f \leq \alpha_c$. The addition of this third term attenuates the minima and shifts them. When $\alpha_i \gg \alpha_c$ and $\alpha_f \gg \alpha_c$ the BA is a good approximation.

2.4.2 GISAXS analysis

Guinier analysis

A first approach to analyse the GISAXS images is based on Guinier approximation [85] in which the scattering at very small angle is of Gaussian form, independent of the shape of the scattering particle.

The scattering amplitude of a sphere of radius R and uniform density ρ_0 is written by

$$\mathcal{S}(q) = \int_V \rho_0 e^{-i\vec{q}\cdot\vec{r}} \mathrm{d}\vec{r} \tag{2.42}$$

After performing spherical average it follows:

$$\mathcal{S}(q) = V\rho_0 \frac{3}{(qR)^2}\left(\frac{\sin(qR)}{qR} - \cos(qR)\right), \tag{2.43}$$

where $V = 4\pi R^3/3$ is the volume of the scattering object, which is a sphere in this case. For very small angle, or $qR << 1$, the following approximations can be written:

$$\frac{\sin(qR)}{qR} \approx 1 - \frac{q^2R^2}{3!} + \frac{q^4R^4}{5!} - ...; \qquad \frac{\cos(qR)}{qR} \approx 1 - \frac{q^2R^2}{2!} + \frac{q^4R^4}{4!} - ... \tag{2.44}$$

The scattered intensity is thus:

$$I(q) = |\mathcal{S}(q)|^2 \approx V^2\rho_0^2\left(1 - \frac{q^2R^2}{10}\right)^2 \approx V^2\rho_0^2\left(1 - \frac{q^2R^2}{5}\right) \approx V^2\rho_0^2 e^{\frac{q^2R^2}{5}}. \tag{2.45}$$

Let one use the definition of *radius of gyration*: $< R_G^2 >= \frac{1}{V}\int r^2 dV$ which is defined as the mean square distance from the centre of gravity. For a sphere of radius R_s it can be shown that $R_G = \sqrt{3/5}R_s$. Substituting into the eq. 2.45 it follows:

$$I(q) =\approx V^2\rho_0^2 e^{\frac{q^2R_G^2}{3}}. \tag{2.46}$$

This expression is valid for any object with an arbitrary shape.

R_G (or R_s) is thus obtained from the slope of the so called Guinier plot: $ln(I)$ vs q^2 for $qR_G << 1$.

Shape analysis

The most interesting specificity of GISAXS is to probe the island morphology, i.e., shape and size, which is defined from the form factor.

Several methods can help in determining simple shapes. First, the variation of the GISAXS pattern, as the sample is rotated around its surface normal allows one to determine the symmetry of the island shape. Secondly, the existence of scattering rods is an indication of facetting. Thirdly, the island shape can be deduced by analyzing the asymptotic behavior of the intensity in the case of a large polydispersity [95].

A complete analysis is done by using the program $isGISXAS$ [96] created by R. Lazzari. It offers two working modes: (i) simulation of GISAXS images or line cuts on a ($2\theta_f$, α_f) grid; (ii) fit of data, employing a Levenberg-Marquadt minimization [97] of a χ^2 criterion on a variable number of line cuts in the reciprocal space. The calculation can be performed in the various frameworks previously described for the scattering process (BA, DWBA) and for the size-position coupling (DA, LMA, SSCA).

2.4.3 Experimental apparatus

D2AM beamline

The GISAXS experiments were performed at the European Synchrotron Radiation Facility (ESRF) on the D2AM (Diffraction et Diffusion Anomale Multilongueurs d'onde)-BM02 beamline.

For better stability with respect to energy, the D2AM optics is symmetrical, with a double monochromator situated between two mirrors. The beamline is located on the BM02 bending magnet and uses the 0.85 Tesla source with a critical wavelength of 0.6Å (20.6 keV). At the entry to the optical hutch, a primary collimator accepts up to 3mrad of the horizontal divergence. Primary slits located upstream of all the optical components are used to define the effective vertical and horizontal divergence. The first mirror, a platinium-coated silicon single crystal, acts as a low pass filter and enables the beam to be focussed in the vertical plane. These first elements lie in a very clean vacuum (10^{-9} without beam, $10^{-7}m$bar with beam) that extends up to the last Beryllium window. The beam is then processed by a double crystal monochromator equipped with Si(111), or occasionally at high energies, with Si(311). This monochromator has a bandwidth of 10^{-4} and focusses the beam sagittally in the horizontal plane. A second mirror, identical to the primary one, provides focussing in the vertical plane. Rear slits, located just after the second mirror and also near the instruments, reduce spurious signals from optical aberrations.

This whole symmetrical arrangement acts as fixed exit optics and should yield a 3:1 demagnification of the source. More details are described on [98]. It delivers photons from 5 to 25 keV to the experimental hutch in a spot of a few hundred microns. Small spots down to 70x100 μm^2 can be attained. The experiments were performed at 7.5 keV

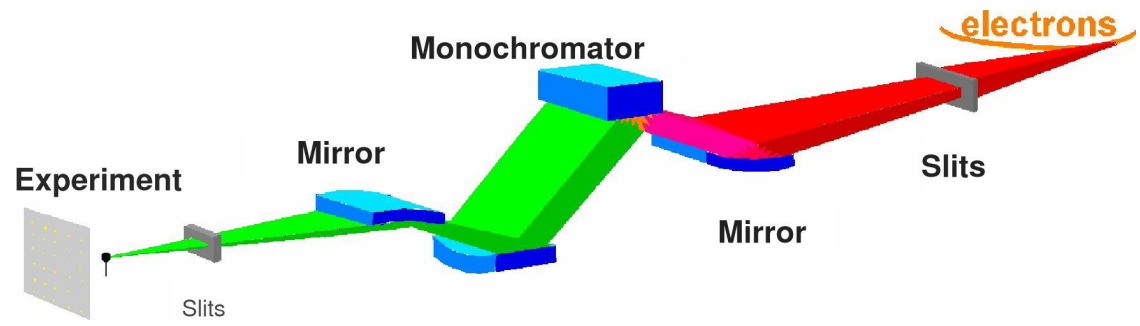

Figure 2.22: Optic schema in BM02 beamline.

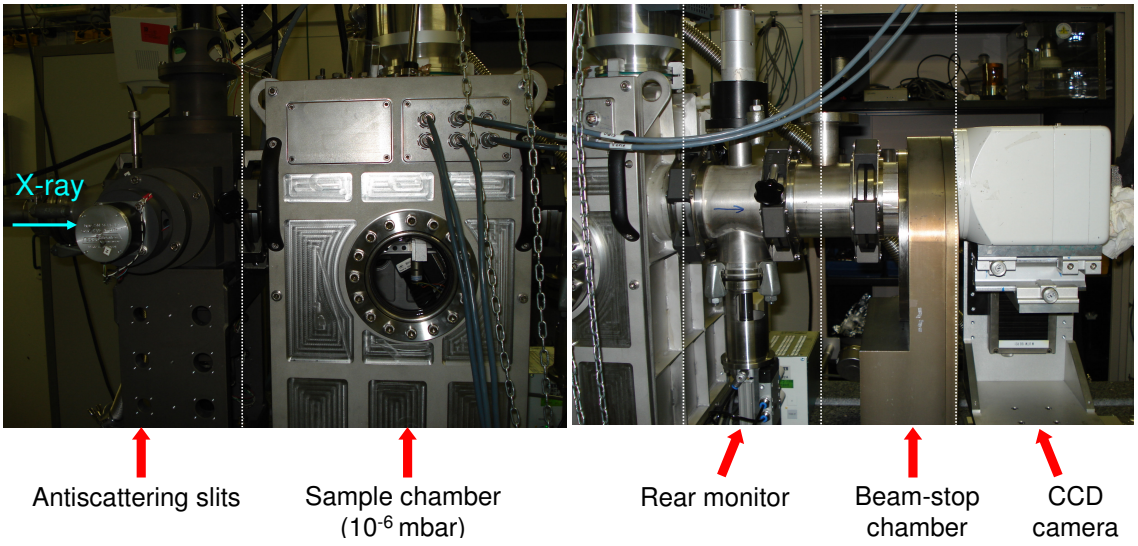

Figure 2.23: GISAXS experimental apparatus.

with a beam spot of 600x100 μm^2 (HxV).

GISAXS camera

The small angle camera is situated at the rear of the experimental hutch and receives the incoming beam through an evacuated pipe passing inside the goniometer (described in figure 2.6). The camera itself, on a single granite bench, is shown in figure 2.23: it consists of a set of antiscattering slits to avoid diffuse scattering, the sample chamber, a rear monitor, some exchangeable vacuum tubes up to the beam stop and a CCD detector.

A special sample chamber has been developed to realize the measurements at $\sim 10^{-6}$ mbar on samples directly transfered from a portable vacuum chamber. The position can be adjusted in the beam by six movement degrees, shown in figure 2.24: the rotation of

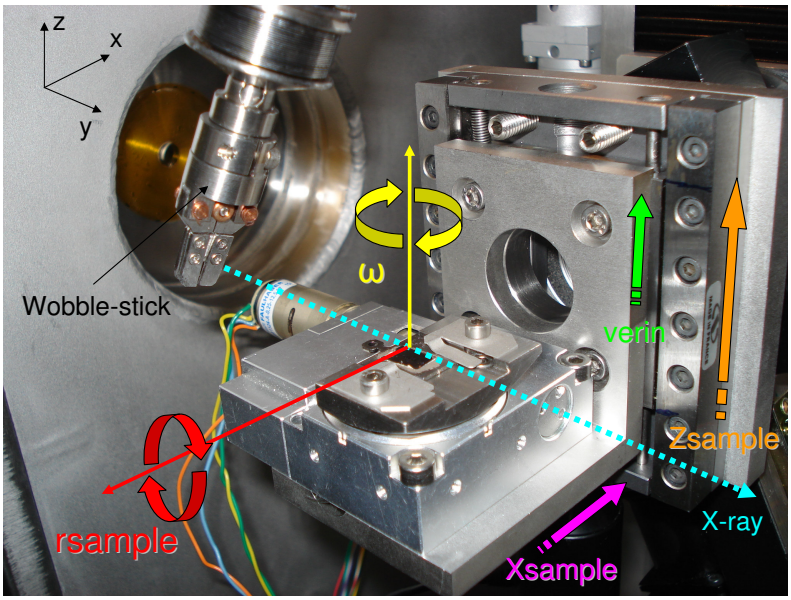

Figure 2.24: Interior of the sample chamber. The principal movement degrees are reported: the rotation of the sample holder around the normal to the surface, ω and around the x-axe, $rsample$; the big, $Zsample$, and small, $verin$, vertical translation; the horizontal translation, $Xsample$, along x-axe.

the sample around the normal to its surface, ω, the rotation around the x-axe, $rsample$, to fix the incident angle; the large, $Zsample$, and small, $verin$, vertical translation; the horizontal translation, $Xsample$, perpendicular to the beam direction. The scans of the rear monitor counting as a function of $Xsample$, $Zsample$, $verin$ and $rsample$ movements allow to align the sample. The critical angle of the substrate was checked by the recording a "pseudo" reflectivity curve with the PM monitor.

The scattered intensity was collected on a 16-bit x-ray charge-coupled device detector (1340x1300) pixels for horizontal and vertical directions with a pixel size of 50x50 μm), located at a distance of 550 mm from the sample. For probing facet effects, GISAXS patterns were recorder for different azimuth direction (ω). A motorized tungsten beamstop with a T shape was positioned perpendicularly to the sample surface in order to mask the transmitted and specularly reflected beams. Several orders of magnitude in intensity separate the diffuse scattering from the reflected beam intensity.

With this setup, the outgoing $2\theta_f$ and α_f angles vary between 0 and approximately 5°. In reciprocal space, the maximal momentum transfers q_y and q_z are equal to 3.0 and 4.0 nm-1 respectively. The q_x coordinate always remains negligible. The data were corrected for the flat field, that takes into account the different pixel efficiencies, and the dark counts to suppress the hot pixels and to take into account of electronics offset.

Experimental issues

A requirement to record good GISAXS images is to use flat and large substrates. The latter condition means to have a substrate larger than the beam footprint which is about 10 mm in grazing incidence. This condition was not always respected in the case of $WSe_2(0001)$ substrates. In fact, because of the preparation method, the larger the substrate the worst its flatness. Figure 2.25 shows the reflected beam of an unperfect substrate, collected removing the beamstop and using several filters in order to not saturate the detector: a broad spot is observed, the extent over q_z is due to the superimposition of reflected beams coming from differently oriented regions. On the GISAXS pattern, reported in figure 2.26, the centre is completely disturbed by the diffuse scattering of WSe_2 (figure 2.26 right) and also the isotropic diffuse scattering coming from the STM plate; this latter contribution is important more especially as the WSe_2 substrate is small.

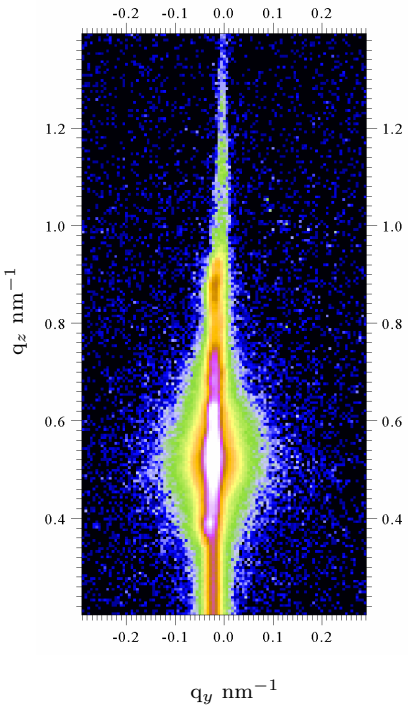

Figure 2.25: Reflected beam

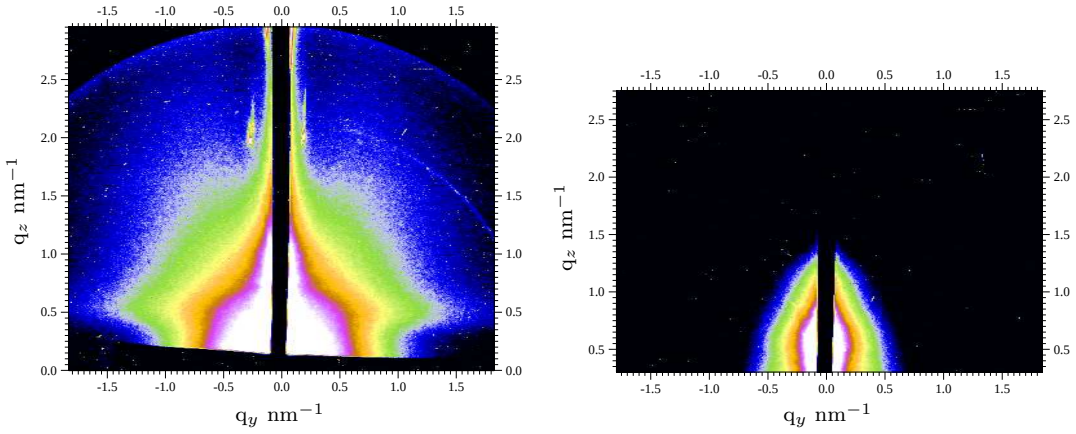

Figure 2.26: (Color) Experimental GISAXS patterns for 0.5 nm thick $CrPt_3$ grown on $WSe_2(0001)$ at 570 K (on the left) and for $WSe_2(0001)$ substrate (on the right).

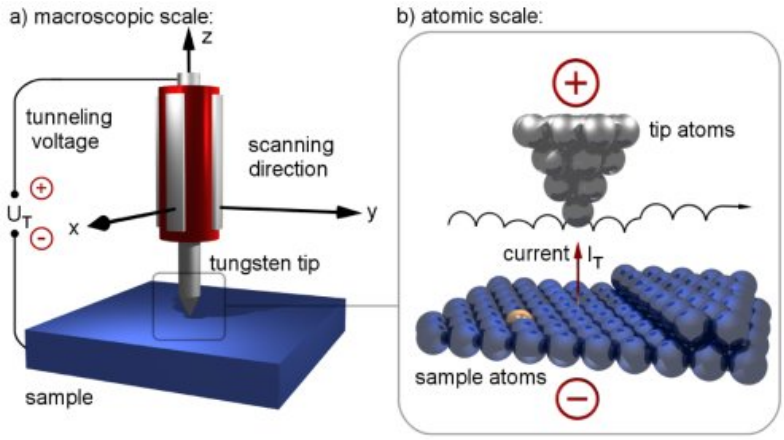

Figure 2.27: 3D view of an STM image of one monolayer high islands with Pt core and an approximately 3 atom wide Co shell [99].

2.5 Complementary techniques

2.5.1 Scanning Tunneling Microscopy (STM)

Scanning tunneling microscopy was developed by G. Binnig and H. Rohrer [100] (Nobel Prize in Physics 1986). Since STM allows imaging on an atomic scale, it belongs to some of the most powerful experimental techniques for surface science studies. In STM, a metal tip is placed in close proximity to the sample surface (typically 0.3 - 2 nm). A small bias voltage U is applied between the tip and the sample (figure 2.27). If the separation between the tip and the sample is small enough, quantum tunneling of electrons from the sample to the tip through the vacuum gap occurs. The tunneling current is the quantity usually monitored during STM measurement. Due to the exponential dependence of the tunneling current on the tip-sample separation, STM measurements give the highest achievable spatial resolution [101, 102].

Nowadays, STM is usually used in the constant current mode: while measuring, the tip scans over the surface and a feedback system attempts to keep the current constant by varying the tip-sample separation. This allows the collection of information about the sample surface in real space. The tunneling current depends not only on the topography of the sample surface, but also on its electronic structure. Therefore, surfaces with different chemical composition may provide different contrasts in STM. This effect makes the interpretation of STM images more complicated. However "chemical" contrast may yield valuable information on the local sample composition (figure 2.28). An exact interpretation of the chemical contrast presupposes the availability of additional information on the electronic structure [99]. This information can be obtained, for instance, by measuring sample properties in one of the scanning tunneling spectroscopy modes [103].

The STM measurements were performed by Y. Gauthier at the Institut Néel in Greno-

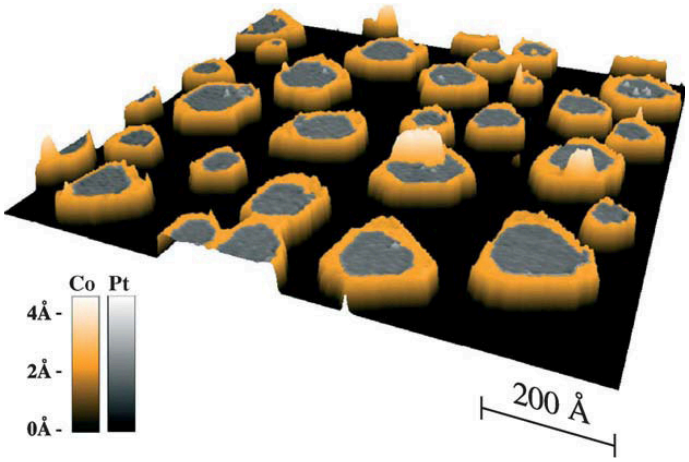

Figure 2.28: 3D view of an STM image of one monolayer high islands with Pt core and an approximately 3 atom wide Co shell [99].

ble and by D. Makarov at the Konstanz University (Germany).

2.5.2 Transmission Electron Microscopy (TEM)

One disadvantage of STM is that it requires a conducting substrate. Since many materials are not conducting, other methods for studying surfaces with atomic resolution have been developed for insulator substrates. The transmission electron microscopy is one of the most useful and widespread methods for materials characterization. It was developed by Koll and Ruska in 1932 and the first transmission electron microscope was built only four years later [104].

TEM consists of an electron gun, a number of electromagnetic lenses and a fluorescent screen, enclosed in vacuum because of the strong electron-material interaction. When a thin specimen (10-100 nm) is irradiated with an electron beam of uniform current density, the electron beam is transmitted through the sample and it is scattered by the coulomb interactions. Electrons are scattered both elastically (e.g. Bragg diffraction) and inelastically (energy loss spectroscopy). The directions of the scattered electrons are changed and a variable electron intensity hits the viewing screen creating an image. This non-uniform electron distribution contains information about structure and chemical composition of the material.

The microscope may be operated to produce diffraction patterns from specific regions or images. Because both diffraction pattern and image of the specimen are always produced by the objective lens, a magnific image of either may be produced on the viewing screen by focussing the next lens in the magnification system on one or the other (details are reported in figure 2.29).

To get information about the cristalline structure, electron diffraction patterns formed

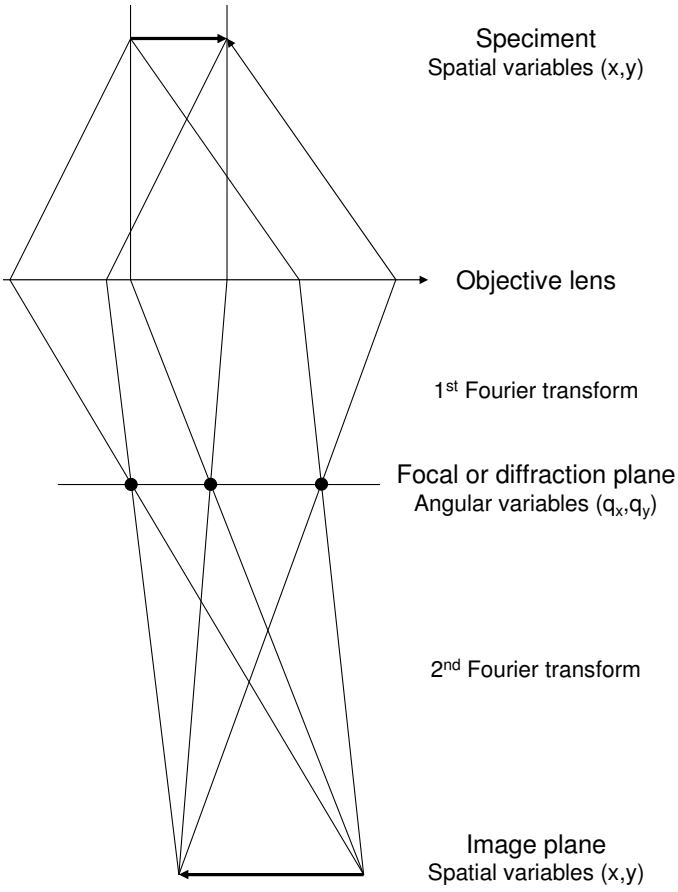

Figure 2.29: Schematic picture of the TEM image formation [105].

in the focal plane of the objective lens are projected on the viewing screen.

High-Resolution Transmission Electron Microscopy

High Resolution Transmission Electron Microscopy (HRTEM) is an imaging mode of the TEM that allows the imaging of the crystallographic structure of a sample at an atomic scale.

All TEM and HRTEM measurements were performed by B. Doisneau on a JEOL 2010 microscope by B. Doisneau at the LMGP laboratory.

2.5.3 Superconducting Quantum Interference Device (SQUID)

Magnetic characterization includes the determination of magnetization, directions of easy/hard axis and anisotropy energy. For it, superconducting quantum interference device magnetometry (SQUID) was used, due to its high sensitivity required for thestudy of nano-objects.

The SQUID consists of two superconductors separated by thin insulating layers to

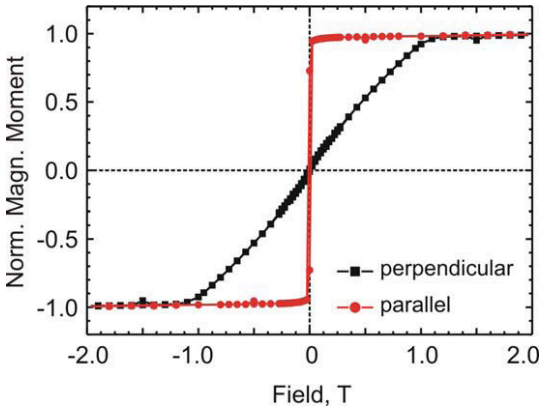

Figure 2.30: SQUID hysteresis loops measured in the out-of-plane and in-plane geometry on [Pt(4 Å)/Fe(4.7 Å)]x12 deposited at room temperature on a planar SiO_2 substrate.

form two parallel Josephson junctions. The device may be configured as a magnetometer to detect incredibly small magnetic fields. Samples can be magnetized in fields of up to ±5 T and measurements can be carried out in a temperature range from 1.7 K to 400 K. Two different types of studies were performed by SQUID.

ZFC/FC measurements: the effects of thermal activation and magnetic relaxation can be studied by measuring zero-field and field cooling (ZFC/FC) curves. In order to perform ZFC measurements, the sample in its paramagnetic state is first cooled down under zero field. Then it is exposed to a small magnetic field (usually 10-50 mT) applied along the samples easy axis and the low-field magnetic susceptibility is measured starting at low temperatures (∼5 K) up to room temperatures. For the FC curve, the sample is cooled from 300 K down to 5 K, in a magnetic field.

Hysteresis loops: The SQUID magnetometer allows to measure the magnetization hysteresis loops for magnetic field applied perpendicular or parallel to the substrate. A "classical" hysteresis loop measured on Fe/Pt multilayers deposited on a planar SiO_2 substrate at room temperature is shown in figure 2.30. The area between the in-plane and out-of-plane loops allows the estimation of the effective anisotropy energy.

All measurements were performed by D. Makarov in Konstanz University (Germany).

Chapter 3

$CoPt_3$ alloy grown on $WSe_2(0001)$

This chapter is focused on the determination of the structural origin of perpendicular magnetic anisotropy observed on nanostructured films of $CoPt_3$ grown on $WSe_2(0001)$, using the polarized EXAFS technique. The samples are previously characterized by x-ray diffraction and SQUID. Moreover, the change of morphology of deposits as a function of the growth temperature and thickness is studied from STM and GISAXS measurements.

3.1 Preliminary characterization of $CoPt_3$ by RHEED, XRD and SQUID

$CoPt_3$ films were prepared by co-deposition of Co and Pt atoms on $WSe_2(0001)$, cleaved prior being introduced to UHV chamber, at the range 300-700 K deposition temperatures. The Co and Pt fluxes were 0.0046Å/s and 0.02Å/s, respectively. The epitaxial growth and the $L1_2$-type ordering were characterized by RHEED.

3.1.1 Epitaxial growth and structural characterization

Figure 3.1 shows the RHEED patterns taken along the [11-2] and [1-10] azimuths of 3 nm thick ($\sim$15 ML) $CoPt_3$ at temperatures ranging from 300 to 700 K. They confirm the epitaxial growth of self-assembled fcc mono-crystalline islands of $CoPt_3(111)$. The planes of $CoPt_3$ are azimuthally aligned with the $WSe_2(0001)$ plane revealing the following epitaxial relationships: [11-20]$WSe_2(0001)$‖[1-10]$CoPt_3$ and [10-10]$WSe_2(0001)$‖[11-2]$CoPt_3$. The separation distance between the WSe_2 streaks and the $CoPt_3$ spots corresponds to the 17% of the lattice mismatch, indicating the growth of the nanostructures almost stress-free.

Double spots appear along the [1-10] azimuth which result from twinning of fcc structure. Using the software package CaRIne [109] it is possible to reproduce the whole reflection patterns in figure 3.1(d) by the superposition of the reflections of the fcc structure grown along the [111] direction with its twin (figure 3.2). Along the two azimuths, superlattice spots appear for T_d=370 K (marked by arrows in figure 3.1(b)) and become more intense at T_d=570 K. It means that the system starts to order in the $L1_2$ phase at 370 K as already observed in [10].

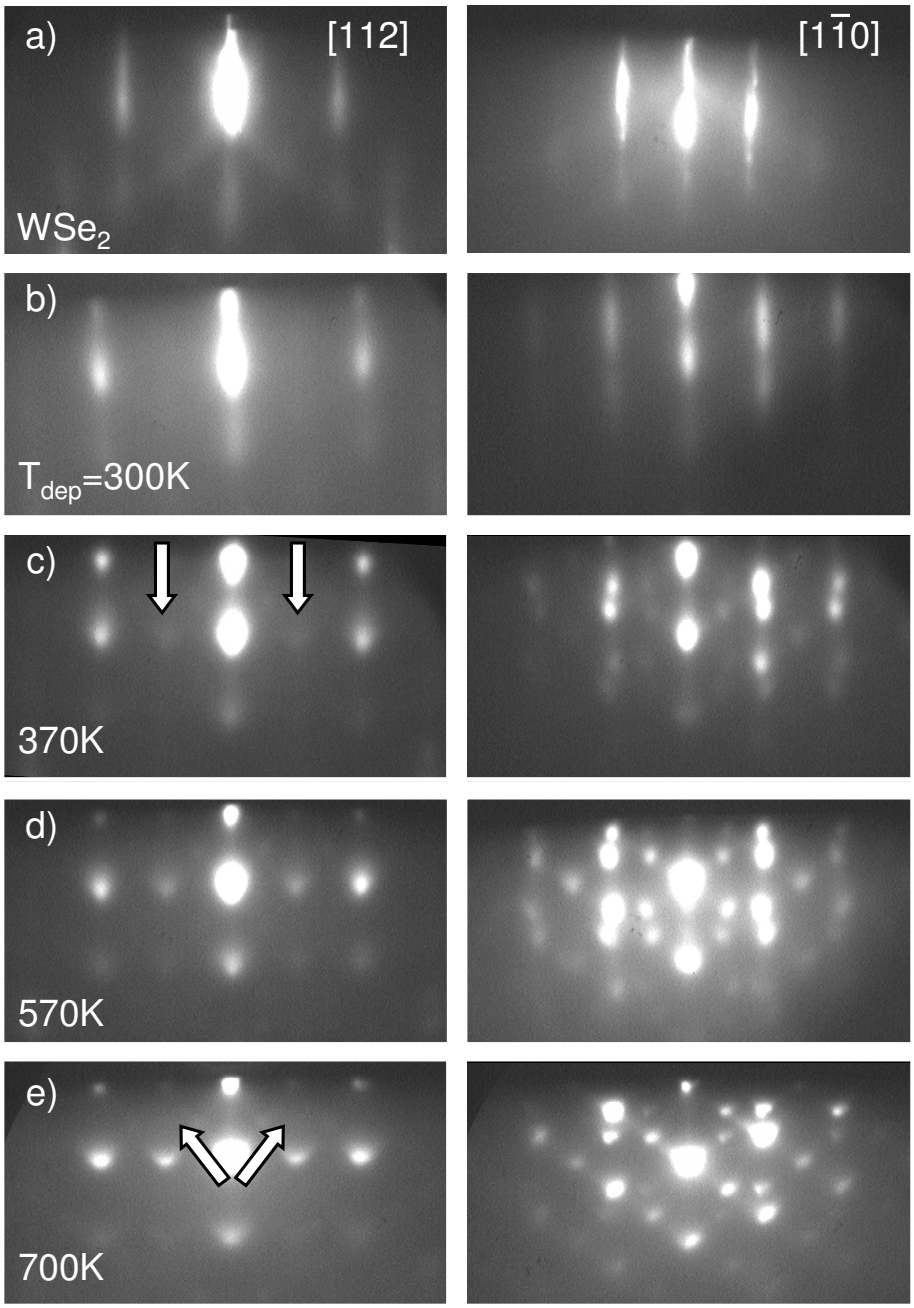

Figure 3.1: RHEED patterns along the [11-2] and [1-10] azimuths of 3 nm thick $CoPt_3$ grown on WSe_2(0001) at different temperatures. Arrows in (b) indicate the superlattice spots. Arrows in (e) indicate the polygonal spots well pronounced at T_d=700 K, signature of faceted islands.

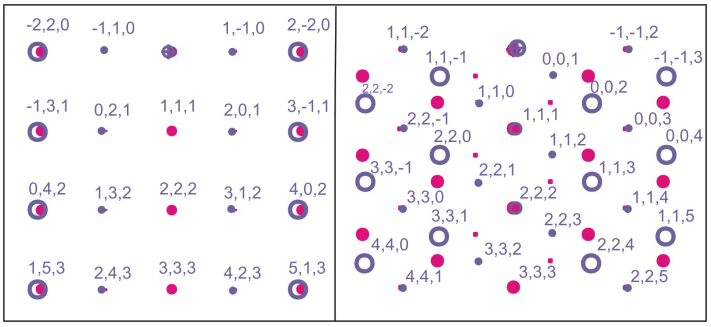

Figure 3.2: Calculated diffraction patterns obtained from the superimposition of the reflections coming from the fcc structure grown along the [111] direction (pink circles) and its twin (violet circles).

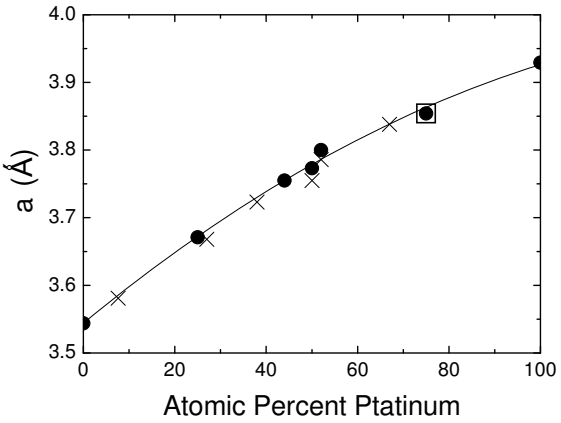

Figure 3.3: Variation of the crystallographic parameter a of the fcc solid solution Co_xPt_{1-x} alloys as a function of Pt concentration. The values are taken in [106] (full circles), [107] (crosses) and [108] (open square). The variation is fitted using a polynomial of second dregree (solid line).

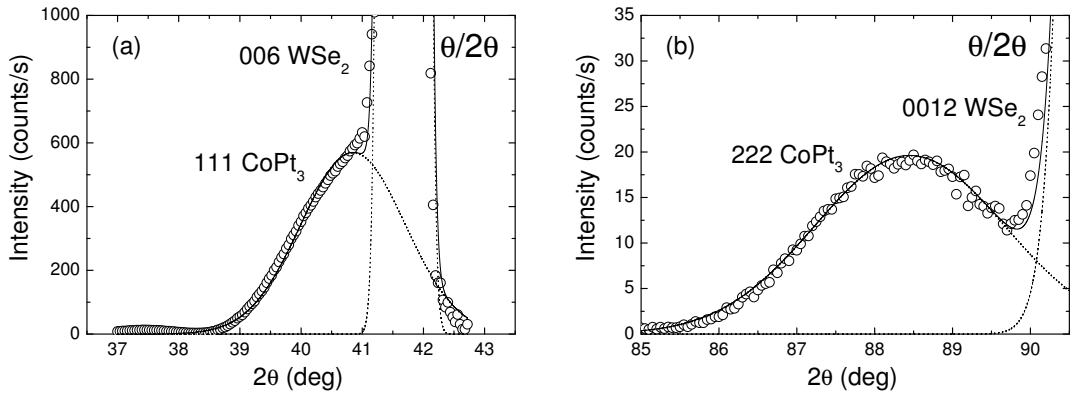

Figure 3.4: XRD $\theta/2\theta$ scans of a $Co_{35}Pt_{65}$ sample grown on $WSe_2(0001)$ at RT around (a) (111) and (b) (222) reflections, with the (006) and (0012) reflections of WSe_2.

X-ray diffraction measurements have been carried out at the SIMaP laboratory in order to characterize the structure from the $CoPt_3$(222) and (111) reflections. These measurements have allowed to estimate the sample compositions. The lattice a parameter of the fcc Co_xPt_{1-x} solid solution depends on Pt concentration. Figure 3.3 reports the experimental a parameters and the fitted curve described by the law $a(X_{Pt}) = 3.544 + 0.0055X_{Pt} - 1.7\times10^{-5}X_{Pt}^2$. The a parameters deduced from the 111 and 222 peak positions is equal to 3.826 Å and leads to a Pt concentration of 65%. Figure 3.4(a) and (b) show the $\theta/2\theta$ scan around the 111 and 222 reflections which are closed to the 006 and 0012 substrate peaks, respectively. Both $CoPt_3$ reflections can be separated from the substrate peaks by a two-Gaussian fit. Therefore, the alloy is characterized by the 65% of Pt. The $Co_{35}Pt_{65}$ alloy is still in the composition range of the $L1_2$ phase.

3.1.2 Magnetic characterization

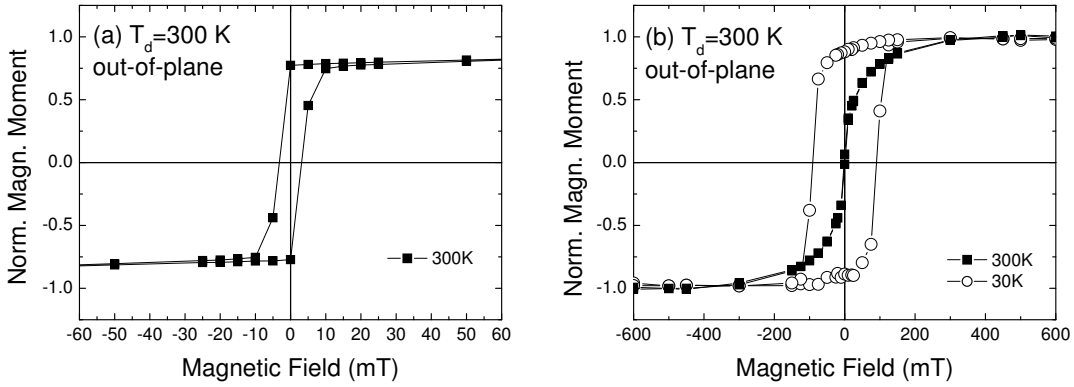

Figure 3.5: Hysteresis curves for $Co_{35}Pt_{65}$ (a) and $Co_{22}Pt_{78}$ (b) nanostructures grown at RT (for a coverage of 3 nm), measured with the magnetic field applied normal to the substrate plane at 300 K (black squares) and 30 K (open circles).

SQUID magnetometry measurements with the field applied normal to the substrate plane were performed in Pt-rich alloy deposits grown at RT, namely $Co_{35}Pt_{65}$ and $Co_{22}Pt_{78}$, in order to verify the PMA, as already observed in [59]. The hysteresis loop in figure 3.5(a) confirms that the $Co_{35}Pt_{65}$(111) nanostructures present an easy axis perpendicular to the substrate plane. Figure 3.5(b) shows the hysteresis loops measured at 30 and 300 K for $Co_{22}Pt_{78}$: an open loop is only visible when the measurement temperature is below its Curie temperature.

3.2 Short-range ordering

Two series of EXAFS measurements were performed at the Co K-edge using the in-plane and out-of-plane polarization in order to probe the short-range order and its eventual anisotropy. The first series was carried out on the CRG-BM30 (FAME) at the European

Synchrotron Radiation Facilities (ESRF, Grenoble), in fluorescent mode. The investigated samples of $Co_{22}Pt_{78}$ were 3 nm-thick and prepared at 300 and 570K on $WSe_2(0001)$. The second series were collected on the BM08 (GILDA) at ESRF using the same geometries in fluorescent mode, for the sample slightly rich in Co (composition $Co_{35}Pt_{65}$), 3 nm thick and grown at 300 and 700 K.

3.2.1 EXAFS data analysis

The experimental XAS spectra, $\mu(E)$, were treated following the standard methods to extract the XAFS structural signal $\chi(k)$: the pre-edge background was fitted with a straight line and subtracted; the post-edge atomic background was modelled with a smooth polynomial spline through the experimental data. The energy scale for the photoelectron wavevector ($k = \hbar^{-1}\sqrt{2m(E-E_0)}$) was defined choosing the edge energy (E_0) at the maximum of the $\mu(E)$ first derivative.

The quantitative analysis of EXAFS spectra is performed fitting the k^2-weighted experimental data $k^2\chi(k)$ using the standard EXAFS formula [76]:

$$k^2\chi_{th}(k) = S_0^2 \sum_j \frac{\tilde{N}_j k}{R_j^2} F_j(k) \exp(-2k^2\sigma_j^2) \exp(-\frac{2R_j}{\lambda(k)}) sin(2kR_j + \phi_j(k)) \qquad (3.1)$$

where R_j and σ_j^2 are respectively the average absorber-to-j-neighbour distance and the mean square relative displacement (Debye-Waller factor). The $F_j(k)$ and $\phi_j(k)$ are the amplitude and phase shift functions. These were calculated by FEFF code [73] using as models the crystallographic structures of the $L1_2$ phase and a fcc disordered solid solution. More details are give further. The $\lambda(k)$ is the photoelectron mean free path and S_0^2 is an empirical parameter taking into account to losses due to many-body effects. $\tilde{N}_j$ is the effective coordination number of the jth contribution, and takes into account the polarization dependence of the photo-absorption process and single-scattering processes (eq. 2.24).

For the two geometries, the contributions of the in-plane and out-of-plane neighbours to $\tilde{N}_j$ are given in table 3.1. For out-of-polarization only the out-of-plane atoms contribute to the signal due to the negligible contribution of in-plane neighbors. In contrast, the in-plane polarized XAFS data contain in-plane ($\tilde{N}_{\parallel}^{in}$) and out-of-plane ($\tilde{N}_{\parallel}^{out}$) contributions with different weights depending on the coordination shell. Note that whatever the polarization and for any shell, $\tilde{N}_{\parallel(\perp)}^{in} + \tilde{N}_{\parallel(\perp)}^{out}$ is equal to the total number of neighbors $N_{tot} = N^{in} + N^{out}$. For this reason, the XAFS signals of a perfectly ordered $L1_2$-type phase or a fully chemically disordered fcc phase are independent of polarization.

The relations between the true coordination numbers (N^{in} or N^{out}) and the measured polarization-dependent (effective) coordination number ($\tilde{N}_j$) for the first three coordination shells in a fcc environment can be deduced from equation 2.24:

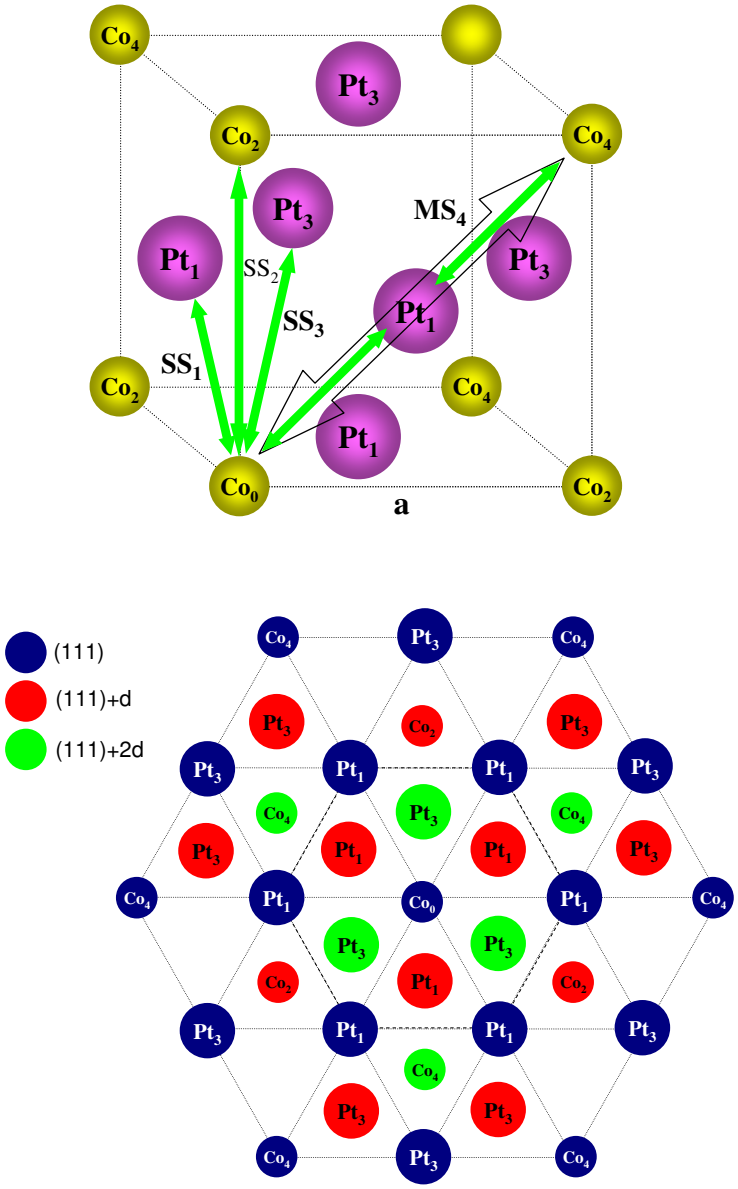

Figure 3.6: Upper panel: schematic view of the $L1_2$ ordered structure showing the scattering paths used in the fitting between absorbing atom Co_0 and the ith neighbourds, Co_i and Pt_i. Lower panel: atoms in the (111) plane (blue circles) and in the upper planes $+d_{111}$ (red circles) and $+2d_{111}$ (green circles)

							Polarization			
Signal	Length (R)		N_{tot}	Scatterer(s)	N^{out}	N^{in}	$\tilde{N}_{\perp}^{out}$	$\tilde{N}_{\perp}^{in}$	$\tilde{N}_{\parallel}^{out}$	$\tilde{N}_{\parallel}^{in}$
SS_1	$a/\sqrt{2}$		12	Pt_1	6	6	12	0	3	9
SS_2	a		6	Co_2	6	-	6	0	6	0
SS_3	$a\sqrt{3/2}$		24	Pt_3	18	6	24	0	15	9
		I	12	Co_4	6	6	12	0	3	9
MS_4	$a\sqrt{2}$	II	24	Co_4-Pt_1	12	12	24	0	6	18
		III	12	Pt_1-Co_4-Pt_1	6	6	12	0	3	9

Table 3.1: Nature and number of scatters in the Single-scattering (SS) and multiple-scattering (MS) processes used in the calculated XAFS spectrum of the $L1_2$ ordered $CoPt_3$ phase. The MS_4 signal is composed of single-(I),double-(II) and triple-(III) scattering paths. The path length is given in units of the lattice parameter a. N_{tot} is the total number of paths per absorbing atoms. N^{in} is the number of independent paths per absorbing atoms occurring strictly in the (111) plane while N^{out} is the number of paths out of the (111) plane. On the right side, $\tilde{N}_{\perp}^{in}(_{\parallel})$ is the effective number of in-plane contributions observed in perpendicular (parallel) polarization geometry, and $\tilde{N}_{\perp}^{out}(_{\parallel})$ is the effective number of out-of plane contributions observed in perpendicular (parallel) geometry.

$$\text{First coordination shell} \quad \begin{cases} \tilde{N}_{\parallel} = 1.5N^{in} + 0.5N^{out} \\ \tilde{N}_{\perp} = 2N^{out} \end{cases} \tag{3.2}$$

$$\text{Second coordination shell} \quad \begin{cases} \tilde{N}_{\parallel} = N^{out} \\ \tilde{N}_{\perp} = N^{out} \end{cases} \tag{3.3}$$

$$\text{Third coordination shell} \quad \begin{cases} \tilde{N}_{\parallel} = 1.5N^{in} + 0.83N^{out} \\ \tilde{N}_{\perp} = 1.33N^{out} \end{cases} \tag{3.4}$$

The procedure for extracting the structural parameters was first refined for the $Co_{35}Pt_{65}$ EXAFS spectra with better statistics. The data for the sample prepared at T_g=300K presenting higher noise were analysed in a k-range from 3 to 12 $Å^{-1}$. The data corresponding to the sample prepared at T_g=700K with better statistics were fitted over a larger k-range from 3 to 14 $Å^{-1}$. $k^{(2)}$-weighting is chosen to amplify the signal at high k, where single-scattering contributions are dominant. The best fits were achieved combining the pair contributions of the $L1_2$ ordered structure and the supplementary ones in the disordered fcc structure.

The $L1_2$-type model relies on four main contributions (table 3.1). Three are single-scattering contributions (SS_i) from Co_0-Pt_1 at the center of the near face, Co_0-Co_2 at the cube edge and Co_0-Pt_3 at the center of the opposite face. The fourth (MS_4) accounts for single-(Co_0-Co_4) and multiple-scattering contributions from Co_0-Pt_1-Co_4 atoms aligned along the face diagonal, namely double-scattering from the Co_0-Pt_1-Co_4-Co_0 and Co_0-Co_4-Pt_1-Co_0 photoelectron paths, and triple scattering from the Co_0-Pt_1-Co_4-Pt_1-Co_0

photoelectron paths (as depicted in figure 3.6). The linear atomic arrangement strongly enhances the amplitude of multiple-scattering terms which cannot be neglected.

In the chemically disordered model, the single-scattering from Co_0-Co_1, Co_0-Pt_2, Co_0-Co_3 and multiple-scattering from Co_0-Co_1-Pt_4, Co_0-Co_1-Co_4, Co_0-Pt_1-Pt_4 configurations have been considered.

The program used for the fit minimizes the expression:

$$\chi^2 = \frac{1}{N}\sum_{i=1}^{N} k_i^2 \frac{(\chi^{exp}(k_i) - \chi^{th}(k_i, P_j)}{\sigma_i^2(k)} \tag{3.5}$$

as a function of the free parameters P_j by means of the MINUIT package of the CERN libraries [110]. $\chi^{exp}(k_i)$ is the experimental value of the signal at the corresponding point k_i while σ_i^2 represents the associated uncertainty and k_i^2 corresponds to a weight. In principle each SS and MS contributions provide three free parameters to the fit (the geometrical length, the number of atoms and the disorder factor). Other quantities which enter into eq.3.5 are the edge energy shift, ΔE_0, S_0^2 and the mean free path λ.

The involved free parameters have a high degree of correlation. In particular it is the case for ΔE_0 with R_j and for N_j with σ_j^2 and S_0^2. For this reason a fit with all the parameters left free may give a low accuracy of the results.

To reduce the number of free parameters in the minimization procedure the following considerations were adopted.

1. For each sample, ΔE_0 was left free for the out-of-plane data and fixed for the in-plane data.

2. S_0^2 was fixed at 0.75.

3. In each shell the total coordination number is constrained to the numbers found in the $L1_2$ and disordered fcc phases (table 3.1).If x is the fraction of Pt in the first-neighbour coordination shell, the multiplicity number $\tilde{N}_{\perp}^{out(in)}$ ($\tilde{N}_{\parallel}^{out(in)}$) is constrained to x times 12, while the multiplicity number for the Co_0-Co_1 nearest neighbours is constrained to a factor of (1-x). This method was applied for the second and third coordination shell too. Whereas, the numbers of atoms in the fourth coordination shell are correlated to those in the first shell, i.e. the probability to find the Co_0-Co_4 correlation depends on the kind of the path, Co_0-Pt_1-Co_4 or Co_0-Co_1-Co_4. Then, the effective coordination numbers in the fourth coordination shell were deduced from the first shell as described in [1].

[1] If P(Co_0-Pt_1)=x is the probability to find Co_0-Pt_1 correlation, then the probabilities of the other configurations are:
P(Co_0-Co_1)=1-x
P(Co_0-Pt_1-Co_4)=x^2
P(Co_0-Co_1-Co_4)=$(1-x)^2$
P(Co_0-Co_1-Pt_4)=$(1-x)x$=$x-x^2$
P(Co_0-Pt_1-Pt_4)=$(1-x)x$=$x-x^2$

4. For fourth shell the path length corresponding to the multiple scattering processes were approximated to

$$R_4^{II} = R_4^{III} - \delta; \quad R_4^{I} = R_4^{III} - 2\delta \tag{3.6}$$

taking into account a possible non alignment of the three atoms. R_4^{III} is the sum of the SS_j composing the whole path, e.g., R_4^{III}(Co_0-Pt_1-Co_4-Pt_1)=R_1(Co_0-Pt_1) $+R_1$(Co_4-Pt_1)=$2R_1$(Co_0-Pt_1).

5. In the first, second and third coordination shells, the Debye-Waller factor was constrained to be the same for any species in order to be more sensible to the coordination number. In the fourth shell, the Debye-Waller factors associated to single, double and triple scattering are different.

Thus, fitting the out-of-plane EXAFS data relies on the determination of the following parameters:

- ΔE_0
- the fraction x, y and z Co atoms which occupy the sites belonging to the first, second and third shell;
- the lengths of path for each species, R_j for SS_1, SS_2 and SS_3 and δ;
- the Debye-Waller factor, σ_j^2, for first three shells, and the three ones for the fourth shell;

i.e. a total number of 17 parameters.

As already mentioned, the out-of-plane EXAFS data ($300_\perp$, $700_\perp$) result only from out-of-plane contributions, while in-plane data ($300_\parallel$, $700_\parallel$) from a combination of in-plane and out-of-plane contributions. In particular, the second coordination shell contains only out-of-plane atoms (see eq. 3.4), so, for in-plane data the coordination numbers and lengths were fixed to the values extracted from the analysis of the out-of-plane data. So, in that case, the free parameters were 13.

The numbers of free parameters is far less than the maximum number of independent parameters associated to the spectra, that, as indicated by '*EXAFS standard criteria for analysis committee*', is:

$$N_{ind} = \frac{2\Delta k \Delta R}{\pi} + 1, \tag{3.7}$$

where Δk (ΔR) is the $k(R)$-range where the experimental data were studied. In the worst case (i.e. with the shortest k interval) it is equal to 30.

P(Co_0-Co_4)=P(Co_0-Pt_1-Co_4) + P(Co_0-Co_1-Co_4)= $2x^2 - 2x + 1$
P(Co_0-Pt_4)=P(Co_0-Co_1-Pt_4) + P(Co_0-Pt_1-Pt_4)= $2x - 2x^2$.
The multiplicity number of each correlation is the total coordination number (table 3.1) multiplied by its probability.

Error bars were calculated using MINOS routine of the MINUIT package that takes into account the correlations between parameters. It calculates χ^2 in the region around the minimum as:

$$\chi^2_{\alpha\%} = \chi^2_{min} + \sum_{ij} \frac{\partial^2 \chi^2}{\partial\beta_i \partial\beta_j} \triangle\beta_i \triangle\beta_j \tag{3.8}$$

where $\triangle\beta_i$ and $\triangle\beta_j$ indicate respectively the variations of β_i and β_j parameters for which χ^2 maintains a level of confidence of $\alpha\%$. In our case $\alpha = 95\%$. 'Contour' option of MINUIT gives the curves with constant χ^2 when both the two selected parameters vary one respect to the other. It points out the correlations between a couple of parameters. Concentric ellipses corresponding to different values of χ^2 are thus obtained and from their widths the uncertainties associated with the involved parameters can be calculated (figure 3.7).

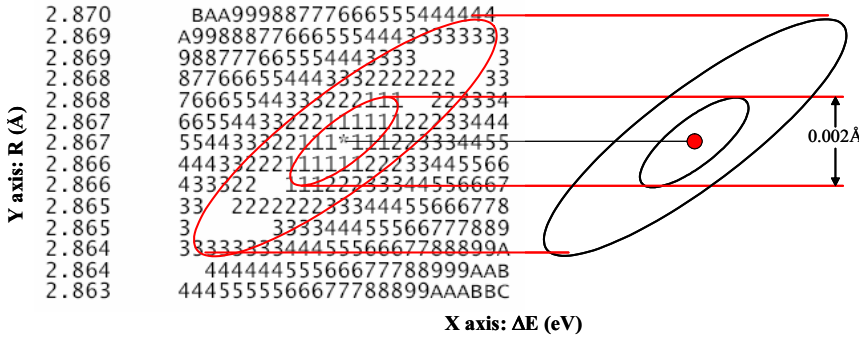

Figure 3.7: Example of calculation of the errors: concentric ellipses correspond to different values of χ^2, the error is thus deduced from the smallest ellipse ($\alpha = 95\%$).

3.2.2 Results and discussion

$Co_{35}Pt_{65}$

The experimental spectra for the $Co_{35}Pt_{65}$ series are reported in figure 3.8, and compared to the simulated spectra for a $L1_2$ ordered $CoPt_3$ structure and a randomly disordered ('Dis') fcc structure. The main features of the experimental spectra of the sample prepared at 700K are close to the $L1_2$ ordered model ones, meaning it is partially ordered; thus it is consistent with RHEED and XRD results indicating the long range ordering associated to a parameter about ~0.6 [10]. Comparing the spectra of the sample prepared at 300K ($300_\perp$, $300_\parallel$) would suggest an intermediate behaviour between the Dis and $L1_2$ models.

Figure 3.9 shows the moduli of the Fourier transform (|FT|) of the k^2-weighted experimental and simulated XAFS spectra. The main peak between 1 and 3.5 Å mainly stems from nearest neighbour correlations, i.e. mainly Co-Pt. The peaks located between 4 and 5.5 Å are dominated by multiple-scattering effects from Co-Pt-Co atomic alignments (see figure 3.6). This peak is more pronounced in the |FT| for the film grown at 700K than in

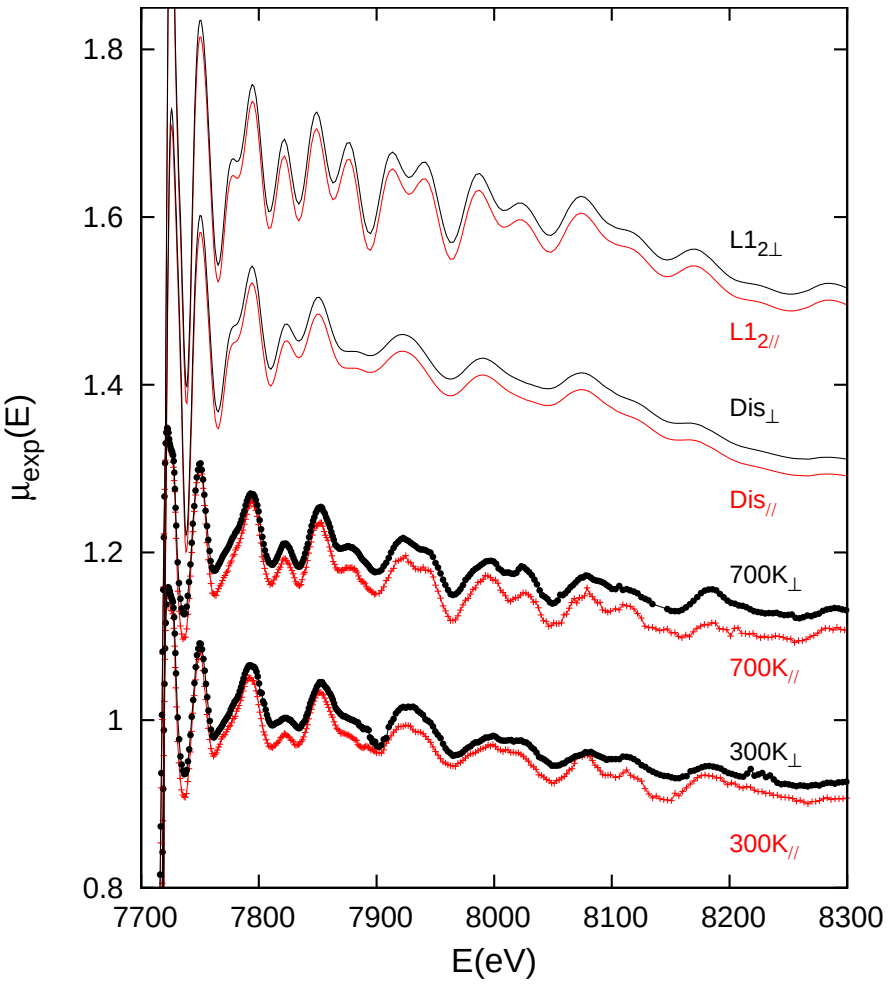

Figure 3.8: Experimental x-ray absorption spectra of the two $CoPt_3$ films prepared at 700K and 300K for in-plane (∥) and out-of plane (⊥) geometry. For comparison, simulated spectra of a $L1_2$ ordered and randomly disordered $CoPt_3$ film are reported for both polarizations. The curves are shifted for clarity.

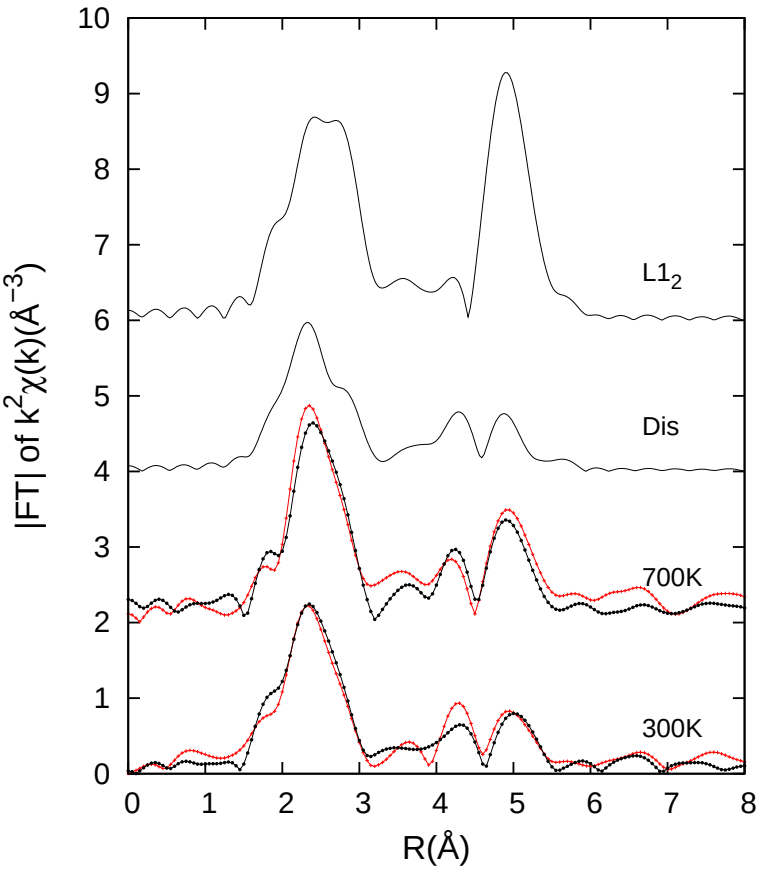

Figure 3.9: Moduli of Fourier transform (|FT|) of the experimental and simulated $k^2\chi(k)$ spectra (k-range: 3-12Å^{-1}) presented in figure3.8 for the two geometries: $\parallel$ (red lines) and $\perp$ (black lines).

the |FT| for the film grown at 300K; this is another signature that the sample prepared at higher temperature is partially ordered.

¿From the comparison between the in-plane and out-of-plane FT data, several fine differences are seen. For example, the differences observed in the second coordination shell, between 3 and 4Å, are not significant because the signal is too small and can be compare to spurious signals. Whereas, a markable difference is observed in the third coordination shell, associated with the peak between 4 and 4.6 Å for the sample prepared at RT, signature of an anisotropic environment.

The structural parameters derived from the best fits are summarized in table 3.2. For MS_4, only the principal contributions are given, corresponding to those of $L1_2$ model.

The best fits for the two samples in both geometries are presented in figure 3.10. The $|FT|$s of the experimental and best fitted spectra calculated in the same k-range 3-12 Å are shown in figure 3.11. Contributions from multiple-scattering were not used for the fitting of the peak at 3.5Å. It was not considered critical for the analysis to include them in the fitting of the spectra, due to the small intensity of the peak. This could be the

			Out-of-plane polarization			In-plane polarization						
Signal		Scatters	$\tilde{N}^j_\perp$	R_j (Å)	$\sigma^2_j(10^3Å^2)$	$\tilde{N}^j_\parallel$	R_j (Å)	$\sigma^2_j(10^3Å^2)$	N^{out}	N^{in}	n^{out}	n^{in}
$Co_{35}Pt_{65}$ for T_d=300K												
SS_1		Pt_1	10.3(1)	2.67(1)	0.58(1)	9.3(1)	2.67(1)	0.59(1)	5.15(5)	4.48(5)	0.87(1)	0.75(1)
		Co_1	1.7(1)	2.64(1)		2.7(1)	2.66(1)		0.85(5)	1.52(5)	0.13(1)	0.25(1)
SS_2		Pt_2	2.6(1)	3.72(1)	0.63(4)	**2.6**	**3.72**	0.80(4)	2.6(1)	-	0.43(2)	-
		Co_2	3.4(1)	3.79(1)		**3.4**	**3.79**		3.4(1)	-	0.57(2)	-
SS_3		Pt_3	17.1(1)	4.70(2)	0.27(3)	15.2(1)	4.65(2)	0.25(3)	12.83(8)	3.01(2)	0.71(1)	0.50(1)
		Co_3	6.9(1)	4.84(2)		8.8(1)	4.73(2)		5.17(8)	2.99(2)	0.29(1)	0.50(1)
MS_4	I	Co_4	9.1(1)	5.32(2)	0.01(2)	7.9(1)	5.32(2)	0.01(2)				
	II	Pt_1-Co_4	17.8(1)	5.33(2)	0.65(2)	14.5(1)	5.33(2)	0.61(2)				
	III	Pt_1-Co_4-Pt_1	8.9(1)	5.34(2)	1.07(2)	7.3(1)	5.34(2)	0.97(2)				
$Co_{35}Pt_{65}$ for T_d=700K												
SS_1		Pt_1	10.2(1)	2.68(1)	0.43(1)	10.0(1)	2.68(1)	0.45(1)	5.10(5)	5.00(5)	0.85(1)	0.83(1)
		Co_1	1.8(1)	2.68(1)		2.0(1)	2.66(1)		0.90(5)	1.00(5)	0.15(1)	0.17(1)
SS_2		Pt_2	0.0(1)	-	1.50(4)	**0.00**	-	1.30(3)	0.0(1)	-	0.00(2)	-
		Co_2	6.0(1)	3.75(2)		**6.00**	**3.75**		6.0(1)	-	1.00(2)	-
SS_3		Pt_3	19.9(1)	4.67(2)	0.52(3)	20.86(2)	4.70(2)	0.56(3)	14.93(8)	5.61(2)	0.83(1)	0.93(1)
		Co_3	4.1(1)	4.69(2)		3.14(2)	4.90(2)		3.07(8)	0.39(2)	0.17(1)	0.07(1)
MS_4	I	Co_4	9.0(1)	5.30(2)	0.20(2)	8.61(2)	5.28(2)	0.20(2)				
	II	Pt_1-Co_4	17.4(1)	5.33(2)	0.43(2)	16.53(2)	5.32(2)	0.43(2)				
	III	Pt_1-Co_4-Pt_1	8.7(1)	5.35(2)	0.43(2)	8.27(2)	5.34(2)	0.43(2)				

Table 3.2: Structural parameters corresponding to the best fits of $Co_{35}Pt_{65}$ grown on WSe_2. The effective numbers of independent paths($\tilde{N}^j$), the path lengths (R_j) and the Debye-Waller factors (σ^2_j) are reported for both polarization. The total numbers of the independent paths (N^{in} and N^{out}) in and out of the (111) plane are calculated from the effective contributions observed in parallel and perpendicular geometry using eq. 3.3-3.4. n^{out} (n^{in}) are the concentrations of each elements in every coordination shell out-of-plane (in-plane). In parenthesis are the errors on the last digits .

reason why this peak is not well fitted.

For the sample prepared at room temperature figure 3.12 shows the partial contributions used in the analysis: for each coordination shell Co-Pt and Co-Co configurations are plotted. The signals coming from Co-Pt_1 and Co-Pt_3 are more intense in $300_\perp$ while the signals associated to Co-Co_1 and Co-Co_3 are more intense in $300\parallel$.

¿From the extracted structural parameters a polarization dependence of the distances between the absorbing atom and its neighbours is visible (figure 3.13). For the sample prepared at RT Co-Co_1 out-of-plane distance is slightly shorter than in-plane one; in both geometries, these distances are shorter than Co-Pt_1 ones. In the third coordination shell, an opposite and more accentuated behaviour is seen: in-plane bonds are shorter than the out-of-plane bonds showing a strong lattice distortion. At higher deposition temperature these effects are reversed. The errors associated to the Co-Co_3 distances for the sample prepared at 700K are underestimated due to their small signals giving the fitting not enough sensitive.

In table 3.2 are reported the true coordination numbers, N^{in} and N^{out}, calculated

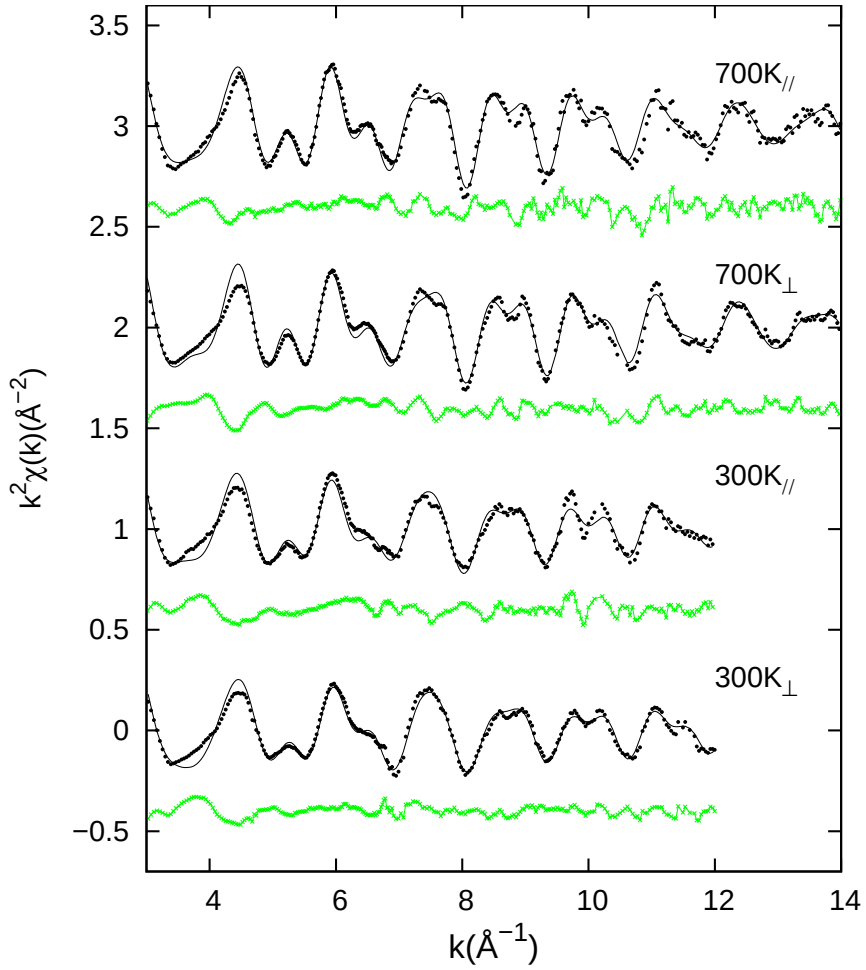

Figure 3.10: Experimental (dots) and best fitted (solid lines) $k^2\chi(k)$ of two films grown at 700K and 300K, for in-plane ($\|$) and out-of plane ($\perp$) polarizations. For each fit the residual $k^2\chi(k)_{exp} - k^2\chi(k)_{fit}$ is shown by green lines.

from the measured polarization-dependent coordination number using eq:3.2-3.4. The Co-Co$_1$, Co-Pt$_2$ and Co-Co$_3$ correlations, absent in a totally ordered L1$_2$-type structure, are necessary to obtain good fitting.

In spite of the absence of LRO, the local structure in the 300K sample is nevertheless partially ordered. The Co-Co$_1$ correlations correspond to 25% (n^{in}) of the in-plane contributions and 13% (n^{out}) of the out-of-plane contributions. This anisotropy is even stronger in the third coordination shell (see table 3.2). The presence of more Co in the film plane explains the strong contraction of Co-Co distance observed in the third coordination shell. Figure 3.14 represents a possible configuration of Co and Pt atoms in the (111) plane of the sample prepared at 300K. As shown in [111], this anisotropic short range order would be induced by the dynamic segregation of Pt at growing surface during the co-deposition, leading to the formation of Co rich disks in the film plane. The preference of Co-Co pairs in the film plane produces an anisotropic orbital moment, as demonstrated experimentally

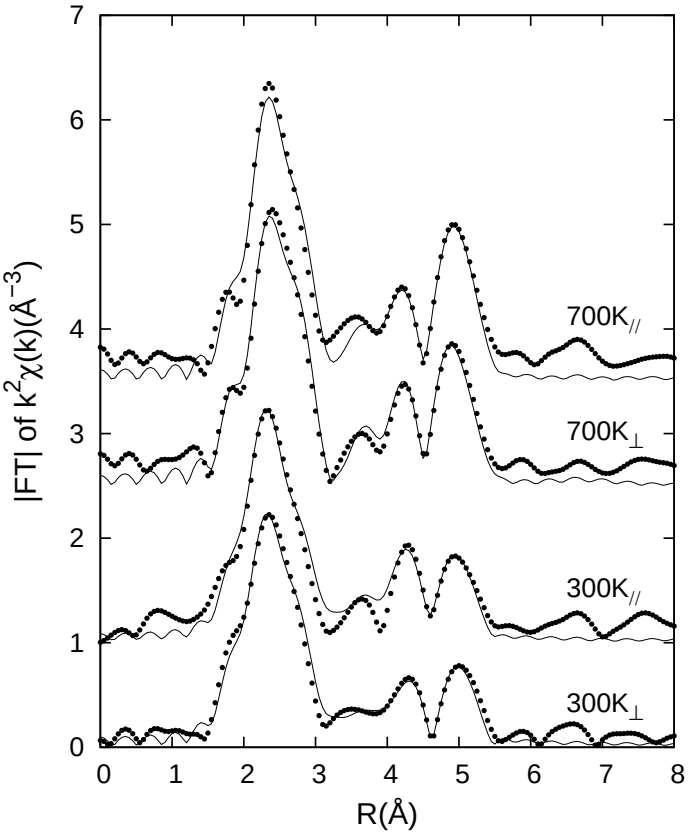

Figure 3.11: Experimental (dots) and best fitted (solid lines) |FT| curves of the two $CoPt_3$ nanostructured films for in-plane (||) and out-of plane ($\perp$) polarizations.

by XMCD [112, 113] for the continuous $CoPt_3$ thin films, leads to a large anisotropy of the $3d$ and $5d$ orbital moments that are the microstructural origin of the perpendicular magnetic anisotropy.

For the $CoPt_3$ grown at 700K, exhibiting partial $L1_2$-type order, the difference between the in-plane and out-of-plane concentrations is weaker in the first shell and is reversed in the third coordination shell. Moreover, the second coordination shell is constituted by only Co-Co_2 correlations as in the $L1_2$ structure. The Debye Waller factor determinate in the first shell is smaller than that extracted in the 300K sample, but it is inverted for the second and third shell. The choice of an unique Debye Waller factor for shell prevents a fine analysis of the topological disorder. These results are consistent with the isotropic $L1_2$-type ordering measured by XRD in this sample.

Finally, the analysis of the Co-edge data reveals that the strong PMA found in the $L1_2$ grown at 300 K is related to the existence of a well-defined anisotropic chemical local order, while in the film grown at 700 K magnetically isotropic, such structural anisotropy is markedly reduced.

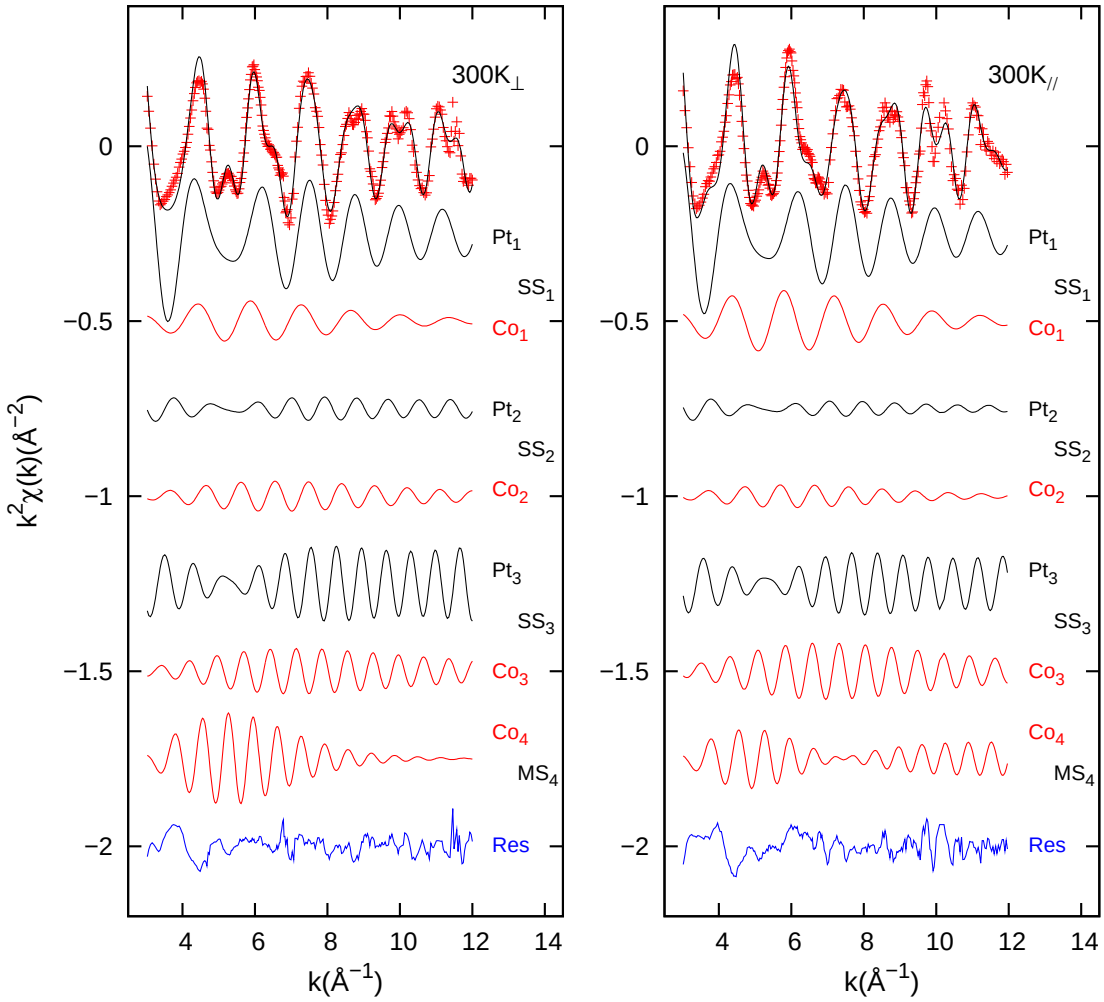

Figure 3.12: Best fits obtained for the 300K sample in the two xperimental geometries shown with their partial contributions (shifted for clarity): for each coordination shell Co-Pt (black lines) and Co-Co (red lines) correlations are plotted. The multiple-scattering partial contributions (MS) are a combination of single-, double- and triple-scattering as described in the text; in this case only Co-Co configuration has been notable.

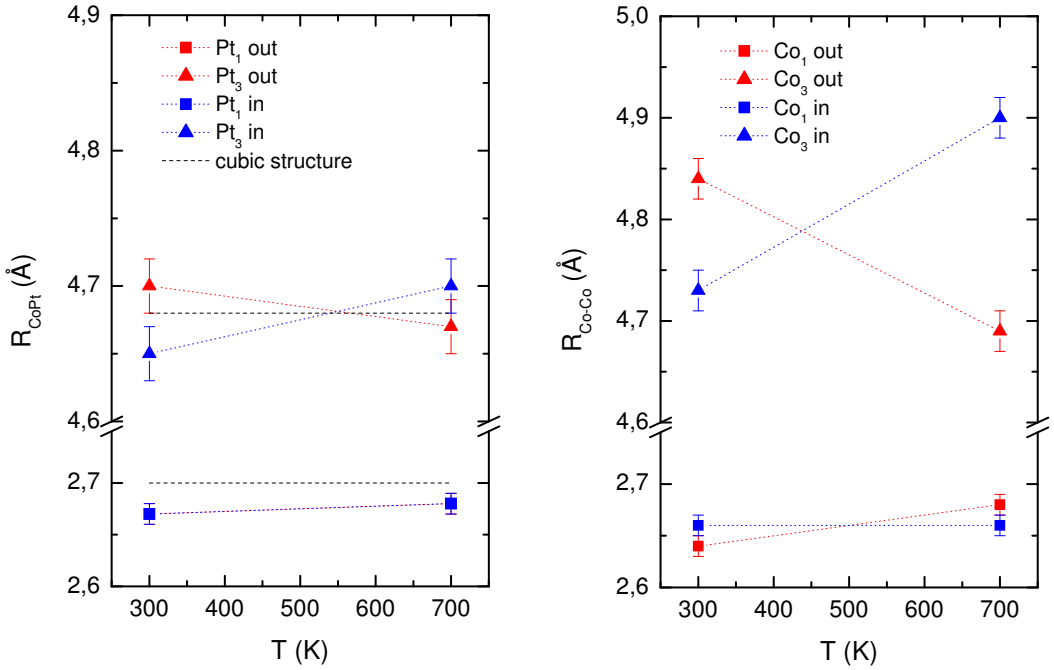

Figure 3.13: Variation of the in-plane and out-of-plane Co-Pt and Co-Co distance in the 1^{st} and 3^{th} coordination shells of the $Co_{35}Pt_{65}$ alloy.

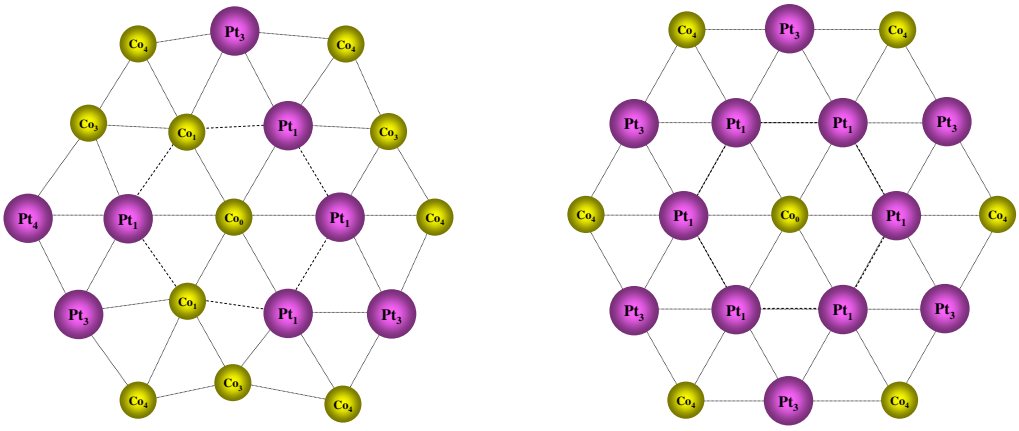

Figure 3.14: Possible arrangement of Co and Pt with (111) plane of the 300K $Co_{35}Pt_{65}$ sample (left) in comparison with the arrangement in the $L1_2$-phase (right).

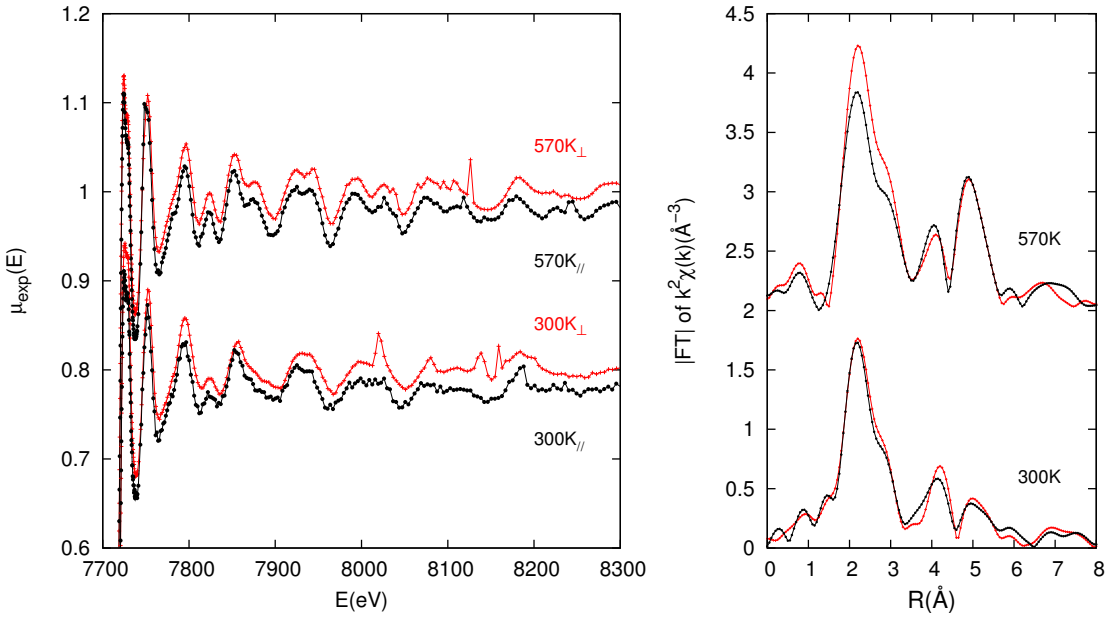

Figure 3.15: Left: experimental x-ray absorption spectra of the three $Co_{22}Pt_{78}$ films prepared at 570 and 300K for in-plane (∥) and out-of plane (⊥) geometry. Right: moduli of Fourier transform (|FT|) of the experimental and simulated $k^2\chi(k)$ spectra (k-range: 3-0.98Å^{-1}) for the two geometries: ∥ (red lines) and ⊥ (black lines). The curves are shifted for clarity.

$Co_{22}Pt_{78}$

The spectra measured for the $Co_{22}Pt_{78}$ alloys are shown in figure 3.15 and above 8000 eV are contaminated by several Bragg peaks. Looking at the $|FT|$ only a small anisotropy effect is seen in the sample prepared at RT. The fourth peak around R=5Å of the sample prepared at 570 K is more intense than that for the RT sample, in agreement with the higher order degree for the 570K sample.

The best fits, done in a smaller k-range from 3 to 9.8 Å, are shown in figure 3.16. The structural parameters are summarized in table 3.3. The sample prepared at 300K presents a small anisotropy in the first coordination shell, similar to that observed in the $Co_{35}Pt_{65}$. This effect would be too weak to be visible in the data because of the high Pt concentration. The out-of plane Pt compositions also indicate a short range chemical order.

At higher deposition temperature this anisotropic effect disappears. However the in-plane and out-of plane compositions estimated for the first shell do not indicate a short range order. Only in the second shell a weak chemical order is observed.

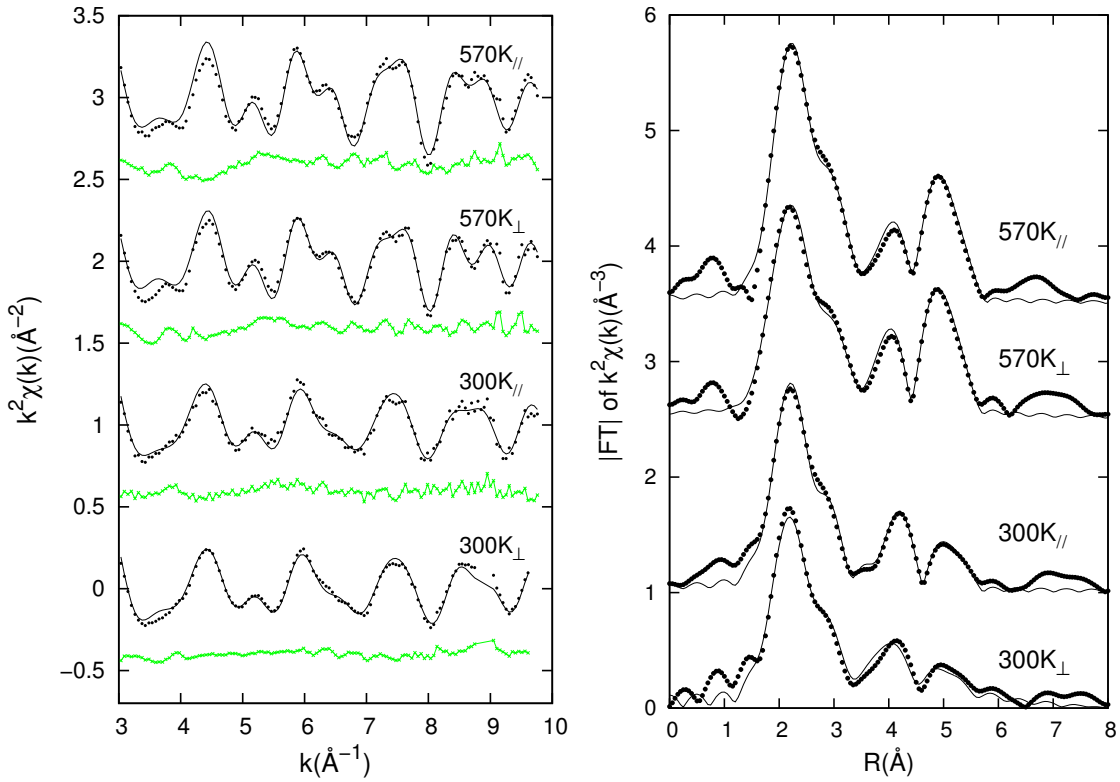

Figure 3.16: On the left, experimental (dots) and best fitted (solid lines) $k^2\chi(k)$ of two films $Co_{20}Pt_{80}$ grown at 300, and 570K for in-plane ($\|$) and out-of plane ($\perp$) polarizations. For each fit the residual $k^2\chi(k)_{exp} - k^2\chi(k)_{fit}$ is shown by green lines. On the right, experimental (dots) and best fitted (solid lines) |FT| curves for in-plane ($\|$) and out-of plane ($\perp$) polarizations.

			Out-of-plane polarization			In-plane polarization						
Signal		Scatters	$\tilde{N}^j_\perp$	R_j (Å)	$\sigma^2_j(10^3Å^2)$	$\tilde{N}^j_\parallel$	R_j (Å)	$\sigma^2_j(10^3Å^2)$	N^{out}	N^{in}	n^{out}	n^{in}
$Co_{20}Pt_{80}$ at 300K												
SS_1		Pt_1	11.1(2)	2.71(1)	0.63(1)	10.1(1)	2.70(1)	0.57(1)	5.6(2)	4.9(1)	0.93(3)	0.82(3)
		Co_1	0.9(1)	2.59(1)		1.9(1)	2.67(1)		0.40(5)	1.10(5)	0.07(1)	0.18(1)
SS_2		Pt_2	3.5(2)	3.75(1)	0.01(1)	**3.5**	**3.75**	0.55(1)	3.5(2)	-	0.58(2)	-
		Co_2	2.5(2)	3.81(1)		**2.5**	**3.81**		2.5(2)	-	0.42(2)	-
SS_3		Pt_3	18.7(2)	4.71(2)	0.01(1)	18.7(2)	4.73(2)	0.12(1)	13.99(8)	4.68(2)	0.78(1)	0.78(1)
		Co_3	5.3(2)	4.84(2)		5.3(2)	4.84(2)		4.01(8)	1.32(2)	0.22(1)	0.22(1)
MS_4	I	Co_4	10.4(3)	5.40(2)	0.82(3)	8.8(3)	5.40(2)	0.10(3)				
	II	Pt_1-Co_4	20.6(3)	5.41(2)	0.91(3)	17.1(3)	5.40(2)	0.78(3)				
	III	Pt_1-Co_4-Pt_1	10.3(3)	5.41(2)	1.72(3)	8.6(3)	5.40(2)	1.29(3)				
$Co_{20}Pt_{80}$ at 570K												
SS_1		Pt_1	9.6(4)	2.72(1)	0.61(1)	9.8(4)	2.71(1)	0.43(1)	4.8(2)	4.9(2)	0.80(3)	0.82(3)
		Co_1	2.4(1)	2.58(1)		2.2(1)	2.61(1)		1.20(5)	1.10(5)	0.20(1)	0.18(1)
SS_2		Pt_2	3.1(1)	3.80(1)	0.01(1)	**3.1**	**3.80**	0.01(1)	3.1(1)	-	0.51(2)	-
		Co_2	2.9(1)	3.85(1)		**2.9**	**3.85**		2.9(1)	-	0.49(2)	-
SS_3		Pt_3	21.8(1)	4.72(2)	0.29(1)	20.2(1)	4.72(2)	0.29(1)	16.37(8)	4.35(2)	0.77(1)	0.73(1)
		Co_3	2.2(1)	4.84(2)		3.8(1)	4.81(2)		1.63(8)	1.65(2)	0.23(1)	0.27(1)
MS_4	I	Co_4	8.1(1)	5.44(2)	0.01(3)	8.4(1)	5.40(2)	0.01(3)				
	II	Pt_1-Co_4	15.2(1)	5.44(2)	0.63(3)	16.0(1)	5.41(2)	0.05(3)				
	III	Pt_1-Co_4-Pt_1	7.6(1)	5.44(2)	0.90(3)	8.0(1)	5.42(2)	0.72(3)				

Table 3.3: Structural parameters corresponding to the best fits of $Co_{20}Pt_{80}$ grown on WSe_2. The effective numbers of independent paths($\tilde{N}^j$), the path lengths (R_j) and the Debye-Waller factors (σ^2_j) are reported for both polarization. The total numbers of the independent paths (N^{in} and N^{out}) in and out of the (111) plane are calculated from the effective contributions observed in parallel and perpendicular geometry using eq. 3.3-3.4. n^{out} (n^{in}) are the concentrations of each elements in every coordination shell out-of-plane (in-plane).

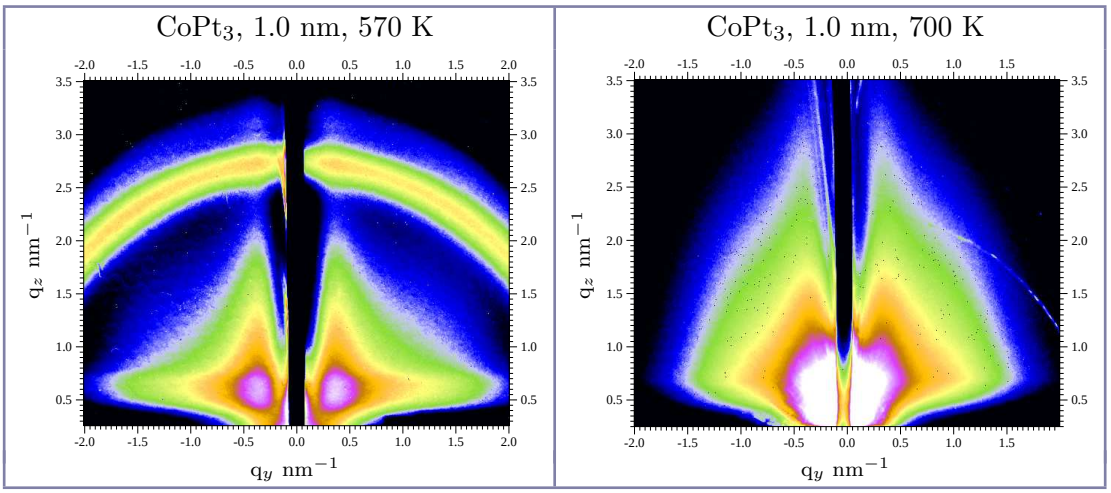

Figure 3.17: (Color) Best experimental GISAXS patterns for 1.0 nm thick $CoPt_3$ grown at 570 and 700K, recorded during the first and second series of measurements respectively.

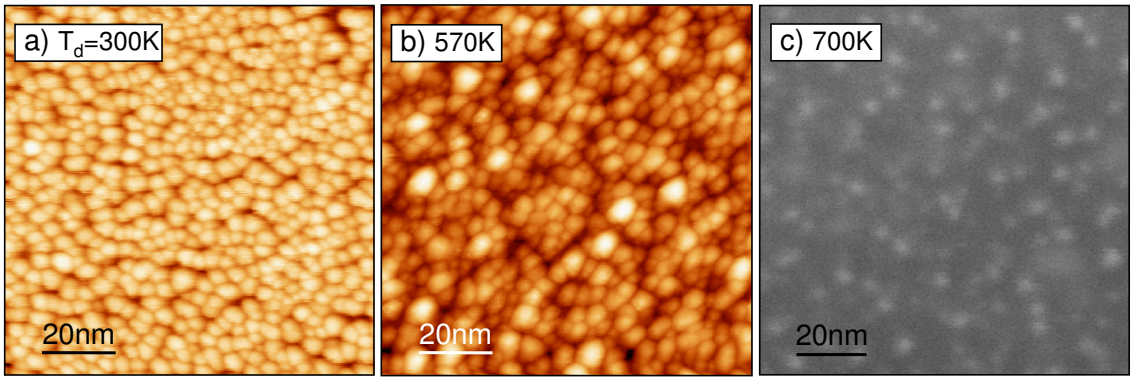

Figure 3.18: STM and FESEM topographic images of 1 nm thick $CoPt_3$ grown on $WSe_2(0001)$ at various temperature: (a) RT (STM), (b) 570 K (STM) and (c) 700 K (FESEM). STM images are taken at U = 1.0 V and I = 0.3 nA.

3.3 Morphology analysis by STM and GISAXS

The morphology of 1 nm thick $CoPt_3$ deposited at 300, 570 and 670 K was studied by STM and GISAXS techniques, without air exposure after the preparation using a portable vacuum chamber. A second series of GISAXS experiments were carried out under primary vacuum after a fast air exposure of the samples. The STM images were collected by Y. Gauthier, the FESEM images by F. Charlot. The difference between the two series is the presence of a kapton window which is required to ensure a pressure of 10^{-6}mbar when connected to the portable chamber. However it has produced a scattering halo.

Figure 3.17 shows the best GISAXS patterns for deposits at 570 and 700K recorded under an incident angle $\alpha_i = 0.5°$ (critical angle of WSe_2: $\alpha_c = 0.43°$). The substrate used for the RT deposit was much smaller than the beam footprint, therefore the signal coming

GISAXS										
CoPt$_3$		Guinier plot		Quantitative analysis with LMA and 1DDL						
ϵ	T	2R$_s$	H	L	σ_L	H	σ_H	H/L	D	w
(nm)	(K)	(nm)	(nm)	(nm)	(nm)	(nm)	(nm)		(nm)	(nm)
1	570	6.0	2.4							
1	700	4.0	2.0	4.0(1)	1.0(1)	1.8(1)	0.2(2)	0.44(1)	15.3(3)	7.0(5)
3	700	10	3.6							

STM - FESEM							
ϵ	T	L	σ_L	H	σ_H	H/L	z
(nm)	(K)	(nm)	(nm)	(nm)	(nm)		(nm)
1	300	4.2(1)	2.5(1)	2.32(2)	0.11(1)	0.55(1)	0.0
		2.5(1)	2.0(1)	0.22(2)	0.11(1)		2.1
1	570	4.1(1)	4.9(2)	0.8(2)-1.8(1)	0.38(9)-1.6(2)		0.0
		2.4(4)-6.7(3)	3.2(1)-1.8(1)	0.34(2)-0.9(1)	0.4(2)-0.20(2)		2.0
1	700	4.7*(1)	1.4*(1)				

Table 3.4: On the top: results obtained from the GISAXS patterns analysis with the Guinier plot and the local monodisperse approximation (LMA) with a Gaussian distribution function. L and σ_L, average and width of lateral size distribution; H, and σ_H, average and width of height distribution; D and w, first neighbor peak and width of the gaussian distribution of 1DDL interference function. On the bottom: results obtained from the STM and (*)FESEM images. The STM and SEFEM lateral size is the diameter of a disk of equivalent surface. A Gaussian distribution is used with a parameter σ

.

from the sample could not be separated from the STM plate scattering. Fortunately, a morphology change is expected between 570 and 700 K based on previous measurements on 3 nm thick CrPt$_3$ grown on WSe$_2$(0001) [62].

The scattering lobes separated by the specular reflectivity, hidden by the beam stop, are visible along the parallel direction in both GISAXS patterns. They became higher and narrower for the sample prepared at T$_d$=700 K, where a strong off-specular scattering due to the substrate is observed. The scattering ring observed in the 570K pattern comes from the kapton window (1st series of GISAXS measurements). GISAXS patterns provide a two-dimensional picture of Fourier transform (FT) of the morphology of any system that is made of nanoscale objects: the extent of the intensity parallel and perpendicular to the surface is inversely proportional to the average lateral size and height, respectively, of the island. The separation between the two lobes is inversely proportional to the average separation between neighbours islands. Then, a quantitative analysis of these images allow to deduce the morphology of the islands and its dependence on the deposition temperature.

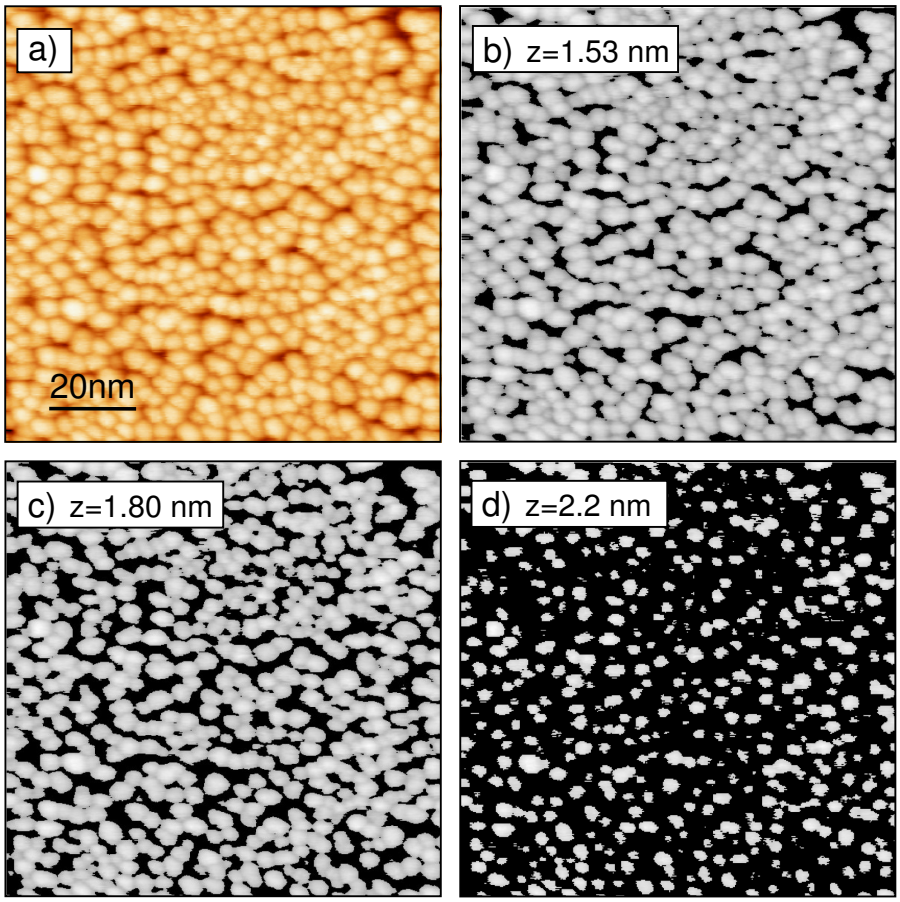

Figure 3.19: STM images of the sample prepared at 300 K original (a) and after a flooding cut at z level equal to 1.53 nm (b), 1.8 nm (c) and 2.20 nm (d).

The structural parameters extracted form the GISAXS patterns were compared with those deduced from the STM images and summarized in table 3.4. The STM images for the 300 and 570K samples and the FESEM image for the 700K sample are reported in figure 3.18.

3.3.1 1 nm $CoPt_3$ grown on WSe_2(0001) at 300 K

STM analysis

Figure 3.19(a) shows the original STM image. The co-deposition on WSe_2(0001) leads to form a very dense self-assembly of $CoPt_3$ nanoparticles as already observed in thinner deposit [59]. Through a flooding method the image was cut at different heights (z levels). At z=1.53 nm, most of nanoparticles touch each other (figure 3.19(b)) and at z=1.8 nm (figure 3.19(d)) they seem to start partially separating from each other. Only at z=2.2 nm the separation would be complete.

Digital processing and numerical analysis of STM images without considering the tip dimention lead to the lateral size distribution shown in figure 3.20(a), where the mean

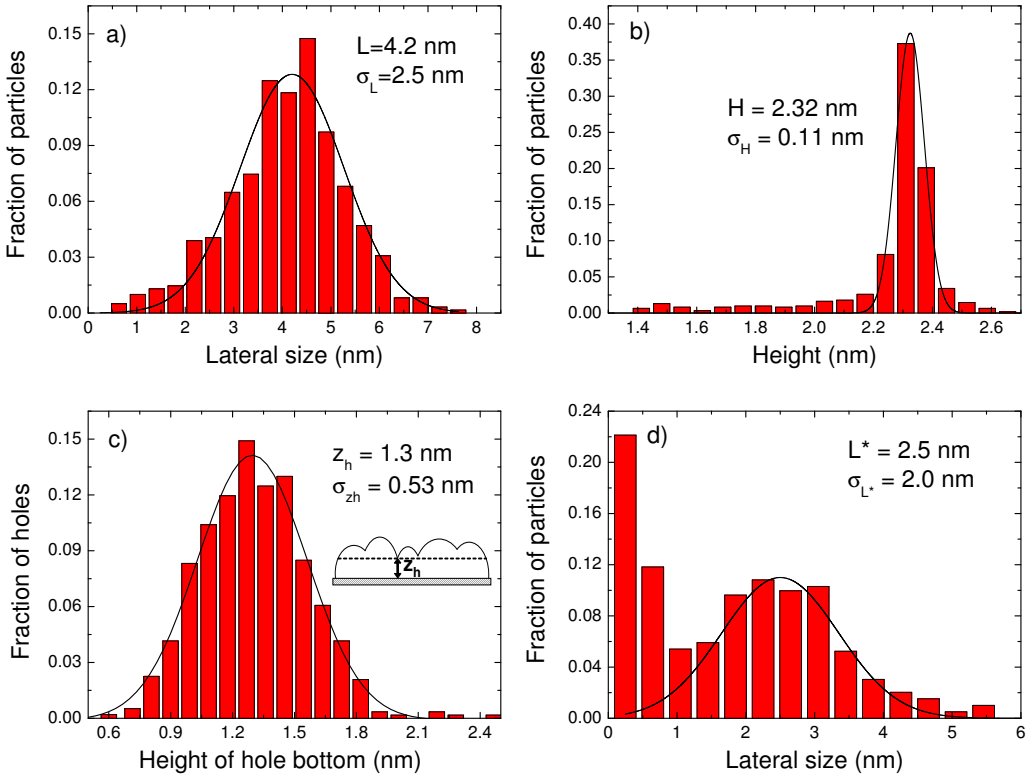

Figure 3.20: Distribution of (a) lateral size, (b) height and (c) the height of hole bottom calculated for the images 3.19(a) of a 1nm $CoPt_3$ deposit at 300 K; d) the lateral size distribution recalculated for z=2.2nm (figure 3.19(d)). The continuous lines are the corresponding Gaussian fits of distributions.

value is (4.2±0.1) nm and the width is σ=(2.5±0.1) nm. The height distribution is very narrow, centred at (2.32±0.02) nm and with a width (0.11±0.01) nm (3.20(b)). Figure 3.20(c) shows the distribution of the height of hole bottom, z_h, calculated for the image 3.19(a). When z=0.6 nm few holes appear meaning the particles start to separate. When z=2.2 nm no more holes are there and the particles are completely separated, as reported in figure 3.19(d). At this z level a flooding cut has been performed and the new lateral size distribution has been calculated and reported in figure 3.20(d). Nanoparticles with lateral size (2.5±0.1) nm and width (2.0±0.1) are observed. The lateral size distribution below 1 nm (in figure 3.20(d)) concerns the small nanoparticles with height ranging from 2.0 to 2.3 nm.

However, the analysis was done by neglecting the STM tip resolution. Based on images performed on model systems, the height of hole bottom (shown in figure 3.20(c)) are overestimated of a value about 0.4 nm. It means that the particle separation is rather complete around 1.8 nm.

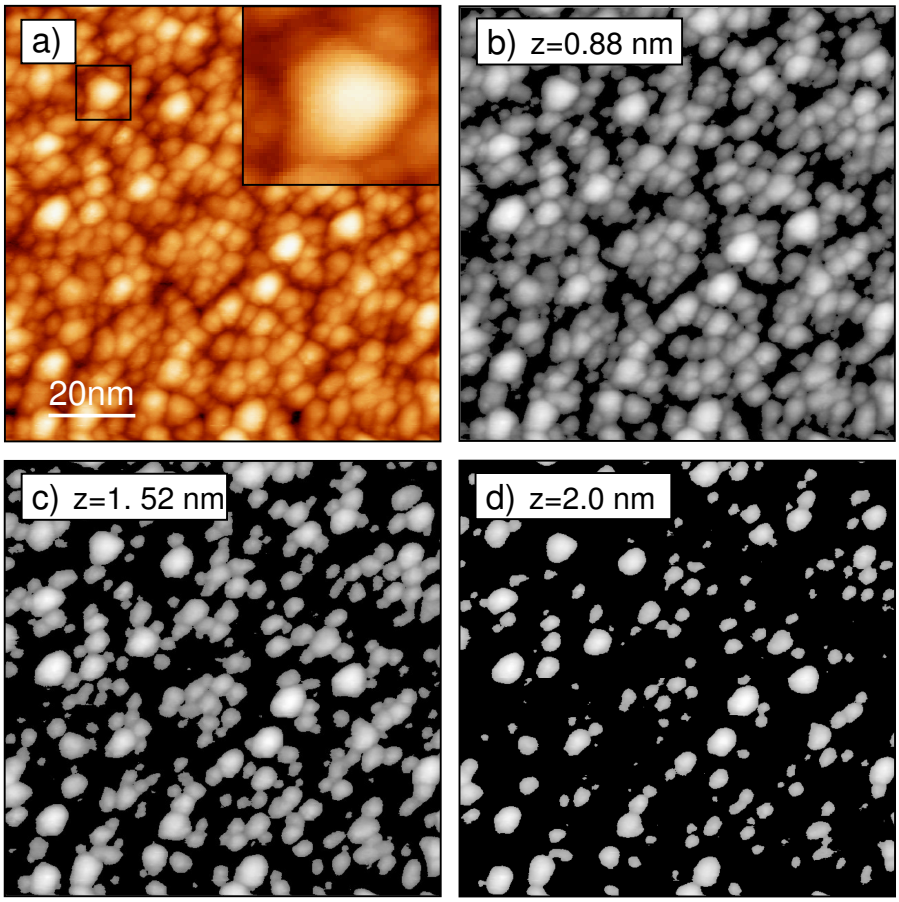

Figure 3.21: STM images of the sample prepared at 570 K original (a) and after a flooding cut at z level equal to 0.88 nm (b), 1.52 nm (c) and 2.0 nm (d).

GISAXS analysis

As indicated before, no satisfying GISAXS pattern was recorded for this sample, due to the small size and unperfect flatness of the $WSe_2(0001)$ substrate.

3.3.2 1 nm $CoPt_3$ grown on $WSe_2(0001)$ at 570 K

STM analysis

The same image analysis was applied to the sample prepared at T_d=570K (figure 3.21(a)). Differently from that observed after deposition of 1 Å, where a narrow distribution was observed [59], a broader lateral size distribution is obtained and reported in figure 3.22(a), centred around (4.1±0.1) nm, with a width of (4.9±0.2). Figures 3.21(b),(c) and (d) represent the flooding cuts at z level 0.88, 1.52 and 2.0 nm. At z=0.88 nm several agglomerations of small and big nanoparticles are visible. At z=1.52 nm, isolated nanoparticles appear clearly and the smallest ones vanish. For $z \geq$2.0 nm the islands are completely

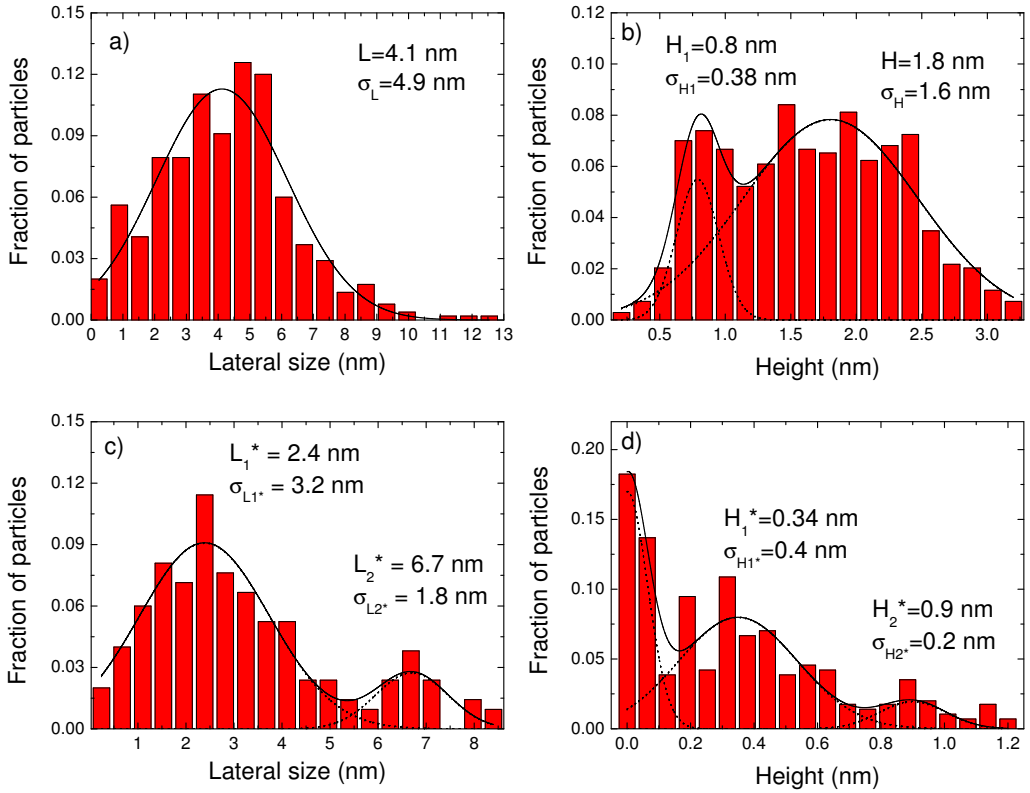

Figure 3.22: The lateral size (a) and height (b) distributions calculated for the images corresponding to the deposition temperatures 570 K (figure 3.21(a)); (c) and (d) the lateral size and height distribution recalculated for z=2.0nm (figure 3.21(d)). The continuous lines are the corresponding Gaussian fits of distributions.

separated and can be described by a double distribution: the smallest particles are characterized by an average lateral size, L_1*, equal to (2.4±0.4) nm, with a large width, σ_{L1*}=(3.2±0.1) nm and by an average height H_1*=(0.34±0.02) with σ_{H1*}=(0.4±0.2) nm, while the biggest particles are characterized by L_2*,=(6.7±0.3) nm with σ_{L2*}=(1.8±0.1) nm and H_2*=(0.9±0.1) nm with σ_{H2*}=(0.20±0.02) nm (figure 3.22(c,d)). As already mentioned, due to the tip resolution the flooding analysis is not exact; the islands are fully separated for $z \geq$1.6 nm.

A zoom of a larger particle in inset of figure 3.21(a) reveals an hexagonal shape, formed by a top (111) facet and alternate side-wall facets {111} and {100} which can been derived form the Wulff construction [59]. Let one compare with previous STM measurements obtained in a thicker deposit of $CoPt_3$ (5 nm) grown also at 570 K. Figure 3.23 shows a triangular shape of nanostructures: a profile section of a large island (3.23(b)) confirms the nature of the side-wall facets with typical angle with the island base equal to 70° for the largest {111} and 54° for the {100} ones.

In the 1 nm deposit, such triangular nanostructure is not observed. However, as observed in the middle of the figure 3.21(b), agglomerations of nanoparticles start to

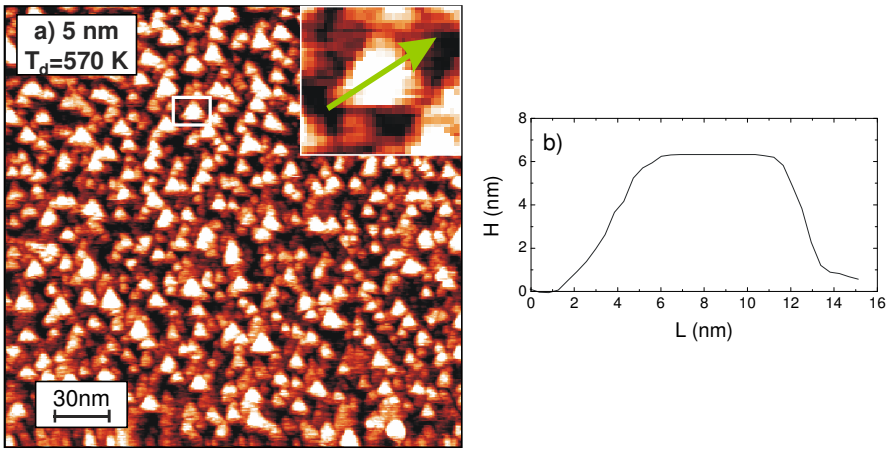

Figure 3.23: (a) STM image of 5 nm thick $CoPt_3$ alloy grown at 570 K; (b) profile of the island reported in the inset of (a).

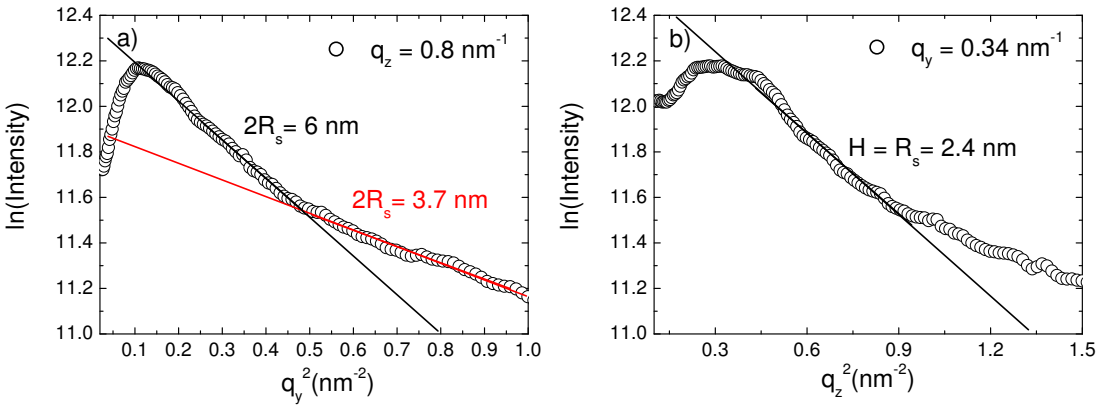

Figure 3.24: Open circles: 1D cuts parallel to q_y and q_z directions from 2D GISAXS patterns of 1 nm of $CoPt_3$ grown at 570 K. Continuous lines: Guinier fits.

adopt a triangular shape.

GISAXS analysis

The GISAXS image of the 570K sample was only analysed qualitatively by Guinier plots. Figure 3.24(a) and (b) show the 1D cuts parallel and perpendicular to the q_y and q_z direction from figure 3.17. The horizontal cut is done at the Yoneda position (q_z=0.3nm^{-1}); the vertical cut is done at the interference maximum position (q_y=0.1nm^{-1}). They give a lateral size and height about 6 and 2.4 nm, respectively, larger than the values obtained by STM (table 3.4).

3.3.3 1 nm CoPt$_3$ grown on WSe$_2$(0001) at 700 K

FESEM analysis

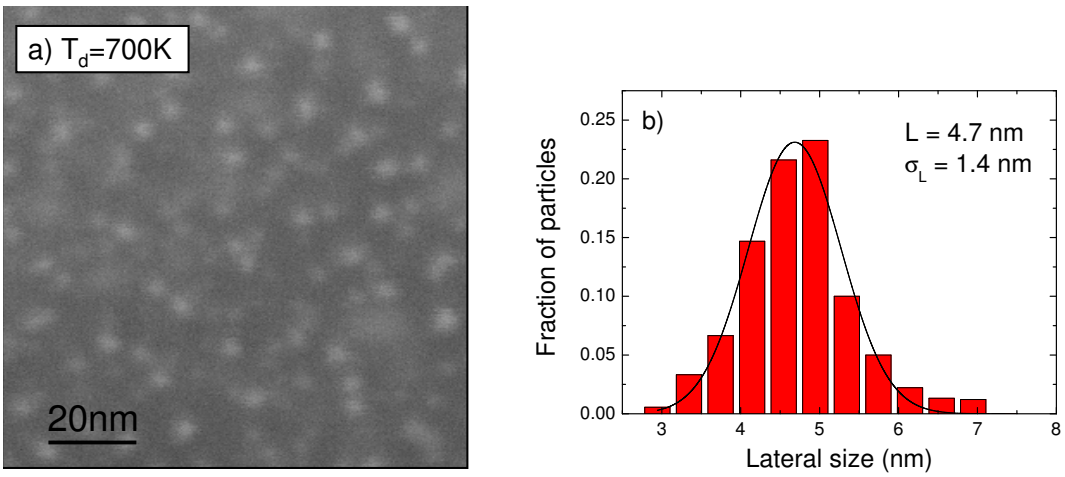

Figure 3.25: (a) FESEM image of 1 nm thick CoPt$_3$ alloy grown at 700 K; (b) lateral size distribution of (a).

Unfortunately, it was impossible to image this sample by STM certainly due to the layered structure of WSe$_2$. That is the reason why FESEM investigation was done for this sample. The image shown in figure 3.25(a) was recorded using the secondary electron (SE) in-lens detector, very sensitive to the height of objects, i.e. the taller the object the higher the SE intensity. The analysis of this SE image leads to an average lateral size equal to 4.7 nm with σ=(1.4±0.1) nm.

Quantitative GISAXS analysis: fitting and simulation

The Guinier plot analysis has the advantage to give estimates of the main size parameters. However, these values can be criticized because the slope of $\ln I(q)$ vs. q^2 can be altered by the presence of the interference peak. Similarly, the position of the interference peak can be influenced by the cluster size so that the separation distance between nanoparticles deduced from this position may be in error[114].

Here a simulation of the full GISAXS patten is presented using the $IsGISAXS$ program [96]. The analysis of GISAXS patterns rely on two approximations already introduced in paragraph 2.4.1. Because of grazing incidence conditions, the substrate has a reflection coefficient close to 1, therefore both incident and reflected beam can interact with the particles. These effects are treated using the Distorted Wave Born Approximation (DWBA). The second approximation concerns the statistical description of self-assembled particles. The used approximation is the Local Mono-disperse Approximation (LMA) in which neighbour islands are assumed to have the same size and shape, over the coherent area of the x-ray beam. The data analysis is done in two steps. The morphological

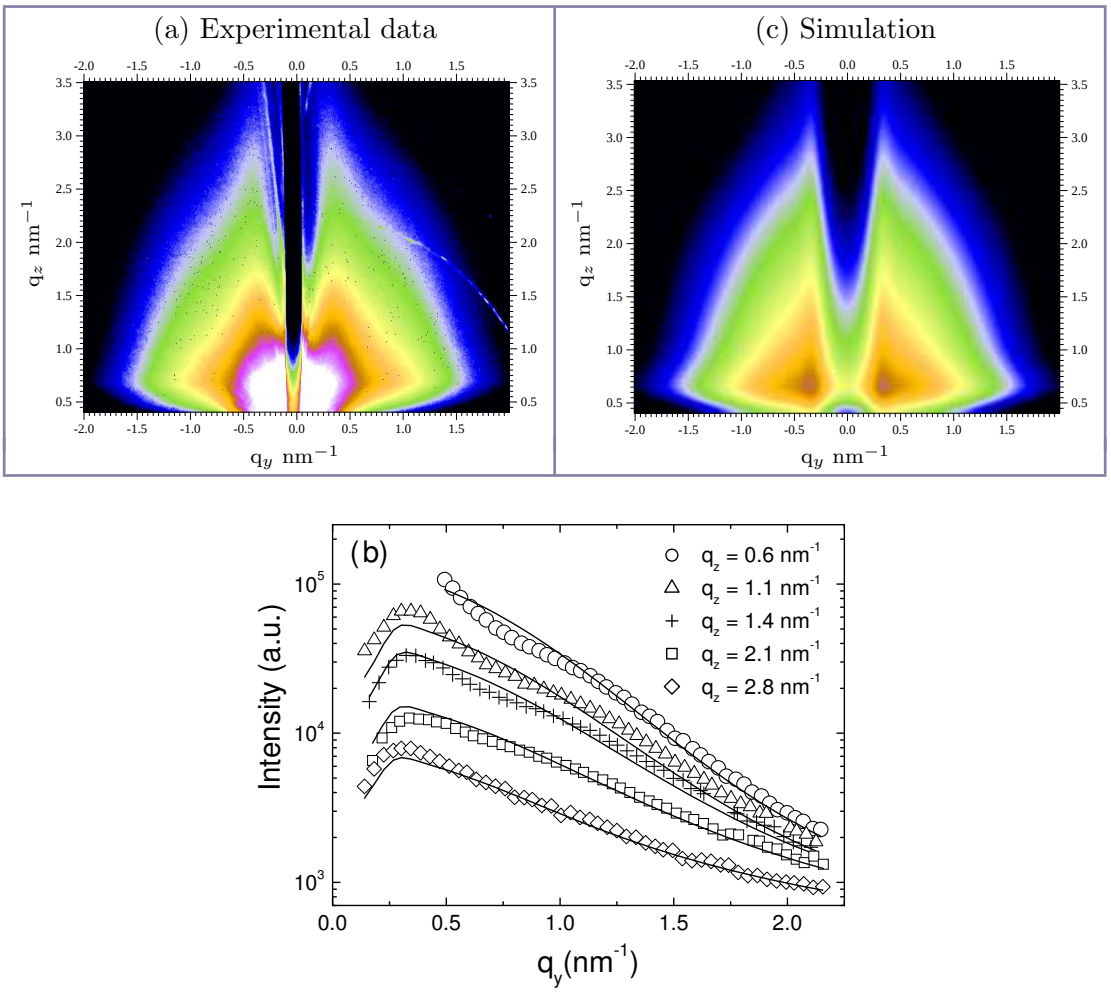

Figure 3.26: 2D GISAXS experimental intensity for a 1.0 nm thick $CoPt_3(111)/WSe_2(0001)$ deposit at 700 K. (a) Experimental pattern. (b) Cuts of the experimental pattern parallel to the surface, at $q_z = 0.6$ (open circles), $q_z = 1.1$ (open triangles), $q_z = 1.4$ (crosses), $q_z = 2.1$ (open squares) and $q_z = 2.8$ (open rhombs); continuous lines: best fit of the experimental cut. (d) 2D pattern simulated with the parameters obtained from the parallel fits. The intensity is represented with a logarithmic scale.

parameters of alloy nanostructures (shape, size, separation distance...) are adjusted simultaneously in several parallel cuts of GISAXS images using a Levenberg-Marquadt χ^2 criterion minimization. These cuts are fitted using the 1D-ideal paracrystal (1DDL) model to describe the interference function. Differently from the MgO or Si substrates used for GISAXS experiments, the $WSe_2(0001)$ substrates are not perfectly flat. Thus, the experimental cuts have not be fitted in the region close to the Yoneda, which is sensible to the interface between substrate and nanoparticles. Then, the 2D GISAXS images are simulated with the adjusted parameters and compared to the experimental pattern. If there is a good agreement, the parameters are valid.

Figure 3.26 displays the GISAXS experimental patterns (a) and simulated (c) as well

the fitting of the parallel cuts (b). The best agreement with experimental data was obtained by using the form factor of a truncated cone with a base angle of 60°. The results obtained from the fitting are reported in table 3.4 and rather close to those extracted from the Guinier analysis.

The lateral size deduced from GISAXS is approximately 15% smaller than that deduced from FESEM. First of all, the statistic of FESEM and GISAXS parameters are very different. As a matter of fact, the microscopy technique probes only a small region of the surface, as opposed to GISAXS. Moreover, by FESEM only the taller particles are observed with a low image contrast.

Certainly due to the high density of the particles on the $WSe_2(0001)$ surface, the expected increase of the lateral size with deposition temperature is not observed by GISAXS. This result would be discussed in the chapter 5, from the GISAXS patterns obtained for the CoPt deposits.

3.3.4 3 nm $CoPt_3$ grown on $WSe_2(0001)$ at 700 K

For the 3 nm thick $CoPt_3$/WSe(0001) deposit at 700 K, figure 3.27(a,b) displays the GISAXS patterns taken with the incident beam along the WSe_2[12-10] (a) and WSe_2[10-10](b) directions. The GISAXS pattern along the WSe_2[12-10] direction is asymmetric and presents an enhancement of scattering (or scattering rod) at $\sim 55°$ from the surface normal. This effect disappears after rotating the sample in the plane from 30° and becomes symmetric. This indicates that the $CoPt_3$ islands are facetted, with {100} side wall facets. In figure 3.27(c) the FESEM image reveals the triangular shape of the islands as already found for 5nm thick $CoPt_3$ deposit at 570 K (see figure 3.23). However, for the 5nm $CoPt_3$ deposit the largest side wall facets are the {111} ones, while here from the GISAXS pattern, the direction of the scattering rod would indicate the formation of large {100} facets. The scattering rod coming from the {111} facets should appear at 70°, close to the Yoneda's peak and probably a small contribution of such {111} facets cannot discard.

In order to interpret these results let one consider the following points.

- The broadening of the scattering rod depends inversely on the facet dimension. In particular, the smaller the projection of the facet in the plane (q_y, q_z), the broader the scattering rod. Here such dimension is 1.23H and 1.06H for {100} and {111} facets, respectively. It means that {111} facets lead to a broader signal more difficult to detect.

- The number of photons which are scattered by the facets is twice smaller for the {111} facets, because they are steeper with respect to the horizontal plane. It is a beam footprint effect along the direction perpendicular to the incident beam.

- Since the Se segregates during co-deposition, one layer of $PtSe_2$ may be formed on {111} facets [53] and may attenuate considerably the signal from this facet.

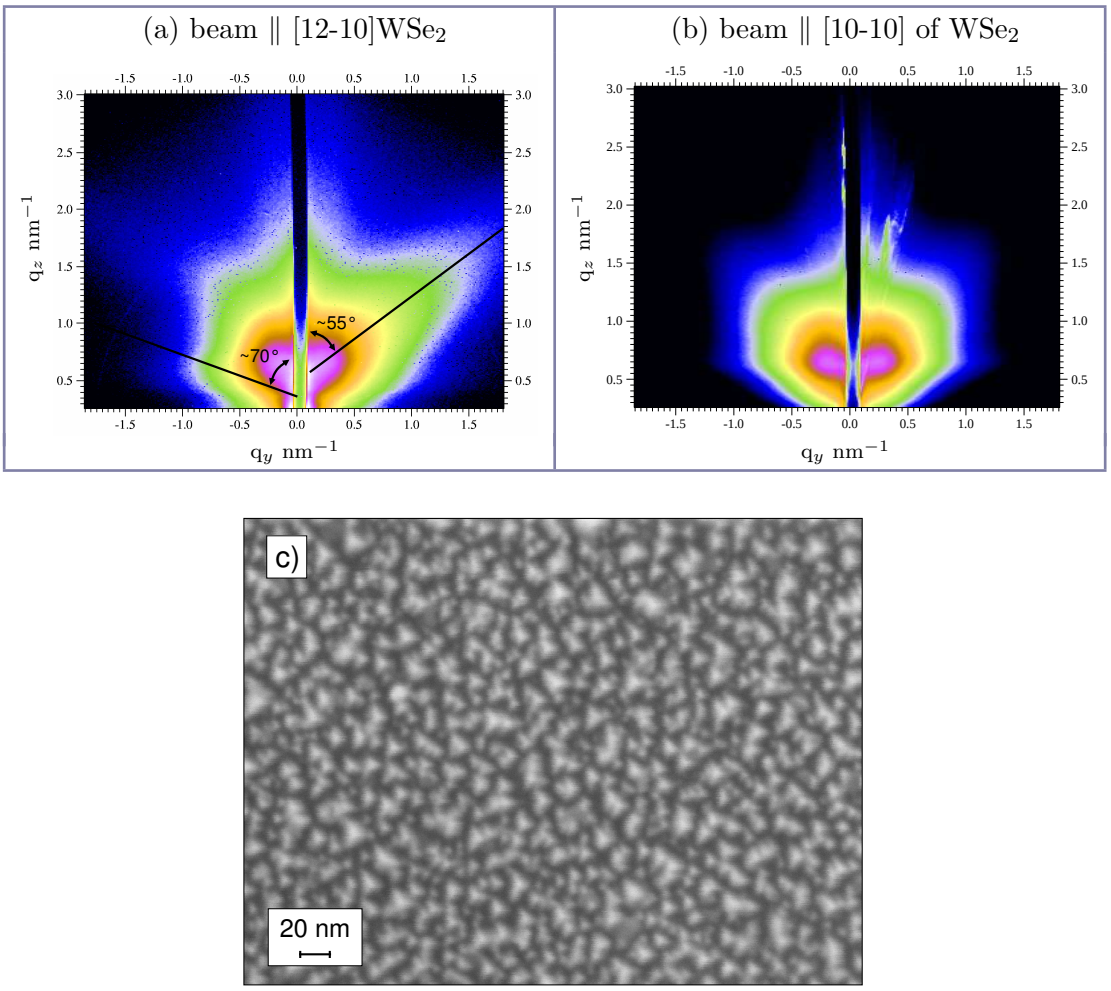

Figure 3.27: 2D GISAXS experimental intensity for a 3.0 nm thick $CoPt_3(111)/WSe_2(0001)$ deposit at 700 K with the beam aligned along the [12-10]WSe_2(0001) corresponding the [1-10]CoPt3(111) (a) and the beam aligned along the [10-10]WSe_2(0001) corresponding the [11-2]CoPt3(111) (b).

These considerations require more work. In particular the calculation of the Form factor corresponding to an hexagonal truncated particle with the alternated {111} and {100} facets has to be done, to include it in the fitting procedure and see the effects in the GISAXS pattern. Furthermore, in order to get rid of Se segregation, the growth of nanostructures on another 111 substrate surface like MgO(111) would be very interesting.

3.4 Summary

The polarized XAFS measurements performed in two epitaxial fcc 3nm thick $CoPt_3(111)/WSe_2(0001)$ nanostructured films, one grown at 300 K exhibiting a perpendicular magnetic anisotropy and another grown at 700 K exhibiting a $L1_2$-type order and magnetically isotropic, reveal the existence of a local structural anisotropy strongly marked in the film

grown at 300 K. It is characterized by preferential CoCo pairs in the film plane extending up to third shell balanced with preferential heteroatomic pairs out of the plane. Such anisotropy can be associated to the formation of Co rich thin disks in the film plane which would produce an anisotropy of the orbital moment of Co atoms, microscopic origin of the perpendicular magnetic anisotropy. The anisotropic order is accompanied with a lattice distortion, where the in-plane bonds are shorter than the out-of-plane bonds. In the film grown at 700 K, such structural anisotropy is attenuated and agrees with the appearance of the $L1_2$-type order, which is isotropic. Therefore, subtle changes at a local range can affect greatly the magnetic properties of these films.

The morphology of 1 nm thick $CoPt_3$ was studied for different deposition temperatures. This thickness is not ideal to study their morphology by GISAXS. In fact, highly dense self assembly of nanoparticles are observed by STM for T_d=300 and 570K. For room temperature deposition the nanoparticles are characterized by a narrow size distribution and they touch each other until a thickness equal to 2.0 nm. When the deposition temperature increases to 570 K, small nanoparticles coalesce to form larger aggregates and a broader size distribution is observed. A complete information was extracted for the GISAXS pattern of the sample grown at 700K and no marked size increase was obtained. Triangular islands were well observed in a 3 nm thick deposit at 700 K by FESEM. However such shape is not well observed by GISAXS due to a very low signal coming from the {111} facets, compared to the signal coming form the {100} facets.

Chapter 4

$CoPt_3$ alloy grown on NaCl(001)

In the previous chapter the origin of the PMA, observed on $CoPt_3$/ WSe_2(0001) grown at RT, has been proven to be due to the anisotropic SRO extended up to the third coordination shell. This type of SRO would be favored by the Se segregation of the WSe_2(0001) substrate observed during deposition. In order to confirm the role played by the substrate, $CoPt_3$ alloy was grown on a another low energy surface namely NaCl(001). For this purpose, the $L1_2$ long range characterized by RHEED and XRD and the short range order by polarized EXAFS were studied in $CoPt_3$ nanostructures formed at different deposition temperatures. The morphology of the $CoPt_3$ nanostructures was characterised by HRTEM and GISAXS.

4.1 Epitaxial growth and structural characterization

Co-deposition of Co and Pt on NaCl(001) was done under UHV at different deposition temperatures after heating the substrate at 600K for 1 hour. Figure 4.1 shows the RHEED patterns taken along the [100] and [110] azimuths for the pure substrate and deposits of 3nm nominal thickness. The rings in the RHEED patterns attest that the sample grown at RT is polycrystalline. For $T_d \geq$370 K fcc $CoPt_3$(001) nanoparticles grow along the [001] direction with the [100]NaCl(001)$\|$[100]$CoPt_3$(001) and [110]NaCl(001)$\|$[110]$CoPt_3$ relationships, in spite of the large lattice mismatch ($f \sim 30\%$). This value was retrieved from the separation distance between the substrate streak and alloy spots. It turns out that the interactions between the substrate and adatoms are sufficiently strong to orientate azimuthally the initial stable clusters but too weak for keeping them under epitaxial stress.

The $L1_2$ long range order is not observed at any deposition temperature until 670 K, while such order is observed for 3nm $CoPt_3$ deposits on WSe_2(0001) at 570K using the same atomic fluxes. This is likely due to a deviation from the expected sample composition on NaCl. In fact, from the $\theta/2\theta$ scan (figure 4.2(a)) measured for the sample prepared at 570K, the position of the 002 $CoPt_3$ reflection corresponds to a Pt composition of 80%, which is beyond the composition range of the $L1_2$ region. The extracted fcc lattice parameter is equal to 3.873 Å. The same value has been found from the 113 reflection

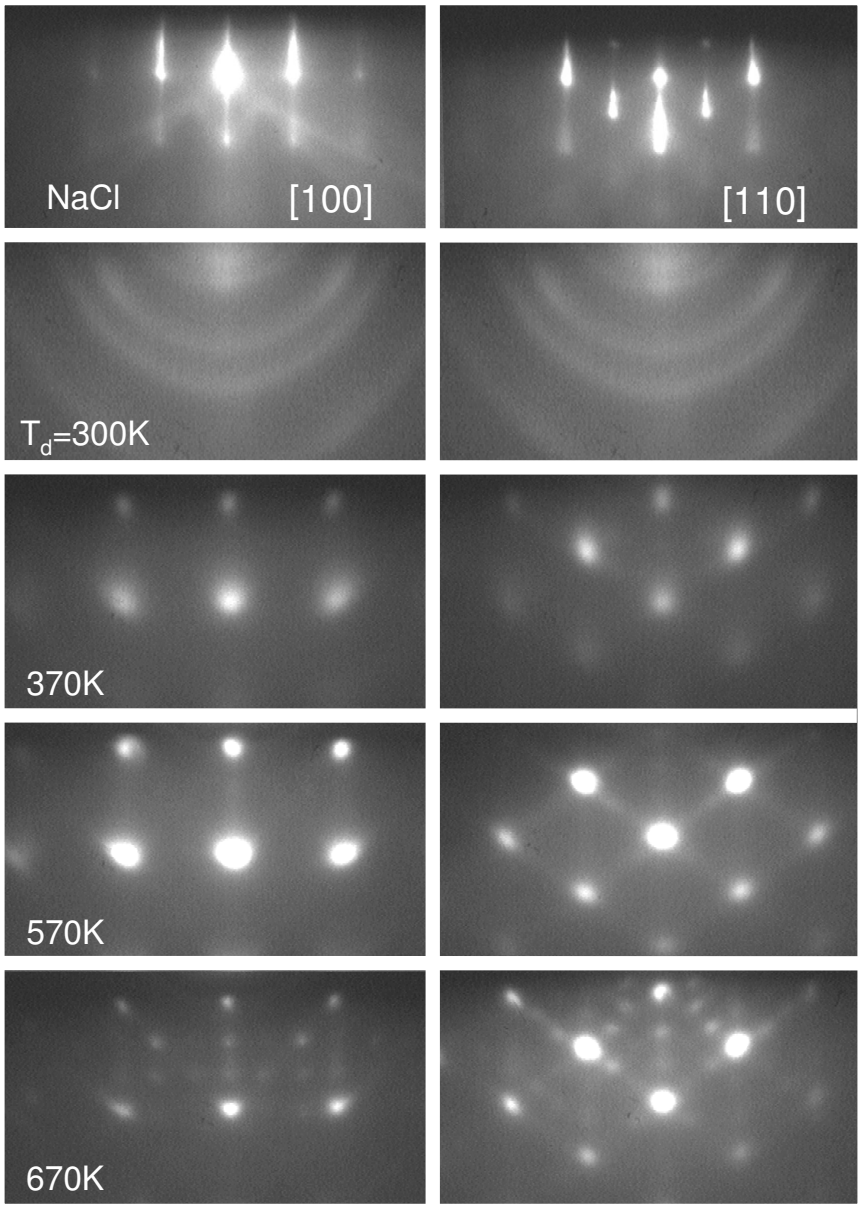

Figure 4.1: RHEED patterns along the [100] and [110] azimuths of 3 nm thick $CoPt_3$ on NaCl(001) for different deposition temperatures.

plotted in figure 4.2(b), meaning the nanostructures are not strained by the substrate. Figure 4.2(c) shows the $\theta/2\theta$ scan around the angular region of the 001 reflection. Only small peaks coming from the NaCl substrate are visible. The absence of the $L1_2$ agrees with the RHEED pattern. Note that the intermediate spots observed in the RHEED pattern of the 670K sample are produced by diffraction on the edges of the NaCl substrate.

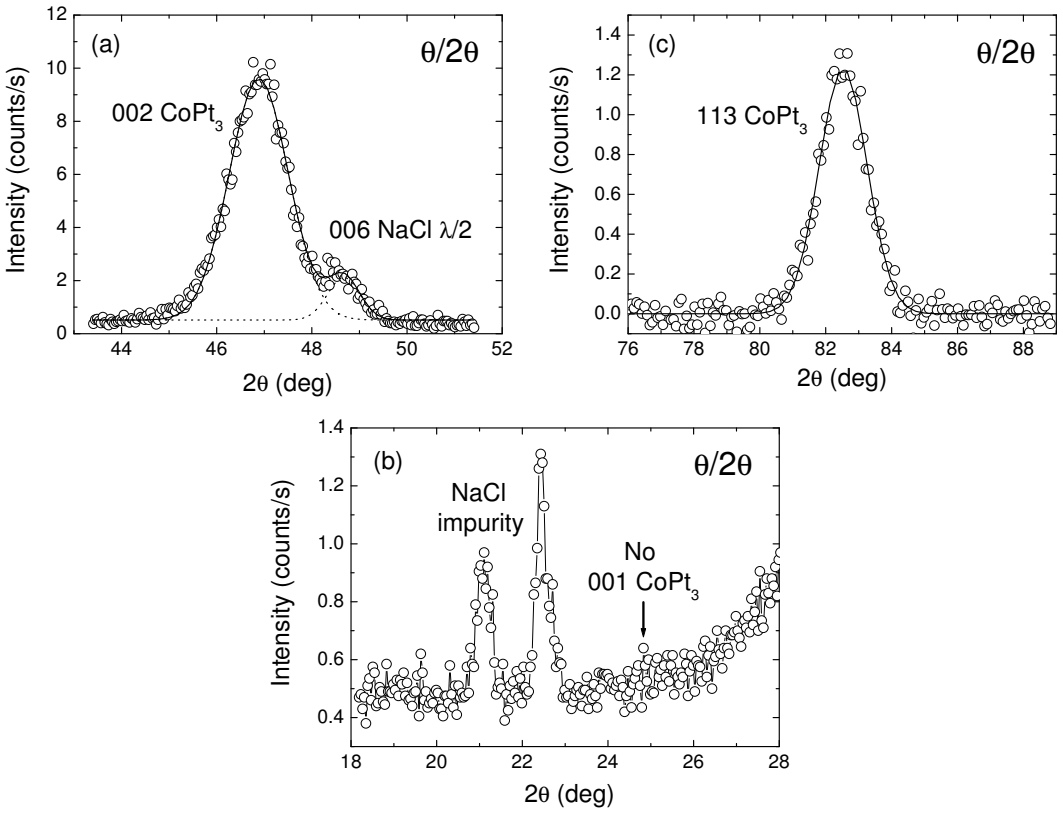

Figure 4.2: XRD $\theta/2\theta$ scans of a $Co_{20}Pt_{80}$ sample grown on NaCl(001) at 570 K around the intensities of (a) (002), and (b) (113) and (c) (001) reflections of $Co_{20}Pt_{80}$. These measurements were carried out at the SIMaP laboratory. (006)NaCl reflection for $\lambda/2$ wavelength and some peaks coming likely from impurities in NaCl are visible.

4.2 Short range ordering

The local atomic environment was studied by polarized EXAFS. The measurements were carried out on the FAME beamline for the samples prepared at 370 and 670 K with nominal thicknesses of 3nm.

4.2.1 EXAFS data analysis

The experimental EXAFS spectra were treated following a method similar to that described in par 3.2.1. The growth along the [001] direction is characterized by the in- and

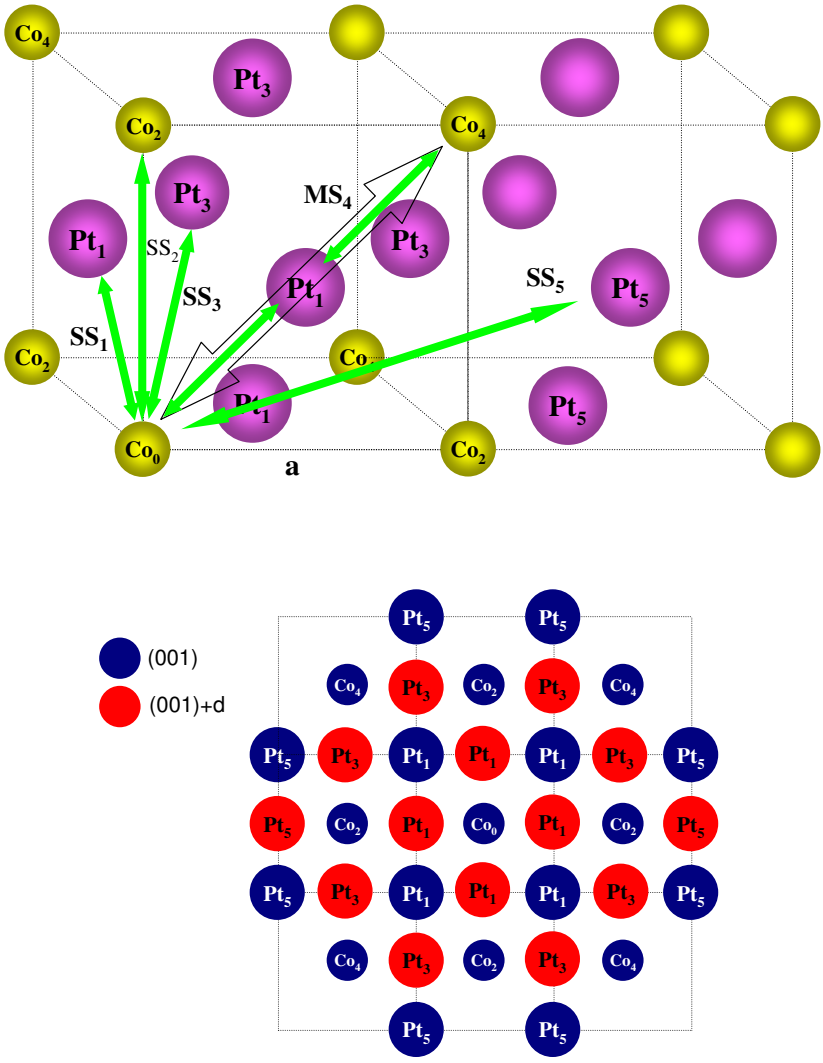

Figure 4.3: Upper panel: schematic view of the $L1_2$ ordered structure showing the scattering paths used in the fitting between absorbing atom Co_0 and the ith neighbourds, Co_i and Pt_i. Lower panel: atoms in the (001) plane (blue circles) and in the upper planes $+d_{001}$ (red circles).

							Geometry			
Signal	Length (R)		N_{tot}	Scatterer(s)	N^{in}	N^{out}	$\tilde{N}_{\perp}^{in}$	$\tilde{N}_{\perp}^{out}$	$\tilde{N}_{\parallel}^{in}$	$\tilde{N}_{\parallel}^{out}$
SS_1	$a/\sqrt{2}$		12	Pt_1	4	8	0	12	6	6
SS_2	a		6	Co_2	4	2	0	6	6	0
SS_3	$a\sqrt{3/2}$		24	Pt_3	-	24	0	24	0	24
		I	12	Co_4	4	8	0	12	6	6
MS_4	$a\sqrt{2}$	II	24	Co_4-Pt_1	8	16	0	24	6	12
		III	12	Pt_1-Co_4-Pt_1	4	8	0	12	6	6
SS_4	$a\sqrt{5/2}$		24	Pt_5	-	24	0	24	12	12

Table 4.1: Single-scattering (SS) and multiple-scattering (MS) signals used in the calculated XAFS spectrum of the $L1_2$ ordered $CoPt_3$ fcc structure. The MS_4 signal is composed of single-(I),double-(II) and triple-(III) scattering paths. The path length is given in units of the lattice parameter a. N_{tot} is the total number of paths per absorbing atom. N^{in} is the number of independent paths per absorbing atoms occurring strictly in the (001) plane while N^{out} is the number of paths out of the (001) plane. On the right side, $\tilde{N}_{\perp}^{in}(_{\parallel})$ is the effective number of in-plane contributions observed in perpendicular (parallel) polarization geometry, and $\tilde{N}_{\perp}^{out}(_{\parallel})$ is the effective number of out-of plane contributions observed in perpendicular (parallel) geometry.

out-of-plane environments shown in figure 4.3. For this orientation the fifth coordination shell has been introduced in the analysis in order to improve the fits of the full spectra and the extraction of structural parameters. The fifth coordination shell corresponds to the single-scattering contributions from Co_0-M_5 (M=Pt or Co), where M_5 is located at the center of the face of the next cube (see figure 4.3).

For the $L1_2$ phase the corresponding polarization-dependent coordination numbers, $\tilde{N}_j$ (eq.2.24) are reported in table 4.1. The relations between the true coordination numbers, N^{in} and N^{out}, and the extracted $\tilde{N}_j$ are:

$$\text{First coordination shell} \begin{cases} \tilde{N}_{\parallel} = 1.5N^{in} + 0.75N^{out} \\ \tilde{N}_{\perp} = 1.5N^{out} \end{cases} \tag{4.1}$$

$$\text{Second coordination shell} \begin{cases} \tilde{N}_{\parallel} = 1.5N^{in} \\ \tilde{N}_{\perp} = 3N^{out} \end{cases} \tag{4.2}$$

$$\text{Third coordination shell} \begin{cases} \tilde{N}_{\parallel} = N^{out} \\ \tilde{N}_{\perp} = N^{out} \end{cases} \tag{4.3}$$

$$\text{Fourth and fifth coordination shells} \begin{cases} \tilde{N}_{\parallel} = 1.5N^{in} + 0.75N^{out} \\ \tilde{N}_{\perp} = 1.5N^{out} \end{cases} \tag{4.4}$$

Since the introduction of the fifth coordination shell requires to adjust other 4 new parameters during the fitting, namely the fraction of atoms which occupy the sites of the

			Out-of-plane polarization			In-plane polarization						
Signal		Scatters	$\tilde{N}^j_\perp$	R_j (Å)	$\sigma^2_j(10^3Å^2)$	$\tilde{N}^j_\parallel$	R_j (Å)	$\sigma^2_j(10^3Å^2)$	N^{out}	N^{in}	n^{out}	n^{in}
$Co_{20}Pt_{80}$/NaCl(001) at 370K												
SS_1		Pt_1	10.8(2)	2.68(1)	0.51(3)	10.8(2)	2.69(1)	0.53(1)	7.20(5)	3.60(5)	0.90(2)	0.90(2)
		Co_1	1.2(1)	2.66(1)		1.2(1)	2.66(1)		0.80(5)	0.40(5)	0.10(2)	0.10(2)
SS_2		Pt_2	0.9(2)	3.65(1)	0.96(6)	1.0(2)	3.60(2)	1.17(6)	0.31(5)	0.64(5)	0.16(2)	0.16(2)
		Co_2	5.1(2)	3.79(1)		5.0(2)	3.79(2)		1.69(5)	3.36(5)	0.84(2)	0.84(2)
SS_3		Pt_3	20.1(2)	4.71(2)	0.57(3)	**20.1**	**4.71**	0.63(3)	20.1(1)	-	0.84(2)	-
		Co_3	3.9(2)	4.47(2)		**3.9**	**4.47**		3.9(1)	-	0.16(2)	-
	I	Co_4	9.8(3)		2.0(4)	9.8(3)		1.17(4)	7.20(5)	3.59(1)	0.90(1)	0.90(1)
MS_4	II	Pt_1-Co_4	19.4(3)	5.36(2)	1.73(4)	19.4(3)	5.38(2)					
	III	Pt_1-Co_4-Pt_1	9.7(3)		1.73(3)	9.7(3)						
SS_3		Pt_5	12.0(2)	6.09(2)	0.79(3)	12.0(2)	6.10(2)	0.81(3)	8.00(5)	4.01(5)	0.50(1)	0.50(1)
		Co_5	12.0(2)	5.93(2)		12.0(2)	5.94(2)		8.00(5)	3.99(5)	0.50(1)	0.50(1)
$Co_{20}Pt_{80}$/NaCl(001) at 670K												
SS_1		Pt_1	11.9(2)	2.70(1)	0.30(3)	11.4(4)	2.70(1)	0.37(1)	7.86(5)	3.67(5)	0.98(2)	0.92(2)
		Co_1	0.1(1)	2.75(1)		0.6(2)	2.69(1)		0.04(5)	0.33(5)	0.02(2)	0.08(2)
SS_2		Pt_2	0.0(2)	3.65(2)	1.37(6)	0.0(3)	3.80(2)	1.22(6)	0.00(5)	0.00(5)	0.00(1)	0.00(1)
		Co_2	6.0(2)	3.79(2)		6.0(4)	3.79(2)		2.00(5)	4.00(5)	1.00(1)	1.00(1)
SS_3		Pt_3	23.3(4)	4.72(2)	0.82(3)	**23.3**	**4.72**	0.76(3)	23.3(2)	-	0.97(1)	-
		Co_3	0.7(2)	4.55(2)		**0.7**	**4.55**		0.7(2)	-	0.03(1)	-
	I	Co_4	11.8(3)		0.04(4)	10.9(3)		0.16(4)	8.00	4.00	1	1
MS_4	II	Pt_1-Co_4	23.6(3)	5.40(2)	2.00(4)	21.7(3)	5.40(2)					
	III	Pt_1-Co_4-Pt_1	11.8(3)		1.80(3)	10.8(3)						
SS_3		Pt_5	14.8(2)	6.01(2)	0.59(3)	16.2(4)	6.02(2)	0.61(3)	9.86(5)	5.87(5)	0.62(1)	0.73(1)
		Co_5	9.2(2)	6.02(2)		7.8(4)	6.04(2)		6.14(5)	2.13(5)	0.38(1)	0.27(1)

Table 4.2: Structural parameters corresponding to the best fits of $Co_{20}Pt_{80}$ grown on NaCl(001). The effective numbers of independent paths($\tilde{N}^j$), the path lengths (R_j) and the Debye-Waller factors (σ^2_j) are reported for both polarization. The total numbers of the independent paths (N^{in} and N^{out}) in and out of the (001) plane are calculated from the effective contributions observed in parallel and perpendicular geometry using eq. 10-14. n^{out} (n^{in}) are the concentrations of each elements in every coordination shell out-of-plane (in-plane).

$L1_2$ model, the lengths of Co_0Pt_5 and Co_0Co_5 paths and the Debye-Waller factor, σ^2_5, the δ parameter, which takes account of a mis-alignment of the three atoms in the MS_4 correlation, was fixed to zero.

4.2.2 Results and discussion

Figure 4.4 shows the experimental spectra collected for the two samples prepared at 370 and 670 K using the two geometries. No notable differences are observed between the two polarizations for both samples. The $|FT|$ of $k^2\chi(k)$ calculated in the same k-range, 4-12Å^{-1}, are reported in figure 4.4; the peak at ∼5Å is more intense for the sample prepared at 670K, signature of a more pronounced short range order.

Figure 4.5 presents the experimental and best fitted spectra and their corresponding $|FT|$s. The resulting structural parameters are listed in table 4.2. No polarization depen-

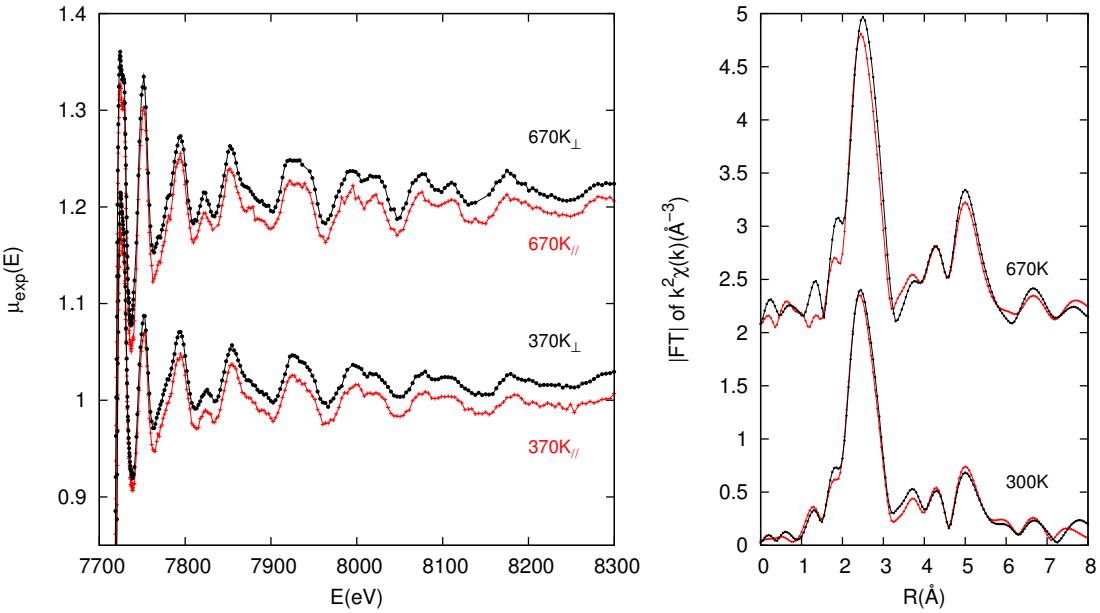

Figure 4.4: Left: experimental x-ray absorption spectra of the three $Co_{20}Pt_{80}$ films deposited on NaCl(001) at 670, 370K for in-plane (∥) and out-of plane (⊥) geometry. Right: moduli of Fourier transform (|FT|) of the experimental and simulated $k^2\chi(k)$ spectra (k-range: 4-12Å^{-1}) for the two geometries: ∥ (red lines) and ⊥ (black lines). The curves are shifted for clarity.

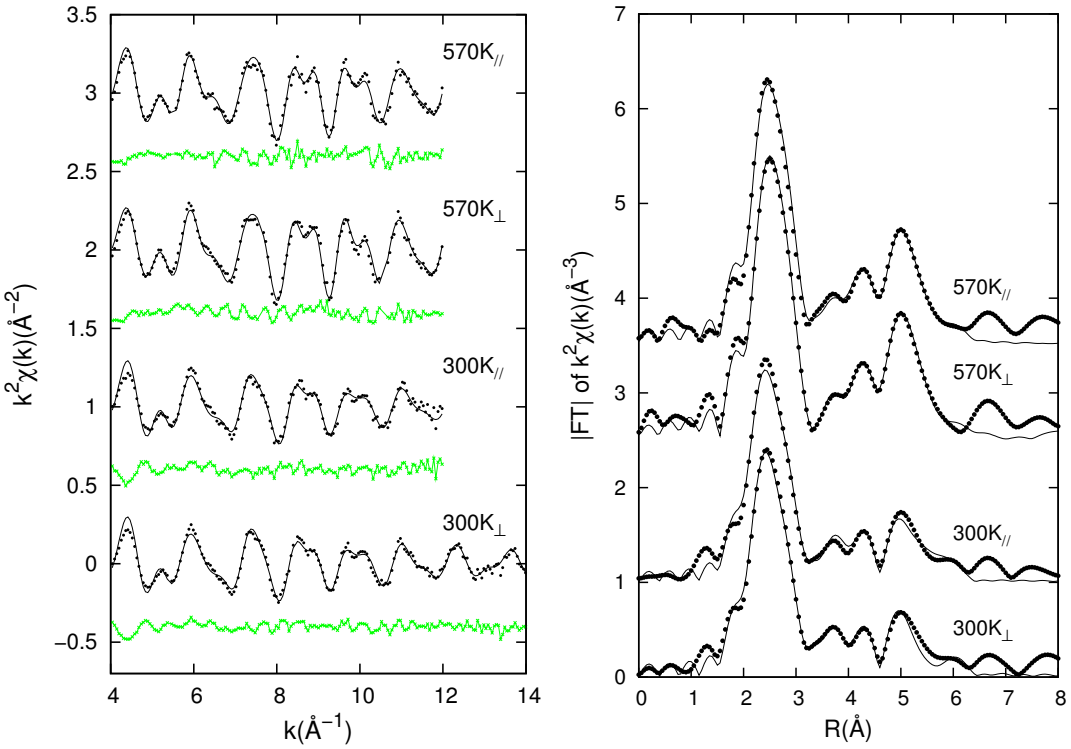

Figure 4.5: On the left, experimental (dots) and best fitted (solid lines) $k^2\chi(k)$ of two films $Co_{20}Pt_{80}$ grown on NaCl(001) at 300, and 670K for in-plane (∥) and out-of plane (⊥) polarizations. For each fit the residual $k^2\chi(k)_{exp} - k^2\chi(k)_{fit}$ is shown by green lines. On the right, experimental (dots) and best fitted (solid lines) |FT| curves for in-plane (∥) and out-of plane (⊥) polarizations.

dence on either the distances or the coordination numbers is observed. It means that in both samples the local atomic environment is isotropic.

Let one compare table 4.2 with table 4.1. If the nanostructures adopt the $L1_2$ order, the first, third and fifth coordination shells are occupied by Pt and the second and the fourth coordination shells only by Co (table 4.1); for the 370K sample, the ∼90% of first and third coordination shells are occupied by Pt, the ∼90% of second and fourth are occupied by Co and the 50% of fifth is occupied by Pt(Co) (table 4.1). This shows that the sample prepared at lower temperature is characterized by a partial SRO until the fourth coordination shell. The degree of the SRO increases with the deposition temperature. A strong SRO is observed in the perpendicular direction; i.e. out-of-plane nearest neighbors of a Co atom are only Pt atoms. This trend is consistent with the relaxation behavior toward the $L1_2$ structure observed in $Cu_3Au(001)$ oriented crystal which was found 20 times faster along the normal to the surface than in the plane [56].

In comparison with the observations in $CoPt_3$ nanostructures grown at 300K on $WSe_2(0001)$, no anisotropy of short range order is detected in the nanostructures grown at 370K on NaCl(001). This difference could be associated to the different growth directions which could modify the importance of the Pt dynamic segregation at the advancing surface. However Shapiro et al. have shown that the deposition temperature range for which PMA is observed in no-long range ordered $CoPt_3$ films does not depend on the growth direction [115]. Therefore, the existence of anisotropic SRO in nanostructures grown at RT on $WSe_2(0001)$ is likely due to the Se segregation during the co-deposition. Such segregation could play a surfactant effect favouring short range arrangements between Co and Pt atoms already at RT and above 370K $L1_2$ order.

4.3 Morphology

The morphology of $CoPt_3$ nanostructures formed on NaCl(001) was studied after deposition of 0.5 nm at 520K and deposition of 3 nm at 570 K. GISAXS patterns were recorded on both samples and TEM measurements were performed on the thinner deposit after deposition of 7 nm thick carbon and the dissolution of NaCl substrate.

4.3.1 0.5 nm $CoPt_3$/NaCl(001)

TEM analysis

Figure 4.6(a) shows the TEM image of an assembley of fcc $CoPt_3$ nanoparticles. The average size of $CoPt_3$ particles is 4 nm with a distribution, σ_R, equal to 1.4 nm (see figure 4.6(d)). The selected area electron diffraction (SAED) pattern reveals that most of nanoparticles are oriented along the [001] direction following a cubic over cubic growth, as indicated by the strong reflection 220 and 200. The high-resolution TEM image of individual nanoparticle (see figure 4.6(c)) shows that the spacing between the lattice fringe

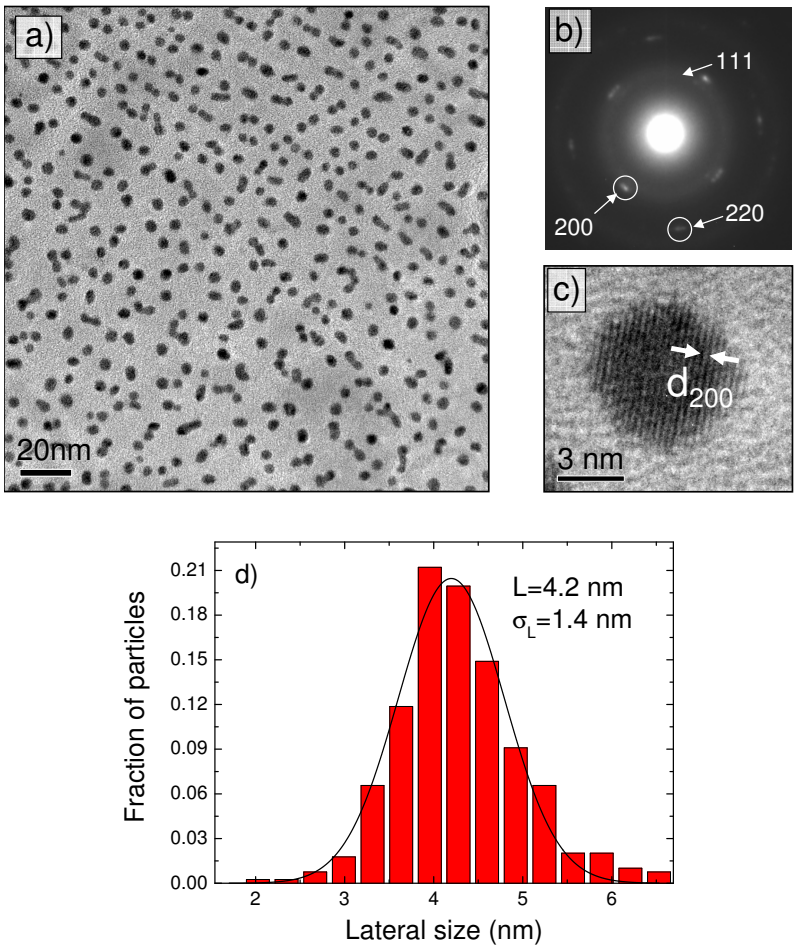

Figure 4.6: a) TEM image of 0.5 nm $CoPt_3$ grown on NaCl(001) at 520 K, b) corresponding SAED pattern and c) HRTEM image of one nanoparticle. The arrows in c) indicate the lattice fringe spacing between (200) planes. d) The lateral size distribution calculated for the image (a).

is 1.94 Å, that corresponds to the distance between (200) planes. Most of the particles have square shape, with {111} side wall facets, which may be truncated at the corners by {110} facets.

In figure 4.6(b) a light ring close to the 200 reflection is also observed and it is correspond to the 111 reflection, characteristic of the growth of particles along another orientation without epitaxy. Figure 4.7(a) shows two 110-oriented nanoparticles (partially coalesced) as revealed by the diffraction patterns obtained by FFT of HRTEM (figure 4.7(b)); the spacing between the (111) planes is well defined. The two particles are slightly disoriented in the plane as indicated by their corresponding 111 reflections. In figure 4.7(c) the (111) and (002) lattice fringes in the 110 oriented particles are observed. The hexagonal shape of the nanoparticle can be retrieved by the projection of the truncated octahedron along the [110] axis (figure 4.7(e)).

To gain further insight into possible particle correlations, a more precise analysis was done on the plane view. The distribution of the nearest neighbor (NN) diameter and

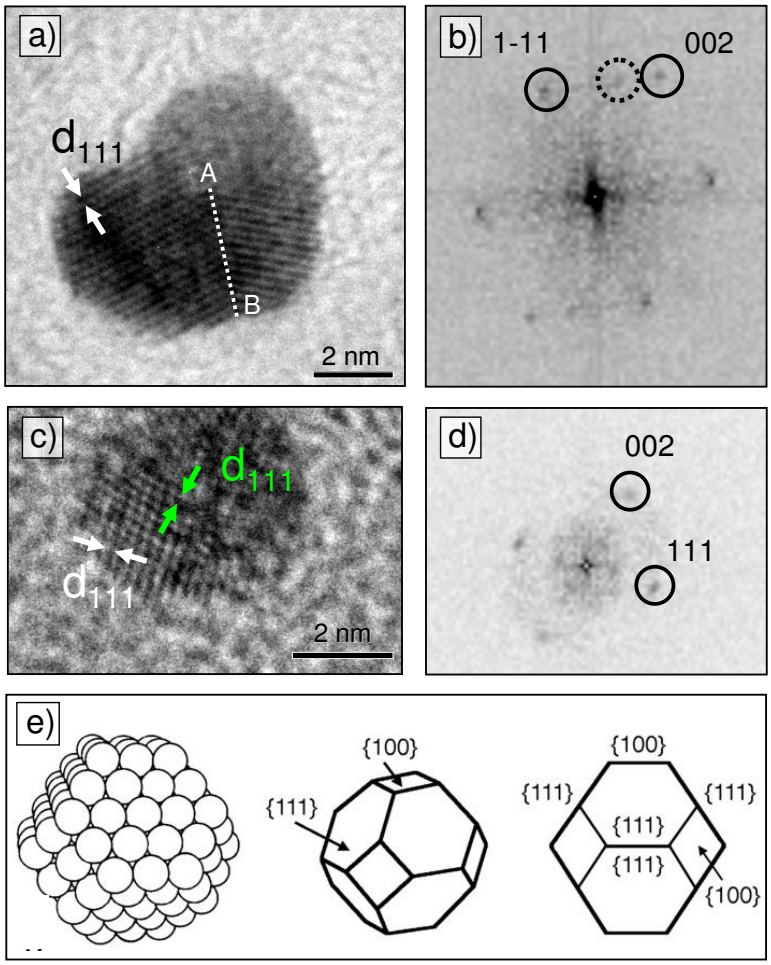

Figure 4.7: (a) and (c) HRTEM images of 110-oriented $CoPt_3$ nanoparticles and (b) and (d) their FFT patterns. (e) The sketches in (g) show a cuboctahedral particle in side-view (left+middle) and in [011] zone axis orientation (right) [116]. The solid and dotted circles in (b) surround the reflections coming from the left and right particles in (a), respectively.

separation distance are shown in figure 4.8. No correlation between the size of neighbour particles is obtained. This means that, in average, an island is surrounded by islands of different sizes according to the overall size distribution. By contrast, a significant correlation between the island size and separation is found. The linear regression of the correlation between the size and separation has a positive slope, 1.40±0.01, meaning that the larger the central island, the larger the distance from its NNs.

GISAXS analysis

Figure 4.9(a) shows the GISAXS pattern of the 0.5 nm $CoPt_3$ grown at 520 K taken under incidence angle, $\alpha_i = 0.4°$ (α_c(NaCl)=0.23°). This GISAXS image was analysed by fitting several horizontal and vertical cuts in the same time introducing the Distorted-Wave Born approximation (DWBA) and the Size-Spacing Correlation Approximation (SSCA), taking

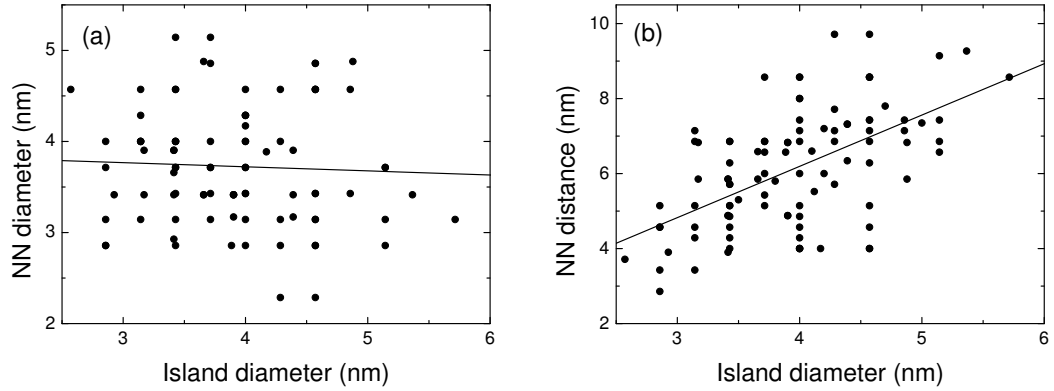

Figure 4.8: (a)Correlation between the central island and the diameter of its NNs for $CoPt_3$/NaCl(001) grown at 520 K. The slope of the linear regression is 0.04±0.01. (b) Correlation between the central island and the distance between NN islands for the same sample. The slope is 1.40±0.01.

GISAXS												
$CoPt_3$		Guinier plot		Quantitative analysis with SSCA								
ϵ	T	$2R_s$	H	Shape	L	σ_L	H	σ_H	H/L	D	w	κ
(nm)	(K)	(nm)	(nm)		(nm)	(nm)	(nm)	(nm)		(nm)	(nm)	
0.5	520	5.0	3.0	Cubooctahedra	4.4(1)	2.6(1)*	3.5(1)	0.04(5)**	0.79(2)	8.2(1)	4.5(2)	2.9(2)
				Sphere	3.7(1)	2.3(1)*	3.1(1)	0.06(5)**	0.83(2)			
3.0	570	9.4	4.4									

Table 4.3: Structural parameters obtained in 0.5 and 3 nm $CoPt_3$ deposits from a Guinier plot analysis and from simulations with $IsGISAXS$ program using the SSCA approximation, cubooctahedral or spherical shape and a Log-normal (*) or Gaussian (**) distribution functions. L and σ_L, average value and width of lateral size distribution; H, and σ_H, average value and width of height distribution; D and w, position of the first neighbor and width of the gaussian distribution for the pair correlation function (1D paracrystal); κ is the size-spacing coupling parameter.

into account the correlation between particle size and distance observed by TEM analysis. Two different form factors have been used, namely those for spherical and cubooctahedrical islands, in order to see if facet effect is detectable by GISAXS. In particular, if one consider the cubooctahedrical shape, {111} facets are expected forming an angle equal to 54° with the (001) base plane. Then, the GISAXS pattern was simulated using the adjusted parameters.

All simulations and fittings are plotted in figures 4.9(b),(c),(d) and (e). All extracted parameters are reported in table 4.3. The use of the form factor of a truncated octahedron with side wall facets does not improve the fitting. In both cases the aspect ratio, H/L, where L is the lateral size and H the height of the particles, is about 0.8, higher than what obtained for the same alloy grown on WSe_2(0001) at the same temperature. The size-spacing coupling parameter, κ, defined in eq. 2.39, is 2.9±0.2. Such correlation is

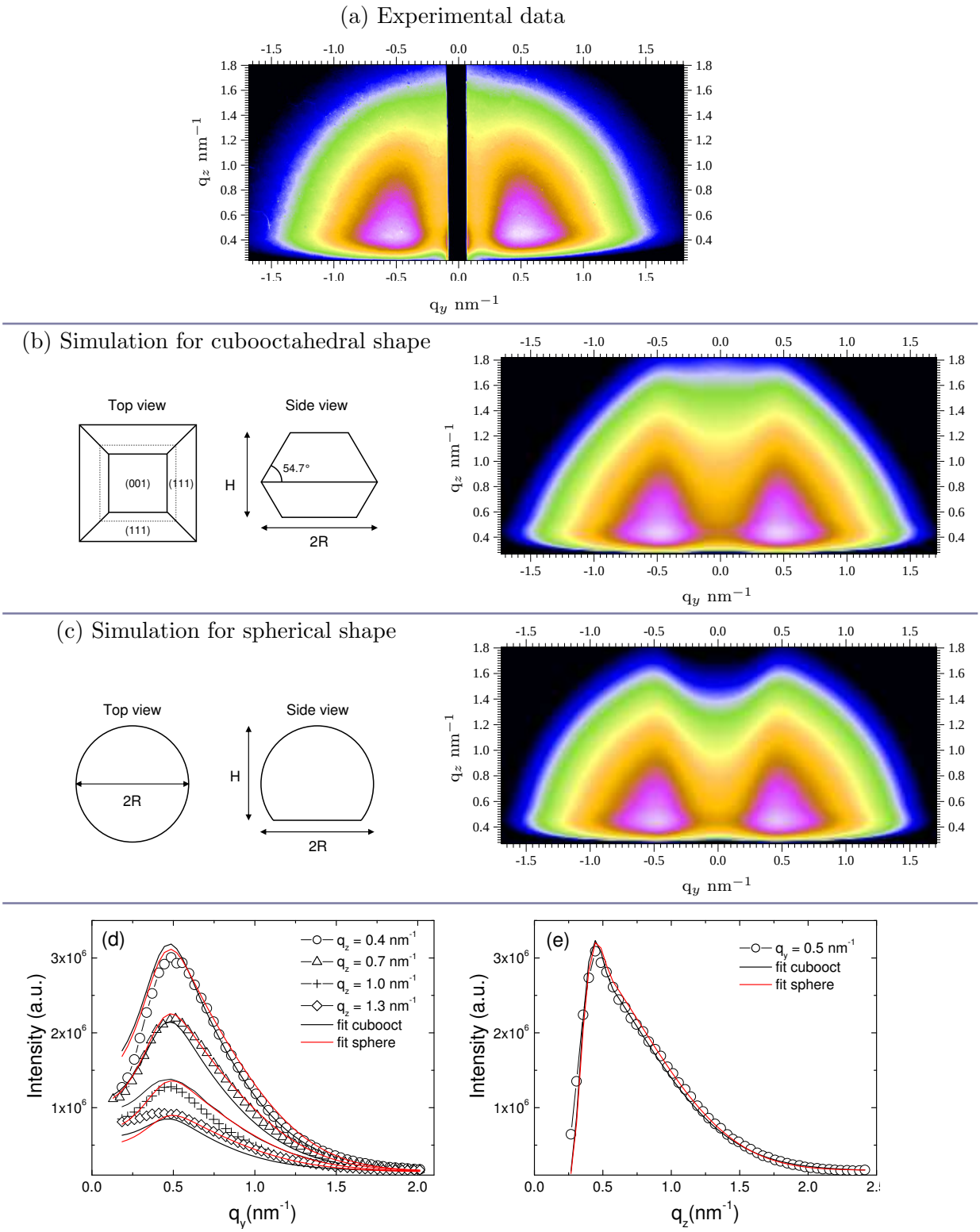

Figure 4.9: (a) GISAXS experimental pattern for a 0.5 nm thick CoPt$_3$(001)/NaCl(001) deposit at 520 K. Patterns simulated using the form factor of (b) cubooctahedron and (c) sphere. The intensity is represented with a logarithmic scale. (d) Cuts of the experimental pattern parallel to the surface, at $q_z = 0.4$ nm^{-1} (open circles), $q_z = 0.7$ nm^{-1} (open triangles), $q_z = 1.0$ nm^{-1} (crosses) and $q_z = 1.3$ nm^{-1} (open rhombs); (e) cuts of the experimental pattern perpendicular to the surface, at $q_y = 0.5$ nm^{-1} (open circles); continuous lines: best fit of the experimental cut.

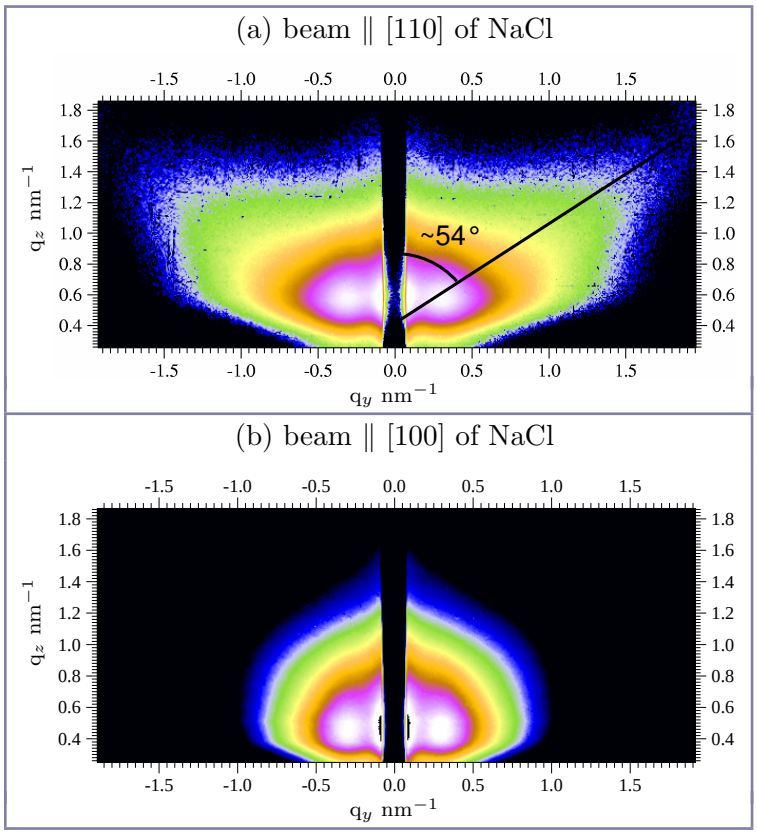

Figure 4.10: 2D GISAXS experimental intensity for a 3.0 nm thick $CoPt_3$(111)/NaCl(001) deposit at 570 K with the beam aligned along the [110]NaCl(001) corresponding the [110]$CoPt_3$(001) (a) and the beam aligned along the [100]NaCl(001) corresponding the [100]$CoPt_3$(001) (b).

required to obtain good fits.

4.3.2 3 nm $CoPt_3$/NaCl(001)

GISAXS analysis

As already observed for $CoPt_3$ nanoparticles grown on WSe_2(0001), scattering from sidewall facets are observed in particles higher than 3nm. To probe such facet effect, GISAXS pattern has been also recorded for a 3 nm thick $CoPt_3$ deposit on NaCl(001) at 570 K.

Figure 4.10 displays the 2D GISAXS experimental patterns with the incident beam parallel to the [110] and [100] directions of NaCl direction. The GISAXS pattern presents a scattered rod at 54.7° with respect to the surface normal only when the beam is parallel to the $< 110 >$ direction. This confirms that $Co_{20}Pt_{80}$ 001-oriented nanoparticles grown on NaCl(001) adopt a cubooctahedrical shape with {111} side wall facets (as depicted in figure 4.9(b)).

The horizontal and the vertical cuts taken at the inteference peak position were analysed by Guinier plots. The extrapolated average values of lateral size and height are equal to 9.4 an 4.4 nm respectively, corresponding to an aspect ratio of 0.46 (table 4.3). In com-

parison with the thinner deposit (0.5 nm) obtained at close temperature, when increasing deposit thickness the nanoparticles would increase in size faster laterally than vertically.

4.4 Summary

The growth of $CoPt_3$ on NaCl(001) leads mostly to the formation of nanoparticles oriented along the [001] direction for $T_d \geq 370$ K, 110-oriented nanoparticles are also observed but without epitaxial relationships with the substrate. No LRO is observed up to T_d=670K, but an isotropic SRO established until the fourth coordination shell. The absence of $L1_2$ long range order is likely attributed to the $Co_{20}Pt_{80}$ alloy composition out of the $L1_2$ phase. A comparison with the results obtained for $CoPt_3$ nanoparticles on WSe_2(0001) allows to attribute the development of an anisotropic SRO in $CoPt_3$ on WSe_2(0001) already at T_d=RT to the Se segregation during co-deposition.

The self-assembled nanostructures of $CoPt_3$ have a truncated octahedron shape, well observed by GISAXS with the presence of symmetrical scattering rods coming from the {111} side-wall facets for a deposit of 3 nm. For smaller nanostructures (L<5nm) (corresponding to deposit of 0.5 nm) such facetting effect is absent, but a good representation of the GISAXS pattern with a cubooctahedral form factor was obtained and TEM observation confirm this shape. However, a good representation using the form factor of a sphere was also obtained, demonstrating the interest of coupled characterization techniques.

Chapter 5

CoPt grown on $WSe_2(0001)$

In this chapter, the growth, structure, morphology and magnetic properties of CoPt nanoparticles grown on $WSe_2(0001)$ at different temperatures are investigated. As shown in chapter 3, the segregation of Se during the co-deposition of Co and Pt on $WSe_2(0001)$ surfaces favors the atomic arrangements and in particular lower the ordering temperature of $CoPt_3$. For CoPt, the formation of the $L1_0$ ordered nanostructures at low temperature is expected to induce perpendicular magnetic anisotropy, making these nanostructured films potential candidates as high density recording media.

5.1 Epitaxial growth and structural characterization at long-range

5.1.1 In-situ characterization

CoPt alloys were prepared by co-deposition of Co and Pt atoms on $WSe_2(0001)$ in the temperature range from 300 to 730 K. The fluxes were 0.02Å/s (Co) and 0.029Å/s (Pt) for samples with nominal thickness of 3 nm and 0.014Å/s (Co) and 0.02Å/s (Pt) for 1 nm.

During the co-deposition at RT, RHEED imaging initially reveals the appearance of spots at specific positions which indicate epitaxial growth of fcc CoPt islands along the [111] direction. These spot became more pronounced with increasing the deposit thickness. Figure 5.1 shows the RHEED patterns after deposition of 3nm thick CoPt alloys taken along the [-211] and [-110] azimuths referring to CoPt(111). The spots are located on each side of the substrate streaks at distances consistent with the lattice mismatch of 17%. The epitaxial relationships between the substrate and CoPt deposit are as follows: [11-20]$WSe_2(0001)$‖[-110]CoPt and [10-10]$WSe_2(0001)$‖[-211]CoPt. Based on a precise analysis of the RHEED patterns, the in-plane nearest neighbor distance for the CoPt film was found to be equal to 2.75Å, which is slightly larger than the value of the disordered bulk CoPt alloy (2.67Å) indicating the presence of a residual epitaxial strain.

With increasing deposition temperature, intermediate RHEED spots start to appear for the CoPt film prepared at 470K (figure 5.1(b)) and become more pronounced with further increase of the deposition temperature (figure 5.1(c,d)). These additional spots

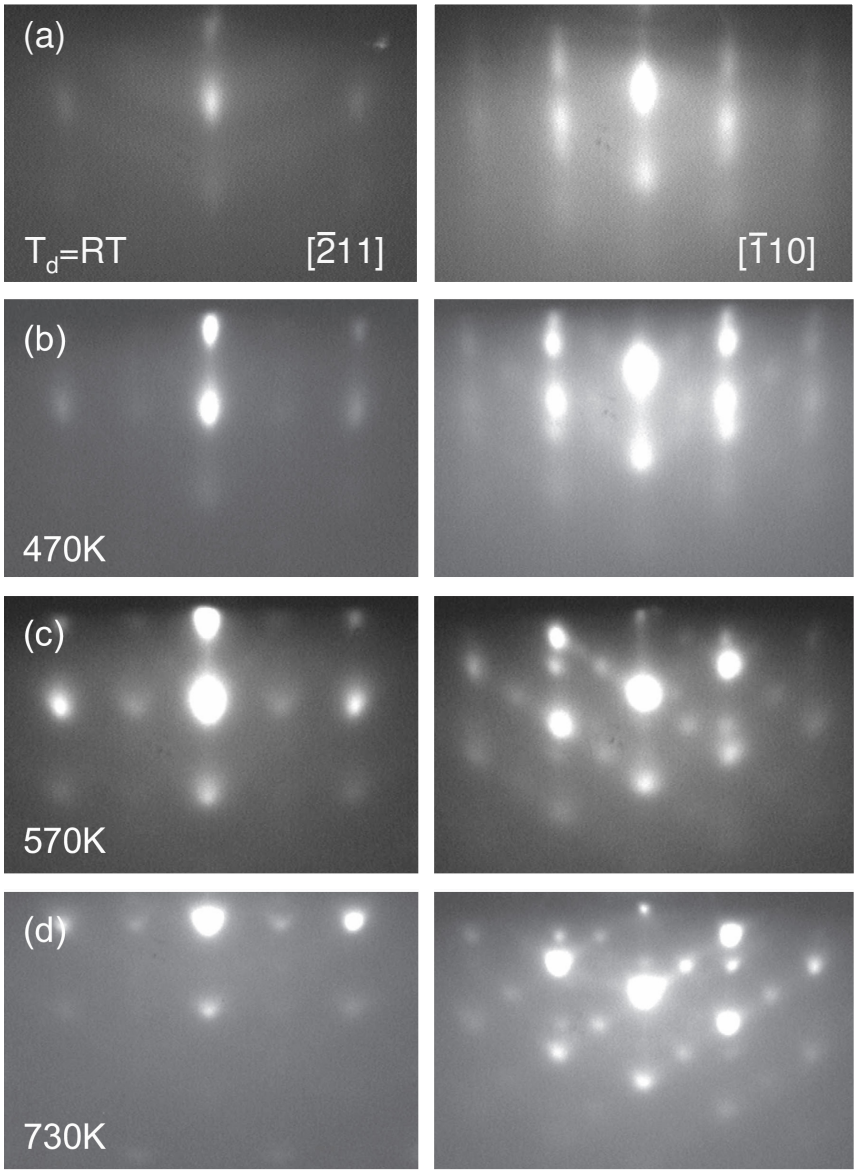

Figure 5.1: RHEED patterns along the [-211] and [-110] azimuths of 3 nm thick CoPt on $WSe_2(0001)$ for different deposition temperatures: (a) RT, (b) 470, (c) 570 and (d) 730 K.

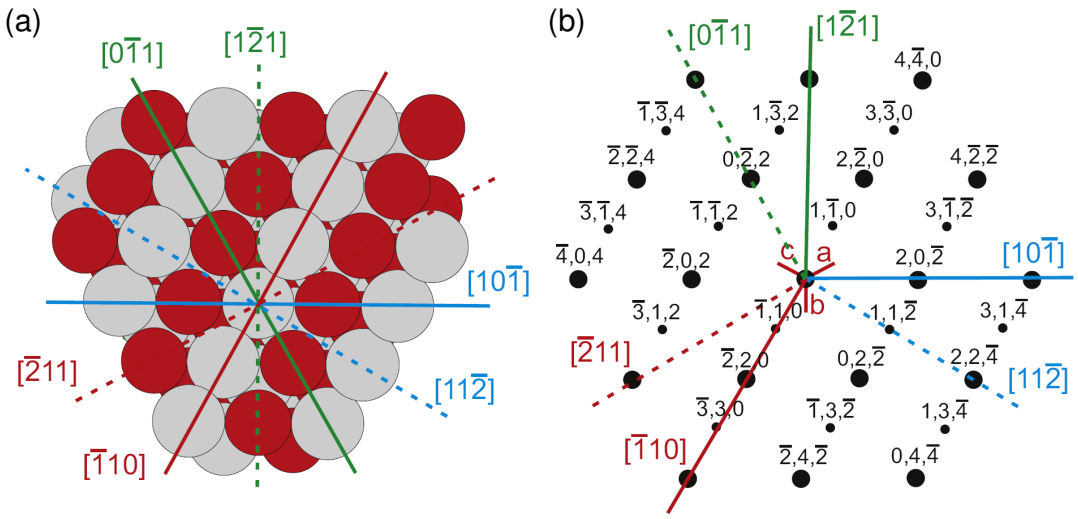

Figure 5.2: (a) Schematic view of the (111) plane of the one variant of the $L1_0$ phase formed with the tetragonal axis along [001]; and (b) the reciprocal plane corresponding to the [111] zone axis.

indicate the onset of $L1_0$-type chemical order in the CoPt(111) alloy. Since CoPt grains grow along the [111] direction, the three $< 001 >$ directions, 54°-tilted with respect to the normal direction, are the potential growth directions for the tetragonal *c*-axis of the $L1_0$ phase. The arrangement of atoms in the (111) plane of one variant is schematized in figure 5.2(a) and the reciprocal plane corresponding to the [111] zone axis is presented in figure 5.2(b). Using the software package CaRIne [109], the reflection pattern in figure 5.1(d) was simulated taking into account the presence of three variants (figure 5.3). Figure 5.3(a,b) shows the diffraction patterns of these three variants along the [-110] and [-211] directions, which are defined with respect to the variant presented in figure 5.2(a). It is important to point out that in both directions the superstructure spots can be produced by only one variant. The superimposition of the three reciprocal planes associated with the three variants is presented for the two main direction [-211] and [-110] in figure 5.3(c,d).

The comparison with figure 5.2(a) shows that the twinning effect also has to be considered, as depicted in figure 5.4 However, superstructure spots of the associated twin phase are not observed in the RHEED images (figure 5.1(c, d)). This can be explained either by the weak intensities of the fundamental spots related to the twin, or by the weak twinning of the variant, which gives rise to the superstructure spots, as shown in figure 5.3. The latter is a peculiar feature of the $L1_0$ phase. The nearest neighbor distance in the (111) plane extracted from the RHEED patterns is equal to 2.68Å, a value which is very close to the homoatomic and heteroatomic nearest pair distances of 2.69 and 2.65Å, respectively, found in the bulk $L1_0$-CoPt(111) phase.

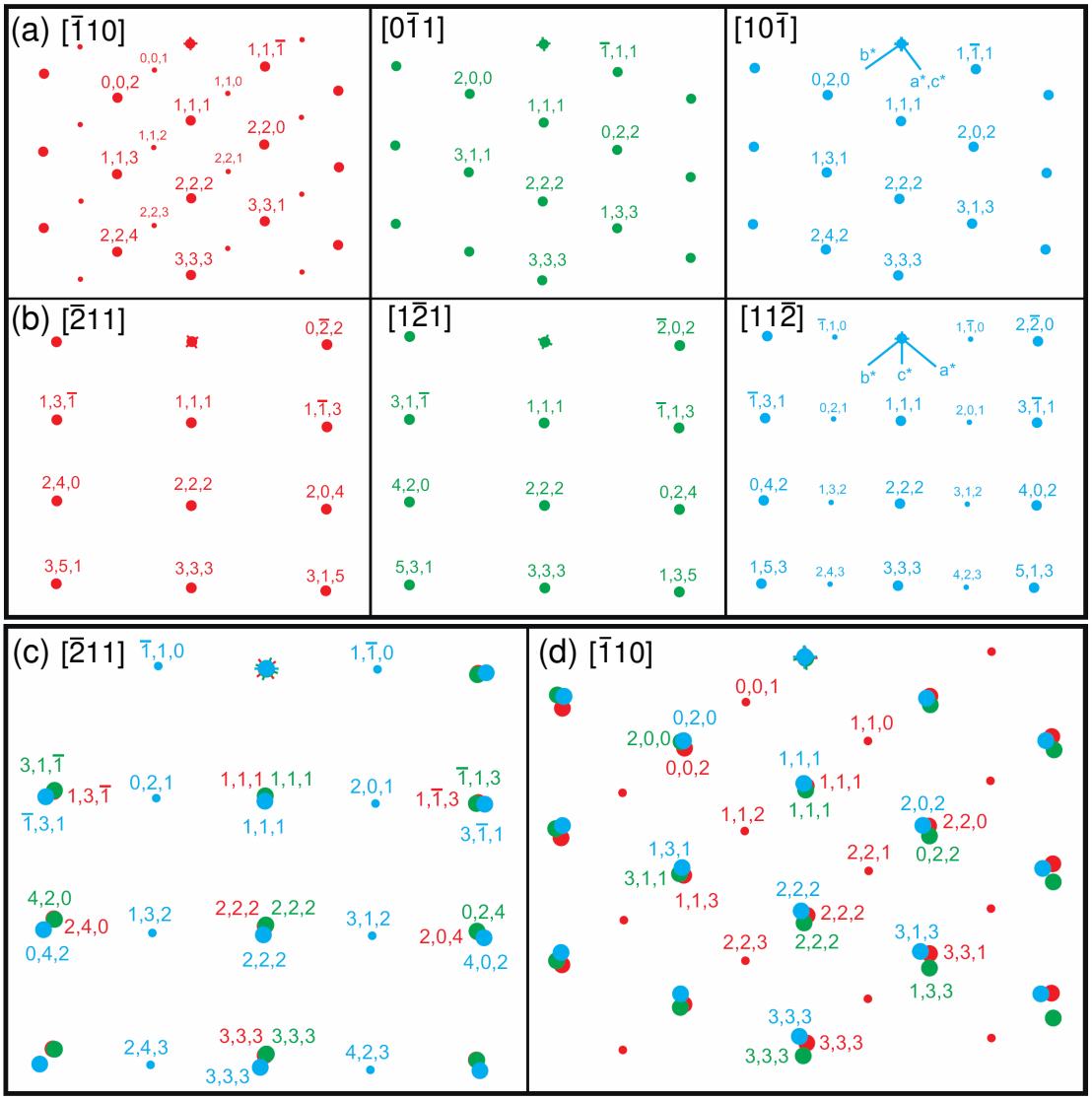

Figure 5.3: The intensity contribution of the diffraction pattern of each of the three variants along the chosen azimuths (a) [-110] and (b) [-210 1] directions. The definition of the directions is given with respect to the variant presented in figure 5.2(a). (c, d) The superimposition of the reflections coming from the three variants. The segments a*, b*, c* correspond to the projections of the primitive vectors of the reciprocal lattice.

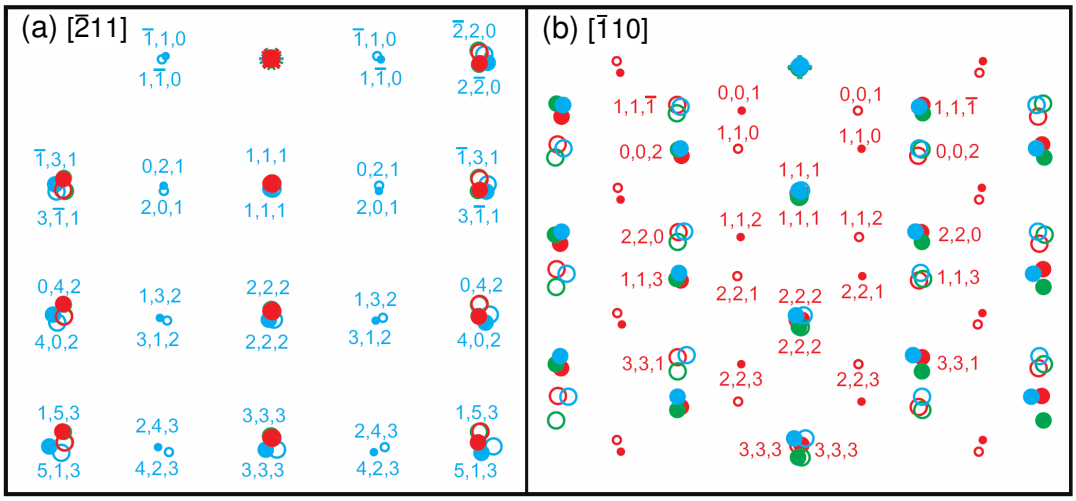

Figure 5.4: The calculated diffraction pattern obtained from the superimposition of the reflections coming from the three variants and their twins of the $L1_0$ phase grown along the [111] direction.

5.1.2 Long-range $L1_0$-type chemical ordering

To determinate the lattice parameters, chemical composition and the degree of the $L1_0$-type chemical ordering, X-ray diffraction measurements in symmetric and asymmetric reflection geometries were performed. Figure 5.5 summarizes the results of the CoPt deposits grown at 730 K. Figure 5.5(a,b) shows $\theta/2\theta$ scans around the 111 and 222 reflections of CoPt, which are close to the substrate peaks. Only the 222 reflection can be separated from the 0012 substrate peak by a two-Gaussian fit. The position of the 222 CoPt peak leads to a spacing of the 222 planes equal to 1.088 Å, which is between the values of the $L1_0$-type ordered (1.087 Å) and fcc disordered (1.090 Å) bulk phase. It full width at half maximum leads to a normal coherence length equal to 6.5nm. Figure 5.5(cf) shows the $\theta - \alpha/2\theta$ scans around the 112 and 113 reflections and their corresponding rocking curves: α represents the angle between the 111 and 112 (or 113) reflections. However, a separation of the 113 reflection from the 311 and 131 reflections is not possible due to the existence of the three variants independently of the twinning effect. In order to calculate the chemical order parameter, the integrated intensities around the 113 fundamental reflections are divided by 3. Note, that this assumes the same formation probability and the same degree of long-range order for the three variants as the 112 and 113 reflections were not measured for the two other variants accessible by rotating the sample with respect to [111] axis. The integrated intensities are corrected for absorption and Lorentz factors taking into account the width of the rocking curves, as described in par 2.2.3. For CoPt grown at 730K, the ratio between the 113 and 112 intensities leads to a chemical order parameter, S, of 0.35±0.05, which is close to the value reported in [117].

The a and c lattice parameters of the tetragonal phase are deduced from the peak

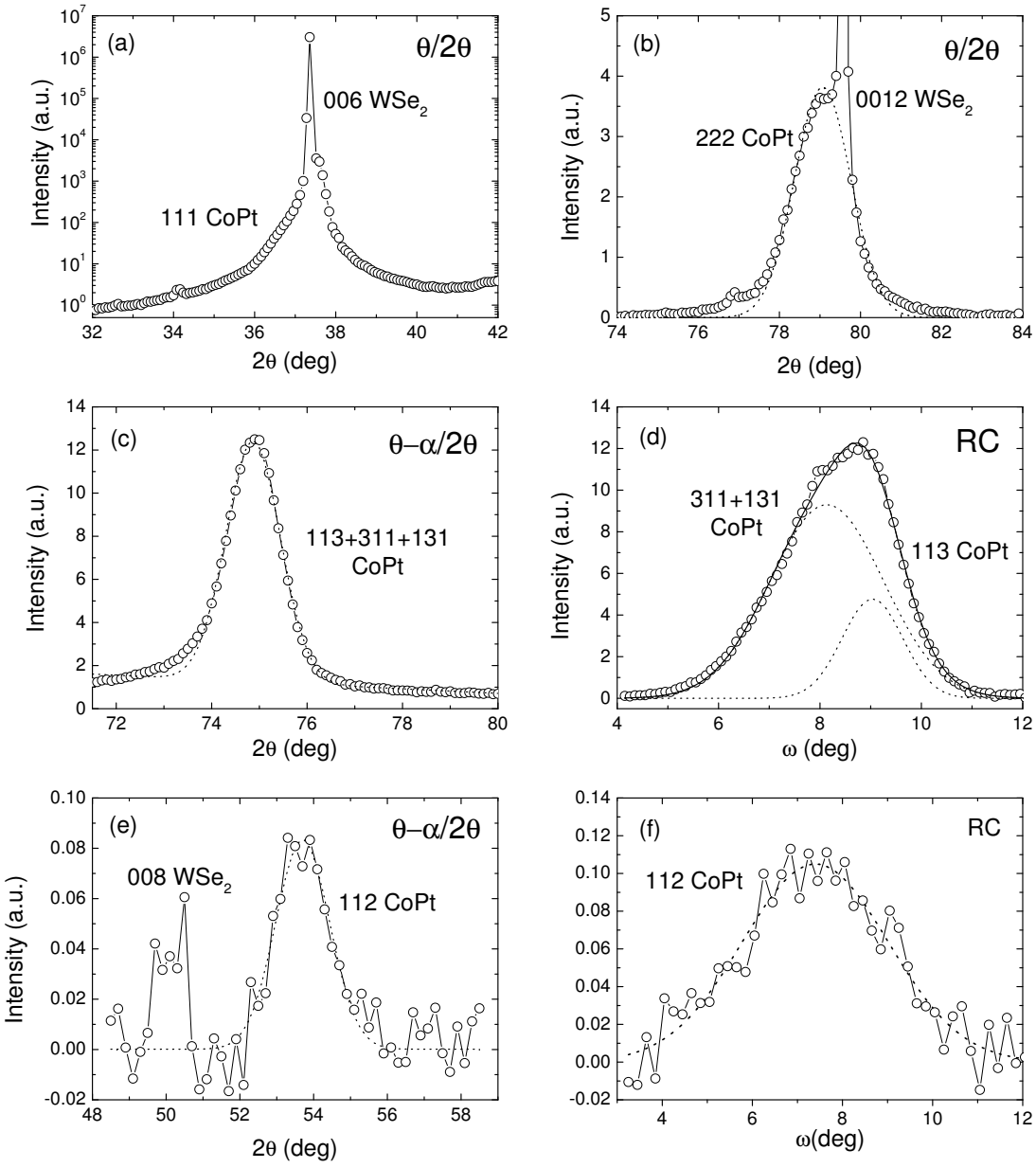

Figure 5.5: XRD measurements in symmetric and asymmetric reflection geometries carried out on CoPt(111) film grown at 730 K. $\theta/2\theta$ scans around (a) 111 and (b) 222 reflections of CoPt(111). $\theta - \alpha/2\theta$ scans and corresponding rocking curves around 113 (c, d) and 112 (e, f) reflections of CoPt(111). α represents the angle between the [111] and [113] (or [112]) directions. Note that the three-index notation is used to identify reflections coming from the substrate and nanostructures.

positions of the 222 and 112 reflections, since the 113 reflection while more intense is mixed with the 311 and 131 reflections. As expected for a low degree of ordering, a reduced tetragonality ratio is found (a=3.78 Å and c=3.75 Å) compared to that in the fully ordered phase (a=3.806 Å and c=3.684 Å). For the film prepared at 570K the same degree of the chemical ordering of 0.35±0.05 was estimated. It is expected, that the segregation of Se at elevated temperatures during deposition of CoPt on WSe_2(0001) and surface disorder effects associated with a large surface-to-volume ratio might limit the long-range order. The same effect was observed for the $CoPt_3$ alloy grown on WSe_2, where the maximum value for the ordering parameter was found to be ∼0.65 at the wide temperature range of 470-870 K. For the CoPt film grown at 470K, the width of the 222 reflection leads to a normal coherence length of about 4 nm. Unfortunately, the average long-range chemical order parameter could not be determined for the sample, because the 112 reflection could not be detected by X-ray diffraction.

5.2 Short-range ordering

The 3nm-thick of $Co_{55}Pt_{45}$, prepared at 300 and 700 K on WSe_2(0001), were investigated by EXAFS. The measurements were collected at Co K-edge on BM30 beamline at the ESRF, in fluorescent mode, with beam polarization in the film plane (∥ polarization) and out of film plane (⊥ polarization).

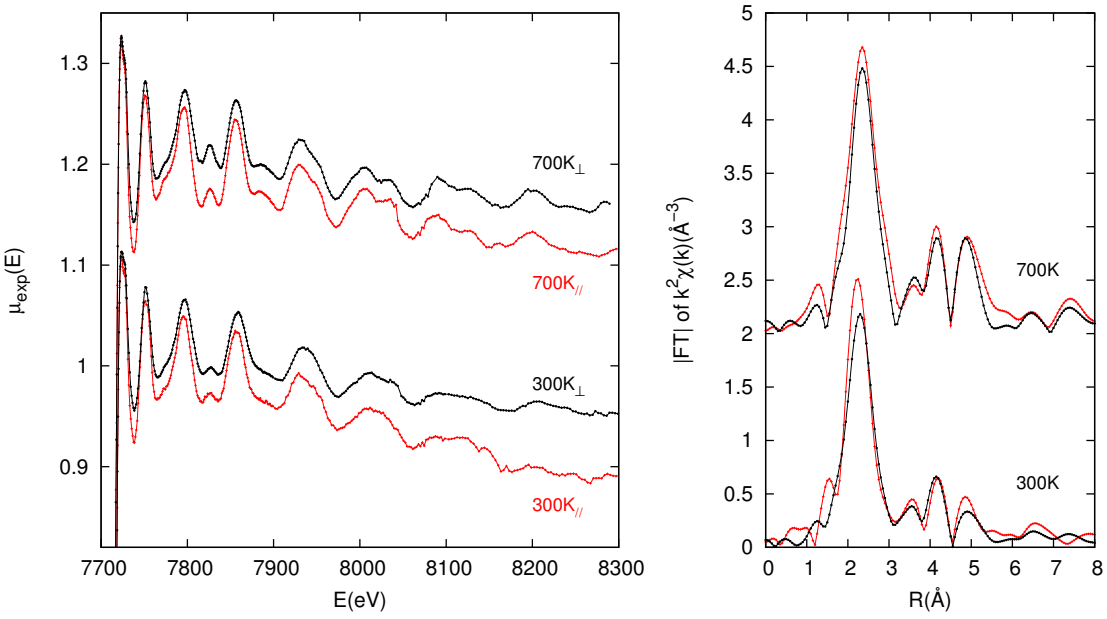

Figure 5.6: Left: experimental x-ray absorption spectra of the three $Co_{55}Pt_{45}$ films deposited on WSe_2(0001) at 300 and 700K for in-plane (∥) and out-of plane (⊥) polarizations. Right: moduli of Fourier transform (|FT|) of the experimental and simulated $k^2\chi(k)$ spectra (k-range: 4-12Å^{-1}) for the two geometries: ∥ (red lines) and ⊥ (black lines). The curves are shifted for clarity.

						Geometry			
Signal	Length (R)	N_{tot}	Scatterer(s)	N^{out}	N^{in}	$\tilde{N}_{\perp}^{out}$	$\tilde{N}_{\perp}^{in}$	$\tilde{N}_{\parallel}^{out}$	$\tilde{N}_{\parallel}^{in}$
SS_1	$a/\sqrt{2}$	12	Pt_1	4	4	8	0	2	6
			Co_1	2	2	4	0	1	3

Table 5.1: Single-scattering (SS) signals used in the calculated XAFS spectrum of the $L1_0$ ordered CoPt $L1_0$ structure. N^{in} is the number of independent paths per absorbing atoms occurring strictly in the (111) plane while N^{out} is the number of paths out of the (111) plane. On the right side, $\tilde{N}_{\perp}^{in}(_{\parallel})$ is the effective number of in-plane contributions observed in perpendicular (parallel) polarization geometry, and $\tilde{N}_{\perp}^{out}(_{\parallel})$ is the effective number of out-of plane contributions observed in perpendicular (parallel) geometry.

5.2.1 EXAFS data analysis

Figure 5.6 reports the experimental spectra for the $Co_{55}Pt_{45}$ series and their k^2-weighted |FT|s calculated in the k-range 4-12 $Å^{-1}$. The integrated intensity of fourth peak, around 5 Å, for the sample prepared at RT constitutes only 8% of the |FT| signal. In this case, the use of all single and multiple scattering contributions MS_4, as it was done for $CoPt_3$ alloys, is not appropriate for the analysis, because the fitting would get the MS_4 signals in anti-phase in order to cancel each other out to minimize their contributions. Since the first shell represents the main contribution to the signal (∼70%), in order to avoid fitting artifacts, the analysis was performed only on the experimental signals filtered at the first coordination shell. For this purpose, the Back Fourier Transform (BFT) of the |FT| was calculated around the first peak, between 1 and 3.2 Å, for each spectrum.

The in- and out-of-plane correlations in the $L1_0$ structure are indicated in the lower panel of figure 5.7 and are defined with respect to the (111) plane containing the Co absorbing atom (Co_0). In table 5.1 are reported the corresponding effective number for the two polarizations. Restricting the XAFS analysis to the two single scattering Co_0-Co_1 and Co_0-Pt_1, the number of the free structural parameters during the fitting is reduced to five, that are the fraction of Co atoms which occupy the sites, the length of the path and the Debye-Waller factor for each pair.

5.2.2 Results and discussion

Figure 5.8 shows the BFT with the best fits (on the left) and their |FT|s (on the right). The structural parameters are reported in table 5.9. An anisotropy is observed in the sample prepared at RT, where the Co-Co correlations correspond to 42% of the in-plane contributions and 30% of the out-of-plane ones. This is amplified by the lower Debye-Waller factor observed for the in-plane Co-Co correlations. The anisotropy disappears for the sample deposited at 700 K, where a local order very close to the $L1_0$ structure is obtained. No noticeable differences between in-plane and out-of-plane distances are obtained.

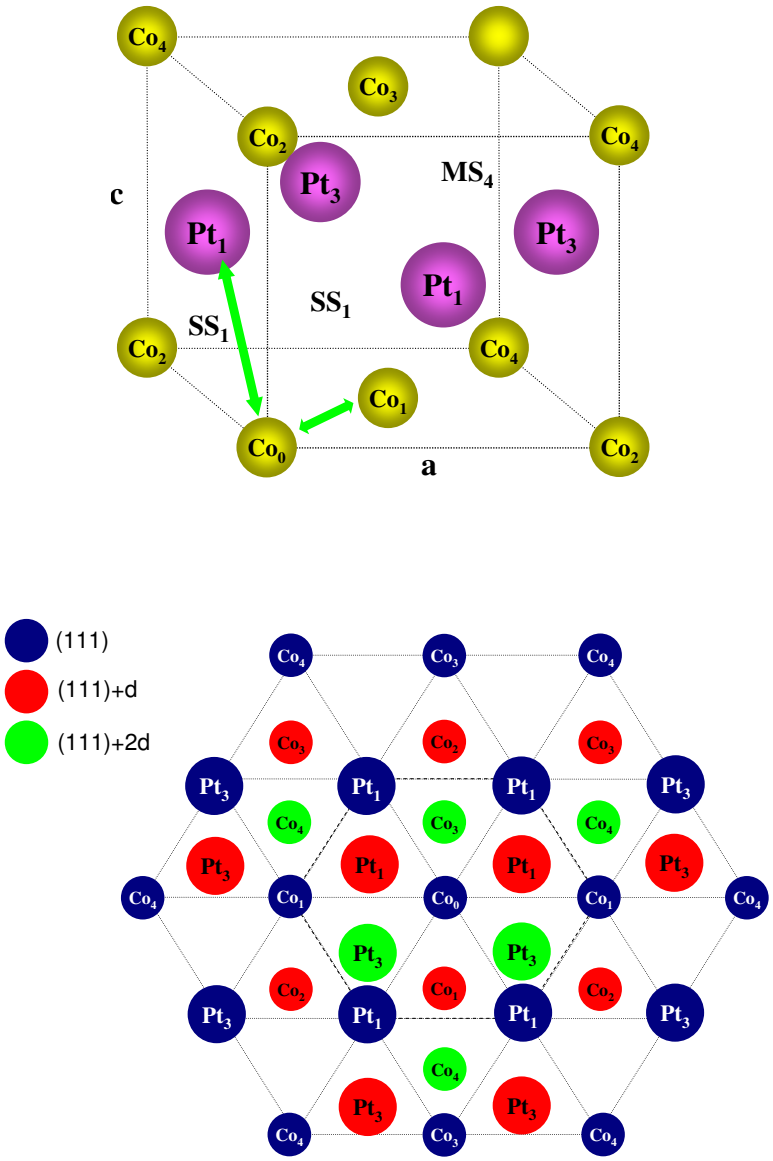

Figure 5.7: Upper panel: schematic view of the $L1_0$ ordered structure showing the scattering paths used in the fitting between absorbing atom Co_0 and the ith neighbourds, Co_i and Pt_i. Lower panel: atoms in the (111) plane (blue circles) and in the upper planes $+d_{111}$ (red circles) and $+2d_{111}$ (green circles)

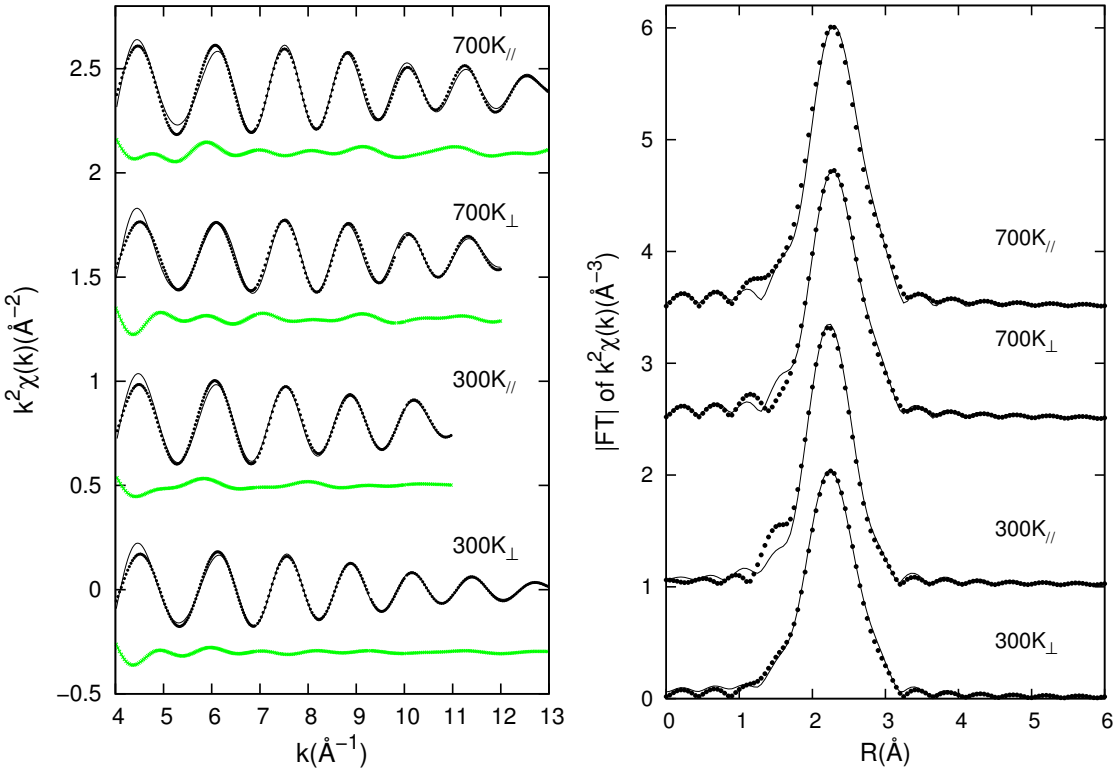

Figure 5.8: On the left, BFT of experimental (dots) and best fitted (solid lines) $k^2\chi(k)$ for the two films $Co_{55}Pt_{45}$ grown on $WSe_2(0001)$ at 300, and 700K for in-plane ($\|$) and out-of plane ($\perp$) polarizations. For each fit the residual $k^2\chi(k)_{exp} - k^2\chi(k)_{fit}$ is shown by green lines. On the right, experimental (dots) and best fitted (solid lines) |FT| curves for in-plane ($\|$) and out-of plane ($\perp$) polarizations (k-range: 4-11Å^{-1}).

		Out-of-plane polarization			In-plane polarization						
Signal	Scatters	$\tilde{N}^j_\perp$	R_j (Å)	$\sigma^2_j(10^3Å^2)$	$\tilde{N}^j_\|$	R_j (Å)	$\sigma^2_j(10^3Å^2)$	N^{out}	N^{in}	n^{out}	n^{in}
$Co_{55}Pt_{45}$ at 300K											
SS_1	Pt_1	8.4(2)	2.62(1)	0.68(1)	7.4(2)	2.60(1)	0.63(1)	4.2(5)	3.5(5)	0.70(1)	0.58(1)
	Co_1	3.6(1)	2.60(1)	0.67(1)	4.6(1)	2.61(1)	0.44(1)	1.8(5)	2.5(5)	0.30(1)	0.42(1)
$Co_{55}Pt_{45}$ at 700K											
SS_1	Pt_1	8.4(2)	2.64(1)	0.46(1)	8.4(2)	2.66(1)	0.42(1)	4.2(5)	4.2(5)	0.70(1)	0.70(1)
	Co_1	3.6(1)	2.64(1)	0.62(1)	3.6(1)	2.63(1)	0.63(1)	1.8(5)	1.8(5)	0.30(1)	0.30(1)

Figure 5.9: Structural parameters corresponding to the best fits of $Co_{55}Pt_{45}$ grown on $WSe_2(0001)$. The effective numbers of independent paths($\tilde{N}^j$), the path lengths (R_j) and the Debye-Waller factors (σ^2_j) are reported for both polarization. The total numbers of the independent paths (N^{in} and N^{out}) in and out of the (111) plane are calculated from the effective contributions observed in parallel and perpendicular geometry. n^{out} (n^{in}) are the concentrations of each element in the first coordination shell, located out-of-plane (in-plane) containing the Co absorbing atom.

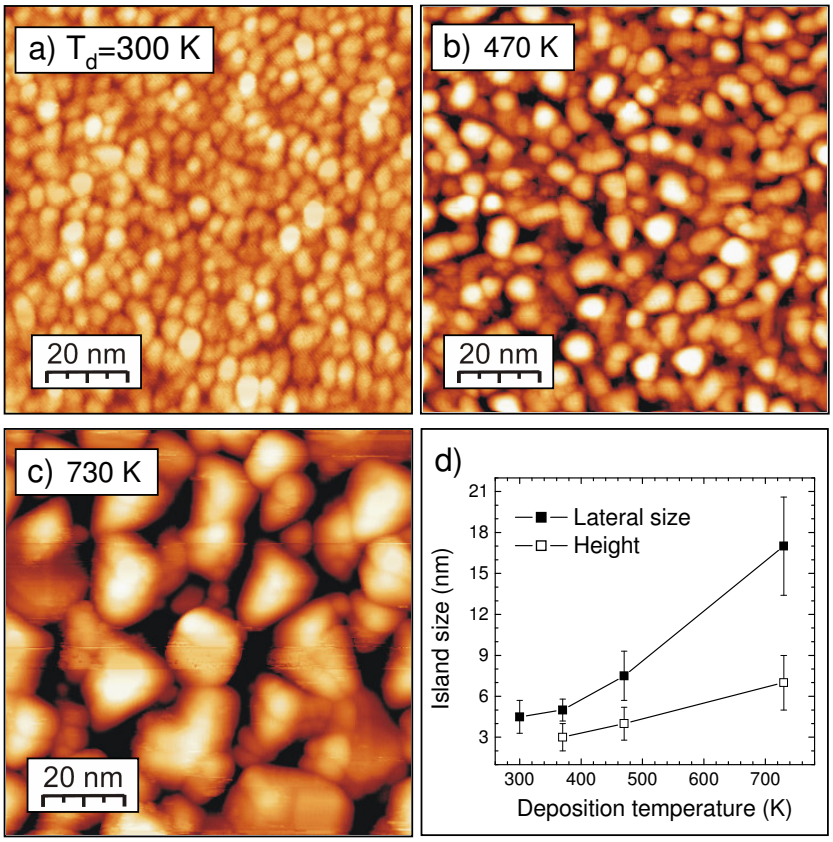

Figure 5.10: Series of STM topographic images taken after the deposition of 3 nm-thick CoPt films on WSe_2(0001) at various growth temperatures: (a) 300 K, (b) 470 K, and (c) 730 K. (d) Grain's mean lateral size as a function of deposition temperature.

5.3 Morphology characterization

5.3.1 STM study of 3 nm CoPt deposits on WSe_2(0001)

Scanning tunneling microscopy observations were performed in 3nm-thick CoPt alloys deposited at different temperatures. Consistent with the RHEED patterns, STM images reveal the formation of the three-dimensional islands at all deposition temperatures. The lateral size, height, and shape of the individual grains strongly depend on the deposition temperature as shown in figure 5.10(a-c). The increase in the lateral size and height of the individual CoPt islands with deposition temperature is summarized in figure 5.10(d); the height values are consistent with the normal coherence length calculated from the 222 reflections. The increase in island size is accompanied with a change in the grain shape due to the $L1_0$ chemical ordering which leads to a modification of the composition of the (001) side wall facets, becoming alternatively pure Co, pure Pt planes. Note that there is neither composition change in the (111) planes, nor in the (100) and (010) planes having all the equiatomic composition. At room temperature a more rounded and even hexagonal shape

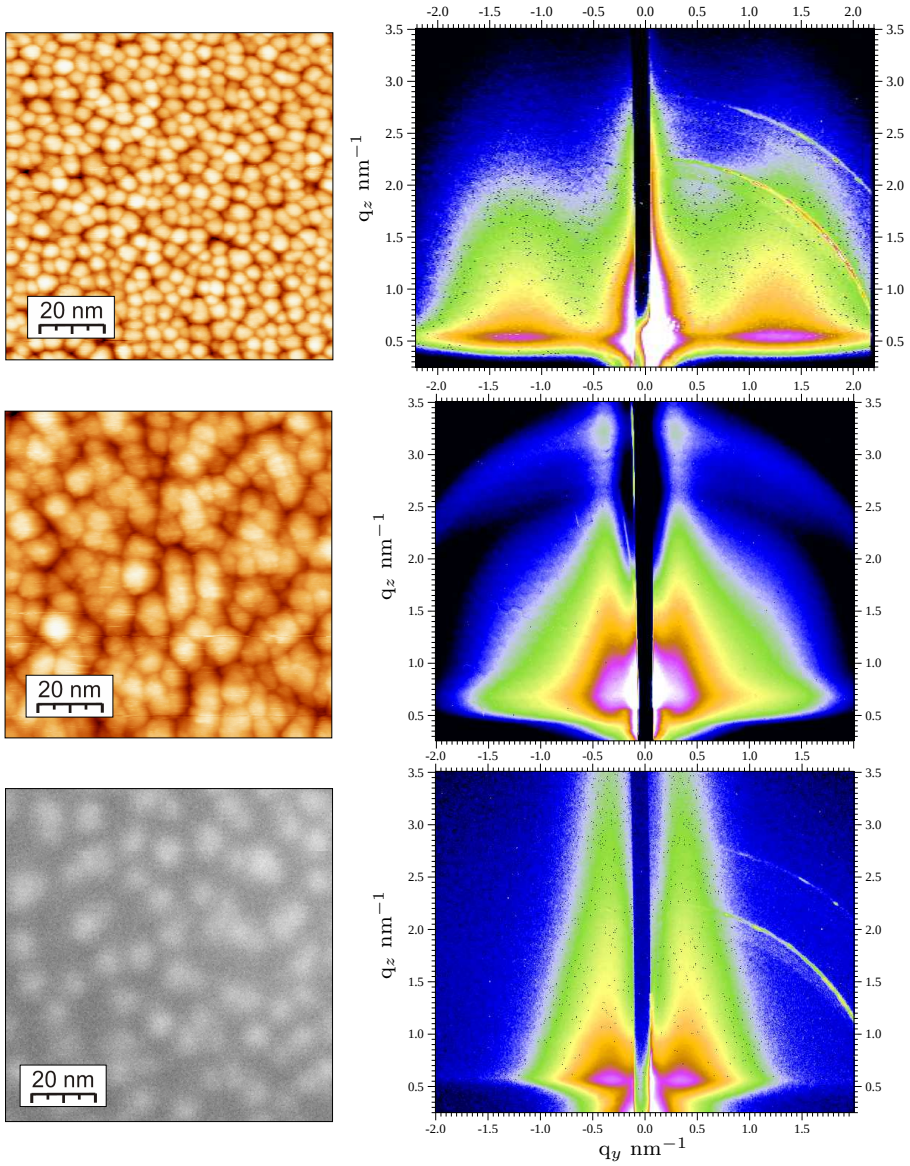

Figure 5.11: Best experimental GISAXS patterns compared with microscopy images for 1.0 nm thick CoPt grown at 300 (a), 570 (b) and 700K (c).

of the grain is obtained, while at 730K a tendency towards a more triangular shape is found. The triangular islands in figure 5.10(c) contain grain boundaries, that are attributed either to the existence of the three variants in the same island or more likely to the coalescence of several islands of different variants, since the equivalent side-wall facets 111 or 001 are differently decorated with respect to the [111] growth direction for $L1_0$ nanostructures. Note, that for $CrPt_3(111)$ islands, adopting the $L1_2$ structure [62] such grain boundaries were not observed.

GISAXS										
CoPt		Guinier plot		Quantitative analysis with LMA and 1DDL						
ϵ	T	$2R_s$	H	L	σ_L	H	σ_H	H/L	D	w
(nm)	(K)	(nm)	(nm)	(nm)	(nm)	(nm)	(nm)		(nm)	(nm)
1	300	2.8	1.9	2.0(3)	2.0*(1)	0.7(2)	0.8(2)	0.35(2)	3.2(5)	1.7(2)
1	570	7.9	1.8							
1	700	9.0	2.6	6.4(3)	2.0(1)	0.6(1)	1.8(2)	0.10(1)	13.5(3)	5(1)

STM - FESEM							
ϵ	T	L	σ_L	H	σ_H	H/L	z
(nm)	(K)	(nm)	(nm)	(nm)	(nm)		(nm)
1	300	5.0(1)	2.17(3)	1.3(1)-2.25(2)	0.5(1)-0.65(2)		0.0
		2.14(5)	2.9(1)	0.32(2)	0.46(1)		1.9
1	570	7.7(1)	6.8(2)	1.05(7)	1.22(5)	0.14()	0.0
		3.0(1)	8.2(2)	0.25(1)	0.68(3)		2.0
1	700**	7.31(7)	2.6(2)				

Table 5.2: On the top: results obtained from the GISAXS patterns analysis with the Guinier plot and the local monodisperse approximation (LMA) with a Gaussian (* Log-normal) distribution function. L and σ_L, average and width of lateral size distribution; H, and σ_H, average and width of height distribution; D and w, first neighbor peak and width of the gaussian distribution of 1DDL interference function. On the bottom: results obtained from the STM and (**)FESEM images. The STM and FESEM lateral size is the diameter of a disk of equivalent surface. A Gaussian distribution is used with a parameter σ

.

5.3.2 STM and GISAXS study of 1 nm CoPt grown on WSe_2(0001)

The morphology of 1nm thick CoPt deposited at 300, 570 and 700 K was studied by STM and GISAXS techniques. However for the 700K CoPt sample since no satisfying STM images could be recorded, FESEM observations were done on this sample. The best experimental GISAXS patterns and the STM and FESEM images are reported for the three samples in figure 5.11.

In all GISAXS patterns the scattering lobes are visible along the parallel direction and they became narrower, closer to the specular beam and higher when the deposition temperature increases. It corresponds to an increase in particle size, confirmed by STM (figure 5.11(a,b)) or FESEM (figure 5.11(c)) images, and a decrease in height and island density. The scattering ring observed in the 570 K pattern cames from the kapton window mounted at the exit of the GISAXS chamber to ensure a pressure of 10^{-6}mbar.

The detailed analysis of the STM or FESEM images and GISAXS patterns is described in the following paragraphs, all extracted parameters are summarized in table 5.2.

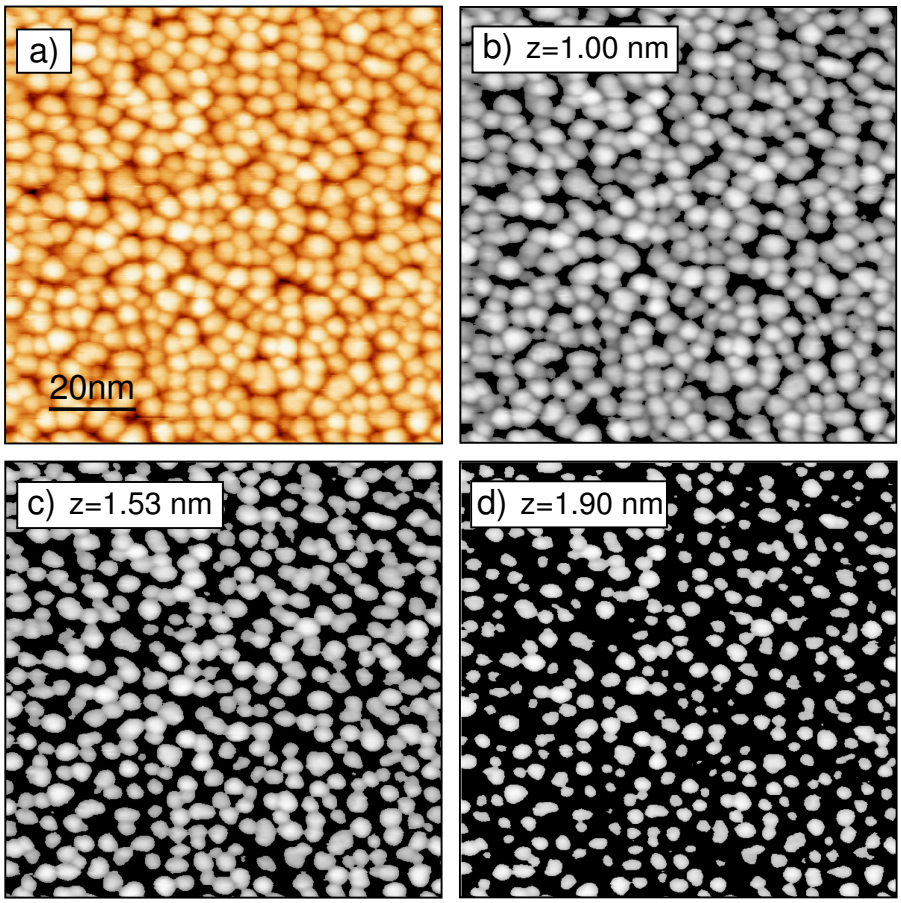

Figure 5.12: STM images of the sample prepared at 300 K original (a) and after a flooding process at z level equal to 1.00 nm (b), 1.53 nm (c) and 1.9 nm (d).

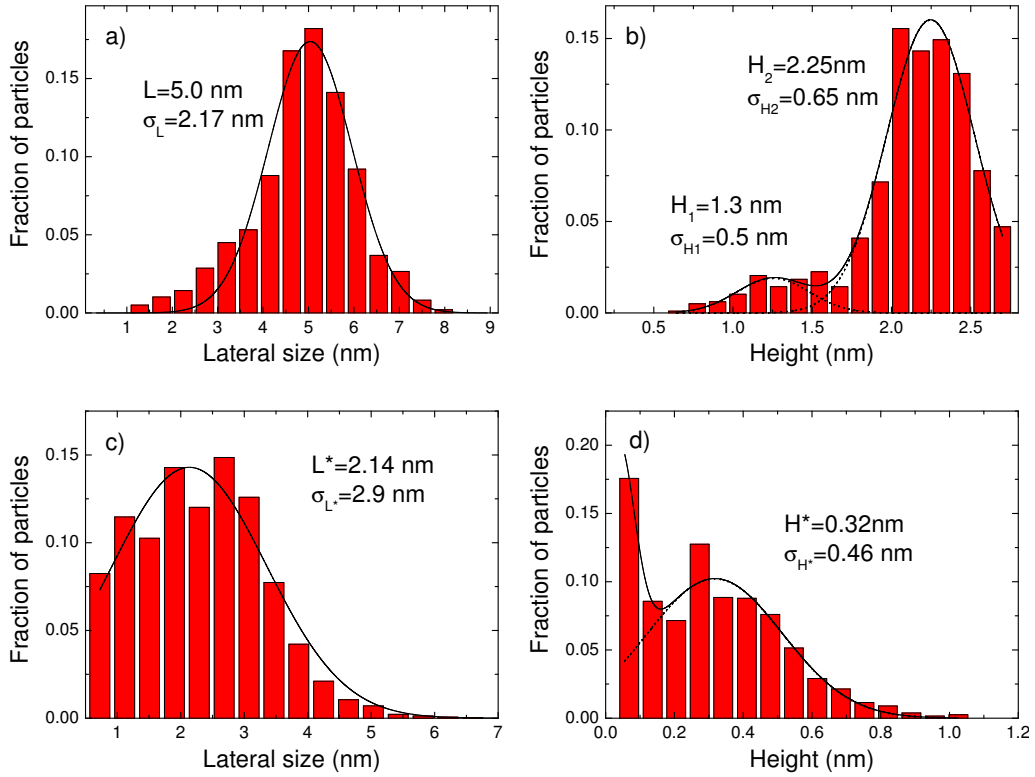

Figure 5.13: The lateral size (a) and the height (b) distributions calculated for the image (figure 5.12(a)) corresponding to the deposition temperatures 300 K; c) and d) the lateral size and height distribution recalculated for z=1.9nm (figure 5.12(d)). The red lines are the corresponding Gaussian fits of distributions.

• 1 nm CoPt grown on WSe_2(0001) at 300 K

STM analysis Figure 5.12(a) shows the original STM image of a very dense assembly of CoPt nanoparticles with a lateral size distribution (figure 5.13(a)) centred around 5 nm and with a width σ_L=2.2 narrower than that observed for the $CoPt_3/WSe_2$(0001) grown at the same temperature(σ_L=2.5). The particles can be described by two height distributions: the lowest particles are characterized by an average height H_1=(1.3±0.1)nm and a width σ_{H1}=(0.5±0.2)nm, while the tallest ones are characterized by H_2=(2.25±0.02)nm and a width σ_{H2}=(0.65±0.02)nm (figure 5.13(b)).

The morphology of particles was studied using the flooding method. The cuts of the image 5.12(a) obtained at different z values are reported in figure 5.12(c-d). Most of the particles touch neighbour particles until about z <1.5 nm and seem to be completely separated from z ∼1.9 nm. However, due to the tip resolution separation height deduced by the flooding analysis is overestimated. At this value, the lowest particles disappear and the tallest ones are characterized by a lateral size distribution centred around (2.14±0.05)nm and a width of (2.9±0.1)nm (figure 5.13(c)).

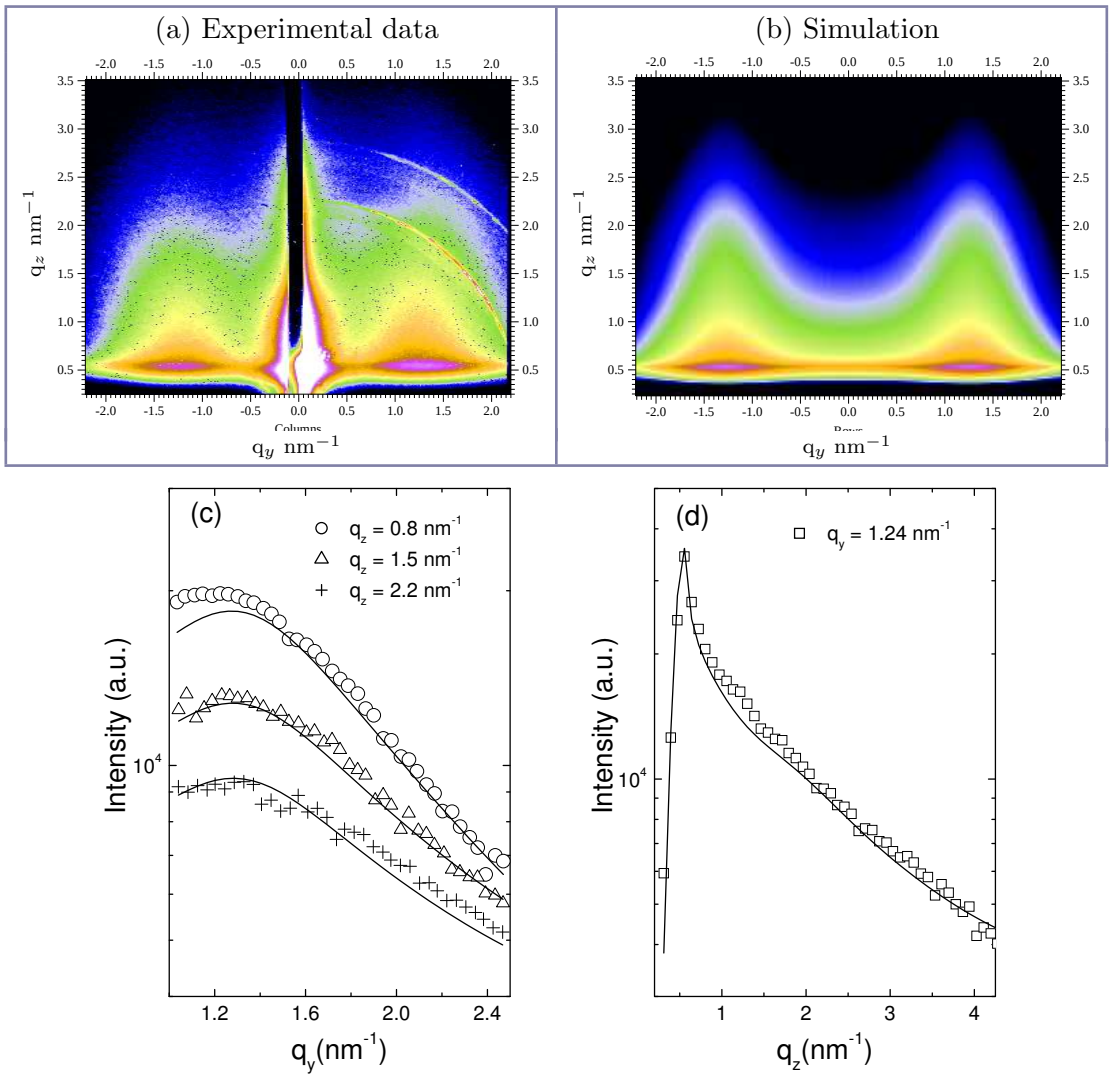

Figure 5.14: (a) 2D GISAXS experimental intensity for a 1.0 nm thick CoPt(111)/WSe_2(0001) deposit at 300 K. (b) Simulated GISAXS pattern. The intensity is represented with a logarithmic scale. (c) Cuts of the experimental pattern parallel to the surface, at $q_z = 0.8$ (open circles), $q_z = 1.5$ (open triangles) and $q_z = 2.2$ (crosses); (d) cuts of the experimental pattern perpendicular to the surface, at $q_y = 1.24^{-1}$ (open squares); continuous lines: best fit of the experimental cut.

GISAXS analysis More statistical information can be obtained for the GISAXS analysis, where fitting of several horizontal and vertical cuts was done simultaneously using the *IsGISAXS* program. The Distorted Wave Born Approximation (DWBA) and the Local Mono-disperse Approximation (LMA) were introduced. The best fit of the experimental cuts is obtained by using the form factor of the truncated cone with a base angle of 61°. Using the structural parameters, extracted from the fitting of the four cuts and summarized in table 5.2, the corresponding simulated GISAXS pattern is shown in figure 5.14. Except for the region close to the reflected beam, where an off-specular scattering coming from the WSe_2 substrate is measured, a good agreement is obtained.

Furthermore, based on the GISAXS parameters and taking into account the apex of the STM tip deduced from model systems, the accessible depth probed by the STM tip was recalculated about 0.35 nm.

Assuming a particle density equal to $1/D^2$, the deposit thickness recalculated from the extracted structural parameters would be equal to 0.2 nm, a value smaller than the real thickness (1 nm). A possible interpretation of these results is shown in figure 5.15. The 1 nm thick CoPt deposit can be considered as formed by two distinct regions: a continuous film made of merged part of the nanoparticles producing no scattering contrast (hatched region in figure 5.15) and separated islands constituted by the upper part of nanoparticles (white island in figure 5.15). The upper parts are indeed the scattering objects detected by GISAXS. Such morphology can explain the small size of CoPt particles obtained by GISAXS and could hold also for the 1 nm thick $CoPt_3$ deposit on $WSe_2(0001)$ at 300K.

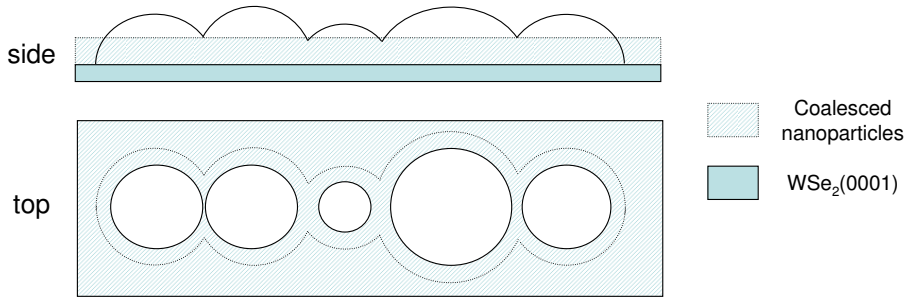

Figure 5.15: Schematic representation of lateral and top views of a 1D array of self-assembled coalesced nanoparticles.

• 1 nm CoPt grown on $WSe_2(0001)$ at 570 K

The particles observed by STM are characterized by a broad lateral size distribution centred around (7.7±0.1) nm as well as by a broad height distribution centred around (1.05±0.07) nm (figure 5.17(a,b)). These parameters give an aspect ratio equals to 0.14, significant smaller than the value obtained for $CoPt_3$ nanoparticles grown at 570K equal to 0.43. At z <0.88 nm the particles are arranged in groups of ten particles. At z=1.8 nm the deposit appears to be formed by isolated small particles and groups of few particles. These groups are completely separated at z=2 nm, while the smallest particles have disappeared. These features were already observed, somewhat more marked, in the 1nm thick $CoPt_3$ deposit at 570K.

The GISAXS pattern of the 570 K sample (figure 5.11(b)) was analysed by Guinier plots for two cuts along the parallel q_y and perpendicular q_z direction, as reported in figure 5.18. The slope on the steepest part of the Guinier plots lead to estimates of the average lateral size equal to 7.2 nm and the average height equal to 1.6 nm, corresponding to an aspect ratio equal to 0.22.

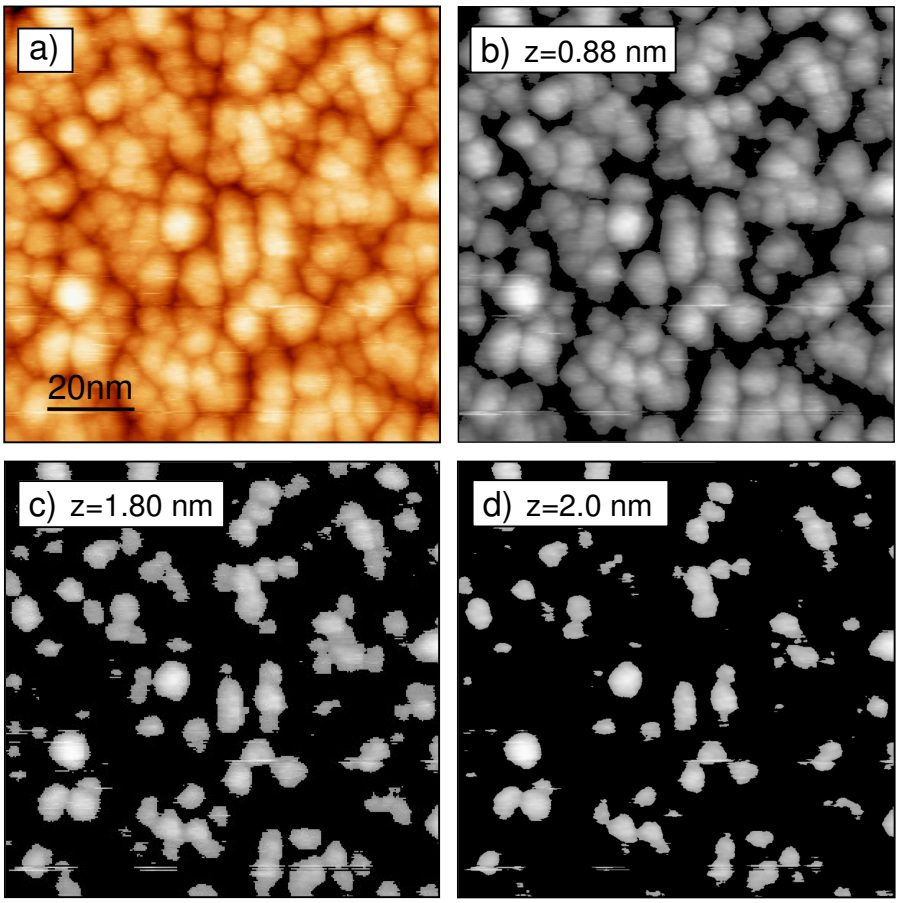

Figure 5.16: STM images of the sample prepared at 570 K original (a) and after a flooding cut at z level equal to 0.88 nm (b), 1.8 nm (c) and 2.0 nm (d).

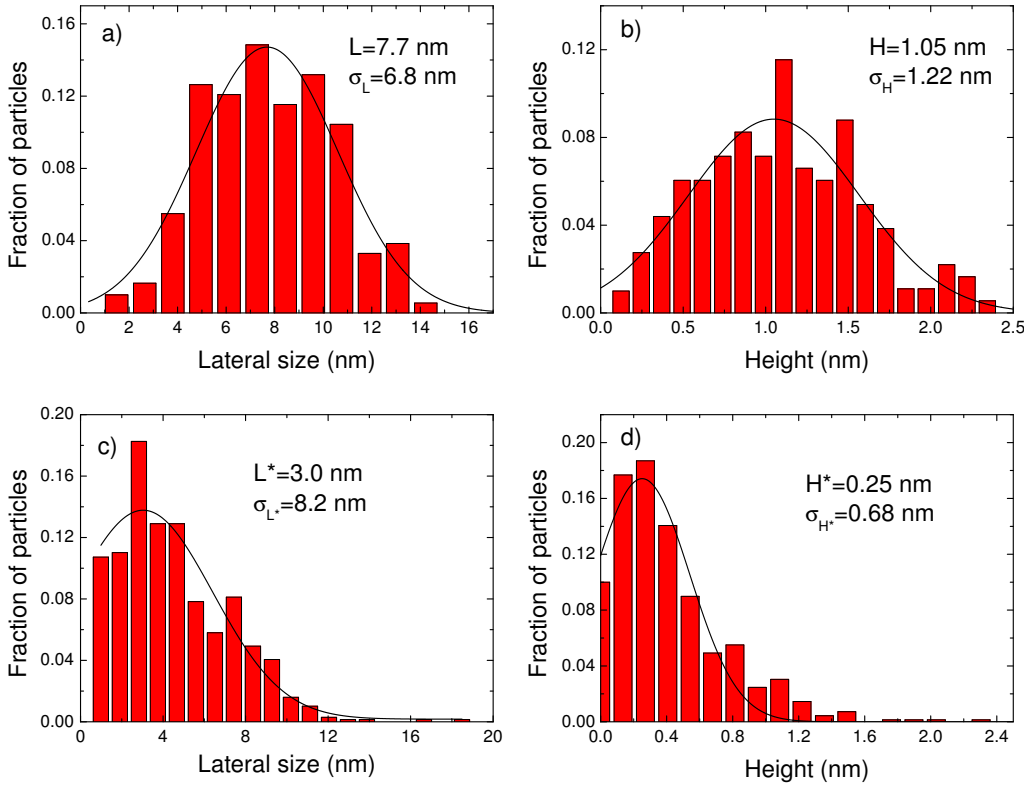

Figure 5.17: The lateral size (a) and height (b) distributions calculated for the image corresponding to the deposition temperatures 570 K (figure 5.16(a)); (c) and (d) the lateral size and height distribution recalculated for z=2.0nm (figure 5.16(d)). The red lines are the corresponding Gaussian fits of distributions.

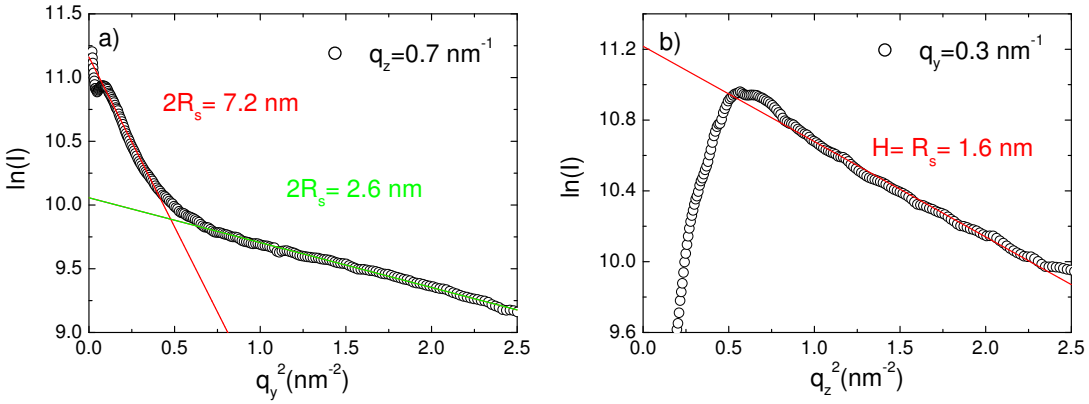

Figure 5.18: Open circles: 1D cuts parallel to q_y and q_z directions from 2D GISAXS patterns of 1 nm of CoPt grown at 570 K. Continuous lines: Guinier fits.

The comparison with the results obtained for the 300K sample indicates that the increase in deposition temperature enhances the mobility of adatoms, thus leading to the formation of larger nanoparticles. Moreover, the coalescence effects are more pronounced

at 570 K than at 300 K. It reduces the substrate area covered by nanoparticles, allowing secondary nucleation and the growth of new particles to take place. These effects explain the very broad lateral size distribution deduced from the STM image.

• **1 nm CoPt grown on $WSe_2(0001)$ at 700 K**

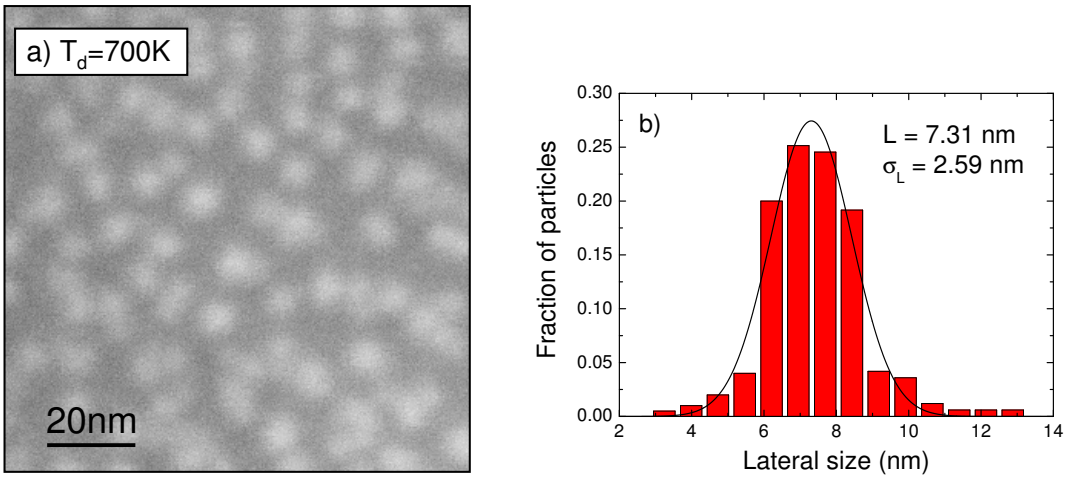

Figure 5.19: (a) FESEM image of 1 nm thick CoPt alloy grown at 700 K; (b) lateral size distribution of (a).

Since the STM measurements have failed for this sample, a FESEM investigation was thus done. Figure 5.19(a) shows the recorded image that leads to an average lateral size equal to (7.31±0.07) nm with σ=(2.6±0.2) nm.

GISAXS analysis

A quantitative analysis using $IsGISAXS$ program was performed on the GISAXS pattern taken under an incidence angle of 0.4° (figure 5.20). The best fits of the horizontal cuts are obtained by introducing the DWBA and LMA and using the form factor of a truncated cone with a base angle of 63°. The structural parameters, reported in table 5.2, give a total thickness of 0.11 nm, smaller than the real value of about 1 nm. As found for the 300K sample, the lower part of deposit produces no scattering due to merging of nanoparticles and this effect is still more marked for the 700K sample, with an average lateral size equal to 6.4 nm. No difference in average height is observed, however a very large distribution is found for the 700K sample.

The increase in particle size with deposition temperature is also observed from the Guinier plots. However, the values deduced from these plots are always larger than the ones extracted from the simulations.

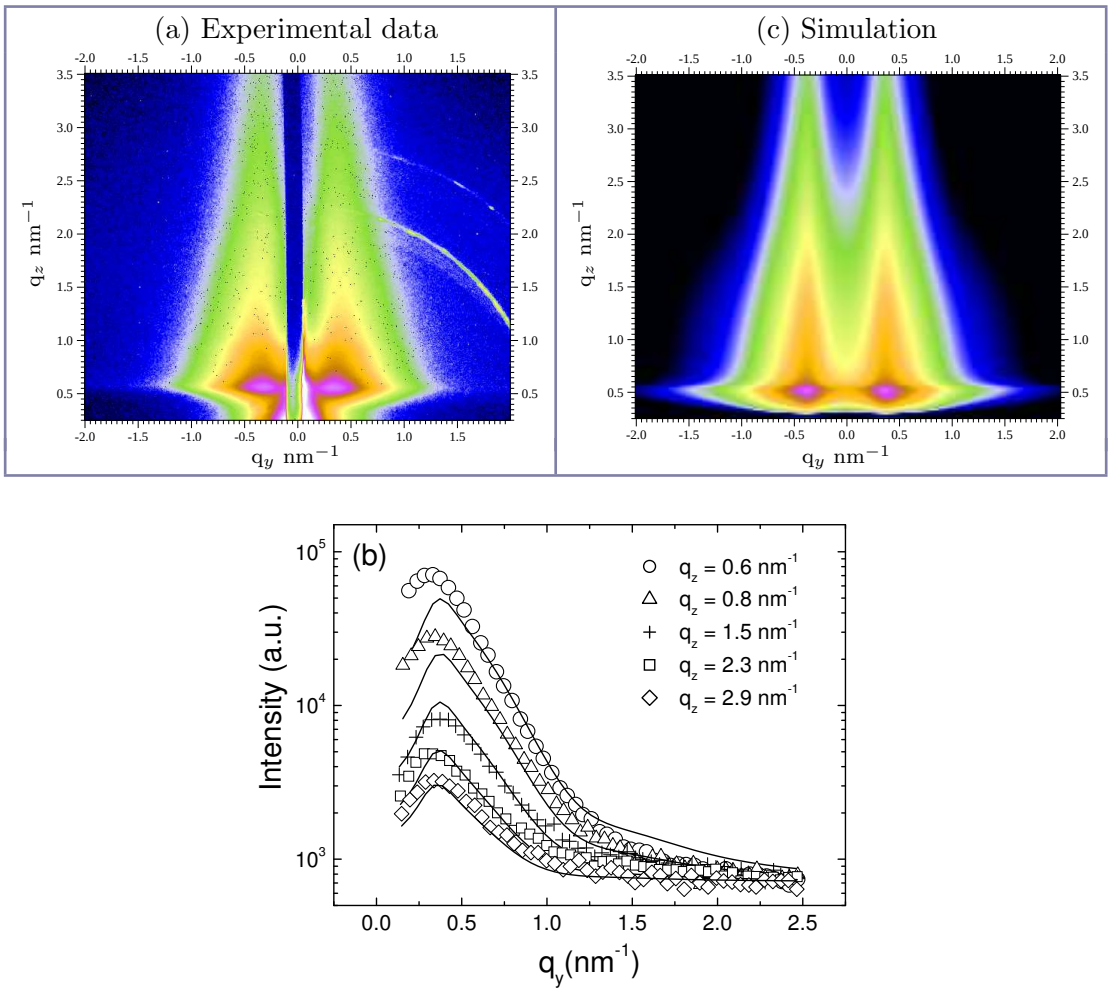

Figure 5.20: 2D GISAXS experimental intensity for a 1.0 nm thick CoPt(111)/WSe_2(0001) deposit at 700 K. (a) Experimental pattern. (b) Cuts of the experimental pattern parallel to the surface, at $q_z = 0.6$ (open circles), $q_z = 0.8$ (open triangles), $q_z = 1.5$ (crosses), $q_z = 2.3$ (open squares) and $q_z = 2.9$ (open rhombs); continuous lines: best fit of the experimental cut. (d) 2D pattern simulated with the parameters obtained from the parallel fits. The intensity is represented with a logarithmic scale.

5.4 Magnetic characterization

The magnetic properties of the 3nm thick CoPt deposits were investigated by SQUID magnetometry. The hysteresis loops were measured at 10 and 300 K with the magnetic field applied parallel and perpendicular to the substrate surface. The effects of thermal activation and magnetic relaxation were studied by measuring the zero-field and field cooling (ZFC/FC) curves, applying a small in-plane field of 30mT.

For the sample grown at RT, the weak anisotropic short-range order observed by EXAFS induces no perpendicular magnetic anisotropy (figure 5.21(a,b)). The hysteresis loops measured at 10K show soft magnetic properties with small in-plane and out-of-plane coercivities of 20 and 60mT, respectively. Due to the morphology (see figure 5.10(a)), the

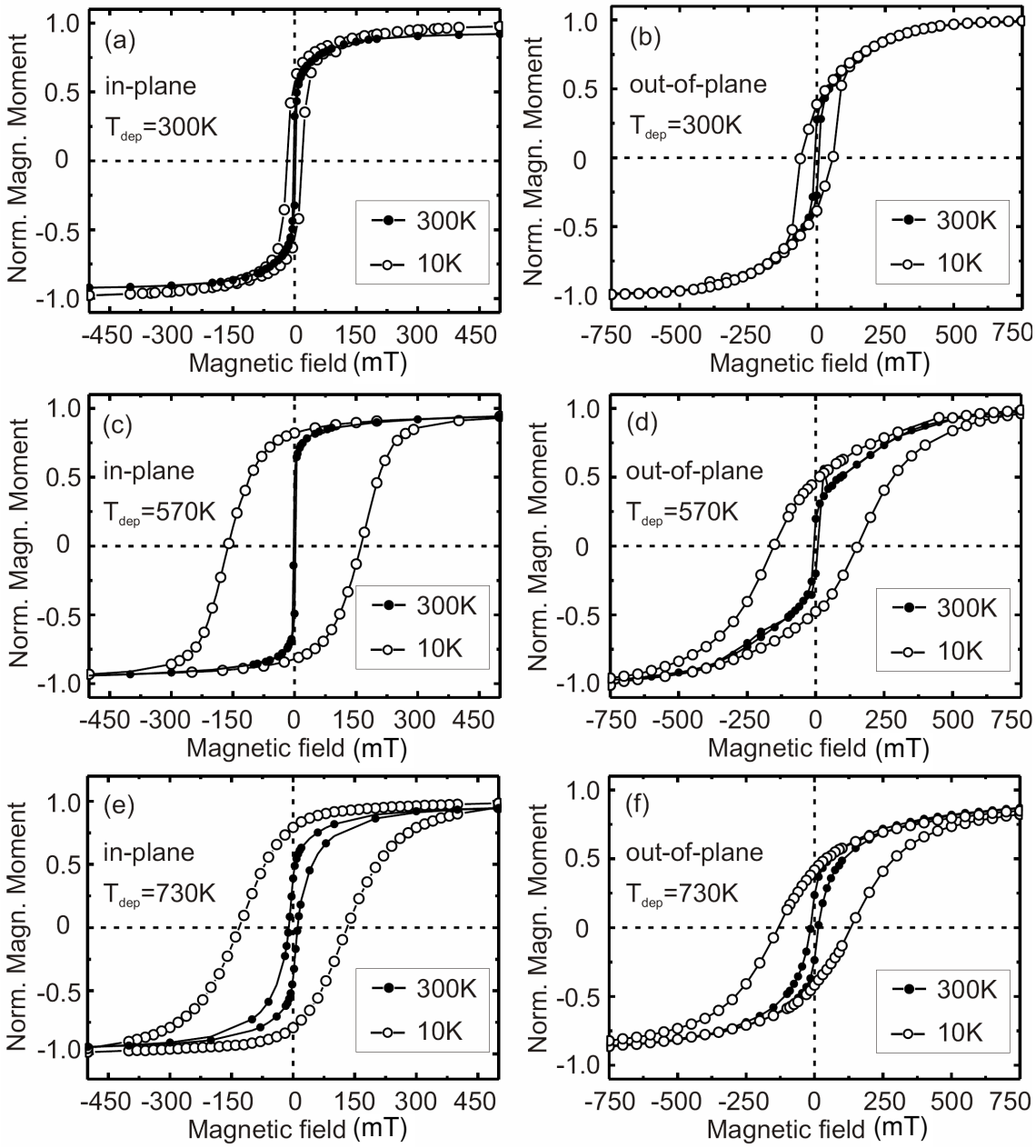

Figure 5.21: SQUID hysteresis loops of 3-nm-thick CoPt(111) deposits grown on $WSe_2(0001)$ at (a, b) 300 K, (c, d) 570K and (e, f) 730 K. Hysteresis loops were measured in the in-plane and out-of-plane geometry.

grains are expected to be strongly exchange coupled leading to an enhanced thermal stability. This behavior is confirmed by the ZFC and FC curves (figure 5.22(a)), which show no indication of a superparamagnetic state despite of the small size of the CoPt particles.

In contrast, the CoPt deposit at 570K reveals a characteristic superparamagnetic transition at about 200K with a broad transition (figure 5.22(b)) which is related to the rather

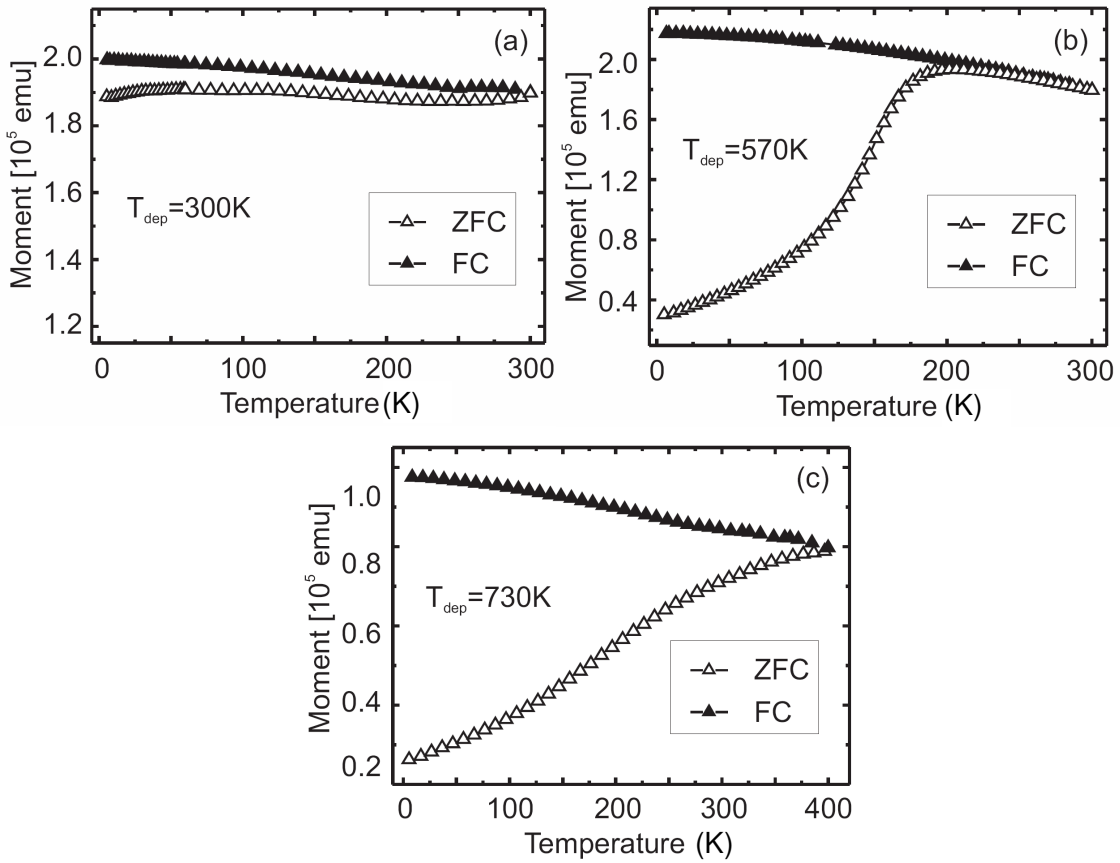

Figure 5.22: ZFC/FC curves measured in the in-plane geometry at 30mT for 3-nm-thick CoPt(111) deposits deposited at (a) 300 K, (b) 570 K, and (c) 730K on WSe_2(0001).

large grain size distribution, as well as to the different degrees of chemical order which determine the magnetic anisotropy energies. It is expected that the grains are magnetically exchange decoupled due to an enhancement of separation between larger particles. The hysteresis loops measured at 10K (5.21(c,d)) prove the presence of partial chemical order in the CoPt particles which is associated with an increase of the in-plane and out-of-plane coercivity up to 160mT. The easy axis of magnetization is clearly in the film plane forced by the shape anisotropy.

The SQUID data presented in 5.21(e,f) indicate that for the film prepared at 730K the easy axis is still lying in the film plane. But, the drastic change in shape and size of CoPt particles should reduce the shape anisotropy contribution in agreement with a decrease of in-plane coercivity at 10 K. Based on our X-ray measurements no increase of the chemical order was found by increasing the temperature from 570 to 730 K. Consequently, the uniaxial anisotropy along $< 001 >$ has to be similar in both deposits. The ZFC curve measured for the 700K sample indicates a superparamagnetic behavior with a broad distribution of blocking temperatures, which compared to that measured for the 570K sample, is shifted to higher temperatures even above room temperature, mainly due to

the increase in size.

5.5 Summary

Co-deposition of Co and Pt on WSe_2(0001) leads to the formation of epitaxial fcc CoPt nanostructures with [111] orientation even for deposition at room temperature. At RT, the analysis of short range order by polarized XAFS restricted to the first coordination shell reveals a structural anisotropy characterized by preferential CoCo correlations in the film plane. Deposition at higher temperatures induces $L1_0$ long range chemical order starting at 470 K, and the disappearance of local order anisotropy. However, the increase of the deposition temperature to 730 K does not enhance the long range order parameter, which is about 0.35. It is expected, that Se segregation at elevated temperatures during the CoPt deposition and surface disorder effects associated with a large surface-to-volume ratio might limit long-range order. Similar effects have been reported for $CoPt_3$ [10], $CrPt_3$ [62] and FePt [54] nanoparticles grown on WSe_2(0001).

A pronounced increase in size with deposition temperature is observed in the 1 and 3 nm CoPt deposits. For the 3 nm deposits it is accompanied by a change of the morphology of particles. Detailed analysis of the STM and GISAXS images shows that in the 1nm CoPt deposits most of particles touch each other and start to merge. The particle merging increases with the deposition temperature, leading to a reduction of surface area covered by particles and allowing the growth of new particles to take place.

In contrast with $CoPt_3$ deposits on WSe_2(0001) at RT, the 3nm thick CoPt deposits at RT do not show perpendicular magnetic anisotropy which could be associated with anisotropic short-range chemical order. This absence can be attributed to the contribution of the shape anisotropy which, for identical particle shape, is higher for CoPt than for $CoPt_3$ particles and leads to align the magnetization in the substrate plane. Nevertheless, different magnetic behaviors are observed for CoPt films grown at various temperatures ranging from exchanged coupled continuous films when grown at room temperature to a superparamagnetic behavior at elevated deposition temperatures consistent with the related film morphology and the degree of chemical order.

Chapter 6

FePt and CoPt grown on NaCl(001)

In this chapter, FePt nanostructures simultaneously prepared on NaCl(001) and MgO(001) substrates at different temperatures are characterized. The aim is to grow $L1_0$-ordered FePt nanoparticles with the tetragonal c axis perpendicular to the surface, i.e. along the easy axis of magnetization. The choice of simultaneous depositions allows to study the influence of the interactions adatoms-substrate on the structural and morphological properties of alloy nanoparticles, closely related with their magnetic properties. In other respects, the structural characterization of CoPt particles grown on NaCl(001) is also reported, for a comparison with the CoPt particles obtained on WSe_2(0001).

6.1 Epitaxial growth

Co-deposition of Fe and Pt was done simultaneously on freshly cleaved NaCl(001) and polished clean MgO(001) substrates at 420, 520 and 620 K. The fluxes of impinging atoms were equal to 0.01 Å/s for Fe and 0.134 Å/s for Pt, the chosen nominal thicknesses were 3 nm. Finally, 1 nm thick Cr layer was deposited at room temperature to protect the samples from oxidation.

The FePt alloy grown directly on MgO(001) leads to the formation of 3D fcc islands partially ordered in the $L1_0$ phase with the following epitaxial relationships:
[100]MgO(001)$\|$ [100]FePt(001) and [110]MgO(001)$\|$ [110]FePt(001), as already observed by Miyazaki et al. [41]. It corresponds to a "cube over cube" growth.

On NaCl(001), as shown by the RHEED patterns taken along the [100] and [110], the growth of FePt at 520 K also leads to the formation of fcc islands with the same epitaxial relationships as observed on MgO (figure 6.1(a)). The separation distance between the FePt spots and the substrate streaks, which are visible in the RHEED pattern of the sample prepared at 520K (see figure 6.2), corresponds to the lattice mismatch ($\varepsilon \sim 30\%$), indicating the growth of stress-free islands. The weak superstructure spots visible in figure 6.1(a) arise from the onset of $L1_0$-type chemical ordering in the (001) planes. The RHEED pattern of the sample grown at 620 K taken along the [100] azimuth (figure 6.1(b)) presents additional spots, stemming from the presence of the two variant-domain structures, with

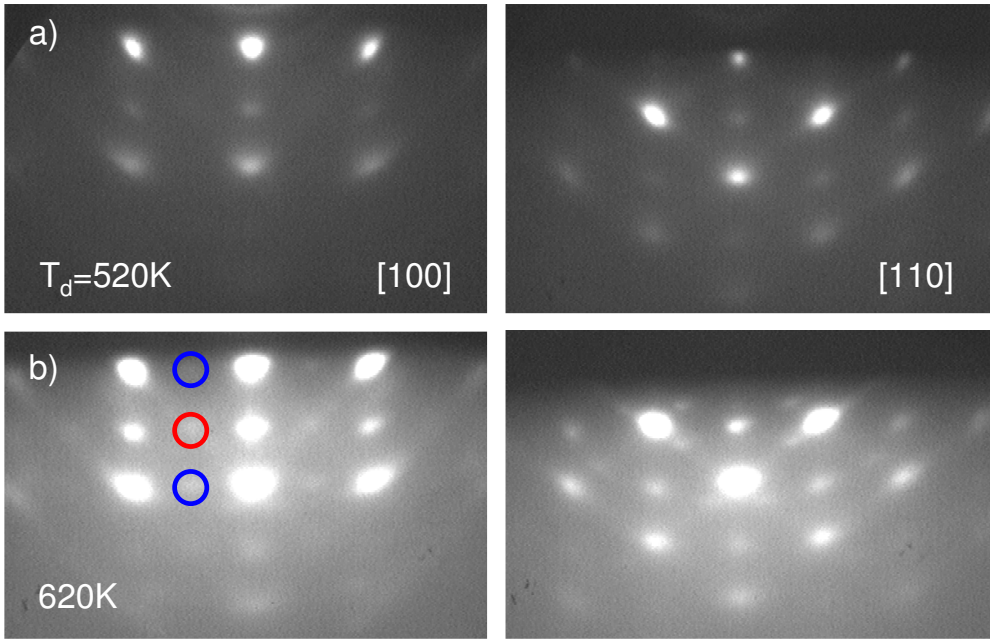

Figure 6.1: RHEED patterns along the [100] and [110] azimuths of 3nm thick FePt grown on NaCl(001) at 520 (a) and 620K (b). The open circles in the (b) pattern are the reflections coming from the two variants with the tetragonal axis in plane: $c \parallel Ox$ (red circle) and $c \parallel Oy$ (blue circles).

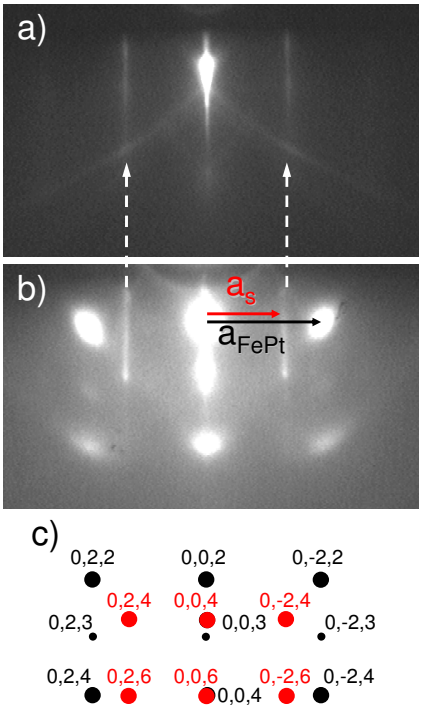

Figure 6.2: RHEED patterns along [100] azimuth before (a) and after (b) the co-deposition of 1.1nm-thick FePt on NaCl(001) at 520K; (c) the calculated diffraction pattern obtained from the superimposition of the reflections coming from the $L1_0$ phase of FePt (black disks) and FCC (red disks) of NaCl grown along the [001] direction. The mismatch parameter value was retrieved from separation distance between the FePt spots and the substrate streaks, which are visible in the image (b).

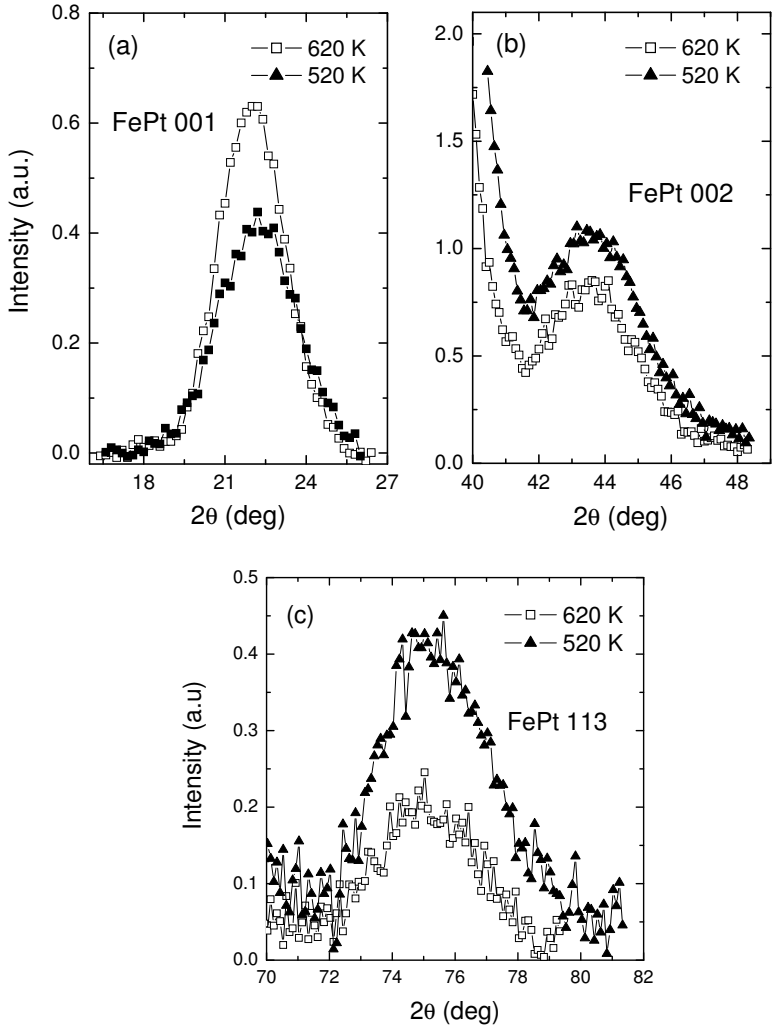

Figure 6.3: X-ray patterns measured in a 3nm deposit of FePt at 520 and 620K on MgO(001) protected by 1 nm of Cr layer. In the b) x-ray pattern, the (002) reflections of FePt are situated on the shoulder of the (002) reflection from MgO. The patterns were recorded at the ESRF (BM02, $\lambda = 1.385\AA$).

their c axis respectively parallel to the [100] and [010] direction of NaCl substrate.

6.2 Structural characterization

A detailed structural analysis was done by X-ray measurements performed at the ESRF on BM02 beamline and at the SIMaP on the 4-circle diffractometer. The lattice and long range chemical order parameters were determined.

Figure 6.3 shows the $\theta/2\theta$ scans around the 001, 002 and 113 reflections for FePt grown on MgO(001) at 520 and 620K. The 002 fundamental peak is less intense for the sample

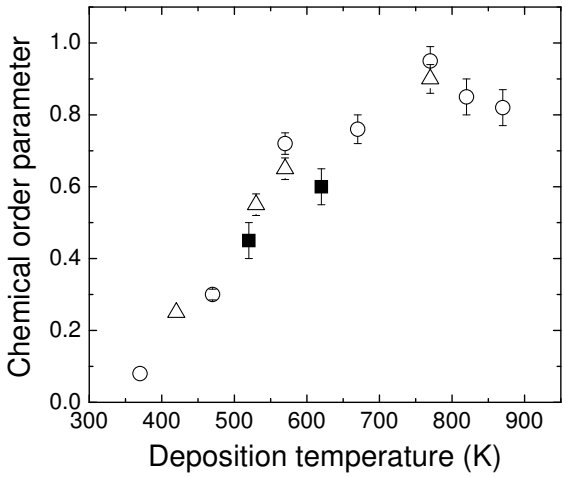

Figure 6.4: Comparison of long range order parameter, S, calculated for nanostructured and continuous films: 3nm thick FePt on MgO(001) (black squares), 100nm thick FePt on MgO with Pt buffer thickness 0.7 nm (triangles) and 1.5 nm (circles).

Samples	T_d (K)	c (Å)	a (Å)	c/a	$L_\perp^{(002)}$ (Å)	$L_\perp^{(001)}$ (Å)	S
FePt/MgO(001)	520	3.742(5)	3.81(2)	0.982(6)	19(1)	23(4)	0.45(5)
	620	3.740(5)	3.88(2)	0.964(6)	21(1)	28(4)	0.60(5)
FePt/NaCl(001)	520	3.82(1)	3.84(1)	0.995(5)	48(3)	33(3)	0.3(1)
	620	3.83(1)	3.84(1)	0.997(5)	74(2)	37(4)	0.4(1)

Table 6.1: Lattice, perpendicular coherence length and long-range order parameters for FePt grown on MgO(001) and NaCl(001) simultaneously at 520 and 620 K.

prepared at higher temperature and it can attributed to a larger Debye Waller attenuation factor associated to mean-square static displacements from lattice sites [108]. The notable increase of the 001 peak is characteristic of a high degree of $L1_0$ ordering. The long-range chemical order parameter (LRO), S, was quantified by the ratio between the integrated intensities of the 001 and 002 peaks, corrected by the absorption and Lorentz factor and taking into account the width of their rocking curves. The values of S are reported in table 6.1, note that no Debye Waller correction was included in their calculation. These values are close to those measured in continuous films [118] as shown in figure 6.4.

The value of the a and c lattice parameters, given in table 6.1, were calculated from the positions of the 002 and 113 reflections. The tetragonal distortion increases with the chemical order, however deviations from the parameters of $L1_0$ bulk alloy (c=3.79Å, a=3.86Å) are observed, suggesting remaining substrate-induced strains.

Figure 6.5 shows the $\theta/2\theta$ scans around the 001 and 002 reflections of FePt grown on NaCl(001) at 520 (a and b) and 620K (c and d). The superstructure peak is on the tail of the 002 NaCl reflection and it is disturbed by a few peaks coming from impurities of the substrate (figure 6.5(a,c)). The peak of the 002 FePt reflection is perturbed by the 006

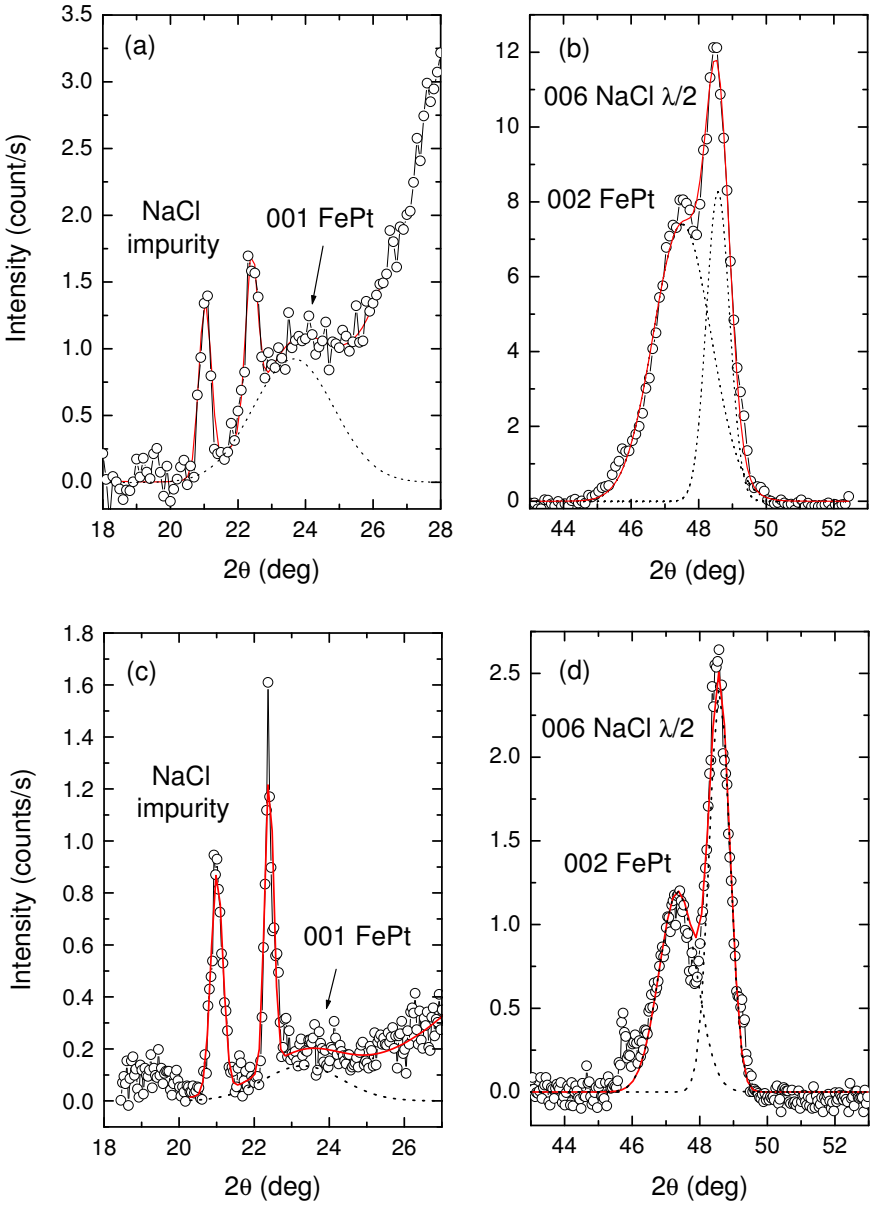

Figure 6.5: XRD patterns of the FePt nanoparticles grown on NaCl(001) at 520K, a) and b), and at 620K, c) and d). In the X-ray patterns a) and c) the dashed lines represent the Gaussian contribution of (001) reflections of FePt alloy, while in b) and d) they represent the (002) reflections of FePt alloy and (006) reflections of NaCl for a $\lambda/2$ wavelength. The measurements were performed at the SIMaP using Cu K_α radiation.

NaCl reflection associated to the $\lambda/2$ wavelength (figure 6.5(c,d)).

The a and c lattice parameters (table 6.1) are deduced from the 002 and 113 peak positions; the $\theta/2\theta$ scans around 113 (not shown) leads to spacings of 113 planes equal to 1.16 Å and 1.15 Å for T_d=520K and 620K, respectively. The LRO parameters are deduced from the ratios between the 001 and 002 integrated intensities taking into account their rocking curves.

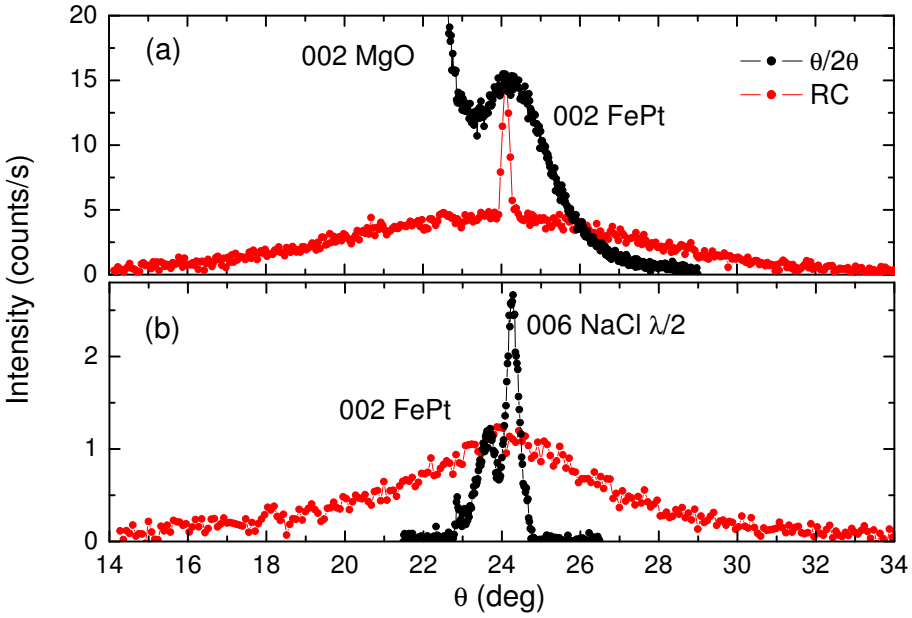

Figure 6.6: $\theta/2\theta$ scan (black dots) and rocking curve (red dots) for 3nm of FePt deposited on MgO(001) (a) and NaCl(001) (b) at 620K.

Since the FePt co-depositions were simultaneously done on MgO(001) and NaCl(001), a comparison between their results allows to understand the role of the substrate:

- The LRO parameter is found smaller on the FePt grown on NaCl(001) for both deposition temperatures and no significant tetragonal distortion is observed. The initial epitaxial strain produced by MgO (as justified below) on the FePt favours the $L1_0$ ordering. On the contrary, the nanostructures formed on NaCl are not constrained and variants of the $L1_0$ phase with c in the plane can be formed.

- Figure 6.6 shows the superposition of the $\theta/2\theta$ scan and the rocking curve of the 002 reflection of FePt grown at 620K on MgO(001) (a) and NaCl(001) (b). The FWHM of their 002 peaks lead to very different normal coherence lengths, related to different film morphologies. The values corresponding to deposits on NaCl about three times larger than the ones for deposits on MgO are an indication of higher island. About the rocking curves, the broad component observed for the two deposits is characteristic of the small lateral dimension of islands while the narrow peak observed only for the deposit on MgO is typical of a wetting layer. These features suggest a Stranski-Krastanov growth mode on MgO and Volmer-Weber growth mode on NaCl. The origin of these different growth modes can be explain by the difference between the surface energies of the substrates, i.e. 1200erg/cm^2 for MgO(001) and 230erg/cm^2 for NaCl(001).

- Moreover, the intensity of the 002 FePt reflection of the sample prepared on NaCl(001)

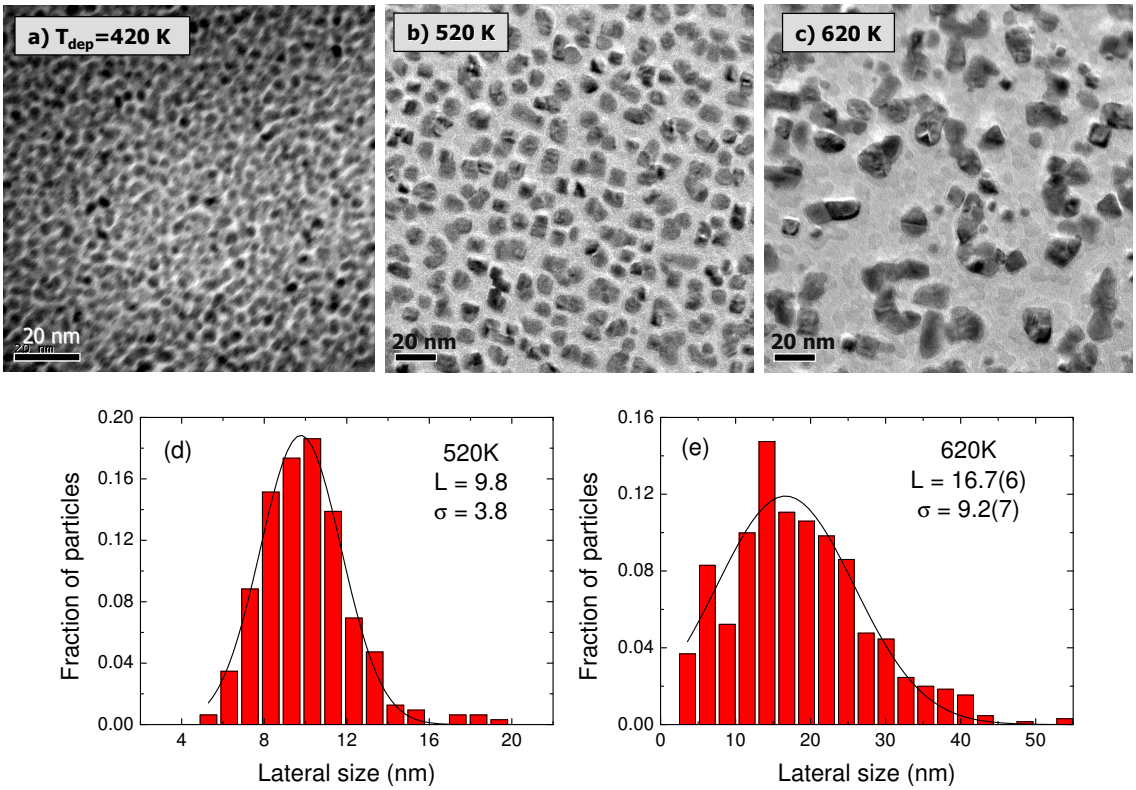

Figure 6.7: A series of TEM images, after NaCl dissolution, of FePt nanoparticles grown at 420 (a), 520 (b) and 620K (c). d) and e) The lateral size distribution calculated for the images corresponding to the deposition temperatures 520 and 620K. The red lines are the corresponding Gaussian fits of distributions.

at 620K, which is expected to be the same for both substrates, is ten times smaller than the one measured on MgO(001) substrate, as reported in figure 6.6. It is a signature that at 620K a significant amount of FePt nanoparticles on NaCl(001) have not grown along the [001] direction. From figure 6.5 the decrease of the 002 peak intensity, when the deposition temperature increases, is related to a degradation of the cube over cube growth mode on NaCl.

6.3 Morphology

The morphology of FePt nanoparticles grown on NaCl(001) was monitored by (HR)TEM observations after NaCl dissolution. Figure 6.7 shows TEM images for the samples prepared at 420, 520 and 620K. The FePt alloy dots were formed directly on NaCl(001) surface without a wetting layer confirming the Volmer-Weber growth mode. The lateral size as well as the separation distance increase with the deposition temperature.

At T_d=520K, the nanoparticles are characterized by a narrow lateral size distribution centred around L=(9.77±0.05) nm with a width σ=(3.85±0.05) nm, as reported in figure

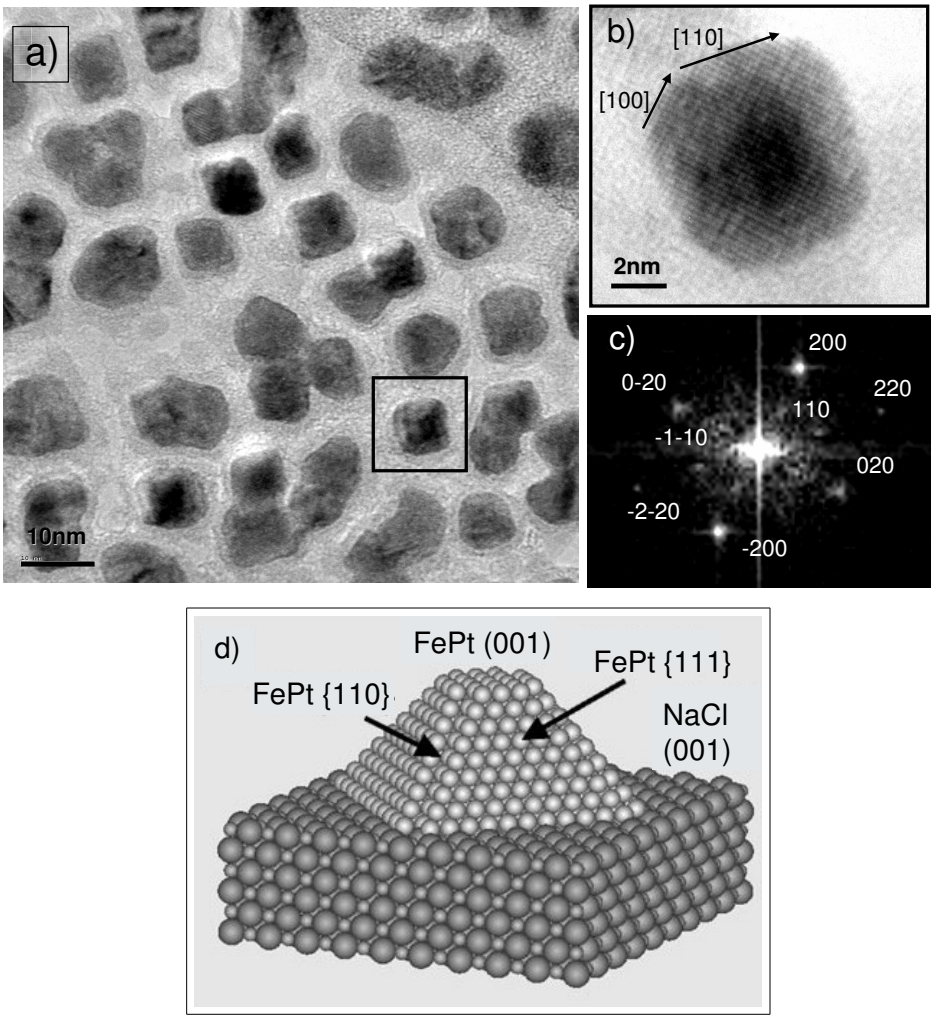

Figure 6.8: a) TEM image of FePt nanoparticles grown on NaCl(001) at 520K. b) High resolution TEM image of a partial ordered $L1_0$ FePt crystal and its Fourier trasform (c). d) A structural model of a pyramidal FePt particle.

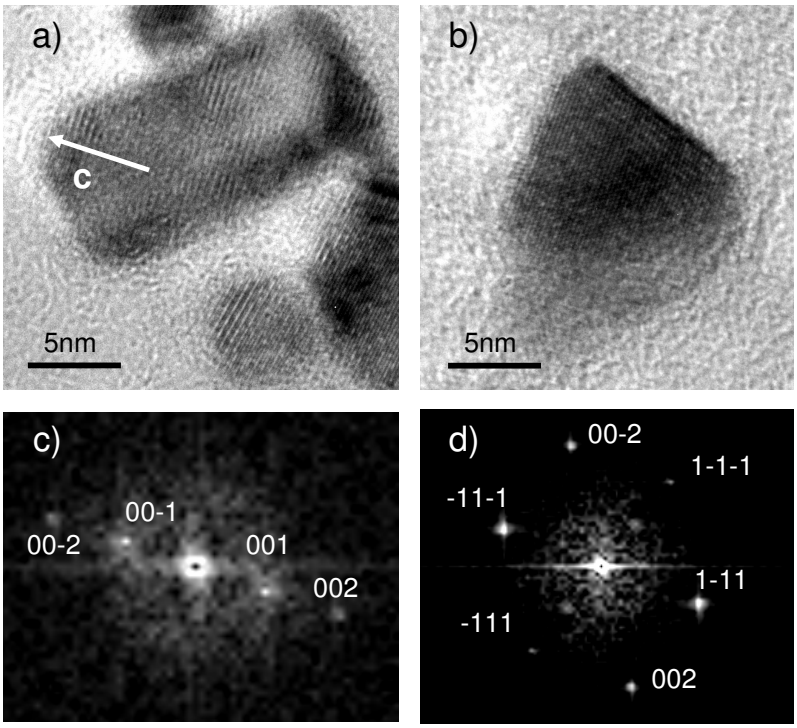

Figure 6.9: HRTEM images of FePt crystals that grow along [001] (a) and [110] (b) directions at 620 K; c) and d) are their Fourier transform, respectively.

6.7(d). Most of nanoparticles exhibit a well-defined square shape. An HRTEM image of a single FePt nanoparticle is shown in figure 6.8(b), where lattice fringes of (200) and (020) planes are visible and correspond to fcc structure with a lattice constant of 3.76Å. The main edge directions of the particle are $< 110 >$, with truncations at the corners along the $< 100 >$ directions. Due to the good quality of the image, its Fourier Transform gives a direct evidence of the epitaxial growth: figure 6.8(c) corresponds to the reciprocal space of a $L1_0$ ordered FePt particle oriented along the [001] zone axis. These results suggest that a possible representation of the 3D shape of the FePt nanoparticle can be a truncated octahedron with {111} and small {110} side wall facets as reported in figure 6.8(d).

At T_d=620K, the FePt nanoparticles are characterized by a broader lateral size distribution centred around L=(16.7±0.6) nm with a width σ=(9.2±0.7) nm. Several particles with different size and shape are observed. Besides a square shape associated to the [001]FePt oriented particles, rectangular shape is observed as reported in figure 6.9(a). It stems from the merging of two square-based particles. Its FT (figure 6.9(c) reveals the fundamental (002) and superstructure (001), characteristic of a $L1_0$ order crystal, with the c axis in the film plane. This variant corresponds to the additional spots observed in the RHEED pattern (figure 6.1(b)). A HRTEM image of a triangular particle is reported in figure 6.9(b); it shows the lattice fringes of (111) and (200) planes corresponding to a particle orientated along the [110] zone axis, as it is confirmed by its FT (figure 6.9(d)).

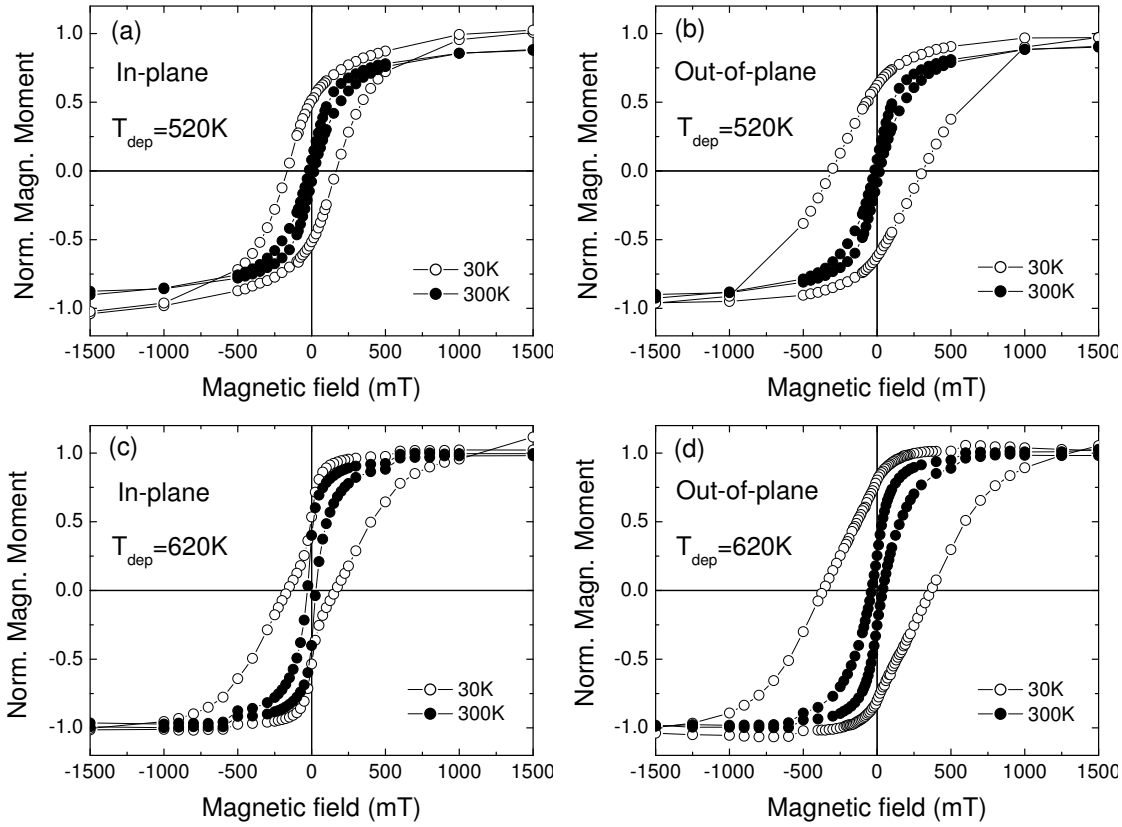

Figure 6.10: SQUID hysteresis loops of 3-nm-thick FePt(001) films grown on NaCl(001) at 520K. Hysteresis loops were measured in the in-plane (a) and (b) out-of-plane.

This particular growth orientation was not detected by x-ray diffraction because the fundamental peak corresponding to the 220 reflection falls at the same position as the strong 004 NaCl reflection. Therefore, the presence of the [110] growth explains in part the lack of intensity in the 002 FePt reflection for the sample grown on NaCl(001) with respect to the one observed for the sample grown on MgO(001). However, the differences in the 002 peak intensities can be also attributed to condensation coefficients of Fe and Pt adatoms lower on NaCl than MgO.

6.4 Magnetic properties

As already mentioned, the $L1_0$-oriented FePt nanoparticles have great application potential because of their high magnetic anisotropy and high coercivity as long as their size is above the superparamagnetic critical dimension. Figure 6.10 shows the perpendicular and parallel hysteresis loops measured at 30 K and 300 K for the samples deposited at 520 and 620K.

For the 520K sample, the two hysteresis loops (figure 6.10(a,b) measured at 300K are characterized by a isotropic magnetic behaviour with a coercivity of 16 mT. The nanopar-

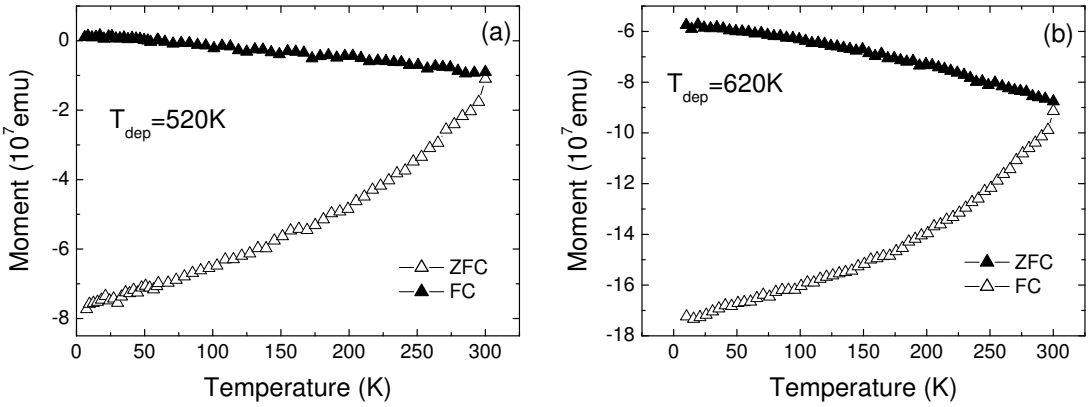

Figure 6.11: ZFC/FC curves measured in the out-of-plane geometry at 10mT for 3-nm-thick FePt(001) deposits grown at (a) 520 K and (b) 620 K, on NaCl(001).

ticles are superparamagnetic as confirmed by ZFC/FC curves reported on figure 6.11(a), with a broad distributions of block temperature extended up to 300K. The hysteresis loops measured at 30 K show an enhancement of the out-of-plane coercivity (300 mT), which is correlated to the partial $L1_0$ long-range chemical order measured by XRD [119].

For the 620K sample, the SQUID data measured at RT, figures 6.10(c,d), and the ZFC/FC curves reported in figure 6.11(b) show that FePt nanoparticles are also superparamagnetic in spite of their larger lateral size. The shape of the loops measured at 30 K (figures 6.10(c,d)) suggests two magnetization reversal behaviours: a hard component associated to $L1_0$ 001-oriented FePt particles displaying a coercivity of 371 mT, slightly higher than the one observed for the 520K sample because of a higher degree of LRO, and a soft component stemming from nanoparticles with the c axis in the plane.

6.5 CoPt grown on NaCl(001)

In this paragraph, the first results concerning the growth of CoPt nanoparticles on NaCl(001) are presented. A 0.2 nm thick of CoPt alloy was deposited on NaCl(001) at 520 K. The growth was followed in-situ by RHEED and the morphology examined by combining TEM and GISAXS measurements.

Figure 6.12 shows the RHEED patterns taken along the [100] and [110] azimuths. Weak spots are observed, typical of an island growth, their positions with respect to the substrate spots indicate a cube over cube growth. However no $L1_0$ order is observed, likely due to the weakness of the fundamental spots.

Figure 6.13(a) shows the TEM images of an assembly of CoPt nanoparticles. The average lateral size is (2.67±0.07) nm with a distribution, σ=(1.22±0.09) nm, as reported in figure 6.13(d). The inset shows the diffraction pattern of this assembly: the red arrows indicate two rings corresponding to the 111 and 002 reflections which are thus characteristic of the 110-oriented islands without orientational relationship with NaCl substrate; the

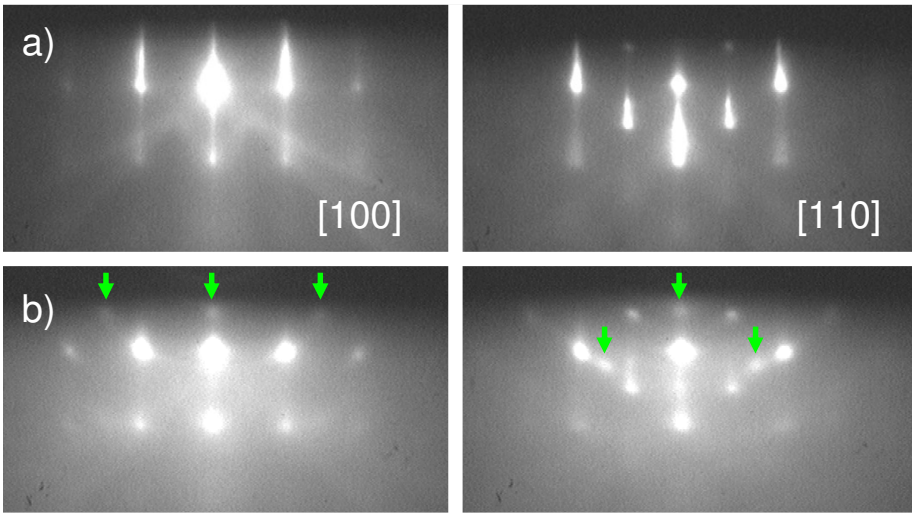

Figure 6.12: RHEED patterns along the [100] and [110] azimuths before (a) and after (b) the co-deposition of 0.2nm thick CoPt on NaCl(001) at 570 K. The green arrows in (b) indicate the spots coming from the CoPt reflections.

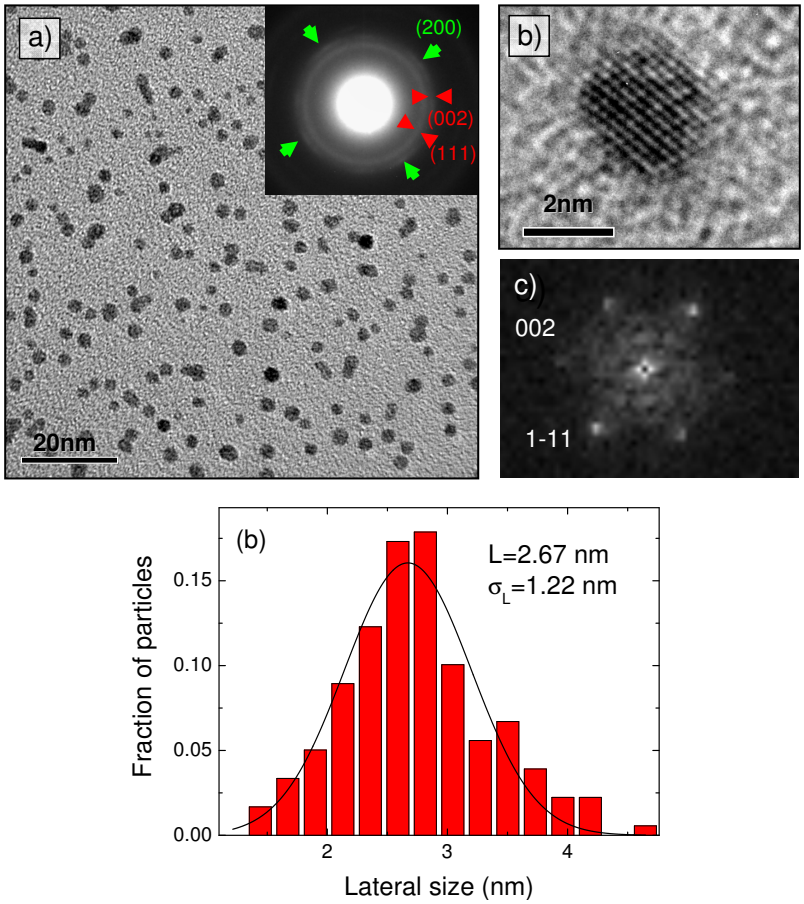

Figure 6.13: a) TEM image of a 0.2 nm CoPt deposit on NaCl(001) at 520K, the corresponding diffraction pattern is in the inset. b) HRTEM of one particle and c) its FT. d) Lateral size distribution calculated for the image (a).

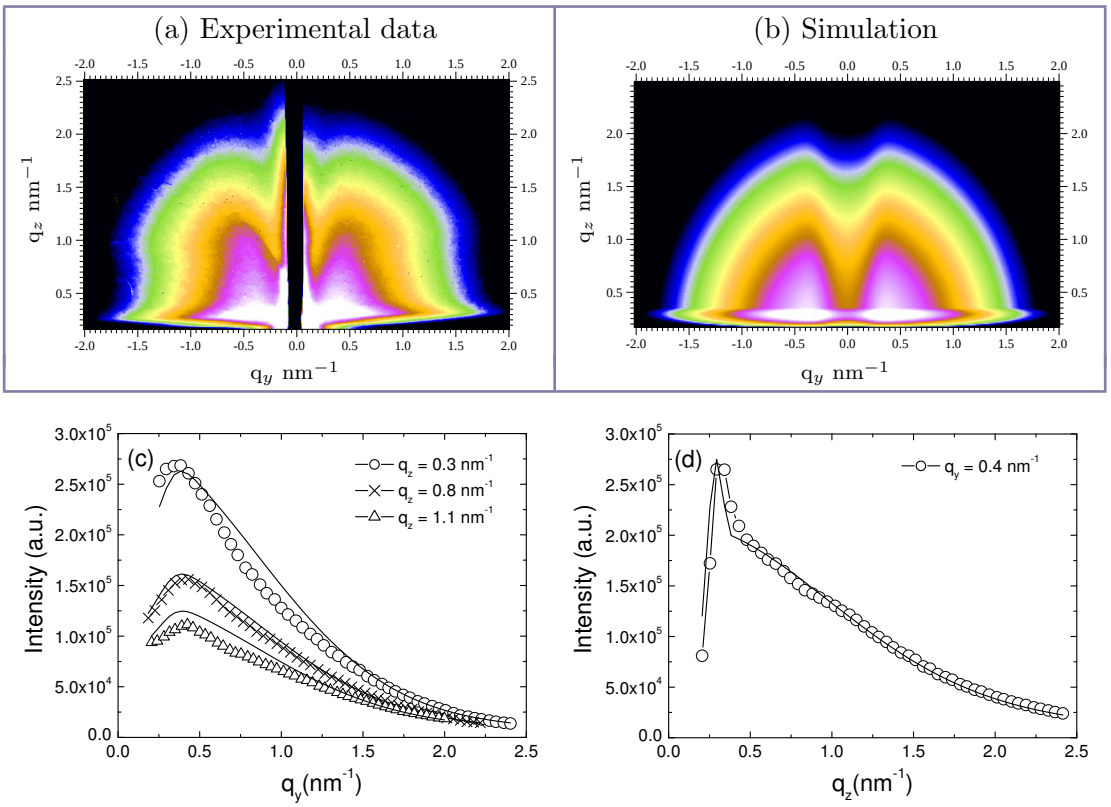

Figure 6.14: 2D GISAXS experimental intensity for a 0.2 nm thick CoPt(001)/NaCl(001) deposit at 520 K. (a) Experimental pattern. (b) 2D pattern simulated with the parameters obtained from the parallel fits. The intensity is represented with a logarithmic scale. (c) Cuts of the experimental pattern parallel to the surface, at $q_z = 0.3\text{nm}^{-1}$ (open circles), $q_z = 0.8\text{nm}^{-1}$ (crosses) and $q_z = 1.1\text{nm}^{-1}$ (open triangles). (d) Cuts of the experimental pattern parallel to the surface, at $q_y = 0.4\text{nm}^{-1}$ (open circles). Continuous lines: best fit of the experimental cuts.

green arrows indicate four broad spots coming from the 200 reflection of the particles oriented along the [001] zone axis.

The HRTEM image of a single particle oriented along the [110] zone axis is shown in figure 6.13(b), where lattice fringes of (111) and (200) planes are visible, as confirmed by its FT (figure 6.13(c)). Although the RHEED patterns have shown the epitaxial growth of 001-oriented particles, HRTEM images of such 001-oriented nanoparticles did not succeeded. Possible explanations are: *i*) the CoPt(110) particles have higher power of scattering because of their more intense 111 reflections and appear more clearly on the bright field image; *ii*) imaging the (111) planes is easier due to their spacing equal to 2.17 Å, i.e. larger than the resolution of the 200kV JEOL 2011 microscope, closer to 1.9 Å (while solving the (002) planes with a spacing of 1.93 Å is more difficult, except for well $L1_0$ ordered (001) particles where the (001) planes could be observed).

Figure 6.14(a) shows the GISAXS pattern of the 0.2 nm CoPt deposit at 520K taken under an incidence angle, α_i=0.2°. This image was analysed by fitting three horizontal and vertical cuts simultaneously, using the DWBA and SSCA as it was done for the

$CoPt_3$ nanostructures grown on NaCl. Because of their small particle size, the detection of side wall facets was not possible and their shape was described by the form factor of a truncated sphere. The extracted lateral size is described by a Log-normal distribution where the mean value is L=(2.2±0.1) nm and the width is (1.4±0.1) nm. The height distribution is, instead, described by a Gaussian curve centred in H=(1.65±0.08) nm with a width of (0.4±0.1) nm. As observed for $CoPt_3$ grown on NaCl at the same temperature, the aspect ratio, H/L=0.75±0.07, is higher than the one extracted for CoPt and $CoPt_3$ nanoparticles grown on WSe_2(0001).

6.6 Summary

The simultaneous deposition of 3nm thick FePt on NaCl(001) and MgO(001) reveals different growth modes and different degrees of chemical ordering, attributed to the strong difference of surface energy and lattice mismatch.

The Stranski-Krastanov growth on MgO(001) was revealed for T_d=520 and 620K, by the appearance of a narrow peak in their rocking curves. The epitaxial FePt(001) deposits have a degree of $L1_0$ order, associated with a the tetragonal distortion, quite similar to that observed in continuous thin films grown on MgO(001) with a buffer layer.

The co-deposition of Fe and Pt atoms on NaCl(001) at 520K leads to the formation of epitaxial 3D nanoparticles oriented along the [001] direction with a degree of $L1_0$ order lower than that determined in FePt particles on MgO(001). Their morphology can be described as truncated octahedra with large {111} and small {110} alternate side-wall facets. The magnetic measurements reveal an easy axis of magnetization perpendicular to the substrate plane and a superparamagnetic behavior at room temperature. The deposition at 620K slightly increases the degree of LRO and, consequently, the out-of plane coercivity, but induces the formation of some nanoparticles orientated along the [110] direction without epitaxial relationships with the substrate and the appearance of the two other variants with the c axis lying in the plane.

No $L1_0$ order was observed in very small 001-oriented CoPt nanostructures (L∼2.5 nm) grown on NaCl(001) at 520 K. Such absence was already observed in particles of FePt when its size was less than ∼2 nm [41]. Furthermore, nanoparticles oriented along the [110] directions were identified by HRTEM. Using the form factor of a truncated sphere shape, a good simulation of the GISAXS pattern was obtained. The nanoparticles are characterized by an aspect ratio higher than the one of CoPt nanostructures grown on WSe_2(0001). Such difference in the particle shape would stem from *i*) the lattice mismatch, much larger on NaCl, favoring small particles, *ii*) the [001] growth direction resulting in the formation of nanoparticles with {111} side-wall facets which for energetic reasons would extend to the detriment of the (001) top facet.

Conclusions

In this thesis the characterization of the structural, morphological and magnetic properties of $M_{1-x}Pt_x$ (M=Co and Fe) nanostructures were presented as a function of the deposition temperature and the nature of substrate. For this purpose, these alloys were grown by molecular beam epitaxy at different deposition temperatures on the low energy surfaces $WSe_2(0001)$ and NaCl(001). Several techniques were used for the characterizations, such as, RHEED to follow the epitaxial growth during the deposition, XRD to characterize the structure and determine the long range chemical order parameter, polarized XAS to probe the local structure in-plane and out-of the film plane, SQUID to investigate the magnetic anisotropy and GISAXS coupled to microscopy techniques TEM, STM and Field Emission-SEM to study the morphology.

Growth on $WSe_2(0001)$: co-deposition of 3nm thick $CoPt_3$ and CoPt on $WSe_2(0001)$ leads to the formation of epitaxial fcc nanostructures with [111] orientation even for deposition at room temperature. Deposition at high temperatures induces long range chemical order, $L1_0$ for the CoPt nanostructures starting at 470 K and $L1_2$ for the $CoPt_3$ nanostructures starting at 370 K. However, the increase of the deposition temperature to about 730 K does not enhance the long range order parameter. This limit might be due to the Se segregation at elevated temperatures during the Co and Pt co-deposition, kinetic effects and surface disorder effects associated with a large surface-to-volume ratio.

Polarized EXAFS analysis performed on both $CoPt_3$ and CoPt nanostructures grown on $WSe_2(0001)$ at RT revealed the existence of a local structural anisotropy characterized by preferential CoCo pairs in the film plane balanced with preferential heteroatomic pairs out of the plane. Such anisotropy was more pronounced for $CoPt_3$ where its extension until the third coordination shell and the lattice distortion characterized by in-plane bonds shorter than out-of-plane bonds, suggest the formation of Co rich thin disks in the film plane. As observed in $CoPt_3$ films, this local atomic arrangement produces an anisotropy of the orbital moment of Co atoms and, therefore, originate the perpendicular magnetic anisotropy, peculiar characteristic observed on this sample.

In contrast, 3nm thick CoPt deposits at RT do not exhibit perpendicular magnetic anisotropy, which could be associated with anisotropic short-range chemical order. This absence can be attributed to the contribution of the shape anisotropy which, for identical particle shapes, is higher for CoPt than for $CoPt_3$ particles and aligns the magnetization in the substrate plane. Furthermore, the STM characterization together with the magnetic

measurements for a 3 nm thick CoPt deposit at RT reveal a dense assembly of nanoparticles strongly exchange coupled leading to an enhanced thermal stability, as fcc disordered continuous films. At higher deposition temperatures the partially $L1_0$ order nanoparticles are larger but also well-separated from each other and present a superparamagnetic behavior with blocking temperatures increasing with size.

The quantitative morphology analysis of 1nm thick CoPt and $CoPt_3$ deposits on $WSe_2(0001)$ at different deposition temperatures was performed. The STM observations in CoPt and $CoPt_3$ grown at RT reveal dense assemblies of hexagonal nanoparticles that touch each other. At higher deposition temperatures, the particles merge to form large agglomerates and leaving free part of the substrate for new nucleations. This leads to an increase of lateral size and its distribution width, particularly on CoPt composition. A decrease of aspect ratio r=H/L (H and L being the height and the lateral size) with increasing the growth temperature was observed. This morphology is not well suited to perform GISAXS analysis because it probes only the upper parts of nanostructures, since lower parts are merged or simply contact each other leading to no scattering contrast.

With increasing deposit up to 3 nm, the $CoPt_3$ particles have rather a triangular shape with {111} side-wall facets when grown above 700K , as already observed for $CrPt_3$ nanoparticles on $WSe_2(0001)$ system [62]. In the case of CoPt nanoparticles, the triangular islands contain grain boundaries, attributed either to the existence of three variants of the $L1_0$ phase in the same island or more likely to the coalescence of several islands of different variants, since the equivalent side-wall facets {111} or {001} are differently decorated for $L1_0$ nanostructures. Facetting is observed by GISAXS with a higher sensitivity to the less inclined {001} side-wall facets, even in minority. This point is still under investigation, the form factor of an hexagonal truncated pyramid shape with alternate {111} and {100} facets is required to perform a detailed study.

Growth on NaCl(001) The growth of $CoPt_3$, CoPt and FePt on NaCl(001) leads to the formation of nanoparticles mostly oriented along the [001] direction, in spite of the large lattice mistmach ($\sim$30%). The epitaxy strongly depends on the deposition temperature.

$CoPt_3(001)$ nanoparticles are observed with epitaxial relationships with the substrate for $T_d \geq$370K. Unfortunately, no $L1_2$ long range chemical order was detected by RHEED and XRD since the composition of particles $Co_{20}Pt_{80}$ was found to be out of the $L1_2$ phase, likely due to different condensation coefficients of Co and Pt atoms. However, an isotropic short range order in the sample prepared at 370 K was detected by polarized EXAFS.

The effects of the large lattice mismatch and the low energy surface of NaCl(001) substrate on the growth and structural properties were studied by simultaneously growing FePt on NaCl(001) and MgO(001) substrates. Different growth modes and degrees of chemical ordering are observed. The Stranski-Krastanov growth is observed by XRD on MgO(001) for T_d=520 and 620K, where the epitaxial FePt(001) deposits have partial $L1_0$

order and tetragonal distortion, similar to that observed in continuous films.

Whereas, the growth on NaCl(001) is characterized by the Volmer-Weber mode; for T_d=520 K the [001]-oriented nanoparticles exhibit weaker $L1_0$ order and no tetragonal distortion. For T_d=620K, a fraction of FePt nanoparticles grows also along the [110] direction without epitaxial relationships with the substrate and the two other variants with the c axis in the film plane are also observed by RHEED. As already observed on WSe_2(0001) the increase of deposition temperature increases the particle size and its distribution. Contrary to that observed on WSe_2(0001), the magnetic studies revealed that the FePt(001) nanoparticles grown at 520 K on NaCl(001) are characterized by an easy axis of magnetization perpendicular to the substrate plane and by a superparamagnetic behavior at room temperature. The perpendicular magnetic anisotropy slightly enhances for T_d=620 K, due to higher chemical order.

HRTEM images show that the FePt(001) nanoparticles grown at 520K have a truncated octahedron shape with four large {111} facets, which can be well-detected by GISAXS as observed for $CoPt_3$ nanostructures with lateral size of 10nm. For higher deposition temperatures the FePt(001) nanoparticles start to coalesce and to form for example rectangular islands with the c axis in the plane, or triangular islands for FePt(110) nanoparticles.

The aspect ratio of CoPt nanoparticles grown on NaCl(001) is observed two times larger than the one of particles grown on WSe_2(0001), which is a favorable feature for perpendicular magnetic anisotropy. Nevertheless, since the epitaxial growth of $L1_0$-ordered nanostructures is not completely achieved, the PMA is far less pronounced than that observed for FePt particles grown on MgO.

In conclusion, the growth of $CoPt_3$ nanostructures on the two studied substrates WSe_2 and NaCl and the accurate study of chemical ordering effects have allowed to highlight the role of Se surfactant atoms during co-deposition. By segregating continuously to the surface of the different growing facets, Se atoms favor even at room temperature the segregation of Pt atoms leading to the formation of the evidenced anisotropic short range order as the origin of the perpendicular anisotropy. Above 400K, Se atoms would behave as vacancies favoring the atomic arrangements to form the long-range $L1_2$ ordering. The formation of a Moiré pattern after deposition of pure Pt atoms on WSe_2 at 700K, coming from the formation of a $PtSe_2$ surface alloy, asserts the idea that the Se surfactant effect favors preferentially the atomic displacements of Pt atoms. Such preferential atomic interactions would explain the reduced Se effect observed in CoPt nanostructures.

While the self-assembling on NaCl(001) allows the tailoring of nanostructures with a very attractive narrow size distribution, the absence of epitaxial stress, as present on MgO(001), and the restricted deposition temperature range for growing 001-oriented nanostructures explain the low degree of $L1_0$ ordering and thus the weak perpendicular magnetic anisotropy.

As outlooks, to enhance PMA effects in CoPt or FePt nanostructured films, different ways can be probed. The first one is to vary the thickness of deposits. As a matter of fact, for $CoPt_3$ deposits on WSe_2 a strong thickness dependence of uniaxial anisotropy was shown. To overcome the larger shape anisotropy in CoPt deposits, the idea would be to reduce the deposited thickness. For applications it is also important to slighlty exchange decouple the magnetic grains, therefore the deposition of a Cr overlayer would be interesting. For the nanostructured films on NaCl(001), the suppression of superaparamagnetic effects as observed in our 1nm deposits, could be achieved by the formation of highly dense assemblies of exchange coupled grains. Moreover, to increase the uniaxial magnetic anisotropy, further higher temperature annealing is required to enhance the degree of L10 ordering.

Appendix A

EXAFS

A.1 EXAFS: the physical process

Let one consider an atom in an initial state $|\psi_i\rangle$ of energy E_i. Through its interaction with the electromagnetic field of the X-ray beam the atom may absorb a photon of energy $\hbar\omega$ undergoing a transition to a final state $|\psi_f\rangle$ whose energy is $E_f = E_i + \hbar\omega$. During the transition an electron will go from a core level up to an external unoccupied level (excitation) or directly in the continuum of free states (ionization). The final state will be characterized by a core hole. The process can be physically described in a semiclassical way, treating the atom from a quantistic point of view and the electromagnetic field classically.

A.1.1 Transition probability: 'Fermi's golden rule'

The atomic absorption coefficient μ depends on the atomic density n of the sample as well as on the transition probability W_{fi} of the absorbing atom from an initial state $|\psi_i\rangle$ to different possible final states $|\psi_f\rangle$ (corresponding, for example, to the excitation of an electron from different core levels or to the excitation of more than one electron):

$$\mu(\omega) = \frac{2\hbar}{\epsilon_0 \omega A_0^2} n \sum_f W_{if}. \tag{A.1}$$

To calculate the transition probability, W_{fi}, one can use time dependent perturbation theory: because photon-electron interaction is weak ($\propto \frac{1}{\alpha}$, with α fine structure constant) the expansion can be limited up to the first order; so making use of the *Fermi golden rule* one has:

$$W_{if} = \frac{2\pi}{\hbar} |\langle \psi_i | \widehat{H}_I | \psi_f \rangle|^2 \rho(E_f) \tag{A.2}$$

where $\widehat{H}_I$ is the hamiltonian operator of atom-electromagnetic field interaction and $\langle \psi_i | \widehat{H}_I | \psi_f \rangle$ is the matrix element between an initial and a final state. $\rho(E_f)$ is the density of final states compatible with the principle of energy conservation: $E_f = E_i + \hbar\omega$. In this way the complex dynamic process of atom-photon interaction is reduced to the calculus of a matrix element that involves only the initial and final states of the process. At first order

the interaction Hamiltonian for photoelectronic absorption is given by:

$$H_I = i\hbar\frac{e}{m}\sum_f \overrightarrow{A}(r_j)\cdot\overrightarrow{\nabla}_j \tag{A.3}$$

where the index j indicate electrons inside the atom while $\overrightarrow{\nabla}_j$ represents the linear momentum operator of the j-th electron. Inserting eq.(A.3) into eq.(A.2) we obtain the transition probability for the photoelectronic absorption of a photon from a polarized monochromatic beam:

$$W_{if} = \frac{\pi\hbar e^2}{m^2}\omega^2|A_0|^2|\langle\psi_j|\sum_j e^{i\overrightarrow{k}\cdot\overrightarrow{r_j}}\widehat{\eta}\cdot\nabla_j|\psi_f\rangle|^2\rho(E_f) \tag{A.4}$$

where $\widehat{\eta}$ and $\overrightarrow{k}$ are the polarization vector and the wave vector of the electric field (with $k = 2\pi/\lambda$) respectively.

A.1.2 Single electron and dipole approximations

The calculus of the matrix element in eq.(A.4) is a quite complex one because all electrons inside an atom are involved during the absorption process. Furthermore the final state $|\psi_f\rangle$ is affected by the potential surrounding the absorbing atom.

The first simplification to be done concerns the single-electron approximation: the electromagnetic field interacts only with a core orbital, whose extension is usually smaller than the wavelength values characteristic of X-rays. If one considers the energy interval typical of the EXAFS region, one can observe that the photoelectron has a quite high energy so that the time employed to exit from the atom is shorter than the time employed by other electrons to relax; these electrons are also called for this reason passive electrons. In virtue of this we can pay attention only to elastic transitions supposing to neglect the relaxing contribution of these passive electrons. In the field of this approximation (*sudden approximation*) the wave functions of the initial and final states can be factorized separating the contributions $|\psi_i^{N-1}\rangle$ and $|\psi_f^{N-1}\rangle$ of the N-1 passive electrons from that of the active one:

$$\begin{aligned}\mu(\omega) &\propto |\langle\psi_i^{N-1}\psi_i|\textstyle\sum_j e^{i\overrightarrow{k}\cdot\overrightarrow{r_j}}\widehat{\eta}\cdot\overrightarrow{r_j}|\psi_f^{N-1}\psi_f\rangle|^2\rho(E_f) = \\ &= |\langle\psi_i^{N-1}|\psi_f^{N-1}\rangle|^2|\langle\psi_i|\textstyle\sum_j e^{i\overrightarrow{k}\cdot\overrightarrow{r_j}}\widehat{\eta}\cdot\overrightarrow{r_j}|\psi_f\rangle|^2\rho(E_f) = \\ &= S_0^2|\langle\psi_i|\textstyle\sum_j e^{i\overrightarrow{k}\cdot\overrightarrow{r_j}}\widehat{\eta}\cdot\overrightarrow{r_j}|\psi_f\rangle|^2\rho(E_f)\end{aligned} \tag{A.5}$$

where ψ_i^{N-1} represents the Slater determinant of the wave functions of the passive electrons; ψ, r and E_f are respectively the wave function, the vector position and the energy of the active electron. S_0^2 is the 'many body' term, an empirical parameter typically comprised between 0.7 and 0.9.

A further simplification in the calculus of μ_{el} can be introduced using the dipole approximation according to which $e^{i\overrightarrow{k}\cdot\overrightarrow{r}} \simeq 1$. This approximation is true when the condition

$|\overrightarrow{k} \cdot \overrightarrow{r}|^2 << 1$ is verified and therefore when the wavelength λ is much greater than the size of the system. Thanks to these considerations eq.(2.10) can be written also as:

$$\mu_{el} \propto \omega S_0^2 |\langle \psi_i | \widehat{\eta} \cdot \overrightarrow{r_j} | \psi_f \rangle|^2 \rho(E_f). \tag{A.6}$$

A.2 Interpretation of the EXAFS function

Consider the contribution of a well defined absorption edge to the absorption coefficient. In the EXAFS region the final states density of the photoelectron, $\rho(E_f)$, is a monotonous function, slowly variable with energy. As a consequence EXAFS oscillations are totally described by the matrix element of eq.(A.6) where $|\psi_i\rangle$ and $|\psi_f\rangle$ represent the initial and final states of the electron.

For an isolated absorbing atom, the photoelectron is free to go away from the atom undisturbed so that its final state $|\psi_f^0\rangle$ can be represented by an outgoing wave whose symmetry is l=1 for a K-edge and whose wave vector is:

$$k = \sqrt{\frac{2m}{\hbar}(\hbar\omega - E_b)} \tag{A.7}$$

where E_b is the binding energy of the photoelectron (that can be also identified with the edge energy). The absorption coefficient of an isolated atom is also called *atomic absorption coefficient*:

$$\mu_0 \propto |\langle \psi_i | \widehat{\eta} \cdot \overrightarrow{r_j} | \psi_f^0 \rangle|^2. \tag{A.8}$$

It has a monotonous decreasing behavior with increasing energy of incident photons.

In the case of a non-isolated atom the photoelectron interacts strongly with the potential generated by the atoms surrounding the absorber so that its wave function cannot be described as a simple outgoing spherical wave. The modifications of the wave function can be described and calculated in the framework of scattering theory: that is we will assume that the photoelectron wave is scattered by the potential of surrounding atoms. In the EXAFS region the photoelectron energy is much greater than the electron-atom interaction energy. This interaction causes a weak perturbation to the final state of the free electron that can be represented as:

$$|\psi_f\rangle = |\psi_f^0 + \delta\psi_f\rangle. \tag{A.9}$$

The perturbation $\delta\psi_f$ corresponds phenomenologically to the wave scattered from the potential of surrounding atoms. The absorption coefficient can then be written as:

$$\begin{aligned} \mu(\omega) &\propto |\langle \psi_i | \widehat{\eta} \cdot \overrightarrow{r} | \psi_f^0 + \delta\psi_f \rangle|^2 = \\ &\cong |\langle \psi_i | \widehat{\eta} \cdot \overrightarrow{r} | \psi_f^0 \rangle|^2 \left[1 + \langle \psi_i | \widehat{\eta} \cdot \overrightarrow{r} | \delta\psi_f \frac{\overline{\langle \psi_f^0 | \widehat{\eta} \cdot \overrightarrow{r} | \psi_i \rangle}}{|\langle \psi_i | \widehat{\eta} \cdot \overrightarrow{r} | \psi_f^0 \rangle|^2} + C.C. \right] \end{aligned} \tag{A.10}$$

where *C.C.* stands for complex conjugate. The absorption coefficient is modified by $\delta\psi_f$ through the dipole overlap integral with the initial state ψ_i (eq.(1.15))

The EXAFS function is defined as the difference between the absorption coefficient μ and the atomic absorption coefficient μ_0 normalized to μ_0:

$$\chi(k) = \frac{\mu(k) - \mu_0(k)}{\mu_0(k)} \tag{A.11}$$

and is generally expressed as a function of the photoelectron wave vector k. Typically the EXAFS signal represents a small fraction, comprised between 1% and 10%, of the atomic absorption coefficient. The main contribution to the χ signal comes from the spatial region very near to the nucleus of the absorbing atom where the core orbital of the extracted electron is localized. This region is at the same time source and detector for the photoelectron that probes the local structure around the absorber.

Given the above definition of EXAFS function we can also express the absorption coefficient in terms of $\chi(k)$:

$$\mu(k) = \mu_0(k)[1 + \chi(k)]. \tag{A.12}$$

Now comparing eq.(3.15) with eq.(A.12) we obtain the fine structure function χ that is:

$$\chi(k) \propto \langle\psi_i|\widehat{\eta}\cdot\overrightarrow{r}|\delta\psi_f\rangle = \int dr\psi_i^*(r)\widehat{\eta}\cdot\overrightarrow{r}\delta\psi_f(r). \tag{A.13}$$

The initial state, ψ_i corresponds to a deeply localized core level and so can be approximated with a delta function (a $1s$ level for an atom whose atomic number is Z extends up to a value equal to a_0/Z where a_0 is the Bohr radius). In this way a simple expression for the EXAFS function result:

$$\chi(k) \propto \int dr\delta(r)e^{ikr}\delta\psi_f(r) = \delta\psi_f(0) \tag{A.14}$$

As a consequence to calculate EXAFS contribution one has to know explicitly the perturbation to the final state wave function of the photoelectron in correspondence of the absorber atom.

A.2.1 Approximated calculus

The simplest system for the calculus of eq.(A.14) is made up of two atoms, A and B, absorber and scatterer atoms respectively, at a distance R_B from each other. The potential in the region between atoms A and B, inside which the photoelectron moves, can be schematized by means of the *muffin-tin* approximation. We can divide this region into three parts:

Region I: spherically symmetric potential centered on atom A;

Region II: inner constant potential connected, in a continuous way, to the potentials

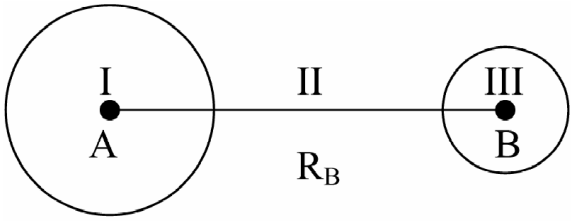

Figure A.1: Schematic picture of the muffin-tin potential in the region surrounding the two atoms, A (absorber) and B (backscatterer).

of regions I and III;

Region III: spherically symmetric potential centered on atom B.

The wave function ψ_i of the initial state 1s (angular momentum l=0) is confined to region I. We call as ψ_f^0 the final state wave function of the isolated atom (angular momentum l=1) associated to region I. In the case of an isotropic system a further simplification can be added: the term $\widehat{\eta} \cdot \overrightarrow{r}$ can be averaged so as to neglect the angular part of the wave functions.

In region I, the outgoing photoelectron can be described by the wave function ψ_f^0, as for the isolated atom. In region II (at constant potential) the radial part of the photoelectron wave function is described by an Hankel function, that for energies high enough ($kr >> 1$) can be approximated as:

$$i\frac{e^{ikr}}{2kr}e^{i\delta_1} \tag{A.15}$$

where δ_1 is the phase displacement necessary to connect the Hankel function of region I with ψ_f^0 of region I.

Now consider the interaction of the photoelectron with atom B in region III. If the photoelectron has enough high energy, it interacts significatively only with electrons of the inner orbitals of atom B. So one can suppose that diffusion will take place in a very small spatial region compared to R_B (*single atom approximation*). If the size of the scattering center tends to zero one can neglect also the curvature of the spherical wave incident on atom B (*plane wave approximation*). This fact allows to describe the process by means of the formalism of the plane wave expansion in partial waves.

Now consider the backscattering of the photoelectron's wave which so returns towards atom A and indicate as $f(k, \pi)$ the complex amplitude of back-diffusion:

$$f(k,\pi) = \frac{1}{k}\sum_{l=0}^{\infty}(-1)^l(2l+1)e^{i\delta_l}\sin\delta_l \tag{A.16}$$

where δ_l represent the phase displacements of the single partial waves.

In region II the radial part of the backscattered wave (l=1) will be expressed as:

$$\left[i\frac{e^{ikR_B}}{2kR_B}e^{i\delta_1}\right] f(k,\pi) \left[\frac{e^{ikr'}}{r'}e^{i\delta_1}\right] \tag{A.17}$$

where r' indicates the distance from the scatterer atom B. The first term represents the incident wave on B while the third term is the wave scattered from B. Also in the scattered wave a phase displacement δ_1 is present; it allows the connection to the wave function ψ_f^0 of region I.

Turning back to region I, the perturbation $\delta\psi_f$, introduced in eq.(A.9) can be expressed as the product of the backscattered wave of eq.(A.17) with the outgoing wave that in this region is represented by ψ_f^0. So in region I, in correspondence of the absorber atom ($r' = R_B$), one obtains:

$$\delta\psi_f = \psi_f^0 i f(k,\pi)\frac{e^{2ikR_B}}{2kR_B^2}e^{i\delta_1}. \tag{A.18}$$

At this point it's rather easy to obtain the expression of the EXAFS function: we can substitute eq.(A.18) into eq.(A.14):

$$\chi(k) = -\frac{1}{kR_B^2} Im[f_B(k,\pi)e^{2i\delta_1}e^{2ikR_B}] \tag{A.19}$$

where the minus sign is for a K-edge. Explicating phase and modulus of the complex backscattering amplitude ($f(k,\pi) = |f_B(k,\pi)|e^{i\phi}$) and grouping phase terms, eq.(A.19) can be written in real form as:

$$\chi(k) = -\frac{1}{kR_B^2}|f_B(k,\pi)|\sin(2kR_B + \phi(k)) \tag{A.20}$$

where $|f_B(k,\pi)|$ is the modulus of the backscattering amplitude, R_B is the interatomic distance while $\phi(k)$ takes into account the total phase displacement undergone by the photoelectron when it gets out from the absorber atom, is backscattered and turns back to the absorber atom: $\phi = 2\delta_1 + \varphi$.

Eq.(A.20) represents the EXAFS signal for a couple of atoms A and B at a distance R_B from each other. It is a sinusoidal trend whose frequency ($2R$) is proportional to the interatomic distance. Its total phase is perturbed by the phase displacement $\phi(k)$ while the amplitude is modulated through the $|f(k,\pi)|$ term.

When one deals with a system constituted of an higher number of atoms we can generalize eq.(A.20) in a quite simple manner neglecting the possibility of multiple diffusion of the photoelectron from surrounding atoms. Inside the single scattering approximation EXAFS function can be written as the sum of many different biatomic contributions of

the type of eq.(A.20):

$$\chi(k) = \sum_j \frac{1}{kR_B^2} Im[f_j(k,\pi)e^{2i\delta_1}e^{2ikR_j}] \tag{A.21}$$

where R_j indicates the position vector of the generic j-th atom respect to the absorber atom. The addition of a term S_0^2 is required to take into account 'many body' effects, hole life-time and structural disorder effects characteristic of every real structure.

Now we can pay attention to the effect of the 'life-time' of the excited state. The picture is made up of a photoelectron and an absorber atom with a core hole. EXAFS signal is related only to those processes that maintain coherence during the photoexcitation process. As a consequence one has to take into account the mean distance covered by the photoelectron before losing coherence, the mean free path λ.

About this two phenomena have to be considered:

- the mean core hole lifetime, τ_h, dependent on the atomic number Z but not linked to photoelectron energy;
- the mean photoelectron lifetime, τ_e, determined by the anelastic interaction of the photoelectron with the other external electrons and dependent on photoelectron energy. Considering $\lambda_e = v\tau_e$ one finds that it assumes quite large values in the XANES region (for energies below 10 eV) while in the EXAFS part of the spectrum it's comprised between 5 and 10 $\mathring{A}$.

The total lifetime, therefore, can be written as:

$$\frac{1}{\tau} = \frac{1}{\tau_h} + \frac{1}{\tau_e}. \tag{A.22}$$

The mean free path can be introduced into the EXAFS region through an exponential factor of the type: $e^{-2R_j/\lambda}$ with $\lambda = \nu\tau = \frac{\hbar k}{2m}\tau$. This factor contributes to the progressive reduction of the amplitude of EXAFS oscillations with increasing distance from back-scatterer atoms. This is one of the causes that make EXAFS sensitive to the short range order around the absorber atom.

Now if we group atoms into coordination spheres, each one containing N_s atoms of the same species at the same distance R_s from the absorber atom, we can express the contributions of the single coordination spheres considering EXAFS signal as given by the sum of all the coordination spheres:

$$\chi(k) = \frac{S_0^2}{k} \sum_s N_s Im \left[f_s(k,\pi)e^{2i\delta_1} \frac{e^{2R_s/\lambda}}{R_s^2} e^{2ikR_s} \right]. \tag{A.23}$$

The summation is made on the s-index that indicate coordination spheres with N_s coordination number of the s-th sphere.

Lastly, disorder effects have to be included. Consider a coordination sphere constituted by a single atomic species: even in a statistically isotropic system, because of disorder contributions, the distance r between the absorber atom and another atom of the selected coordination sphere has not a well defined value R_s. Instead it varies according to a probability distribution $g(r)$ properly normalized ($\int_0^\infty g(r)dr = 1$).

When one deals with a radial distribution of distances $g(r)$ EXAFS function associated to the s-th coordination sphere can be written as:

$$\chi_s(k) = \frac{S_0^2}{k} N_s Im \left[f_s(k,\pi) e^{2i\delta_1} \int_0^\infty g(r) \frac{e^{2r/\lambda}}{r^2} e^{2ikr} dr \right]. \tag{A.24}$$

In the case of small disorder the radial distribution $g(r)$ can be parametrized by a gaussian function:

$$g(r) = \frac{1}{\sigma\sqrt{2\pi}} e^{-\frac{(r-r_s)^2}{2\sigma}} \tag{A.25}$$

of mean value R and square deviation σ^2. In such a way the above formula assumes a quite simple form, best known also as *standard formula*:

$$\chi(k) = \frac{S_0^2}{k} \sum_s N_s |f_s(k,\pi)| \frac{e^{2r_s/\lambda}}{r_s^2} e^{-2k^2\sigma_s^2} \sin(2kr_s + \phi_s(k)). \tag{A.26}$$

where the factor $e^{-2k^2\sigma_s^2}$ is called *Debye-Waller factor*.

Bibliography

[1] H. S. Nalwa. Encyclopedia of Nanoscience and Nanotechnology (American Scientific, New York, 2004)

[2] S. A. Majetich and Y. Jin. *Science* **284**, 470 (1999)

[3] C. Back, R. Allenspach, W. Weber, S. Parkin, D. Weller, E. Garwin and H. Siegmann. *Science* **285**, 864 (1999)

[4] S. Sun, C. B. Murray, D. Weller, L. Folks and A. Moser. *Science* **287**, 1989 (2000)

[5] S. N. Piramanayagam. *J. Appl. Phys.* **102**, 011301 (2007)

[6] D. Weller and A. Moser. *IEEE Trans. Magn.* **35**, 4423 (1999)

[7] R. F. C. Farrow, D. Weller, R. F. Marks, M. F. Toney, A. Cebollada and G. R. Harpd. *J. Appl. Phys.* **79**, 5967 (1996)

[8] K. R. Coffey, M. A. Parker and J. K. Howard. *IEEE Trans. Magn.* **31**, 2737 (1995)

[9] M. Albrecht, A. Maier, F. Treubel, M. Maret, R. Poinsot and G. Schatz. *Europhys. Lett.* **56**, 884 (2001)

[10] A. Maier, B. Riedlinger, F. Treubel, M. Maret, M. Albrecht, M. Maret, E. Beaurepaire, J. M. Tonnerre and G. Schatz. *J. Magn. Magn. Mater.* **240**, 377 (2002)

[11] P. W. Rooney, A. L. Shapiro, M. Q. Tran and F. Hellman. *Phys. Rev. Lett.* **75**, 2843 (1995)

[12] M. Maret, M. Cadeville, R. Poinsot, A. Herr, E. Beaurepaire and C. Monier. *J. Magn. Magn. Mater.* **166**, 45 (1997)

[13] A. Moser, K. Takano, D. T. Margulies, M. Albrecht, Y. Sonobe, Y. Ikeda, S. Sun and E. E. Fullerton. *J. Phys. D: Appl. Phys.* **35**, R157 (2002)

[14] H. Zhou and H. N. Bertram. *IEEE Trans. Magn.* **35**, 2712 (1999)

[15] H. N. Bertram. Theory of Magnetic Recording (Cambridge University Press, 1994)

[16] L. Néel. *Ann. Geophys.* **5**, 99 (1949)

[17] S. Iwasaki and K. Takemura. *IEEE Trans. Magn.* **11**, 1173 (1975)

[18] L. B. Freund and S. Suresh. Stress, Defect Formation and Surface Evolution (Cambridge University Press, 2003)

[19] R. Kern, G. L. lay and J. J. Metois. *Curent topics in materials science* **3** (1979)

[20] E. Bauer. *Z. Kristallographie* **110**, 372 (1958)

[21] E. Bauer and H. Popper. *Thin Solid Films* **12**, 167 (1972)

[22] M. Volmer and A. Weber. *Z. Phys. Chem.* **119**, 277 (1926)

[23] F. C. Frank and J. H. V. D. Merwe. *Proc. Roy. Soc.* **A198**, 205 (1949)

[24] J. N. Stranski and L. Krastanov. *Ber. Akad. Wiss. Wien* **146**, 797 (1938)

[25] P. Müller and R. Kern. *Surf. Sci.* **457**, 229 (2000)

[26] H. Okamoto. *Phase Diagrams of Binary Iron Alloys* **ASM Int. 3**, 330 (1993)

[27] A. Sakuma. *J. Phys. Soc. Jap.* **63**, 3053 (1994)

[28] T. Massalski. *Binary Alloy Phase Diagram* **ASM Int. 2**, 1226 (1990)

[29] G. Inden. *Mat. Res. Soc. Symp. Proc.* **19**, 175 (1983)

[30] B. D. Cullity. Introduction to Magnetic Materials (Addison-Wesley, Reading, MA, 1972)

[31] S. H. Liou, Y. Liu, S. S. Malhotra, M. Yu and D. J. Sellmyer. *J. Appl. Phys.* **79**, 5060 (1996)

[32] M. R. Visokay and R. Sinclair. *Appl. Phys. Lett.* **66**, 1692 (1995)

[33] R. Boom, F. R. de Boer, A. K. Niessen and A. R. Miedema. *Physica* **115B**, 285 (1983)

[34] A. K. Niessen, A. R. Miedema, F. T. de Boer, and R. Boom. *Physica* **151B**, 401 (1988)

[35] G. G. V. Parasote, M. C. Cadeville and E. Beaurepaire. *J. Magn. Magn. Mater.* **198**, 375 (1999)

[36] S. H. Liou, S. Huang, E. Klimek and R. D. Kirby. *J. Appl. Phys.* **84**, 4334 (1999)

[37] Y. Xu, Z. Sun, Y. Qiang and D. Sellmyer. *J. Appl. Phys.* **93**, 8289 (2003)

[38] T. Seto, K. Koga, H. Akinaga, F. Takano, T. Orii and M. Hirasawa. *J. Nanoparticle Res.* **8**, 1572 (2006)

[39] J. J. Lin, Z. Y. Pan, S. Karamat, S. Mahmood, P. Lee, T. L. Tan, S. V. Springham and R. S. Rawat. *J. Phys. D: Appl. Phys.* **41**, 095001 (2008)

[40] N. Shukla, C. Liu and A. G. Roy. *Materials Letters* **60**, 995 (2006)

[41] T. Miyazaki, O. Kitakami, S. Okamoto, Y. Shimada, Z. Akase, Y. Murakami, D. Shindo, Y. K. Takahashi and K. Hono. *Phys. Rev. B* **72**, 144419 (2005)

[42] R. V. Chepulskii and W. H. Butler. *Phys. Rev. B* **72**, 134205 (2005)

[43] D. Alloyeau, C. Ricolleau, T. Oikawa, C. Langlois, Y. L. Bouar and A. Loiseau. *Ultramicroscopy* **108**, 656 (2008)

[44] C. Rong, D. Li, V. Nandwana, N. Poudyal, Y. Ding, Z. L. Wang, H. Zeng and J. P. Liu. *Adv. Mater.* **18**, 2984 (2006)

[45] J. E. Inglesfield and E. Wikborg. *J. Phys. F: Metal Phys.* **5**, 10392–10399 (1975)

[46] A. Rettenberger, P. Bruker, M. Metzler, F. Mugele, T. W. Matthes, M. Böhmisch, J. Boneberg and P. Leiderer. *Surf. Sci.* **402**, 409 (1998)

[47] M. Traving, M. Boehme, L. Kipp, M. Skibowski, F. Starrost, E. E. Krasovskii, A. Perlov and W. Schattke. *Phys. Rev. B* **55**, 1475 (1975)

[48] A. Koma, K. Sunouchi and T. Miyajima. *J. Vac. Sci. Technol. B* **3**, 724 (1985)

[49] A. Koëbel, Y. Zheng, J. F. Pétroff, J. C. Boulliard, B. Capelle and M. Eddrief. *Phys. Rev. B* **56**, 12296–12302 (1997)

[50] M. Gillet and A. Renou. *Thin Solid Films* **52**, 23 (1978)

[51] M. Dippel, A. Maier, V. Gimple, H. Wider, W. E. Evenson, R. L. Rasera and G. Schatz. *Phys. Rev. Lett.* **87**, 95505 (2001)

[52] M. Lämmlin. Diploma Thesis, Konstanz University, Germany (2003)

[53] D. Makarov, R. Pallesche, M. Maret, T. Ulbrich, G. Schatz and M.Albrecht. *Surf. Sci.* **601**, 2032 (2007)

[54] M. Maret, B. Gilles, I. L. Guhr, B. Riedlinger, M. Albrecht, G. Schatz and E. Beaurepaire. *Nanotechnology* **15**, 1590 (2004)

[55] C. Meneghini, M. Maret, V. Parasote, M. Cadeville, J. Hazemann, R. Cortes and S. Colonna. *Eur. Phys. J. B* **7**, 347 (1999)

[56] H. Reichert and altri. *Phys. Rev. Lett.* **78**, 3475 (1997)

[57] T. Schülli, J. Trenkler, I. Mönch, D. L. Bolloc'h and H. Dosch. *Europhys. Lett.* **58**, 737 (2002)

[58] M. Maret, A. Maier, F. Treubel, B. Riedlinger, M. Albrecht, E. Beaurepaire and G. Schatz. *J. Magn. Magn. Mater.* **242**, 402 (2002)

[59] M. Albrecht, M. Maret, A. Maier, F. Treubel, B. Riedlinger, U. Mazur, G. Schatz and S. Anders. *J. Appl. Phys.* **91**, 8153 (2002)

[60] S. Hashimoto, Y. Ochiai and K. Aso. *J. Appl. Phys.* **66**, 4909 (1989)

[61] C. Bourgognon, S. Tatarenko, J. Cibert, L. Carbonell, V. H. Etgens, M. Eddrief and B. Gilles. *Appl. Phys. Lett.* **76**, 1455 (2000)

[62] I. L. Guhr, B. Riedlinger, U. Mazur, A. Barth, F. Treubel, M. Maret, M. Albrecht and G. Schatz. *J. Appl. Phys.* **98**, 063520 (2005)

[63] M. Maret, M. Albrecht, J. Köhler, R. Poinsot, C. Ulhaq-Bouillet, J. Tonnerre, J. Berar and E. Bucher. *J. Magn. Magn. Mater.* **218**, 151 (2000)

[64] K. Elkins, D. Li, N. Poudyal, V. Nandwana, Z. Jin, K. Chen and J. P. Liu. *J. Phys. D: Appl. Phys.* **38**, 2306 (2005)

[65] Z. Gai, J. Y. Howe, J. Guo, D. A. Blom, E. W. Plummer and J. Shen. *Appl. Phys. Lett.* **86**, 023107 (2005)

[66] F. Gimenez, C. Chapon and C. R. Henry. *New J. Chem.* 1289 (1998)

[67] Y. Hirotsu and K. Sato. *J. Cer. Pros. Res.* **6**, 236 (2005)

[68] W. Hebenstreit, M. Schmid, J. Redinger, R. Podloucky and P. Varga. *Phys. Rev. Lett.* **85**, 5376 (2000)

[69] W. Braun. TApplied RHEED: reflection high-energy electron diffraction during crystal growth (Springer-Verlag Berlin Heidelberg, 1999)

[70] W. Friedrich, P. Knipping and M. V. Laue. *Sitzungsberichte der (kgl.) bayerische akademie der wissenschaften* **303** (1912)

[71] W. H. Bragg and W. L. Bragg. *Proc. R. Soc. A* **88**, 428 (1913)

[72] N. W. Ashcroft and N. D. Mermin. Solid state physics (Saunders College / Harcourt Brace College Publishers, 1976)

[73] S. I. Zabinsky, J. J. Rehr, A. Ankudinov, R. C. Albers and M. J. Eller. *Phys. Rev. B* **52**, 2995 (1995)

[74] 'Link: cars9.uchicago.edu/feff/feffusers/msg00078.html'

[75] D. C. Konigsberger and R. Prins. X-Ray Absorption. Principles, Applications, Techniques of EXAFS, SEXAFS and XANES (Wiley/Interscience, New York, 1988)

[76] P. A. Lee, P. H. Citrin, P. Eisenberger, and B. M. Kinkaid. *Rev. Mod. Phys.* **53**, 769 (1981)

[77] S. Pascarelli, F. Boscherini, F. D'Acapito, J. Hrdy, C. Meneghini and S. Mobilio. *J. Synchrotron Rad.* **3**, 147 (1996)

[78] 'Link: http://www.esrf.eu/info/science/newsletter/apr98/pdf/pages42to44.pdf'

[79] 'Link: http://www.esrf.eu/usersandscience/experiments/crg/bm30b'

[80] J. Levine, J. Cohen, Y. Chung and P. Georgopoulos. *J. Appl. Cryst.* **22**, 528 (1989)

[81] J. Levine, J. Cohen and Y. Chung. *Surf. Sci.* **248**, 215 (1991)

[82] A. Naudon and D. Thiaudiére. *J. Appl. Cryst.* **30**, 822 (1997)

[83] G. Renaud, R. Lazzari, C. Revenant-Brizard, A. Barbier, M. Noblet, O. Ulrich, Y. Borenstzein, J. Jupille, C. R. Henry, J. P. Deville, F. Scheurer and O. Fruchart. *Science* **300**, 1416 (2003)

[84] R. Lazzari. *J. Appl. Cryst.* **35**, 406 (2002)

[85] A. Guinier and G. Fournet. Small-Angle Scattering of X-rays (New York: Jonh Wiley, 1955)

[86] R. Hosemann and S. N. Bagchi. Direct Analysis of Diffraction by Matter (North-Holland, Amsterdam, 1962)

[87] A. Guinier. X-ray Diffraction in Crystals, Imperfect Crystals and Amorphous Bodies (New York: Dover, 1963)

[88] R. Lazzari, G. Renaud, J. Jupille and F. Leroy. *Phys. Rev. B.* **76**, 125412 (2007)

[89] J. S. Pedersen. *J. Appl. Cryst.* **27**, 595 (1994)

[90] J. S. Pedersen, P. Vysckocil, B. Schönfeld and G. Kostorz. *J. Appl. Cryst.* **30**, 975 (1997)

[91] A. Messiah. Quamtum Mechanic, volume 1-2 (Dunod, Paris, 1964)

[92] S. K. Sinha, E. B. Sirota, S. Garoff and H. B. Stanley. *Phys. Rev. B* **38**, 2297 (1988)

[93] M. Rauscher, R. Paniago, H. Metzger, Z. Kovats, J. Domke, J. Peisl, H.-D. Pfannes, J. Schulze and I. Eisele. *J. Appl. Phys.* **86**, 6763 (1999)

[94] J. Als-Nielsen and D. McMorrow. Elements of Modern X-ray Physics (Wiley, New York, 2001)

[95] C. Revenant, F. Leroy, R. Lazzari, G. Renaud and C. R. Henry. *Phys. Rev. B* **69**, 035411 (2004)

[96] R. Lazzari. 'http://www.insp.jussieu.fr/axe2/oxydes/isgisaxs/isgisaxs.htm'

[97] W. H. Press, S. A. Teukolsky, W. T. Vetterling and B. P. Flannery. Numerical Recipes in Fortran (Cambridge University Press, 1992)

[98] J. Ferrer, J. Simon, J. Berar, B. Caillot, E. Fanchon, O. Kaikati, S. Arnaud, M. Guidotti, M. Pirocchi and M. Roth. *J. Synchrotron Rad.* **5**, 1346 (1998)

[99] P. Gambardella, S. Rusponi, T. Cren, N. Weiss and H. Brune. *C. R. Physique* **6**, 75 (2005)

[100] G. Binning, H. Rohrer, C. Gerber and E. Weibel. *Phys. Rev. Lett.* **49**, 57 (1982)

[101] J. Tersoff and D. Hamann. *Phys. Rev. Lett.* **50**, 1998 (1983)

[102] J. Stroscio, R. Feenstra, D. Newns and A. Feinl. *J. Vac. Sci. Technol. A* **6**, 499 (1988)

[103] R. Shantyr. Ph.D. thesis, Martin-Luther-Universität (2004)

[104] D. B. Williams and C. B. Carter. Transmission Electron Microscopy (New York: Plenum Press, 1996)

[105] H. Gross, W. Singer and M. Totzeck. Handbook of Optical Systems, volume 2 (Wiley-VCH Verlag GmbH & Co. KGaA, 2005)

[106] C. E. Dahmani. Ph.D. thesis, Louis Paster Univeristy, Strasbourg, Germany (1985)

[107] W. B. Pearson. The Crystal Chemistry and Physics of Metals and Alloys (Wiley-Interscience, New York, 1972)

[108] H. Berg and J. Cohen. *Metall. Trans.* **3**, 1797 (1972)

[109] 'Carine crystallography software 3.1'

[110] F. James. 'Minuit: Function minimization and error analysis cern program library entry d506'

[111] V. Pierron-Bohnes, M. Maret, L. Bouzidi and M. Cadeville. *MRS'98 Spring Meeting, MRS Symposium Proceedings Series* **57**

[112] W. Grange, M. Maret, J. Kappler, J. Vogel, A. Fontaine, F. Petroff, G. Krill, A. Rogalev, J. Goulon, M. Finazzi and N. Brookes. *Phys. Rev. B* **58**, 6298 (1998)

[113] P. Bruno. *Phys. Rev. B* **39**, 865 (1989)

[114] R. Triolo, E. Caponetti and S. Spooner. *Phys. Rev. B* **39**, 4588 (1989)

[115] A. L. Shapiro, P. Rooney, M. Tran, F. Hellman, K. M. Ring, K. L. Kavanagh, B. Rellinghaus and D. Weller. *Phys. Rev. B* **60**, 12826 (1999)

[116] G. Rupprechter. *Phys. Chem. Chem. Phys.* **3**, 4621 (2001)

[117] O. Ersen, V. Parasote, V. Pierron-Bohnes, M. C. Cadeville and C. Ulhaq-Bouillet. *J. Appl. Phys.* **93**, 2987 (2003)

[118] R. F. C. Farrow, D.Weller, R. F. Marks, M. F. Toney, S. Hom, G. R. Harp and A. Cebollada. *Appl. Phys. Lett.* **69**, 1166 (1996)

[119] Y. K. Takahashi and K. Hono. *Scripta Mater.* **53**, 405 (2005)

Résumé

Nanostructures magnétiques auto-assemblées sur des surfaces à faible énergie par épitaxie par jets moléculaires

Les nanostructures d'alliages M_xPt_{1-x} (M=Co et Fe) développent des anisotropies magnétiques perpendiculaires, très intéressantes pour des applications dans le domaine de l'enregistrement à haute densité. Dans ce travail de thèse, la nature du substrat (structure, symétrie et énergie de surface) et l'influence de la température de co-déposition sur les propriétés structurales et magnétiques des nanostructures ont été étudiés. La méthode a consisté à déposer des atomes de métaux de transition par épitaxie à jets moléculaires sur les surfaces $WSe_2(001)$ et NaCl(001) de faible énergie. Elle a conduit à la formation de nanostructures modèles, non contraintes dont les propriétés ont été déterminées par différentes techniques (diffraction X, XAFS, GISAXS, MET, STM et magnétométrie SQUID). Les effets de mise en ordre chimique à courte et à longue distance et l'influence de la morphologie et de la direction de croissance sur les propriétés magnétiques ont été clairement démontrés.

Mots-clés : Nanostructures ; FePt, CoPt et $CoPt_3$ alliages ; Ordre chimique à longue distance ; Anisotropie magnétique ; Spectroscopie d'absorption de rayon x ; Diffusion aux petits angles en incidence rasante.

Abstract

Self-assembled magnetic nanostructures prepared by molecular beam epitaxy on low energy surfaces

Nanostructures of M_xPt_{1-x} (M=Co and Fe) alloys have perpendicular magnetic anisotropy which makes them good candidates as high density magnetic recording media. In this thesis work, the structural and magnetic properties of these nanostructures were studied as a function of the substrate (structure, symmetry and surface energy) and the co-deposition temperature. The nanostructures were prepared by co-deposition of transition metal atoms on low energy surfaces $WSe_2(0001)$ and NaCl(001) by molecular beam epitaxy. This led to the formation of stress-free nanostructures whose properties were characterized by techniques including X-ray diffraction, XAFS, GISAXS, TEM, STM and SQUID magnetometry. The chemical order effects at short- and long-range and the influence of morphology and growth direction on magnetic properties were clearly shown.

Key Words: Nanostructures; FePt, CoPt and $CoPt_3$ alloys; Long-range chemical order; magnetic anisotropy; X-ray absorption spectroscopy; Grazing-Incidence Small-Angle X-ray Scattering.